Program

LUNAR AND PLANETARY INSTITUTE

USRA

Seventh International Conference on Mars Polar Science and Exploration

January 13–17, 2020
Ushuaia, Tierra del Fuego, Argentina

Institutional Support

York University

Planetary Science Institute

Centro Austral de Investigaciones Cientificas (CADIC-CONICET)

University of Bern

International Association of Cryospheric Sciences

International Association of Geomorphologists

Lunar and Planetary Institute

Universities Space Research Association

Conveners

Isaac Smith
York University
Planetary Science Institute

Patricio Becerra
Space Research and Planetary Sciences, University of Bern

Local Organizers

Andrea Coronato
Centro Austral de Investigaciones Cientificas (CADIC)
Consejo Nacional de Investigaciones Cientificas y Técnicas (CONICET)

Jorge Rabassa
Centro Austral de Investigaciones Cientificas (CADIC)
Consejo Nacional de Investigaciones Cientificas y Técnicas (CONICET)

Lunar and Planetary Institute 3600 Bay Area Boulevard Houston TX 77058-1113

Science Organizing Committee

Isaac Smith
York University
Planetary Science Institute

Patricio Becerra
Space Research and Planetary Sciences, University of Bern

Ali Bramson
Lunar and Planetary Laboratory, University of Arizona

Shane Byrne
Lunar and Planetary Laboratory, University of Arizona

Serina Diniega
NASA Mars Program Office

Paul Hayne
Astrophysical and Planetary Sciences, University of Colorado, Boulder

Clemence Herny
Space Research and Planetary Sciences, University of Bern

Briony Horgan
Earth, Atmospheric, and Planetary Sciences, Purdue University

Christine Hvidberg
Niels Bohr Institute, University of Copenhagen

Melinda Kahre
NASA Ames Research Center

Anya Portyankina
Laboratory for Atmospheric and Space Physics, University of Colorado, Boulder

Aymeric Spiga
Laboratoire de Météorologie Dynamique, Sorbonne Université

Nicolas Thomas
Space Research and Planetary Sciences, University of Bern

Timothy Titus
U.S. Geological Survey Astrogeology Science Center

Jennifer Whitten
Tulane University

Conference Organizing Committee

Isaac Smith
York University
Planetary Science Institute

Patricio Becerra
Space Research and Planetary Sciences, University of Bern

Dave Beaty
NASA Mars Program Office

Maria Laura Borla
Conference Logistics

Wendy Calvin
University of Nevada, Reno

Andrea Coronato
Centro Austral de Investigaciones Cientificas (CADIC)
Consejo Nacional de Investigaciones Cientificas y Técnicas (CONICET)

Serina Diniega
NASA Mars Program Office

Jorge Rabassa
Centro Austral de Investigaciones Cientificas (CADIC)
Consejo Nacional de Investigaciones Cientificas y Técnicas (CONICET)

Student and Early Career Travel Grant Award Recipients

Seventh International Conference on Mars Polar Science and Exploration In-House Grant
Narissa Patel

International Association of Cryosphere Sciences (IACS)
Jacqueline Campbell
Shannon Hibbard

International Association of Geomorphologists (IAG)
Mauro Gabriel Spagnuolo
Prakhar Sinha

Abstracts for this conference are available via the conference website at
https://www.hou.usra.edu/meetings/marspolar2020/
Abstracts can be cited as
Author A. B. and Author C. D. (2020) Title of abstract. In *Seventh International Conference on Mars Polar Science and Exploration,* Abstract #XXXX. LPI Contribution No. 2099, Lunar and Planetary Institute, Houston.

Guide to Sessions

Sunday, January 12, 2020

6:00–8:00 p.m.	Conference Room at Centro Austral de Investigaciones Cientificas (CADIC), Ave. Bernardo Houssay 200, Ushuaia	6:00 p.m. Icebreaker/Welcome Reception and Sign-In 7:00 p.m. Special Presentation: The Geomorphology of Tierra del Fuego and Patagonia — Dr. Jorge Rabassa and Dr. Andrea Coronato

Monday, January 13, 2020

8:30 a.m.	Sala Niní Marshall Room	Welcome and Introductions
10:00 a.m.	Sala Niní Marshall Room	The Atmosphere Around the Martian Poles
1:30 p.m.	Sala Niní Marshall Room	Ice and Climate History — Part I: Observations
3:15 p.m.	Sala Niní Marshall Room	Ice and Climate History — Part II: Modeling

Tuesday, January 14, 2020

8:30 a.m.	Sala Niní Marshall Room	Recipes for Ice, Dust, and a Pinch of Salt
10:00 a.m.	Sala Niní Marshall Room	Geology of the Polar Regions
1:30 p.m.	Sala Niní Marshall Room	Scratching the Surface of the Polar Ice
3:30 p.m.	Sala Niní Marshall Room	Ice, Ice, Dry Ice
6:00 p.m.	Sala Niní Marshall Room Foyer	Poster Session

Wednesday, January 15, 2020

Wednesday Field Trips, Two Options

Thursday, January 16, 2020

8:30 a.m.	Sala Niní Marshall Room	Ice Off the Poles — Part I
10:15 a.m.	Sala Niní Marshall Room	Ice Off the Poles — Part II
1:30 p.m.	Sala Niní Marshall Room	Seasons Come and Seasons Go
3:30 p.m.	Sala Niní Marshall Room	Martian Icy Geomorphology... On Earth
6:00 p.m.	Sala Niní Marshall Room	Keynote Presentation Open to the Public: El Hielo de Marte: La Glaciología Marciana Visita Ushuaia

Friday, January 17, 2020

8:30 a.m.	Sala Niní Marshall Room	Gullies, Dust Devils, Wind... and More Ice
10:00 a.m.	Sala Niní Marshall Room	Robots, Rovers, and Roadmaps to the Future
1:45 p.m.	Sala Niní Marshall Room	Mars Polar Conference 2020 Synthesis Panel
3:15 p.m.	Sala Niní Marshall Room	Future Plans: Preparing for the Decadal Survey
4:15 p.m.	Sala Niní Marshall Room	Decadal Survey Discussion and Wrap-Up

Program

Sunday, January 12, 2020
WELCOME RECEPTION
6:00–8:00 p.m. Conference Room at Centro Austral de Investigaciones Cientificas (CADIC)

Times	Authors (*Denotes Presenter)	Abstract Title and Summary
6:45 p.m.	Smith I. B. and Becerra P.	*Welcome and Speaker Introduction*
7:00 p.m.	Rabassa J. and Coronato A.	*The Geomorphology of Tierra del Fuego and the Argentinian Patagonia*

Monday, January 13, 2020
WELCOME AND INTRODUCTIONS
Chairs: Isaac Smith and Patricio Becerra

Times	Authors (*Denotes Presenter)	Abstract Title and Summary
8:30 a.m.	Smith I. B. *	*Welcome*
8:45 a.m.	Becerra P. *	*Introductions and Requests for Synthesizers*
9:00 a.m.	Diniega S. *	*MEPAG Representative, Goals Update*
9:15 a.m.	Diniega S. *	*Report on the Findings of the Ice and Climate Evolution Science Analysis Group (ICE-SAG)*
9:30 a.m.		BREAK

Monday, January 13, 2020
THE ATMOSPHERE AROUND THE MARTIAN POLES
Chairs: Jeffrey Plaut and Chimira Andres

Times	Authors (*Denotes Presenter)	Abstract Title and Summary
10:00 a.m.	Kleinboehl A. * Kass D. M. Piqueux S. Hayne P. O. Noguchi K. **[INVITED]**	*Interhemispheric Differences in CO_2 Supersaturation and CO_2 Gas Depletion in Mars' Polar Winter Atmosphere from Mars Climate Sounder Observations* **[#6017]** MCS data reveal that atmospheric temperatures in the south polar winter repeatedly drop below the CO_2 frost point, in contrast to the north polar winter. These differences are evaluated with respect to CO_2 supersaturation and CO_2 gas depletion.
10:30 a.m.	Piqueux S. * Kleinböhl A. Hayne P. O. Kass D. M. Heavens N. McCleese D. J. Richardson M. I. Schofield J. T. Shirley J.	*Atmospheric CO_2 Depletion at the Surface in the Polar Regions of Mars* **[#6016]** The kinetic temperature of the north and south seasonal ice caps is derived using MCS data, and shown to be depressed by up to ~3 K. This depression is interpreted as an enrichment of non-condensable gasses by factors up ~7 at the surface.
10:45 a.m.	Kuroda T. *	*GCM Simulations of the Martian Winter Polar Atmosphere and CO_2 Snowfalls: Dependence of Horizontal Resolution and Radiative Effects of CO_2 Ice Clouds* **[#6035]** Investigations about the properties of the winter polar atmosphere and CO_2 snowfalls on Mars using a global climate model, especially about the dependence of horizontal resolution and radiative effects of CO_2 ice clouds, will be presented.
11:00 a.m.	Aye K.-M. * Hayne P. O.	*Polar Vortex Investigations Using MRO MCS Data* **[#6079]** We are doing multi-year comparisons of cloud structures using MCS data to learn if there are differences in polar vortex stability between the north and south pole.

11:15 a.m.	Andersson L. * Pillinski M.	*Influence of the Solar Wind on the Polar Upper Atmosphere of Mars* **[#6060]** Using the observations by the NASA MAVEN missions, we investigate the importance of energy input from the solar wind into the lower atmosphere, how the polar regions participate in this energy input, and what this means for ion escape.
11:30 a.m.		*Discussion of this morning's presentations about the polar atmosphere*
12:00 p.m.		LUNCH

Monday, January 13, 2020
ICE AND CLIMATE HISTORY — PART I: OBSERVATIONS
Chairs: Takeshi Kuroda and Jennifer Whitten

Times	Authors (*Denotes Presenter)	Abstract Title and Summary
1:30 p.m.	Paige D. A. * **[INVITED]**	*Snowball Mars: What the Current State of the Martian CO_2 Cycle Tells Us About Mars' Past Climate History* **[#6080]** The current state of the Mars CO_2 cycle is not coincidental, but the predictable consequence of a nearly perpetually frozen planet.
2:00 p.m.	Becerra P. * Nunes D. Smith I. B. Sori M. M. Thomas N.	*Two Views of the Martian North Polar Layered Deposits: Toward a Correlation of Radar and Visible Stratigraphic Records* **[#6055]** We present a preliminary correlation of SHARAD data of the NPLD to bedding outcrops imaged by HiRISE. This has the potential of improving constraints on accumulation models, and relating exposed beds and radar reflectors to dust content.
2:15 p.m.	Lalich D. E. * Raguso M. C. Poggiali V. Hayes A.	*Advances in the Use of Radar Reflectivity as a Climate Proxy in the North Polar Layered Deposits* **[#6051]** New radar processing techniques and more advanced reflectivity modeling allow us to better estimate how layer dust content changes both geographically and with depth in the NPLD.
2:30 p.m.	Ojha L. * Karimi S. Nerozzi S. Lewis K. Smrekar S. E. Siegler M.	*Martian North Polar Cap: Compositional Constraints and Geodynamical Response* **[#6022]** We use gravity, topography, and radar data to constrain the bulk density of the basal unit. We then constrain the mantle heat flow by modeling the response of the lithosphere to the stress imposed by the north polar cap.
2:45 p.m.		BREAK

Monday, January 13, 2020
ICE AND CLIMATE HISTORY — PART II: MODELING
Chairs: Alfred McEwen and Alicia Rutledge

Times	Authors (*Denotes Presenter)	Abstract Title and Summary
3:15 p.m.	Buhler P. B. * Piqueux S. Ingersoll A. P. Ehlmann B. L. Hayne P. O.	*Co-Evolution of the Martian Atmosphere and South Polar Massive CO_2 Ice Deposit* **[#6006]** Mars' massive south polar CO_2 deposit exchanges mass with its CO_2 atmosphere as its orbit evolves. We model this exchange to yield Mars' pressure history and the deposit's stratigraphic development.
3:30 p.m.	Patel N. * Lewis S. R. Hagermann A. Balme M.	*Stability of Subsurface Carbon Dioxide Ice Over the Obliquity Cycle* **[#6012]** We use the LMD-UK Mars Global Circulation Model with a new subsurface scheme to investigate how timescales for the stability of CO_2 ice are affected by overlying regolith at different obliquities within the range expected for Mars.

3:45 p.m.	Emmett J. A. * Murphy J. R. Kahre M. A.	*Quantifying Net Annual Polar Deposition Rates of Water Ice and Dust on Mars at Various Obliquities with the NASA/Ames Legacy Mars Global Climate Model* **[#6046]** The sensitivity of net annual polar deposition rates of water ice and dust on Mars to varied obliquity parameters and water ice reservoir locations is investigated with the NASA/Ames Legacy Mars GCM, and applied to a model of long-term NPLD layering.
4:00 p.m.	Vos E. * Aharonson O. Schorghofer N. Forget F. Millour E.	*The Role of Mid-Latitude Ground Ice in North Polar Layered Deposits Formation* **[#6037]** Subsurface ice can affect the NPLD physical stratigraphy via several mechanisms. In this work, we examine if the ground ice can act as a source and how it effects the accumulation via changing the seasonal thermal cycle.
4:15 p.m.	Naar J. * Forget F. Madeleine J.-B. Millour E. Spiga A. Vals M. Bierjon A. Benedetto de Assis L.	*Recent Formation of Ice-Rich Latitude-Dependent Mantle from Polar Ice Reservoirs* **[#6041]** New paleoclimatic simulations with improved parametrization of frost albedo and cloud microphysics allow for recent mid-latitude ice accumulation rates compatible with the deposition of ice-rich latitude-dependent mantle on Mars.
4:30 p.m.		*Discussion of the climate history of Mars via the PLD and lower latitude ice*
5:00 p.m.		*Adjourn*

Tuesday, January 14, 2020
RECIPES FOR ICE, DUST, AND A PINCH OF SALT
Chairs: Margaret Landis and Patricio Becerra

Times	Authors (*Denotes Presenter)	Abstract Title and Summary
8:30 a.m.	Yoldi Z. * Hvidberg C. Vallelonga P. Kjær H.	*Assessing Terrestrial Dust Within Ice Cores as a Proxy for Dust Trapped in the Polar Layered Deposits of Mars* **[#6033]** We present a collaboration between martian and terrestrial scientists. We will give an overview of the dust/climate coupling on Earth and show particle size measurements from ice cores. Then, we will discuss the comparison to the dust in the PLDs.
8:45 a.m.	Sinha P. * Horgan B.	*The Mineralogy of Lithic Sediments Within the North and South Polar Layered Deposits, Mars* **[#6077]** Comparing the primary mineralogy of lithic sediments within the north and south polar layered deposits of Mars using the technique of visible and near-infrared (VNIR) spectroscopy from orbit.
9:00 a.m.	Hanley J. * Bandelier Z. Murphy C. Carmack R. Horgan B.	*Strategies for Remotely Detecting Chlorine Salts on Mars* **[#6052]** How to detect salts? / Spectral features look alike / We test new methods.
9:15 a.m.	Cartwright S. F. A. * Calvin W. M. Seelos K. D.	*Spectral Variation Between South Polar Residual Ice Deposits in Mars Years 28 and 29* **[#6074]** We evaluate spectral variation in south polar water and carbon dioxide ice deposits between early and late Ls in Mars Years 28 and 29 in preparation for detailed spectral modeling.
9:30 a.m.		BREAK

Tuesday, January 14, 2020
GEOLOGY OF THE POLAR REGIONS
Chairs: Zuriñe Yoldi and Jennifer Hanley

Times	Authors (*Denotes Presenter)	Abstract Title and Summary
10:00 a.m.	Holt J. W. *	*Sand, Sun, Ice, Wind, Dust, and Time: An Updated History of Planum Boreum* **[#6071]** The latest big-picture view of Planum Boreum, from cavi to the surface.
10:15 a.m.	Nerozzi S. Holt J. W. * Spiga A. Forget F. Millour E.	*The Early History of Planum Boreum: An Interplay of Water Ice and Sand* **[#6064]** Ice crystals, sand grains / Small when alone; joined, they build / Immense polar caps.
10:30 a.m.	Abu Hashmeh N. A. * Whitten J. L. Campbell B. A.	*Areal Extent of Subsurface Basal Reflectors Within the South Polar Layered Deposits* **[#6047]** Using SHARAD and MARSIS data, we are mapping basal reflectors within the south polar layered deposits (SPLD). SHARAD basal reflectors predominantly occur along the periphery of the SPLD corresponding to the thinnest regions of the deposit.
10:45 a.m.	Plaut J. J. *	*Topographic, Compositional, and Textural Variations in Basal Interfaces Beneath the South Polar Plateau of Mars from MARSIS Radar Sounding* **[#6048]** Three-dimensional radar sounding image compilations of MARSIS data for south polar region are used to examine the variable properties of the basal interface.
11:00 a.m.	Smith I. B. *	*A Hypothesis for the "No-Flow" Mars' North Polar Layered Deposits Observations* **[#6040]** The observed stratigraphy and bulk properties of the POL do not match any predictions, on any scale for flowing ice. Here I explain the controversy and then propose a hypothesis that stratified layers disallow flow on the large scale.

11:15 a.m.	Whitten J. L. * Campbell B. A. Plaut J. J.	*Placing Constraints on the Composition and Emplacement of the Dorsa Argentea Formation* **[#6057]** The Dorsa Argentea Formation (DAF) is analyzed using SHARAD, MARSIS, CTX, and MOLA data to investigate the composition of the deposit, and determine if any ice is present. Results suggest the DAF does not preserve massive water ice deposits.
11:30 a.m.		*Discussion of Tuesday morning topics*
12:00 p.m.		LUNCH

Tuesday, January 14, 2020
SCRATCHING THE SURFACE OF THE POLAR ICE
Chairs: Leslie Tamppari and Michael Sori

Times	Authors (*Denotes Presenter)	Abstract Title and Summary
1:30 p.m.	Langevin Y. * Gondet B.	*Observations of the Polar Caps of Mars by OMEGA/Mex in the Visible Range* **[#6043]** Since early 2016, only the visible channel of the OMEGA imaging spectrometer on board Mars Express is operational. Using relevant spectral indexes, it can be used for extending investigations of polar processes over more than 8 martian years.
1:45 p.m.	Landis M. E. * McEwen A. S. Daubar I. J. Hayne P. O. Byrne S. Dundas C. M. Sutton S. S. Britton A. Herkenhoff K. E.	*South Polar Layered Deposits Near-Surface Properties Inferred from a Dated Impact Crater* **[#6025]** We present results from analyzing a new, dated ~18 m diameter SPLD impact and the implications for SPLD surface-properties. We find that the upper few meters of the SPLD are dominated by dust.
2:00 p.m.	Bapst J. * Piqueux S.	*Thermophysical Properties of Exposed South Polar Water Ice* **[#6070]** Derived thermophyscial properties of exposed water ice can be used to infer recent accumulation (e.g., snowpack with high porosity). Our preliminary findings support significant porosity, consistent with an episode of recent water-ice accumulation.
2:15 p.m.	Wilcoski A. X. * Hayne P. O.	*Modeling North Polar Residual Cap Surface Texture and Recent Resurfacing* **[#6058]** We model the evolution of surface texture on the NPRC caused by differential accumulation/ablation of ice. The spatial wavelengths of observed surface features are reproduced in 1000s of Mars-years, consistent with relatively recent resurfacing.
2:30 p.m.	Herkenhoff K. E. * Byrne S. Dundas C. M. Baugh N. F. Hunter M. A.	*HiRISE Observations of Recent Phenomena in the North Polar Region of Mars* **[#6059]** High-resolution images of the north polar region of Mars were used to quantify ongoing mass wasting of the polar layered deposits and complex redistribution of water frost. However, recent topographic changes are not observed in the residual cap.
2:45 p.m.	Pascuzzo A. C. * Melendez L. Mustard J. F.	*Present-Day and (Very) Recent Past Influences on Trough Migration: Measuring the Spatial Variation in Ice Sublimation of Equatorial-Facing Spiral Trough Walls* **[#6076]** Is there a measurable lateral difference in the amount of water ice sublimating along the trough walls? If so, what's the cause?
3:00 p.m.		BREAK

Tuesday, January 14, 2020
ICE, ICE, DRY ICE
Chairs: Jacqueline Campbell and Jonathan Bapst

Times	Authors (*Denotes Presenter)	Abstract Title and Summary
3:30 p.m.	McKeown L. E. * Diniega S. Portyankina G. Aye K. M. **[INVITED]**	*A Review of Martian CO_2 Sublimation Processes and Their Field and Laboratory Analogs* **[#6075]** We present a review of martian CO_2 sublimation processes and their Earth and laboratory analogues.
4:00 p.m.	Campbell J. D. * Schmitt B. Brissaud O. Muller J-P.	*Hyperspectral Mapping of the Martian South Polar Residual Cap Using Laboratory Analogues and Orbital Imagery* **[#6021]** In this work, we show the results of laboratory experiments designed to establish diagnostic spectra of organic signatures CO_2 ice, and apply the data to orbital hyperspectral imagery to look at dust composition and changes over time.
4:15 p.m.	Schmitt B. * Philippe S. Beck P. Brissaud O.	*Sublimation at Grain Boundaries of Polycrystalline CO_2 Slab Ice: The Clue to the Strong Spring Albedo Increase of the Martian Seasonal Polar Caps* **[#6069]** Experiments show that dust sinking and thermal cracking are not efficient at increasing the reflectance as observed on the martian seasonal caps during spring, but grain boundary opening during sublimation of CO_2 slab ice can do the job.
4:30 p.m.	Cesar C. * Pommerol A. Herny C. Hansen C. J. Portyankina G. Thomas N.	*CO_2 Ice and MGS-1 Mars Global Simulant: Experimental Work to Recreate Dark Spot Evolution Activity and Self-Cleaning Processes Observed by CaSSIS* **[#6044]** Dark spots, observed by the CaSSIS imager, are believe to come from jet-like activity from sublimating CO_2 seasonal caps. We explore experimentally the self-cleaning processes to understand odd spot features seen on several acquisitions.
4:45 p.m.		*Discussion of Tuesday afternoon topics*
5:15 p.m.		BREAK

Tuesday, January 14, 2020
POSTER SESSION
6:00–8:00 p.m. Sala Niní Marshall Room Foyer

Authors (*Denotes Presenter)	Abstract Title and Summary
Zirnov S. Z.	*Mars Abstract* **[#6002]** This paper outlines the importance of Mars lava tubes and how they may be used as emergency storages for supplies and emergency dwellings, once humans will step on Mars' surface again.
Gondet B. Bibring JP. Langevin Y.	*Atmospheric Phenomena Observed by OMEGA/MEX Over High Latitudes* **[#6036]** We will present atmospheric phenomena observed by OMEGA on board of Marx Express during 15 years, in particular gravity waves, vortex, and dust storms.
Streeter P. M. Lewis S. R. Patel M. R. Holmes J. A.	*Martian Polar Vortex Dynamics and the 2018 Global Dust Storm* **[#6042]** Mars' polar vortices play key roles in the planet's general circulation and atmospheric transport. The 2018 Global Dust Storm had a strong impact on dynamics at both poles, with implications for tracer transport into and around the polar regions.
Kahre M. A. Haberle R. M.	*Water Ice Cloud Feedbacks Over the North Polar Residual Cap at Moderate Obliquity* **[#6068]** We present a global climate model investigation of water ice cloud feedbacks over the north polar residual cap at moderate obliquity.
Karimova R. Smith I. B.	*An Experimental Setup to Study CO_2 Ice in a Simulated Martian Environment* **[#6014]** We have created an experimental setup to investigate the formation, behavior, and optical properties of CO_2 ice under martian conditions. We create CO_2 ice and record variability of textures related to the differences in formation conditions.
Collins-May J. L. Carr J. R. Balme M. R. Brough S. Gallagher C. Ross N. Russell A. J.	*The Comparative Distribution of Flowing and Non-Flowing Icy Material in the Nereidum Montes; Mars* **[#6007]** The aim of this work is to investigate whether there are significant topographical differences in the locations of flowing versus non-flowing deposits of ice in the Nereidum Montes.
Obbard R. W. Sarrazin P. Vo N. Zacny K. Byrne S.	*In Situ MicroCT Instrument for the North Polar Layered Deposits of Mars* **[#6078]** The Mars In Situ Tomography System is a miniaturized micro computed tomography (CT) instrument concept intended for deployment to the Mars North Polar Layered Deposits (NPLD) on a lander or rover.
Serla J. K. Christensen P. R. Grau Galofre A.	*Ice in the Mid-Latitudes of Mars: An Initial Study of Ice Dynamics* **[#6073]** This is our first attempt at developing a physics-based model to quantitatively characterize the ice dynamics of mid-latitude ice on Mars. Our focus for this conference is on lobate debris apron landforms.
Diniega S. Hansen C. J. Portyankina G.	*Proxy Records of Frost: Frost-Driven Geomorphic Changes on Martian Sandy Slopes* **[#6010]** Frost forms and sublimes / Sand rapidly displaces / Frost marker remains.
Zirnov S. Z.	*Building an Archive Library on Mars* **[#6003]** This paper outlines the importance and necessity of building an archive library on Mars moon, and the effect it may have on future generations and our distant descendants. Building an archive library will help in many ways and one of them.
Hvidberg C. S. Yoldi Y. Grinsted A.	*Surface Patterns of Terrestrial Ice Sheets — From In-Situ to Space Observations* **[#6039]** The large terrestrial ice sheets are observed continuously from space. Ice-atmosphere interactions are imprinted into the surface patterns. We discuss the potential to infer surface processes from space with potential applications for Mars.
Sinha P. Horgan B. H. N. Ewing R. Rampe E. B. Lapotre M. G. A. Nachon M. Thorpe M. Bedford C. Mason K. Champion E. Gray P. C. Reid E. Faragalli M.	*Sand-E: A Rover-Based Analog Study of Polar Science an a Mafic Sedimentary Environment, Iceland* **[#6056]** SAND-E is a NASA-supported analog research project to both advance the current state of rover operations and science framework within a mafic detrital environment by conducting Mars analog research in the glacio-fluvial-eolian landscapes of Iceland.

Wednesday, January 15, 2020
WEDNESDAY FIELD TRIPS

Mid-conference field trips will be guided full-day trips focused on the physical geography and glacial geomorphology of the areas around Ushuaia and along the Beagle Channel. Participants must choose between two options.			
7:45 a.m.	Meeting Point: Sala Niní Marshall	Option 1: Tierra del Fuego National Park	This trip will take participants 12 km outside Ushuaia by bus to Tierra del Fuego National Park, where they will enjoy the park's hiking trails and its unique combination of glacial and coastal environments. The park is part of the natural habitat of native species such as guanaco, huillin, red fox, and many species of birds.
6:30 a.m.	Meeting Point: Peurto de Ushuaia, corner of Avenida Costanera with Comodoro Augusto Laserre	Option 2: Boat trip along the Beagle Channel	The Beagle Channel, named after the famous HMS Beagle that had Charles Darwin as a passenger during its hydrographic survey of South America, is a strait that connects the Atlantic and Pacific Oceans, separating the larger main island of Tierra del Fuego from various smaller islands. The port of the city of Ushuaia is located within the Beagle Channel. Participants will take a boat along a portion of the western channel within Argentina, enjoying a view of the ancient glacial landscapes from the coast, as well as the possibility of seeing native fauna, such as seals, cormorants, and the colony of penguins on Martillo Island.

Thursday, January 16, 2020
ICE OFF THE POLES — PART I
Chairs: Laila Andersson and David Paige

Times	Authors (*Denotes Presenter)	Abstract Title and Summary
8:30 a.m.	Bramson A. M. * Molaro J. L. Petersen E. I. Bain Z. M. Putzig N. E. Morgan G. A. Smith I. B. Sizemore H. G. Baker D. M. H. Perry M. R. Mastrogiuseppe M. Hoover R. H. Campbell B. A. Pathare A. V. **[INVITED]**	*Polar Is in the Eye of the Beholder: Ice-Rich Units Across the Mid-Latitudes of Mars* **[#6015]** We present the results of mapping subsurface radar reflectors in the northern mid-latitudes of Mars as part of the SWIM Project and model ice sintering processes to understand lateral and vertical heterogeneities within ice-rich units.
9:00 a.m.	Viola D. *	*Age-Dating of Mid-Latitude Martian Thermokarst and Mantle Deposits: A Preliminary Assessment* **[#6054]** A preliminary analysis of an effort to age-date intact ice-rich mantle material and thermokarstic degradation features in Utopia and Arcadia Planitiae, with implications on the history of ice mantle deposition in the martian mid-latitudes.
9:15 a.m.	Sori M. M. * Bramson A. M. Byrne S. James P. B. Keane J. T.	*Gravitational Constraints on Mid-Latitude Ice... And the Need for More Gravity Data at Mars* **[#6026]** Gravity provides constraints on the volume of buried mid-latitude ice on Mars. Future missions that acquire more precise and higher resolution gravity measurements hold promise for addressing many outstanding problems in Mars polar science.
9:30 a.m.	El-Maarry M. R. * Diot X.	*Geologic Investigation of a Debris-Covered Mountain Glacier in Argyre Basin, Mars: Implications for Past Climate and History of Non-Polar Ice* **[#6034]** We present results from an ongoing investigation of a mountain glacier in the Argyre Basin to try to understand the origin of the ice in this region.
9:45 a.m.		BREAK

Thursday, January 16, 2020
ICE OFF THE POLES — PART II
Chairs: Ali Bramson and Timothy Titus

Times	Authors (*Denotes Presenter)	Abstract Title and Summary
10:15 a.m.	Meng T. M. * Petersen E. I. Christoffersen M. S. Tober B. S. Holt J. W.	*Lack of Meltwater May Prevent Radar Sounding Measurements of Supraglacial Debris Thickness in the Martian Midlatitudes* **[#6066]** Debris is sorted / Does water play a big role? / Let's talk about it.
10:30 a.m.	Wang K. Y. * Yin A.	*Surface Textures of Lunear Round-Topped Ridges in the Southern Highlands: Evidence for a Cold-Based Glacaited Landscape* **[#6065]** In the southern highland of Mars, origins of the linear round-topped ridges could be evidence for a cold-based glaciated landscape. They commonly bound linear troughs radiating from the south polar ice cap.
10:45 a.m.	Yin A. * Wang K. Y.	*Boulder-Layer Pavement Across the Southern Highlands and Cold-Based Continental-Scale Glaciation* **[#6067]** A first-order question in the studies of Mars is whether most or the entire southern hemisphere highlands were once occupied by a single ice sheet.
11:00 a.m.	Grau Galofre A. * Whipple K. X. Christensen P. R. Osinski G. R. Jellinek A. M. Chartrand S. M.	*The Apparent Lack of Wet-Based Glaciation Fingerprints on Mars* **[#6049]** The landforms expected for wet-based glaciation on Mars may differ from those on Earth: We present evidence for how the lower martian gravity may fundamentally alter glacial drainage under wet-based ice masses, halting glacial sliding.

11:15 a.m.	Rutledge A. M. * Graly J. A. Horgan B. Rampe E. B. Scudder N. A. Smith R. J.	*Mineralogical Signatures of Cold and Icy Alteration on the Surface of Mars* **[#6024]** Terrestrial glacier analogs show that cold and icy alteration results in poorly crystalline, silica-rich secondary minerals. Amazonian/Hesperian surfaces on Mars contain these phases, consistent with glacial/periglacial weathering in cold climates.
11:30 a.m.		*Discussion of the morning topics*
12:00 p.m.		LUNCH

Thursday, January 16, 2020
SEASONS COME AND SEASONS GO
Chairs: K.-Michael Aye and Wendy Calvin

Times	Authors (*Denotes Presenter)	Abstract Title and Summary
1:30 p.m.	Hansen C. J. * Aye K.-M. Diniega S. Hayne P. McEwen A. Portyankina G. Schwamb M. E. **[INVITED]**	*Dynamic Seasons on Mars — Polar Images and Investigations* **[#6019]** Multi-Mars year datasets reveal interannuability in seasonal processes and changes in landforms.
2:00 p.m.	Portyankina G. * Aye K.-M. Schwamb M. E. Hansen C. J. Michaels T.	*Near-Surface Winds and Seasonal Surface Phenomena Analyzed by the Planet Four Project* **[#6062]** We used a catalog of seasonal fans and blotches measured by citizen scientists participating in the project Planet Four to analyze the spring evolution of deposits from CO_2 jets and determine wind speeds and directions during their formation.
2:15 p.m.	Titus T. N. * Williams K. E. Cushing G. E.	*North Polar Springtime Removal of Cold-Trapped H_2O Ice Through Insolation-Induced Basal Sublimation of CO_2* **[#6001]** CO_2 gas from insolation-induced basal sublimation fractures cold-trapped water ice on the CO_2 ice surface, removing the H_2O ice from direct thermal contact with the CO_2 ice. Smaller fragments can be lofted while larger fragments are pushed aside.
2:30 p.m.	Calvin W. M. * Seelos K. D.	*Evolution of Seasonal Ice in Reynolds Crater and Promethei Rupes from CTX and CRISM* **[#6031]** CTX and CRISM observations are used to examine terrain within and adjacent to the cryptic region to understand processes governing the regional development of jets and evolution of the subliming ice surfaces.
2:45 p.m.	Hu R. *	*The Role of Regolith in the D/H Variation on Mars from the Poles to the Equator* **[#6009]** We find that the D/H can vary by 300–1400‰ diurnally in the equatorial and polar locations driven by the regolith-atmosphere exchange.
3:00 p.m.		BREAK

Thursday, January 16, 2020
MARTIAN ICY GEOMORPHOLOGY... ON EARTH
Chairs: Serina Diniega and Clémence Herny

Times	Authors (*Denotes Presenter)	Abstract Title and Summary
3:30 p.m.	Knightly J. P. * Tullis J. Dixon J. Chevrier V. F.	*Micromorphology of Relic Terrestrial Patterned Ground as a Mars Analog* **[#6030]** Relic patterned ground / By drone photogrammetry / Insight from HiRISE.
3:45 p.m.	Hibbard S. M. * Osinski G. R. Godin E. Kukko A.	*Terrestrial Brain Terrain and the Implications for Martian Mid-Latitudes* **[#6023]** Brain terrain on Earth / Periglacial or glacial? / What about on Mars?

4:00 p.m.	Andres C. N. * Osinski G. R. Godin E.	*3D-Modelling of Subsurface Ice Using Ground Penetrating Radar on Axel Heiberg Island, Canadian High Arctic* **[#6032]** Ground penetrating radar (GPR) is a geophysical technique that allows high-resolution, non-destructive stratigraphic imaging of the subsurface. 3D-GPR was used to model near-surface ice beneath periglacial ice-wedge polygons as seen on Earth and Mars.
4:15 p.m.	Petersen E. I. * Meng T. M. Holt J. W. Levy J. S. Tober B. S. Christoffersen M. S.	*Sulphur Creek and Galena Creek, Wyoming: Laboratories for Understanding the Preservation of Debris-Covered Glaciers on Mars* **[#6053]** Tale of two glaciers / One preserved by much debris / The other, not quite.
4:30 p.m.		*Discussion of Thursday afternoon presentations*
5:00 p.m.		*Adjourn*

Thursday, January 16, 2020
KEYNOTE PRESENTATION OPEN TO THE PUBLIC:
EL HIELO DE MARTE: LA GLACIOLOGÍA MARCIANA VISITA USHUAIA
6:00–7:30 p.m. Sala Niní Marshall Room

Times	Authors (*Denotes Presenter)	Presentation Title
6:00 p.m.	Becerra P. *	*Keynote Presentation in Spanish — The Ice of Mars: Martian Glaciology*

Friday, January 17, 2020
GULLIES, DUST DEVILS, WIND... AND MORE ICE
Chairs: John Holt and Ganna Portyankina

Times	Authors (*Denotes Presenter)	Abstract Title and Summary
8:30 a.m.	Dundas C. M. *	*Frequency and Morphological Consequences of Martian Gully Activity* **[#6028]** Extensive gully activity in the modern climate indicates that CO_2 frost may be the driver of all gully formation, without liquid water.
8:45 a.m.	Herny C. * Merrison J. Iversen J. J. Yoldi Z. Bordiec M. Carpy S. Bourgeois O. Thomas N.	*Wind Tunnel Experimentation of Ice Particles Transport in Martian-Like Environment* **[#6050]** We performed experiments of ice particles transport in a wind-flow under low temperatures and low pressures. The threshold shear velocity is estimated to evaluate the plausibility of ice particle transportation by wind at the surface of Mars.
9:00 a.m.	Chojnacki M. * Bapst J. Smith I. B. Herkenhoff K. E.	*Rates and Trends of Circum-Polar Aeolian Dune Evolution* **[#6045]** The purpose of this work is to quantify and characterize major elements of polar landform evolution, such as sand dune formation, bedform dynamics, and deposition of sand into the polar sedimentary record.
9:15 a.m.	Tamppari L. K. * Ochoa V. Sun V.	*Dust Devil Orientation and Mars Surface Winds* **[#6011]** Dust devil tracks from CTX data are cataloged for 65–72N. Images overlapping Phoenix in space and time show changes which are correlated to wind speed and direction and to a passing low-pressure system.
9:30 a.m.		BREAK

Friday, January 17, 2020
ROBOTS, ROVERS, AND ROADMAPS TO THE FUTURE
Chairs: Paul Streeter and Candice Hansen

Times	Authors (*Denotes Presenter)	Abstract Title and Summary
10:00 a.m.	Byrne S. * Hayne P. O. Calvin W. M. Tamppari L. K. Kleinböhl A. Smith I. B. Becerra P.	*Climate Orbiter for Mars Polar Atmospheric and Subsurface Science (COMPASS)* **[#6013]** COMPASS is a Discovery-class mission that provides key missing datasets to leverage our understanding of terrestrial climate records and meteorology to Mars. It links current climate with past climate variations recorded in Mars' icy deposits.
10:15 a.m.	Thomas N. * Becerra P. Smith I. B. Cremonese G.	*Current and Future Hardware Contributions to Mars Polar Science* **[#6038]** Presentation of CaSSIS data from the martian poles (up to 74 deg latitude) and discussion of future missions building on the European orbital hardware contribution.
10:30 a.m.	McEwen A. S. * Sutton S. S. Bramson A. M. Byrne S. Petersen E. I. Levy J. S. Golombek M. P. Williams N. R. Putzig N. E.	*Phlegra Montes: Candidate Landing Site with Shallow Ice for Human Exploration* **[#6008]** The Phlegra Montes may be the best region for human exploration of Mars due to abundant shallow ice at relatively low latitude, the presence of compositional and topographic diversity, and flat and smooth (boulder-free) areas.
10:45 a.m.	Hoffman S. J. * Lever J. H. Andrews A. D. Watts K. D.	*Experimental Heat Transfer Supporting Simulated Water Well Performance on Mars* **[#6027]** An experiment at the NASA Johnson Space Center is gathering data for convective heat transfer and evaporation rates at Mars surface conditions to support computer simulation of a subsurface water well (Rodriguez Well) and predict performance on Mars.

11:00 a.m.	Cook C. W. * Byrne S. Viola D. Drouet d'Aubigny C. Mikucki J.	*Detection Limits for Chiral Amino Acids Using a Polarization Camera* **[#6018]** We assess the potential of optical rotation measurements of polarized light to quantify enantiomeric excesses, a biosignature, in amino acid and bacterial samples.
11:15 a.m.	Stoker C. R. * Noe Dobrea E. Z.	*We Should Search for Life in Mars N. Polar Ground Ice* **[#6061]** We describe the rational and approach of a mission to search for life in north polar ground ice that is habitable during high obliquity periods.
11:30 a.m.	Glass B. * Goordial J. Parro V. Seitz S. Bergman D. Eigenbrode J. Dave A. Rogg A.	*A Dual Architecture for Subsurface Access to Mars Volatiles Deposits* **[#6063]** A dual architecture for volatiles: An ice prospecting rover locates and retrieves ice-bearing samples, bringing to a stationary "lab lander" base for in-situ analysis. Proposed for testing at Mars polar analogs (Haughton impact site).
11:45 a.m.		*Discussion of Friday morning topics*
12:15 p.m.		LUNCH

Friday, January 17, 2020
PANELS AND DISCUSSIONS

Times		
1:45 p.m.	Mars Polar Conference 2020 Synthesis Panel	*Here we receive a synthesis of the conference from our volunteers. Synthesis of the conference and feedback from the audience.*
2:45 p.m.	BREAK	
3:15 p.m.	Future Plans: Preparing for the Decadal Survey	*Panel discussion leading to the preparation of white papers for the Decadal Survey*
4:15 p.m.	Decadal Survey Discussion and Wrap-Up	*Open discussion to address the upcoming Decadal Survey and advocating for Mars Polar Science. Conference wrap up and consider timing and location for an 8th ICMPSE in 2024.*
5:15 p.m.		*Adjourn*

Notes

CONTENTS

AREAL EXTENT OF SUBSURFACE BASAL REFLECTORS WITHIN THE SOUTH POLAR LAYERED DEPOSITS. N. Abu Hashmeh[1], J. L. Whitten[1], B.A. Campbell[2], [1]Tulane University, New Orleans, LA, 70118, USA. [2]Center for Earth and Planetary Studies, Smithsonian Institution, MRC 315, PO Box 37012, Washington, DC 20013. Contact: nabuhashmeh@tulane.edu, jwhitten1@tulane.edu.

Introduction: Among the most areally extensive reservoirs of water ice on Mars, the south polar layered deposits (SPLD) in particular contain compelling evidence of variations in the planet's recent climatological history. The SPLD exhibits interbedded dust of varying thicknesses accumulated at different stages of Mars' recent orbital history [1, 2]. Early analysis of the SPLD stratigraphy was focused along the margins where layers were exposed at the surface [3-5]. Since then, radar instruments in orbit have been used to penetrate the surface of the ice to observe the stratigraphic variations throughout the interior of the SPLD [6-8]. Variations of ice and dust thicknesses show that the SPLD has undergone identifiable erosional and depositional processes before its current stagnation, providing more insight into climate behaviors during its emplacement [9]. Radar investigations have also shown the SPLD interior to exhibit low reflectivity zones, some of which are known to host sequestered carbon dioxide ice that may have played a role in the retention of surface water during past climate conditions [10, 11].

The continued collection of radar data from the SPLD will play a large role in the study of Mars' recent climate history. However, there are observable gaps in the radar datasets that may yield important information about certain parts of the SPLD interior. In particular, the ability of radar to penetrate through the entire SPLD appears to vary with signal frequency [6]. The preliminary work presented here aims to begin addressing the cause of this phenomenon by first mapping out the regions where the signal reaches the base of the SPLD.

Methods: Two orbital radar sounders prove useful for studying the SPLD interior. The Shallow Radar (SHARAD) instrument aboard the Mars Reconnaissance Orbiter (MRO) [12] emits a signal frequency of 20 MHz with a bandwidth of 10 MHz. SHARAD's along-track resolution is 0.3-1.0 km and has a vertical resolution of ~15 m in free space (~8 m in geologic materials). The Mars Advanced Radar for Subsurface and Ionosphere Sounding (MARSIS) instrument aboard Mars Express (MEX) [13] is capable of emitting at 1.8, 3.0, 4.0, and 5.0 MHz with a bandwidth of 1 MHz and an along-track resolution of 5-10 km.

The signal reflections are processed to produce radargrams that highlight some of the underlying stratigraphy within the SPLD. One hundred and seventeen incoherently summed SHARAD radargrams [6] covering the south polar region of Mars were analyzed to identify potential basal reflectors. The identified reflectors were then sorted by confidence level with the following classifications: distinct, somewhat distinct/uncertain, and very uncertain.

Distinct features are interpreted with high confidence to be part of the basal reflector; they tend to be vertically removed from and do not exactly conform to the shape of the overlying reflectors (Fig. 1). Somewhat distinct/uncertain reflectors are unmistakably visible but can be harder to distinguish as unique from the overlying reflectors of the SPLD. In particular, somewhat distinct reflectors have a strong signal but could be questionable when trying to distinguish from the lowest reflector in a packet of reflectors. Some of the more uncertain reflectors are detected at the edge of the SPLD and often follow the shape of the ground surface just outside the edges of the ice; however, these signals tend to disappear very quickly and are harder to distinguish from overlying reflectors. The very uncertain reflectors are mostly of the same nature

Figure 1. *Example of an incoherently summed SHARAD radargram showing a distinct basal reflector. Track number 9376-01. Only a portion of the radargram is shown.*

as the somewhat distinct/uncertain class, but are faint enough that their edges become difficult to define with precision; alternatively, these signals can be visually apparent but lack a distinct enough shape to resemble a basal reflector surface.

Some radargrams have more than one visible reflector. These potential reflectors were spatially projected in map view to visualize their locations within the SPLD (Fig. 2). Beyond map projections, further analysis will be done to determine the influence of the SPLD's surface morphology and characteristics on the presence of basal reflectors.

Preliminary Results: MARSIS is able to penetrate through and detect a basal reflector throughout most of the SPLD [8], while SHARAD is unable to penetrate through the entire thickness of the ice before being scattered and attenuated. The SHARAD signal is greatly attenuated in the thickest regions of the SPLD, but the signal is also observed to be scattered and attenuated in the thinnest portions of the SPLD, like Ultimate Lingula. This scattering creates a fog-like appearance most readily observable in the thicker regions of the deposit [6]. Due to the different frequency ranges between these two instruments, it is apparent that this phenomenon is frequency dependent.

SHARAD radargrams typically show features at the edges of the SPLD which could be interpreted as the basal reflector. These edge reflectors quickly disappear towards the thicker parts of the SPLD, but they can provide a constraint on some of their boundaries. Out of the 117 radargrams analyzed, 19 contained distinct basal reflectors, 19 contained somewhat distinct features, 57 were uncertain, and 22 were very uncertain.

The majority of these reflectors are found in SHARAD tracks that overlap. Overlapping tracks were referenced to each other to confirm the existence of a reflector; some of these same features appear with different distinctiveness across these overlapping tracks. Most of the identified reflectors are associated with thinner regions along the perimeter of the SPLD, but some notable detections exist beneath the residual polar cap in thicker ice (Fig. 2). In addition, there is an apparent cluster of distinct reflectors around 225º degrees that extend considerably far into the SPLD; another less distinct but still notable cluster exists around 350º degrees. Very few observed reflectors appear to be completely isolated. Since they appear to exist within a reasonably close proximity to one another, clusters of less distinct detections may provide more confidence for identifying the basal reflector within that region.

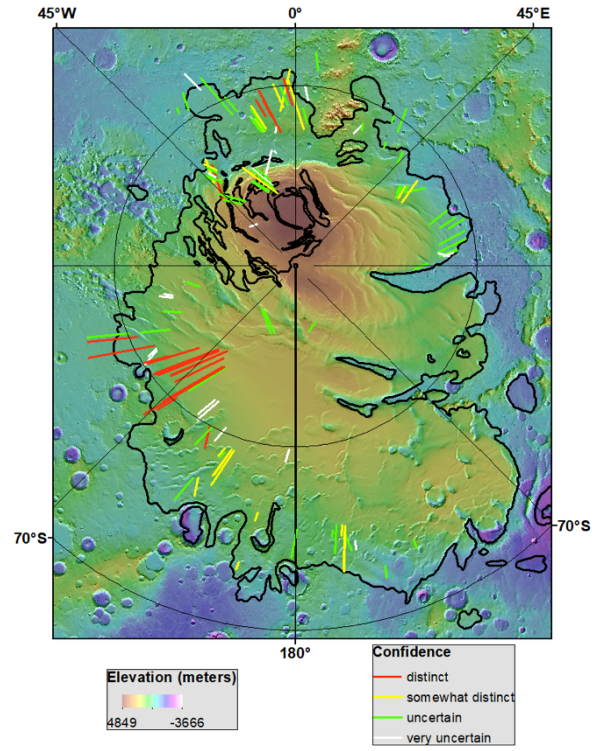

Figure 2. *Basal reflector detections in SHARAD radargrams projected onto the SPLD. Mars Orbiter Laser Altimeter (MOLA) hillshade maps at 128 ppd.*

Future Work: Following this preliminary work, more incoherently summed SHARAD radargrams will be analyzed and added to the dataset. MARSIS has recorded much more data since it was initially used to map the basal interface [14], so these data will also be heavily utilized to re-map the basal interface. MARSIS data will be analyzed using the same techniques presented here to map the basal interface of the SPLD, which will then be used as a reference for the SHARAD reflectors to better constrain the nature of their response.

References: [1] Thomas P. et al. (1992) *Mars* pp. 767-795. [2] Laskar et al. (2002) *Nature, 419,* 375-377. [3] Toon O. B. et al. (1980) *Icarus, 44,* 552-607. [4] Cutts J. A. and Lewis B. H. (1982) *Icarus, 50,* 216-244. [5] Byrne S. and Ivanov A. B. (2004) *JGR, 109,* E11001. [6] Whitten J. L. and Campbell B. A. (2018) *JGR: Planets, 123,* 1541-1554. [7] Milkovich S. M. and Plaut J. J. (2008) *JGR, 113,* E06007. [8] Milkovich et al. (2009) *JGR, 114,* E03002. [9] Smith I. B. et al. (2016) *Nature, 352* (6289), 1075-1078. [10] Phillips et al. (2011) *Science, 332,* 838-841. [11] Bierson et al. (2016) *GRL, 43,* 4172-4179. [12] Seu et al. (2004) *PSS*, *52,* 157-166. [13] Picardi et al. (2005) *Science, 310,* 1925-1928. [14] Plaut J. J. et al. (2007) *Science, 316,* 92-95.

Influence of the Solar Wind on the Polar Upper Atmosphere of Mars. L. Andersson[1] and M. Pillinski[1], [1]LASP at University of Colorado, USA (laila.andersson@lasp.colorado.edu).

Introduction: Even though Mars does not have an intrinsic magnetic field directing solar wind energy into the thermosphere, there are key differences between the equator and the polar upper atmosphere. For instance, the seasonal variability in the polar region ionosphere and thermosphere is different from that at the equator due to the way that the tilt-axis alignment conspires with the ellipticity of the Martian orbit.

The solar wind interacts with the atmosphere mainly as a draped magnetic field with the clock angle of that magnetic field varying over time. On average however, the interplanetary magnetic field lies dominantly in the ecliptic resulting the draped magnetic field 'sliding' over the planet from lower latitudes towards the poles. This results in a magnetospheric 'sling-shot' effect wherein the ionosphere can be effectively eroded.

The polar regions are located at 'high' solar zenith angles leading to smaller atmospheric scale heights and moving many of the transition regions down in altitude. As a result, the electron temperature profiles at high latitudes are different from those at the equator. This affects the chemical reaction speeds when comparing polar and equatorial regions.

Using the observations by the NASA MAVEN missions made over 5 Earth-years (2.5 Mars-years) we investigate the importance of energy input from the solar wind into the lower atmosphere, how the polar regions participate in this energy input, and what this means for ion escape. The result is compared to Earth, where the energy from above the polar region drives the global thermosphere.

Ionospheric Shielding: At Earth the main magnetospheric energy input to the thermosphere is through the polar regions. Due to the lack of an intrinsic dipole magnetic field at Mars this is not the case, and the upper ionosphere can shield the lower ionosphere from external forces. Consequently, the Martian polar region does not contribute as much in channeling energy into the thermosphere.

The polar regions tend to be close to the terminator where day-to-night transport and ionospheric currents are developed. The upper ionosphere will shield the lower atmosphere from most increases in solar wind pressure buffering the lower ionosphere from instantaneous changes. Given a large enough solar pressure that is sustained over time however, ionospheric erosion will couple into the lower ionosphere and to the enhanced thermospheric winds which are expected to behave similarly to the 'fly-wheel' currents at Earth [1]. The effect of this is a nonlinear response of the polar atmosphere/ionosphere to solar wind forcing that might lead to the more quiet times being more effective in driving changes in the atmosphere.

Diurnal Variation: At Earth, the day-night thermospheric difference is relatively small and the EUV illumination at dawn mainly affects the ionosphere which takes 1-2 hours of local time to reach a 'semi-equilibrium' state. On Mars, where both the thermosphere and ionosphere change significantly from day to night, it takes up to 6 hours local time (closer to noon) to reach this state [2].

The diurnal variations at the polar regions are not as strong when compared to the equator due to the smaller variation in solar zenith angles at higher latitudes. As a result, the ionospheric relative abundance is different at the poles and the equator.

Atmospheric Loss: The properties of the Martian polar atmosphere/ionosphere described above lead to more heavy ion escape than at Earth.

With the lower exobase and a changing magnetic field direction, magnetic flux tubes can be mass loaded and heavy particles can be transported to higher altitudes where their lifetimes can be long. Examples of these erosion processes will be presented.

References:

[1] Deng W., Killeen T. L., Burns A. G., (1991), GRL, Vol. 18, No. 10, 1845~1848, "The flywheel effect: Ionospheric currents after a geomagnetic storm"

[2] Pilinski M. D., Andersson L., Fowler C., Peterson W.K., Thiemann E., Elrod M. K., (2019), JGR accepted, "Electron Temperature Response to Solar Forcing in the Low-Latitude Martian Ionosphere"

Additional Information: This work is supported by the MAVEN NASA project.

.

3D-MODELLING OF SUBSURFACE ICE USING GROUND PENETRATING RADAR ON AXEL HEIBERG ISLAND, CANADIAN HIGH ARCTIC. C. N. Andres[1], G. R. Osinski[1], and E. Godin[2]. [1]Department of Earth Sciences/Institute for Earth and Space Exploration, University of Western Ontario, London, ON, Canada, N6A 5B7, candres5@uwo.ca, [2]Centre d'Études Nordiques, Université Laval, Québec, QC, Canada, G1V 0A6.

Introduction: Ground penetrating radar (GPR) is a geophysical technique that allows high-resolution and non-destructive stratigraphic imaging of the subsurface. The GPR method records the two-way travel time of electromagnetic (EM) waves reflected at boundaries between subsurface layers with contrasting relative permittivity. Dielectric contrasts develop due to variations in sediment grain size, water content, and mineral composition.

The overall objective of this research is to survey an area of Axel Heiberg Island, Nunavut, to identify and map near-surface ice and other structural features beneath the ground. This will be used to correlate potential similar scale geomorphologic features on Mars. Comparatively, theoretical models indicate that water ice is stable in the shallow subsurface (depths of <1–2 m) of Mars at high latitudes [1,2]. Landsystem analysis techniques are also used to investigate different components of the periglacial landscape (i.e. gullies, polygons) to better inform our understanding of the formation/interaction of these features on Mars.

Study Site: Using an Earth analogue site similar to environments on Mars, the GPR survey was conducted on an alluvial "fossil" fan deposit from a mass wasting event. Due to the relative inactivity of this fan, it has been overprinted with polygonized terrain as well as dominated by periglacial processes of repeated freezing and thawing (**Figure 1**). The region of interest is located in Strand Fjord, Axel Heiberg (79°09'43"N, 90°13'44"W) that shows different tonalities of the "fossil" fan due to the past flow of water in this region.

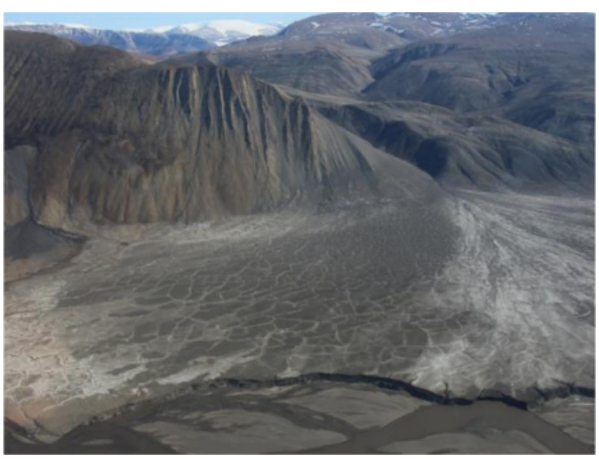

Figure 1. A polygonized "fossil" fan on Strand Fjord, Axel Heiberg Island. The high albedo or light colour-toned features on the fan are water-marker indicators of mineral deposits (i.e. gypsum). There is a smaller, more recently active fan to the left-most of the image.

At the present day, Strand Fjord is dominated by periglacial landscape processes (i.e. freeze-thaw, cryogenic cooling, etc.). However, upon its formation, the region was volcanically active in the Late Cretaceous (~100.5 Ma) as part of the Sverdrup Basin succession. Strand Fiord volcanics are encased with a maximum thickness of ~789 m on the northwestern part of Axel Heiberg mainly composed of volcaniclastic conglomerates, sandstones, mudstones, and coal deposits [3].

Methods: For this procedure, a 25 m x 25 m grid was set up, while following the "zamboni" method making a zigzag pattern with a step-size of 1 m intervals. 25 lines were oriented north-south and 25 lines were oriented in the west-east direction. This resulted in a total of 50 radar files and a total of ~180 time slices from the interpolated GPR map (**Figure 2**). The equipment used in the survey is the Sensors and Software 250 MHz Noggin GPR with a 0.4 m to 3 m penetration depth. Additionally, a series of calibration tests were done to ensure the least signal deviation.

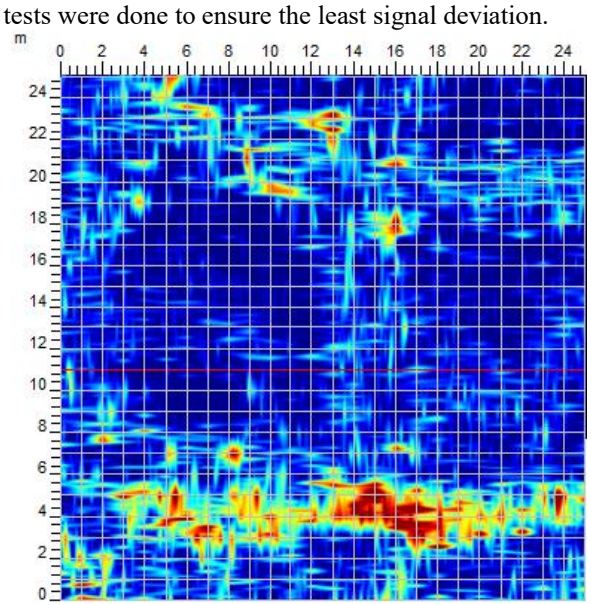

Figure 2. Time slice at depth z = 0.8 m highlighting ice-rich features in red/green that are widely concentrated at polygon troughs (x = 15 m, y = 4 m). There are a total of 5 polygons covered by the survey grid as seen from the shape of the signal returns.

Results: Data collected from this survey was interpreted via extrapolation/calculation of conductivity, permittivity, travel-time velocity, penetration depth, and radar reflection coefficient (RC) using the EKKO_Project software along with topographic data.

The goal of the GPR reflection survey is to determine valuable amplitude traces that can potentially be mapped to locate the position/saturation of ice-wedges in the subsurface and to distinguish probable stratigraphic boundaries in frozen ground.

GPR Radargram Profiles. There were a total of 50 radargrams produced by the survey. By calibrating radargrams to extract velocity information, the calibrated velocity of the survey was found to be 0.064 m/ns, which indicates a wet clay/sand subsurface. This extracted velocity can then be used for further analysis and more accurate stratigraphic observations thereby making plausible interpretations (**Figure 3**). In the radargram, there are various subsurface features that can be seen as summarized in **Table 1**.

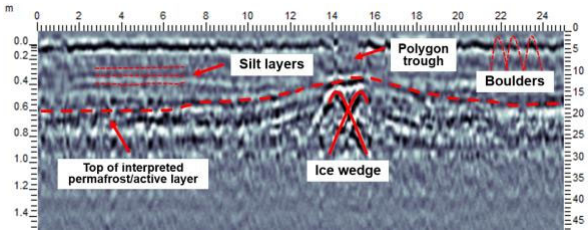

Figure 3. Stratigraphic cross-section of one GPR line along a polygon center-trough-center showing features such as, ice at x = 15 m and z = 0.8 m (depth of ice).

Table 1. Sub-surface features as seen on radargram responses using the Noggin 250 MHz GPR in Figure 3.

Depth (z)	Feature
0.0 m – 0.4 m	polygon trough
0.3 m – 0.5 m	layering of silt/sand horizons
0.6 m	top of the active layer (frozen ground)
0.8 m	ice-wedge
>1.0 m	signal attenuation due to the poor GPR response from the thawing of permafrost

GPR-derived 3D Model. In order to model GPR data, an isosurface needs to be created in order to illustrate 3D shaded renderings from lattice files. They reflect the concept of a contour line (2D) and frames it in 3D space using matrices. Isosurfaces also display constant data values for a component that dissects a 3D volume, which in this case are the highest returns (filtered for ice-rich GPR signals).

Using the Voxler 4 software, a 3D simulation of ice-wedges can be modelled not only as a visualization tool but also as a calculator for subsurface ice volume (**Figure 4**). Volume calculations are generated from voxels (3D pixels) that are either partially or fully included in the isosurface. The total volume (isovalue) is the sum of the individual volumes from these voxels. Using this approach, the volume of the ice-rich isosurface within the 25 m x 25 m GPR survey grid has been calculated to contain 43.28 m^3 of ice.

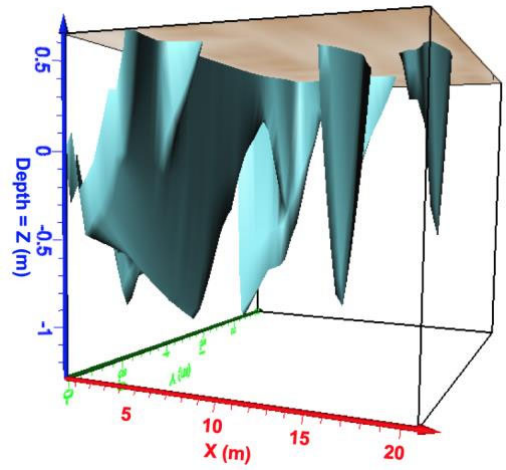

Figure 4. A snapshot of a 3D lattice video simulation, showing ice-wedge geometry and volume in cyan. The bounding box corresponds to dimensions in Figure 2, with the ice-wedge in Figure 3 mapped at x = 15 m.

Discussion: Previous work has been able to approximate the amount of ice from GPR depth slices without isolating the ice [4, 5]. However, 3D modelling of GPR data can be limited by several factors, two of which are near-surface water and mineral concentration. Due to the soil's conductive nature, the GPR signals get "scattered" before it can return to the antenna when travelling through damp or wet soils, especially when they have high salt content. GPR data is a crucial tool to validate cored-and-cached samples that may be indicative of paleoenvironments. To validate this GPR model, a 12m sedimentological log of the "fossil" fan along with 9 sediment pits were also dug/recorded in order to ground-truth features that we're seen on the scan. The sedimentological column strongly validates the depth of the active layer at z = 0.6 m and the ice-wedge at z = 0.8 m. This was repeated for other GPR cross-sections with accurate correlations.

Future Work: Although this work is currently being done on subsurface ice on polar desserts on Earth as a reference point, subsurface ice on Mars also exists in regions that are highly dominated by periglacial regimes. Moreover, it is important to expand on the broad capabilities of subsurface radar imaging as it is a powerful tool in seeing the invisible especially when supplemented by analysis of soil, mineral composition, and remote sensing. 3D GPR offers considerable potential for imaging, interpreting, and 3D mapping of near-surface ice in periglacial environments.

References: [1] Bandfield, J.L. (2007). *Nature*, 447(7140), p.64. [2] Levy, J. et al. (2009). *JGR: Planets, 114(E1).* [3] Ricketts, B. et al. (1985). *Polar Research 3, no. 1*: 107-122. [4] Munroe, J.S. et al. (2007). *Permafrost and Periglacial Processes,* 18(4), pp.309-321. [5] Stuurman, C.M. et al. (2016). *Geophysical Research Letters*, 43(18), pp.9484-9491.

POLAR VORTEX INVESTIGATIONS USING MRO MCS DATA. K.-M. Aye[1] and P. O. Hayne[1], [1]Laboratory for Atmospheric and Space Physics, University of Colorado at Boulder, CO 80303, USA (michael.aye@colorado.edu).

Introduction: The multi-year Mars Reconnaissance Orbiter (MRO) Mars Climate Sounder (MCS) data-set offers rich insight into the Martian polar atmospheres which are driving the whole planet's atmosphere due to its significant CO_2 freeze-out during local winters of up to 30%.

The main objective of this work is to look for variations in the extent and morphology of the polar vortices. We think that the north polar vortex is more unstable than the south. This may lead to differences in the pole-ward transport of heat, dust, and water ice.

Methods: We have established a new full MCS data-set database that allows us to study data slices through time and space with relatively low effort. We are studying how the polar vortex develops over time and altitude/pressure levels by tracking clouds. We are using the "dust opacity" higher level data column of MCS as a proxy for CO_2 cloud opacity during polar winter.

For the preliminary work in here, we have chosen to compare north and south cloud activity 30 Ls after the coldest day of the local winter, because MCS has previous reported on cloud structures at those times [1]. Binning data for 10 Ls together, this results in an Ls range of 300 to 310 for the north pole, and 120 to 130 for the south. The chosen level of altitude is a pressure value of 50 +- 5 Pa. All plots show the dust opacity multiplied by 3 in km^-1, which has previously been used as an indicator of CO2 clouds in MCS data.

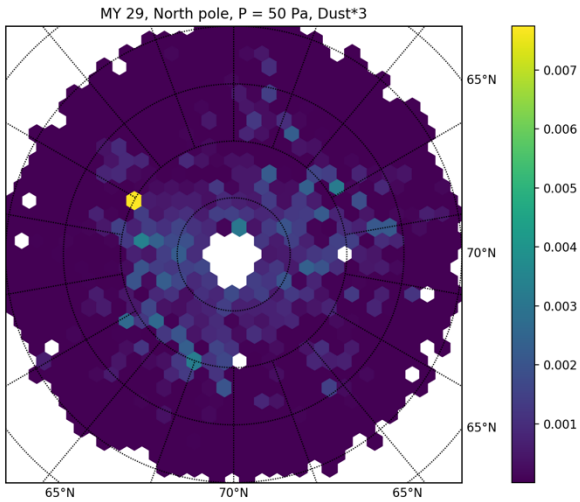

MY 29, North pole, "dust" opacity at pressure altitude 50 Pa.

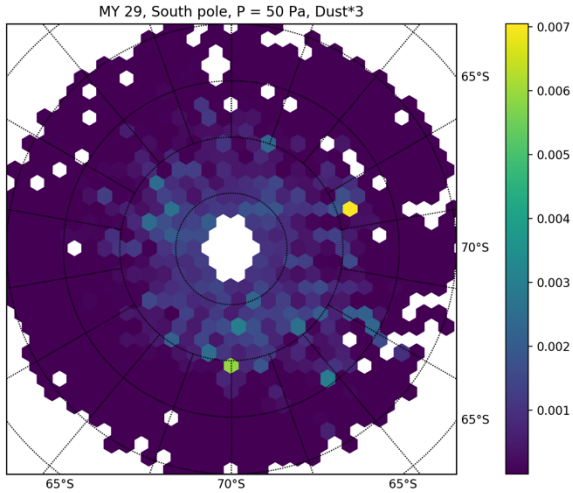

MY 29, South pole, pressure level 50 Pa.

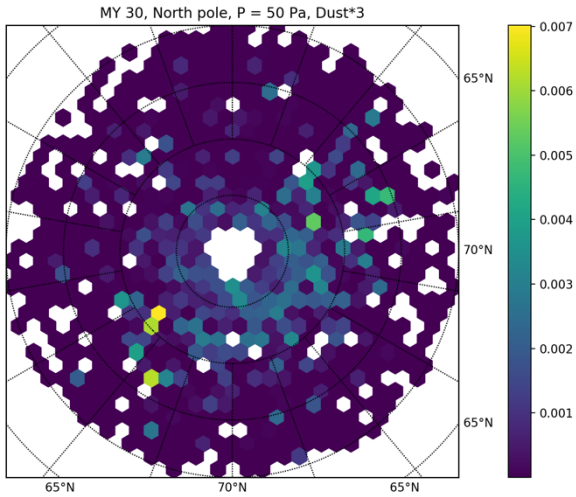

MY 30, North pole, pressure level 50 Pa.

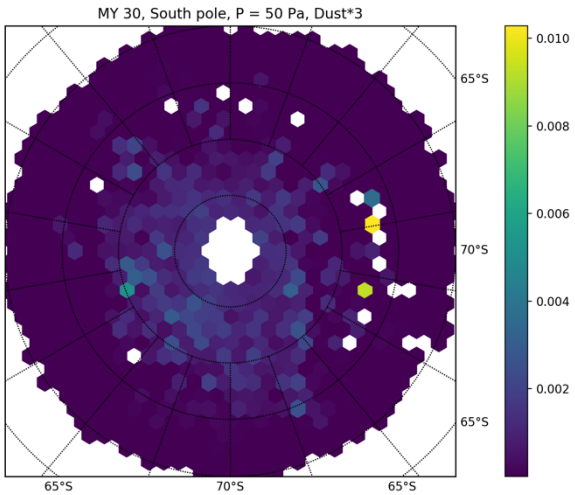

MY30, South pole, pressure altitude 50 Pa.

Preliminary conclusions: Looking at 2 years of data and only 1 pressure level, it is not necessarily evident that the north pole has a weaker polar vortex structure. In MY 30, the structures seem more clear in the north than in the south. We will present a thorough study through the parameter space at the conference.

References:

[1] P.O. Hayne, D.A. Paige, J.T. Schofield, D.M. Kass, A. Kleinböhl, N.G. Heavens, D.J. McCleese, J. Geophys. Res. 117 (2012).

THERMOPHYSICAL PROPERTIES OF EXPOSED SOUTH POLAR WATER ICE. J. Bapst[1] and S. Piqueux[1], [1]Jet Propulsion Laboratory, California Institute of Technology, Pasadena, CA 91109, USA, jonathan.bapst@jpl.nasa.gov

Introduction: Comprising the vast majority of Mars' known water inventory are large deposits of water ice at the poles, the polar layered deposits [1]. The history of these deposits is not well understood, including their recent evolution and present mass balance. Mars' orbital elements vary in a cyclical fashion [2,3]. The resulting changes in solar flux over time (Figure 1) will drive the exchange of water ice between the polar regions and lower latitudes. Substantial geologic evidence exists for this exchange (e.g., [4]), and the process is also predicted by climate models (e.g., [5,6]).

In general, ice is stable at the poles during periods of low obliquity and is unstable during high obliquity. Over the past 200–300 kyr, the expected changes in obliquity are small relative to preceding fluctuations (Figure 1). What does this mean for the current state of the climate? Is there net-transport of water ice to the poles or away from the poles to lower latitudes? This work addresses the above questions and brings us closer to understanding the current water cycle. Extrapolating to climates under different orbital configurations is impossible if we cannot understand the behavior at present.

Although recent obliquity changes have been muted, water ice is sensitive to small changes in insolation as its vapor pressure is exponentially dependent on temperature (i.e., the Clausius-Clapeyron relationship). Climate models [7] and thermophysical properties of exposed ice [8] support both accumulation and ablation occurring across the north polar at present or in the geologically-recent past.

Here, we focus our efforts on characterizing thermophysical properties at the southern pole of Mars. The southern polar region is much more limited regarding water-ice exposures when compared to the north (Figure 2; [9]). Based on climate model simulations, recent accumulation has been invoked as a source for a large fraction of this exposed water ice [10]. However, no test of its thermophysical properties has been made to establish consistency with that hypothesis. In addition, we can directly compare derived properties in the south to water ice properties in the north, in order to test for systematic differences [8].

Methods: To examine whether water is being transported to the pole (i.e., net accumulation), or to low latitudes (i.e., net ablation), we characterize the physical properties of exposed water ice deposits. Accumulation of water ice can be inferred by the presence of porous ice at the surface. Porous ice at the surface will densify over time [11] and therefore old ice should exhibit low porosities. The absence of porosity is compatible with

Water Ice

CO Ice

Figure 2. Exposed south polar ices in summertime, discriminated by measured surface temperature from the Thermal Emission Imaging System (reproduced from [9]). Surface temperature data within the red square is shown in Figure 3.

Figure 1. The past 1 Myr of Mars (a) obliquity or axial tilt, (b) eccentricity, and (c) insolation at the north pole at summer solstice (L_S=90°). From [2].

both accumulation and ablation as modeled under martian conditions [12], but other lines of evidence are used to support/reject ablation, such as geographic location and the surface albedo relative to other exposures. It is along these lines we assess the youthfulness of exposed ice in the southern polar region.

Deriving thermophysical properties is accomplished by testing a series of simulated surface temperatures against those measured from orbit. Three datasets of surface temperature will be analyzed: Thermal Emission Spectrometer (TES; [13]) bolometer- and spectrometer-derived surface temperature as well as surface temperature measured by Mars Climate Sounder (MCS; [14]).

Modeled temperatures are produced using KRC [15], a well-established and validated 1-D thermal model with many capabilities that are of use to the broader planetary science and engineering communities (see http://krc.mars.asu.edu for additional information). KRC has primarily been used for studies concerning Mars and is well suited for analysis of temperatures from the aforementioned datasets. We first test homogeneous models of thermal inertia (TI) ranging from ~50–2000 J m^{-2} K^{-1} $s^{-1/2}$. Fits between the model and observed sets of temperature will be evaluated by their RMS error.

Preliminary Results: A preliminary analysis is given here, focusing on a single example concerning a small patch within the exposed water ice mapped by [9]. At the meeting, the analysis of surface properties will be expanded for water ice exposures south of 65°S.

The region of exposed water ice investigated here (see red box in Figure 2) includes sufficient numbers of observations from each dataset, in order to interpret and compare against modeled cases (Figure 3). A qualitatively-derived model fit for a prescribed TI = 500 J m^{-2} K^{-1} $s^{-1/2}$ and albedo = 0.45 provides good agreement. These properties imply 10s of cm-thick water ice of significant porosity (>40%; [8]) which is consistent as being a product of recent accumulation.

Discussion and Future Work: Significant porosity is suggested by our preliminary fitting of temperature data, implying recent accumulation, in line with [10]. This has important implications for the current trend in climate and the water cycle. Our findings affect related areas of research, such as impact crater density at the south pole [16].

The behavior of temperatures prior to defrosting (L_S~300°) is indicative of dust loading in the atmosphere. To avoid erroneous fits this must be removed from our analyses and fitting procedure (similar to [8]).

Lastly, a number of layered models will be tested which may reveal a vertically-heterogeneous deposit. This line of evidence would support cycles of accumulation, where a porous water-ice layer at the surface represents only the latest episode.

Acknowledgement: Part of this work was performed at the Jet Propulsion Laboratory, under a contract with NASA. US Government support acknowledged.

References: [**1**] Byrne, S. (2009) *Annu. Rev. Earth Planet. Sci.* **37,** 535–560 [**2**] Laskar, J., et al. (2002) *Nature* **419,** 375–377. [**3**] Laskar, J. *et al*. (2004) *Icarus* **170**, 343–364. [**4**] Head, J. W. *et al.* (2003) *Nature* **426**, 797–802. [**5**] Levrard, B. *et al*. (2004) *Nature* **431**, 1072–1075. [**6**] Levrard, B., et al. (2007) *JGR Planets* **112,** 1–18. [**7**] Tyler, D., & Barnes, J. R. (2014) *Icarus* **237**, 388–414. [**8**] Bapst, J. et al. (2019) *JGR Planets* **124**, 1315– 1330. [**9**] Piqueux, S *et al*. (2008) *JGR Planets* **113**, E08014. [**10**] Montmessin, F. *et al*. (2007) *JGR Planets* **112**. [**11**] Herron, M. M., & Langway, C. C. (1980) *J. Glaciology* **25**, 373–385. [**12**] Arthern, R. J., et al. (2000) *Icarus* **144,** 367–381. [**13**] Christensen, P. R. *et al.* (2001) *JGR Planets* **106,** 23823–23871. [**14**] McCleese, D. J. *et al*. (2007) *JGR Planets* **112**, E05S06. [**15**] Kieffer H. H (2013) *JGR Planets* **118**, 451–470. [16] Koutnik, M. *et al*. (2002) *JGR Planets* **107**, 5100.

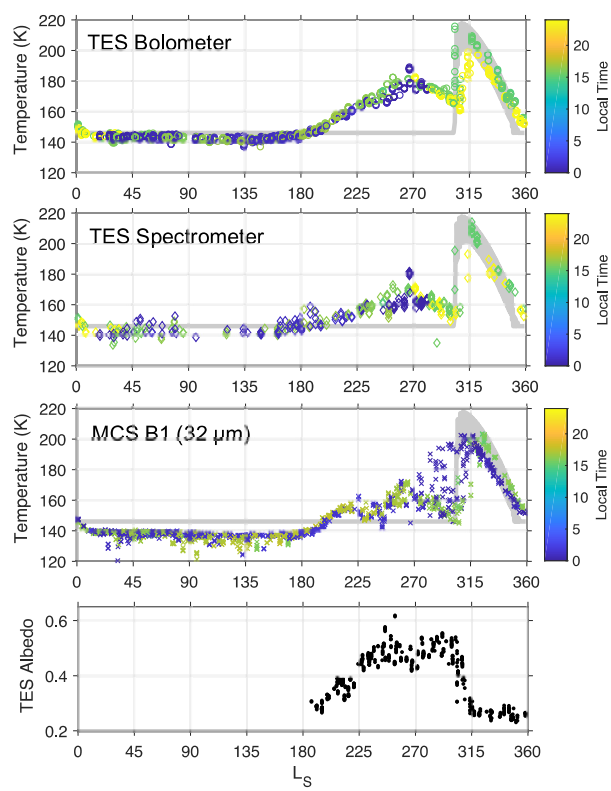

Figure 3. The top three panels show surface temperatures for the region in red from Figure 1, with each dataset listed. The large squares in the plot with MCS temperatures represent atmospherically-corrected surface temperature while other points are uncorrected brightness temperature at 32 μm. Our model fit to the data is shown in gray.

Two views of the Martian North Polar Layered Deposits: Toward a correlation of radar and visible stratigraphic records

P. Becerra[1], D. Nunes[2], I.B. Smith[3,4], M.M. Sori[5], N. Thomas[1]; [1]Physikalisches Institut, Universität Bern, Switzerland, [2]Jet Propulsion Laboratory, Pasadena, USA. [3]Planetary Science Institute, Colorado, USA, [4]York University, Toronto, Ontario, Canada. [5]University of Arizona, Tucson, USA.

Introduction: A long-standing problem in Mars Polar Science is the interpretation of the stratigraphic record preserved in Mars' icy North Polar Layered Deposits (NPLD) [1] (Fig. 1a), whose accumulation patterns of ice and dust are associated with recent climate change forced by variations in the planet's astronomical parameters [2]. The internal bedding is visible from orbit in exposures within spiraling troughs that dissect the NPLD dome (Fig. 1a,b). Studies have used images of these troughs to map the stratigraphy [3-6] and describe links between NPLD accumulation and astronomical forcing [7-10]. Sub-surface radar sounding also observes this internal structure. The Shallow Radar (SHARAD) [11] detects changes in dielectric properties with depth. As these vary for layers with different amounts of dust, layering is observed as "reflector" surfaces [12].

The optical and radar-based stratigraphies have predominantly been studied in isolation. In terrestrial climate science [13], orbital climate forcing was confirmed by correlation of sedimentary, geochemical and paleo-magnetic records, suggesting that integration of datasets is key to understanding the record in the NPLD. In general, both radar and optical layers are assumed to result from varying amounts of dust in the ice [14,15], but differences in vertical resolution have prevented 1-to-1 correlation.

Here, we test the hypothesis that highly protruding 'Marker Beds (MBs)' have sufficient dielectric contrast with neighboring beds to create radar reflections. If true, this would associate individual reflectors to exposed beds, allowing for dust/ice columns based on the combined data, which could constrain orbitally-forced accumulation models [16,17] to decipher the climate record of the NPLD.

Methods: Becerra et al. [8] mapped the stratigraphy of the NPLD by identifying sequences of MBs in "protrusion profiles" of bed exposures in troughs made from HiRISE [18] Digital Terrain Models (DTMs; [19]), and correlating these from different locations (Fig. 1; [8]). Protrusion is a proxy for resistance to erosion and is calculated by measuring the difference between the topography of a trough wall, and a linear fit to the wall within a certain window (Fig. 1a). A protrusion profile for site N0 is shown in Fig. 2b. With these data, our approach to correlation is a 4-step process:

(1) Average SHARAD data near the exposures to obtain representative radargrams. The variability of the SHARAD response within small regions of interest (ROIs) next to exposure sites is not negligible. To assess this, we selected segments of three SHARAD radar tracks that fall within a 3 km ROI near a study site, and averaged all soundings in each segment (Fig. 2a,c). This is representative of the variations in radar response within the ROI.

(2) Compare average radargrams directly to the protrusion profiles of [8] to search for an MB-reflector correlation. For this, we subtract the linear attenuation in the data and normalize all quantities to mean = 0 and variance = 1. We then search for the maximum cross-correlation between protrusion profiles and average radargrams. This is shown in Fig 2d.

(3) Model the radar wave propagation [14] through synthetic permittivity (ε') profiles, which are constrained by the best-fit correlations from step 2. MBs translate into layers of varying ε depending on their initial correlation with the radargram. We can then compare the model radargrams to the real ones at each location. We tested a preliminary model, selecting the MBs from the N0 profile that appeared to fit the radar peaks and assigning them ε' = 4 over a water ice background with ε' = 3.12. Fig. 2e shows the dielectric profile modeled after the protrusion profile of site N0, and Fig. 2f shows the resulting simulated radargram.

(4) Correlate the simulated radargrams to real SHARAD data using spectral analysis and pattern-matching algorithms. This correlation will result in representative HiRISE/SHARAD-based stratigraphic columns of ε', which can be transformed to fractional dust-content [20,21] that can serve as virtual ice cores and be used to constrain accumulation models.

Preliminary Results: Results of the cross-correlation of SHARAD with the protrusion profiles for sites N0, N2, and N11 are shown in Fig 3. For the direct cross-correlation with protrusion we select only the sections of the radargrams that correspond to the estimated relevant depth range [~2–8 μs]. For N0, we also ran a comparison with the preliminary model results. All three sites show a relatively good correlation between peaks in each data profile, but some peaks in the radargram match troughs in protrusion instead. However, radar reflections represent interfaces between materials of different ε', so it is not implausible that a transition to a low-dust, less-protruding layer would also produce a relatively strong reflection. Although the direct protrusion-radar comparison at N0 shows promising results, the model radargram-to-real-radargram comparison at this same site appears to have lost the correlation. More work is

needed in the model radargrams to be able to produce representative multi-data columns.

Conclusions and Future Work: Beds of high protrusion appear to match radar reflectors at three sites. An attempted correlation at site N6 failed at the first stage however, and the model at N0 does not show the expected correlation with the real radagram. We must study all geometrically favourable locations and test for statistical significance at each one. In addition, we will use the correlations with protrusion to inform the model and then use Dynamic Time Warping [7,22] to tune the model and find the best-fit dielectric profile at each site. The final step of the work will be to transform these profiles into dust/ice ratio columns [20,21] for use as input on accumulation models [17]. Naturally, a higher spatial-resolution radar in orbit around Mars would greatly improve the chances of subsurface-surface integration. Such an instrument is being proposed as a NASA Discovery mission [23], and this work can help predict the results that would be returned.

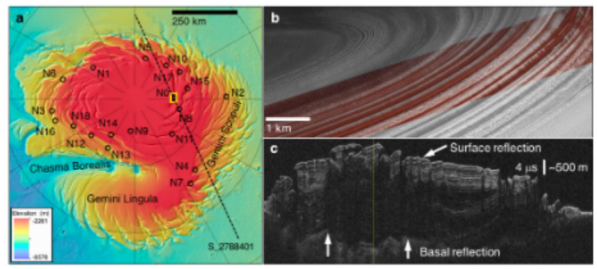

Figure 1. (a) Topographic map of the NPLD. Circles = locations of sites with HiRISE DTMs. Line = ground track of SHARAD radargram in (c). **(b)** HiRISE image of exposed layers in the N0 trough from (a). **(c)** SHARAD radargram 2788401. Yellow line marks the approximate location of N0.

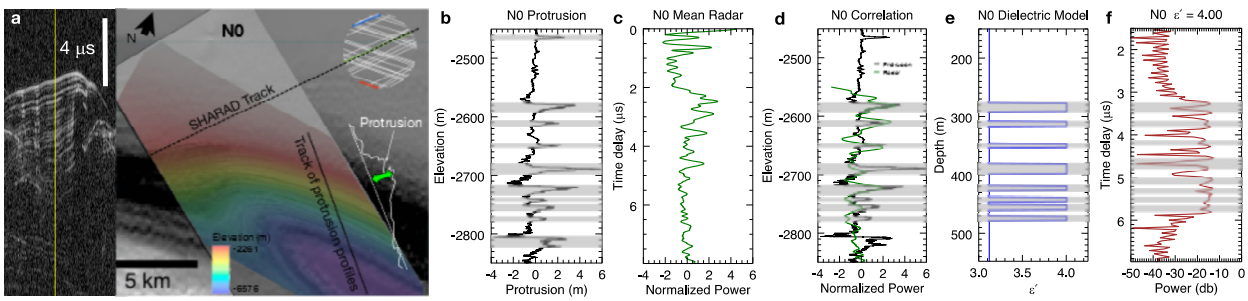

Figure 2. Preliminary radar-protrusion correlation. **(a)** SHARAD radargram (left) and HiRISE DTM (right) of site N0 from Fig.1a. Yellow line on the radargram indicates approximate location of the circular ROI on the top right, which shows the tracks of all soundings that were averaged to produce the mean radar profile. **(b)** Protrusion profile. Protruding beds are shaded in grey. The green arrow in the diagram in (a) explains the calculation of protrusion schematically. **(c)** Mean radar profile. **(d)** Cross-correlation of protrusion to radar profiles. Here, grey shading indicates protruding beds matched to radar reflectors. **(e)** Synthetic dielectric column assuming matched beds are dust-rich (ε' = 4). **(f)** Simulated radar profile generated by propagating a radar pulse through the column in (e).

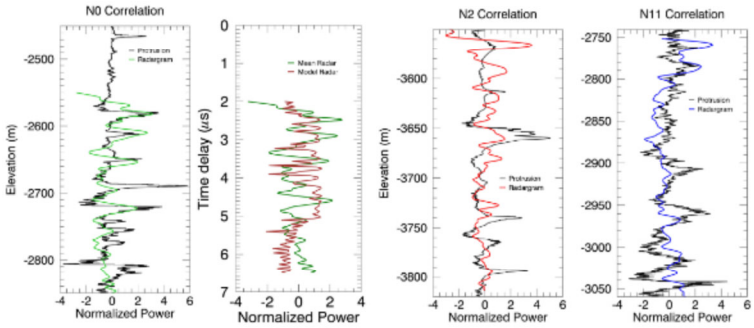

Figure 3. From left to right: Direct cross-correlation of mean N0 radargram with protrusion, cross-correlation between N0 model and mean radargram, cross-correlation of mean N2 radargram with protrusion, and the same for N11

References

[1] Smith, et al. Icarus (2017) [2] Cutts, et al. Science (1976) [3] Fishbaugh et al. (2006) [4] Fishbaugh et al. GRL (2010) [5] Limaye et al. JGR (2012) [6] Becerra et al. JGR (2016) [7] Laskar et al. Nature (2002) [8] Milkovich and Head, JGR (2005) [9] Perron and Huybers, Geology (2009) [10] Becerra et al. GRL (2017) [11] Seu et al. JGR (2007) [12] Putzig et al. Icarus (2009) [13] Imbrie, Icarus (1982) [14] Nunes & Phillips, JGR (2006) [15] Christian, et al. Icarus (2013) [16] Levrard et al. JGR (2007) [17] Hvidberg et al. Icarus (2012) [18] McEwen et al. JGR (2007) [19] Kirk et al. JGR (2008) [20] Stillman, et al. J.Phys.Chem. (2010) [21] Brouet et al. Icarus (2018) [22] Sori et al. Icarus (2014). [23] Byrne et al. this conference.

POLAR IS IN THE EYE OF THE BEHOLDER: ICE-RICH UNITS ACROSS THE MID-LATITUDES OF MARS. A.M. Bramson[1], J.L. Molaro[2], E.I. Petersen[1], Z.M. Bain[2], N.E. Putzig[2], G.A. Morgan[2], I.B. Smith[2,3], H.G. Sizemore[2], D.M.H. Baker[4], M.R. Perry[2], M. Mastrogiuseppe[5], R.H. Hoover[6], B.A. Campbell[7], and A.V. Pathare[2]. [1]Lunar and Planetary Laboratory, University of Arizona (bramson@lpl.arizona.edu), [2]Planetary Science Institute, [3]York University, [4]NASA Goddard Space Flight Center, [5]California Institute of Technology, [6]Southwest Research Institute, [7]Smithsonian Institution.

Introduction: In addition to water's necessity in sustaining human life, H_2O is also the most valuable Martian resource due to its utility in conversion to fuel. Surface ice exists on Mars in plentiful volumes at the poles. However, polar locations, with their extremely cold temperatures and long, dark winter nights make these locales less viable for both robotic and crewed exploration. Therefore, knowledge of the distribution and properties of water ice at warmer and sunnier non-polar latitudes is vitally important for future exploration of the planet. In addition to water ice's importance as an in situ resource, understanding the distribution, properties, and stability of non-polar ice (including its emplacement and evolution) has important scientific implications as a record of Martian climate processes.

The Subsurface Water Ice Mapping (SWIM) Project [1–3] supports an effort by NASA's Mars Exploration Program to determine in situ resource availability by integrating data and analyses from numerous missions and instruments. Here, we present the results of focused mapping and analysis of subsurface radar reflectors found within observations by SHARAD, the Mars Reconnaissance Orbiter (MRO) Shallow Radar [4], which senses the deepest (>15 m) of the instruments whose data were considered by the SWIM Project.

Radar Mapping: SHARAD transmits a signal swept from 25 to 15 MHz, yielding a wavelength in free space of 15 meters [4]. When the radar wave encounters material interfaces with a contrast in the dielectric properties (e.g., boundaries between atmosphere and surface or layers in the subsurface), a portion of the radar wave is reflected back toward the instrument, causing an increase in the power sensed at that delay time. In locations where the depth to a reflecting interface can be estimated from topographic measurements, that depth and time delay measured with SHARAD can be used to constrain the relative dielectric constant, also referred to as the real dielectric permittivity ($\boldsymbol{\varepsilon}'$), of the material through which the radar signals have traveled. This property provides constraints on composition. Values close to 3 are consistent with pure water ice [5] while values approaching 6–12 are consistent with basaltic, ice-poor regolith or bedrock [6]).

As part of the SWIM Project, we mapped subsurface radar interfaces throughout the northern hemisphere and estimated $\boldsymbol{\varepsilon}'$ based on surrounding topographic features, when possible, at the locations of the reflectors (Fig. 1).

Ice Consistency and the SWIM Equation: To enable a quantitative assessment of how consistent (or inconsistent) diverse remote sensing datasets are with the presence of buried ice across these regions, we introduce the concept of ice consistency values for each dataset [1–3]. A consistency value of +1 means that the data are wholly consistent with the presence of ice, 0 means that the data give no indications of the presence or absence of ice, and -1 means that the data are wholly inconsistent with the presence of ice. Based on our dielectric constants estimates, we calculated the radar dielectric consistency values, C_{RD}, as follows:

$C_{RD} = +1$ where $\boldsymbol{\varepsilon}' \leq 3$
$C_{RD} = ½ (5 - \boldsymbol{\varepsilon}')$ where $3 \leq \boldsymbol{\varepsilon}' \leq 7$ ($C_{RD}=0$ where $\boldsymbol{\varepsilon}'=5$)
$C_{RD} = -1$ where $\boldsymbol{\varepsilon}' \geq 7$

The SWIM Team also developed the SWIM Equation [1–3] to combine the consistency values from each dataset considered in the SWIM Project (subscripts N = neutron detected hydrogen, T = thermal signature, G = geomorphology, RS = radar surface reflectivity, and RD = radar dielectric using subsurface reflectors). The resulting composite ice consistency provide a tangible representation of the overall likelihood of ice, C_i:

$$C_i = (C_N + C_T + C_G + C_{RS} + C_{RD}) / 5$$

Results: The radar subsurface reflector mapping yielded nine *radar units* across the northern hemisphere. The median dielectric permittivity estimates $\boldsymbol{\varepsilon}'$, corresponding C_{RD}, and full SWIM Equation C_i result for each of these units are provided in Table 1 (below).

Mapped Radar Units	ε'	C_{RD}	C_i
Arcadia Unit 1 Main Plains	4.1	0.45	0.37±0.16
Arcadia Unit 2 Layered Ejecta Crater (LEC)	4.2	0.4	0.34±0.10
Utopia Unit 1 Thermokarstic Mesas	2.9	+1	0.05±0.12
Utopia Units 2–5	3.2	0.9	0.18±0.11
Utopia Units 6–10	8.1	-1	-0.04±0.14
Utopia Unit 11	8.3	-1	-0.14±0.13
Onilus LDA/LVF/CCF	3	+1	0.22±0.16
Onilus Unit 1 Upper Plains Mantle	4	0.5	0.03±0.09
Onilus Unit 2 Misc. Mantle	5.2	-0.1	0±0.13

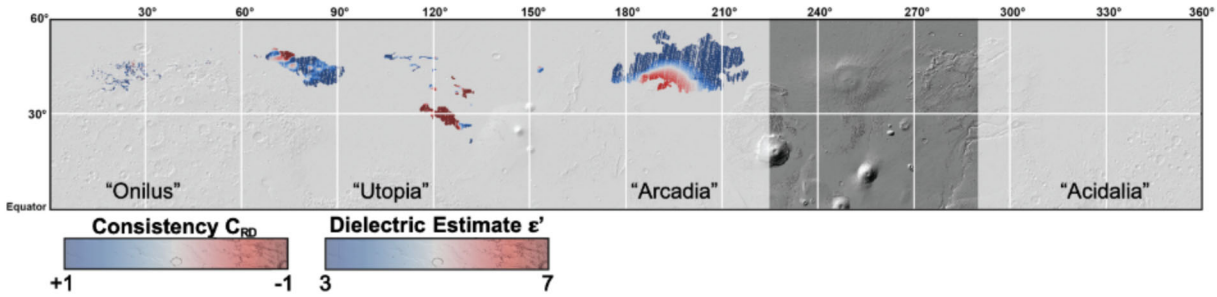

Figure 1. Map showing location of radar subsurface reflectors mapped in The SWIM Project, with colorbar representative of the dielectric permittivity estimates and corresponding ice consistency value from our radar analysis, C_{RD}.

Our dielectric estimates and SWIM Equation results suggest multiple units across the northern mid-latitudes of Mars that may contain ice: *Arcadia Unit 1 Main Plains* (widespread reflector previously mapped in [7] which cuts across multiple large-scale volcanic units mapped by [8]); *Arcadia Unit 2 LEC* (reflector present around a large Layered Ejecta Crater west of Phlegra); *Utopia Unit 1 Thermokarstic Mesas* (reflectors previously mapped in [9] and interpreted by [8] to be ice-rich loess and periglacial terrain); *Utopia Units 2–5* (sinuous feature within lacustrine deposits perhaps modified by thermokarst [8]); *Onilus LDA/LVF/CCF* (reflectors mapped beneath large glacier-like landforms – lobate debris aprons, lineated valley fill, and concentric crater fill – previously mapped in [10], and includes regions mapped by [11]); *Onilus Upper Plains Unit Mantle* (reflectors associated with an LDA-mantling unit identified by [12]); *Onilus Northern Plains Mantles* (reflectors associated with miscellaneous layered mantle).

Meanwhile, our dielectric estimates and ice consistency values for Utopia Units 6–11 are indicative of basaltic, ice-free materials, corroborated by the geologic mapping of [8] which interpreted these regions as lava flows from Elysium Mons and Olympus Mons.

Role of Densification Processes on Observed Heterogeneities: There are numerous lines of evidence that Martian mid-latitude ice is heterogenous, both laterally and vertically. Lateral variations in bulk dielectric permittivity can be observed in Figure 1. Geomorphologic features support the presence of vertical heterogeneities, which our bulk permittivity estimates do not capture. Such features include the scalloped terrain associated with Utopia "Thermokarstic Mesas Unit" [9], terracing in simple craters throughout Arcadia "Main Plains Unit" [7], and a scarp exposure in northern Arcadia of a ~100 meter-thick deposit of massive ice [13].

Microstructural ice evolution through sintering is a possible mechanism for generating heterogeneities in ice, especially given its strong dependency on temperature and grain size (e.g., [14]). The primary stages of sintering are characterized by growth of the contact region ("neck") between grains and mass redistribution forming grain agglomerates (Stage 1 from [15]) and densification via the shrinkage of isolated pores after the ice has become a cohesive aggregate (Stage 3 from [15], with Stage 2 being a transitional period between stages). Negligible densification occurs during Stage 1.

Smaller and warmer grains sinter faster. At 200 K, 100 and 200 micron grains take ~2 and 9 years, respectively, to complete Stage 1 (neck growth) [14]. At 170 K, the same modification for 100 and 200 micron grains takes ~350 and 1500 years, respectively [14]. Annual average temperature at the top of northern mid-latitude ice deposits (which are insulated under dust) are likely around 190–210 K throughout the last ~20 Myr of Mars' history [16], suggesting the initial neck growth phase will occur quickly under Martian conditions.

In contrast, the densification stage occurs over much longer timescales [14], which are not well constrained for planetary environments. We are working to address this knowledge gap using laboratory experiments of ice under different thermal and atmospheric conditions to build on the sintering model of [14]. We will present preliminary results of this model, especially as it pertains to creating heterogeneities within ice across the Martian mid-latitudes. We will explore the role that diurnal, seasonal, and orbital thermal cycling may play in the formation of subsurface density gradients and relate results to observations of ice heterogeneities.

References: [1] SWIM Data Products, swim.psi.edu [2] Morgan et al. (2019) LPSC Abstract #2918. [3] Putzig et al. (2019) 9th Int'l Conf. on Mars Abstract #6427. [4] Seu et al. (2007) JGR, 112. [5] Ulaby, Moore, & Fung (1986) Microwave Remote Sensing, active and passive. [6] Campbell and Ulrichs (1969) JGR, 74. [7] Bramson et al. (2015) GRL, 42. [8] Tanaka et al. (2014) Geologic map of Mars: USGS Map 3292. [9] Stuurman et al. (2016) GRL, 43. [10] Petersen et al. (2018) GRL, 45. [11] Levy et al. (2014) JGR-Planets, 119. [12] Baker & Head (2015) Icarus, 260. [13] Dundas et al. (2018) Science, 359. [14] Molaro et al. (2018) JGR-Planets, 124. [15] Swinkels & Ashby (1981) Acta Metallurgica, 29. [16] Bramson et al. (2017) JGR-Planets, 122.

Co-Evolution of the Martian Atmosphere and South Polar Massive CO_2 Ice Deposit. P. B. Buhler[1], S. Piqueux[1], A. P. Ingersoll[2], B. L. Ehlmann[1,2], and P. O. Hayne[3], [1]Jet Propulsion Laboratory, California Institute of Technology (peter.b.buhler@jpl.caltech.edu), [2] California Institute of Technology, [3]University of Colorado Boulder

Introduction: A Massive CO_2 Ice Deposit (MCID) that rivals the mass of Mars' current, 96% CO_2 atmosphere was recently discovered to overlie part of Mars' southern H_2O cap [1]. The MCID is layered: a top layer of 1-10 m of CO_2, the Residual South Polar Cap (RSPC) [2], is underlain by ~10-20 m of H_2O ice, followed by up to three 100s-meter-thick layers of CO_2 ice, separated by two layers of ~20-40 m of H_2O ice [3] (Fig. 1). Previous studies invoked orbital cycles to explain the layering, assuming the H_2O ice insulates and seals in the CO_2, allowing it to survive recent high obliquity periods [3,4]. We present a model, also driven by orbital cycles [5], but in which the near surface of the MCID exchanges with the atmosphere rather than being sealed. Pervasive meter-scale polygonal patterning and km-scale collapse pits observed on the sub-RSPC H_2O layer [1,3,6] are consistent with it being fractured and permeable to CO_2 mass flux. Using currently observed optical properties of martian polar CO_2 ice deposits [7], our model demonstrates that the present MCID is a remnant of larger CO_2 ice deposits laid down during epochs of decreasing obliquity that are ablated, liberating a residual lag layer of H_2O ice, when obliquity increases. With these assumptions, our energy balance model explains why only the south polar cap hosts an MCID, the observed MCID stratigraphy, and why the enigmatic [8] RSPC exists. We use our model to calculate Mars' pressure history and the age of the MCID.

Methods: We use a 1D energy balance model to find the equilibrium frost temperature T_{eq} for which thermal emission flux equals mean annual absorbed insolation flux for various orbital configurations. T_{eq} sets the equilibrium pressure P_{eq} at the MCID top through vapor pressure equilibrium. We account for changes in altitude of the MCID top due to mass exchange and simultaneously solve for MCID mass, atmospheric mass, and zero-elevation reference pressure $P_{eq,0}$ normalized to the current pressure $P_{present,0}$. We calculate Mars' $P_{eq,0}$ history from a lookup table of polar insolation as a function of orbital elements.

Model Results: *H_2O Layer Formation.* Our model predicts that the MCID loses mass during epochs of rising polar insolation (Mars' present state), and gains mass when insolation falls. H_2O ice impurities (~1%) also accumulate onto the MCID along with the CO_2 ice in both epochs of rising and falling insolation (Fig. 2). During epochs of rising insolation, the MCID loses ~10^{-3} m yr^{-1} CO_2, leaving behind impurities (~10^{-4} m yr^{-1} H_2O) that consolidate into a lag layer.

RPSC existence. H_2O lag is darker and less volatile than CO_2 ice, so annual absorbed solar flux exceeds emitted thermal flux if H_2O is exposed at any time. Excess energy (heat) is conducted to the CO_2 below, causing CO_2 to sublime beneath the H_2O layer. Thus, H_2O exposure self regulates. If CO_2 sublimation in a given year overshoots equilibrium atmospheric pressure because the extent and/or duration of exposed H_2O is too large then the excess pressure leads to increased persistence of surface CO_2 (covering the H_2O) during the next year, and vice versa. Consequently, the CO_2 layer covering the H_2O layer (i.e., the RSPC) has near net-neutral mass balance (consistent with observation [2]) while the MCID beneath the H_2O layer is presently losing net mass as insolation increases.

Pressure history. Mars' $P_{eq,0}$ has been increasing for the past 40 kyr from a 0.7 × $P_{0,present}$ low (Fig. 2A). The current 0.01 Pa yr^{-1} increase implies ~0.4 Pa gain from Viking 1 to Mars Science Laboratory, not inconsistent with no mean annual pressure change detected between these missions, given the ~10 Pa measurement error [9]. Using the statistical distribution of Mars' chaotic orbital states over the past 3 Gyr [5], we find median $P_{eq,0}$ throughout the Amazonian is 1.3 × $P_{present,0}$ with an interquartile range of 0.7 to 1.7 × $P_{present,0}$ (not including any secular change to Mars' CO_2 inventory).

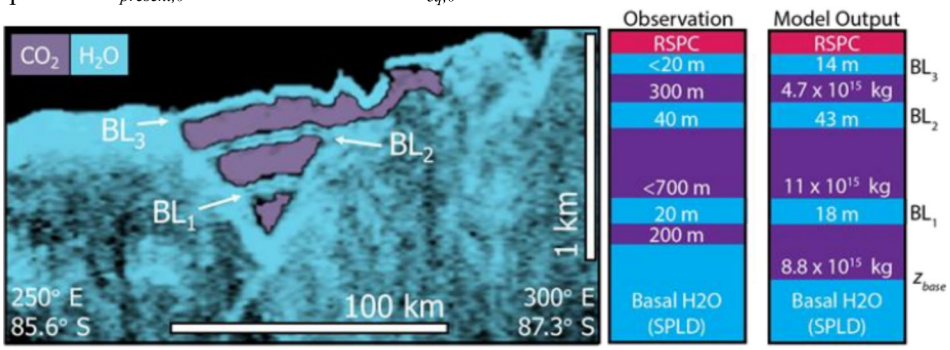

Figure 1: Radar cross-section across a portion of the MCID with H_2O ice "Bounding Layers" (BL) and latitude-longitude end points. Observed mean layer thicknesses [3] compared to our model-predicted H_2O layer thicknesses and CO_2 mass in each layer. CO_2 layer thicknesses are depicted to scale.

MCID Stratigraphy. The MCID stratigraphy co-evolves with $P_{eq,0}$ (Fig. 2). As insolation increases, H_2O lag consolidates as CO_2 sublimes until an insolation maximum. Lag layers formed at relative insolation maxima that are followed by greater insolation maxima are subsumed into the lag that forms at the greater maxima. If insolation is intense enough (e.g., at 510 kyr; Fig. 2B), the entire MCID ablates and all H_2O lag merges with the underlying South Polar Layered Deposit (SPLD), resetting the MCID stratigraphy. Condensing CO_2 buries lag layers when insolation decreases. Fractions of prior CO_2 deposits remain because the amplitudes of the obliquity maxima have been mostly decreasing during the past ~510 kyr (Fig. 2). Our model produces a stratigraphy comparable to observation (Fig. 1).

Discussion: Our model highlights the importance of regional factors (e.g., dustiness, snowfall, etc.) to explain the north-south differences in the polar caps [7]. Our model yields a southern (not northern) MCID for all orbital configurations so long as currently observed martian CO_2 optical properties hold, a result robust for up to a 50% increase in northern emissivity or albedo.

Finally, our model predicts that the interface between the MCID and underlying SPLD should be at altitude +4 km, similar to observation [3], suggesting that the top of the H_2O-rich SPLD may have adjusted over many orbital cycles such that the MCID just barely disappears at especially high peaks in absorbed mean annual polar insolation (e.g., at 510 kyr). In this scenario, the SPLD below the MCID may record a climate history not preserved elsewhere in Mars' polar deposits.

Conclusions: Our model in which the martian atmosphere and MCID co-evolve through vapor contact at all times [6] offers a self-consistent interpretation of the MCID's stratigraphic development and age that also provides a prediction of the RSPC and its equilibration with present atmospheric pressure. The process of CO_2 and H_2O co-evolution and pressure history we describe here is important for deciphering Mars' Amazonian climate and its record preserved in polar cap stratigraphy.

Acknowledgements: NASA's NPP, NESSF, and MFRP programs supported this work. Part of this work was performed at the Jet Propulsion Laboratory, California Institute of Technology, under a contract with NASA. Government support acknowledged.

References: [1] Phillips, R. et al. (2011) Science 332, 838-841 [2] Thomas, P.C. et al. (2016) Icarus 268, 118-130 [3] Bierson, C. et al. (2016) GRL 43, 4172-9 [4] Manning, C.V., et al. (2019) Icarus 317, 509-517 [5] Laskar, J. et al. (2004) Icarus 170, 343-364 [6] Buhler, P.B. et al., in review, Nat. Aston. [7] Paige, D.A. & Ingersoll, A.P. (1985) Science 228, 1160–8 [8] Murray, B.C. & Malin, M.C. (1973) Science 182, 437-443 [9] Haberle, R.M. et al. (2014) JGR Plan. 119, 440-453.

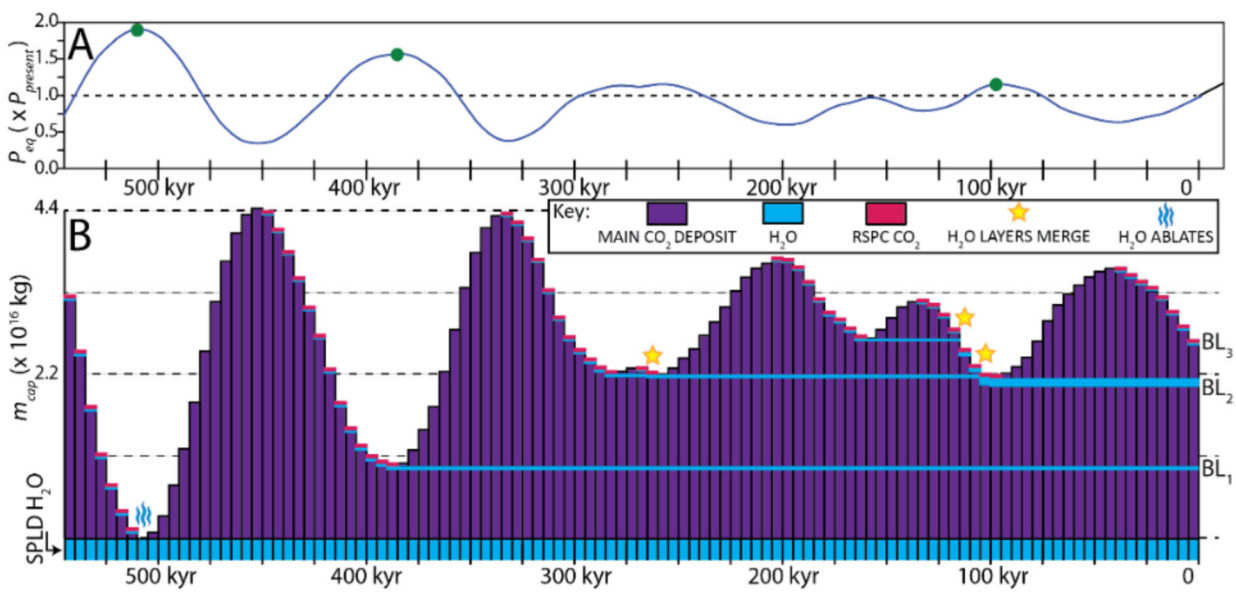

Figure 2: A. Model-predicted pressure history over the past 550 kyr, with monotonically decreasing $P_{eq,0}$ maxima (green dots) since the last total ablation of the MCID. **B.** Model-predicted evolution of MCID stratigraphy in 5-kyr steps. MCID mass shown to scale. H_2O layer thicknesses are depicted proportionally to each other, but at a different scale than the CO_2 for clarity. During epochs of rising polar insolation, CO_2 ablates and H_2O lag covered by a thin layer of CO_2 forms at the top of the deposit. At ~510 kyr, the entire MCID ablates, H_2O lag liberated from the MCID merges with the SPLD and the top of the SPLD ablates to the model-predicted z_{base}. During epochs of decreasing insolation, CO_2 accumulates, burying prior stratigraphy. Stars indicate times when all the CO_2 between two H_2O layers ablates so the H_2O layers merge.

CLIMATE ORBITER FOR MARS POLAR ATMOSPHERIC AND SUBSURFACE SCIENCE (COMPASS)

S. Byrne[1], P. O. Hayne[2], W.M. Calvin[3], L.K. Tamppari[4], A. Kleinböhl[4], I.B. Smith[5], P. Becerra[6], The COMPASS Team. [1]U. Arizona, Tucson, AZ, USA, shane@lpl.arizona.edu, [2]U. Colorado Boulder, CO, USA. [3]U. Nevada, Reno, NV, USA. [4]JPL, Caltech, Pasadena, CA, USA. [5]York U., Toronto, Canada. [6]University of Bern, Bern, Switzerland.

Introduction: In many ways, Mars' icy climate record is recognizable to a terrestrial paleoclimatologist. Polar Layered Deposits (PLD) of water ice and dust at the north and south poles (NPLD & SPLD) are together similar in volume to the Greenland ice sheet and their stratified structure likely records climate over millions to tens of millions of years (Fig. 1) [1]. Surface water ice deposits that cover the NPLD interact with the current climate and may be the dominant source of water vapor in the annual global cycle [2]. Models suggest that depths to buried ice-sheets and pore-filling ice in the mid-latitudes should adjust with changing atmospheric conditions in a similar way to ice in the Antarctic Dry Valleys [3]. However, Mars has a host of unfamiliar ice deposits that also record climate: the geomorphology of a surficial CO_2 ice cap at the South Pole evolves by meters per year [4,5], and a buried CO_2 ice deposit at least equivalent in mass to the current atmosphere also resides in this area [6].

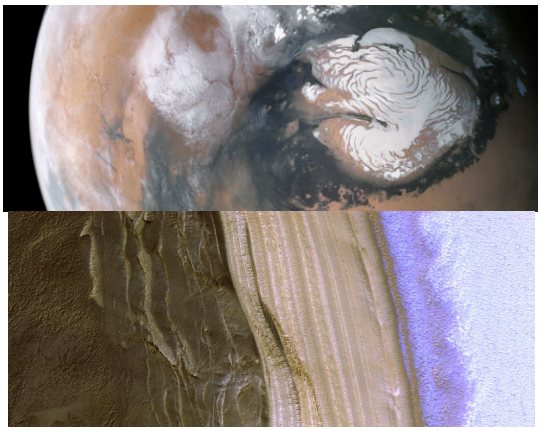

Fig. 1: COMPASS focuses on the interaction of the climate and ice deposits (top, HRSC image of the north polar region with clouds) and the climate record of the deposits themselves (bottom, HiRISE image of exposed bedding in the NPLD).

Despite decades of research based on remote sensing observations, key knowledge gaps prevent a full understanding of the martian climate and how it is recorded in icy deposits. Interaction of the atmosphere with surface and subsurface ice depends critically on atmospheric humidity near the surface, yet water vapor has only been quantified in column-integrated measurements or at specific landing sites. Winds have never been systematically measured on Mars – introducing large uncertainties into the modeling of atmospheric volatile transport. Buried ice sheets in the mid-latitudes have been detected by various means, but systematic measurements have cannot be made of their locations, depths, thicknesses and internal layering with current instrumentation. PLD layers can only be viewed at heavily-mantled outcrops or in radar data that do not fully resolve them.

The Climate Orbiter for Mars Polar Atmospheric and Subsurface Science (COMPASS), is a Discovery-class mission that will provide the key missing datasets to leverage and apply our understanding of terrestrial climate records and meteorology to Mars. COMPASS will study Mars from the subsurface through the atmosphere using unprecedented measurements to definitively answer the question, "*How is the climate we observe today related to past climate variations recorded in Mars' ice deposits?*"

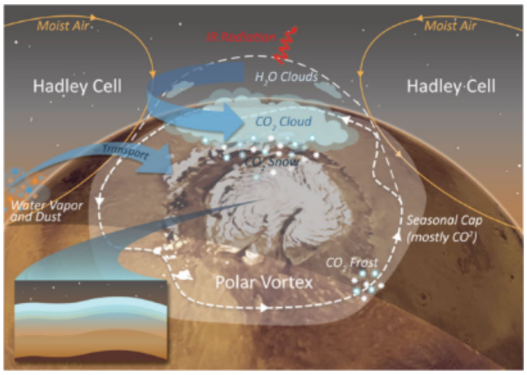

Fig. 2: COMPASS investigates interconnected processes in Mars' climate-ice system, including those illustrated here for the north polar winter. (Adapted from [9])

Science Objectives: Ice is the key to understanding past climate variations on Mars, because volatiles are sensitive tracers of atmospheric and surface temperatures through time [7]. Surface and subsurface ices interact with the atmosphere on different timescales, ranging from the diurnal and seasonal CO_2 cycle to the multi-year advance and retreat of ground ice, to glacial/periglacial landforms and the polar layered deposits, which formed ~1 – 10 Myr ago [1,3,8]. The atmosphere acts as a conduit between these different ice reservoirs under changing conditions.

To fully understand past volatile exchange and the underlying climate forcings, COMPASS will observe present climate processes and volatile transport contemporaneously with measurements of icy reservoirs (Fig. 2) to achieve two science goals:

1. Understand interactions between the current climate and icy deposits
2. Map locations, quantify volumes and characterize layering of Amazonian-aged ice reservoirs globally

Proposed Mission Overview: The COMPASS mission accomplishes its science goals through atmospheric, surface and subsurface measurements taken with four instruments (Figs. 3,4):

CROME (COMPASS Radar Observer for Mars Exploration), a dual-mode L-band radar (Fig. 2) allows COMPASS to locate and resolve sub-meter scale layering within ice deposits on Mars. Buried ice within 2 m of the surface will be detected and located by near-global Synthetic Aperture Radar (SAR) coverage. SAR data will also penetrate and characterize the dust that covers one third of the martian surface and overlies subsurface ice deposits. Layers of ice and dust within the PLD and buried mid-latitude ice-sheets will be examined in a radar sounder mode. At an order of magnitude higher vertical-resolution than MRO's SHARAD, these sounder data allow the detailed correlation of stratigraphic beds with oscillations of orbital elements and the detection of buried ice within 15 m of the surface.

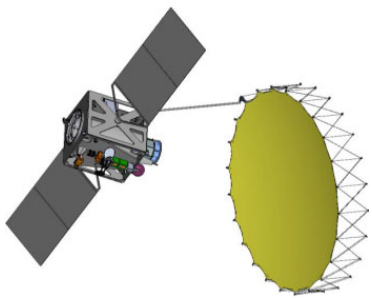

Fig. 3: COMPASS spacecraft with deployed six-meter mesh antenna. Orbital motion parallel to solar panels. CROME is located on the deck facing the antenna.

AMCS (Advanced Mars Climate Sounder), a thermal IR limb sounder based on MRO's MCS [10] and LRO's Diviner will retrieve temperature, water vapor, dust, and condensates as a function of height. Nadir observations can monitor surface frosts and surficial thermal behavior to deduce the presence of the shallowest and lowest-latitude ground ice. AMCS will have twice the vertical resolution of MCS and new filters specifically designed to discriminate water vapor from the other atmospheric components.

WAVE (Wind And Vapor Experiment), a sub-mm limb sounder [11], allows the systematic measurement of winds for the first time. Two antennae observe the limb allowing for reconstruction of both horizontal velocity components as a function of height. Water vapor and temperature profiles will be retrieved under higher optical depth conditions than suitable for AMCS. Isotopic abundances will be tracked as tracers between sources and sinks of water vapor.

MAVRIC (Mars Atmosphere Volatile and Resource Investigation Camera), a wide-angle camera with a near-simultaneous stereo imaging capability, images limb-to-limb each dayside pass in several visible and short-wave IR bands. Daily global coverage permits characterization of seasonal frost, clouds and dust storm evolution. Short-wave IR bands allow discrimination of CO_2 and H_2O frosts, while multiple visible bands allow discrimination of dust and volatile clouds.

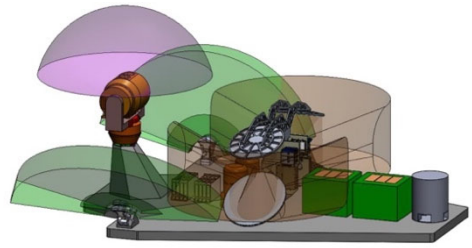

Fig. 4: COMPASS nadir instrument panel with FOVs indicated for AMCS (purple), WAVE (brown) and MAVRIC (green). Orbital motion into page.

COMPASS will have a low-eccentricity sun-synchronous orbit during its one-Mars-year (2-Earth-years) primary science mission. With an inclination of 93°, such an orbit is naturally concentrated in the ice-rich higher latitudes and provides near-global coverage. An equator-crossing local time of 3 pm allows integration of the IR sounder and wide-angle imaging data with the legacy datasets of MRO, Mars Odyssey and Mars Global Surveyor. An orbital altitude of 250–300 km enables high-resolution observations and low atmospheric drag over the course of the primary mission.

COMPASS brings together highly-experienced partners and high-heritage technology resulting in high science return at low risk and cost. The University of Arizona (UA) runs the PI office and Science Operations Center utilizing experience from the Osiris-Rex mission and the Phoenix Lander. The Laboratory for Atmospheric and Space Physics (LASP) provides the Astrolabe spacecraft bus (similar to that used by the Emirates Mars Mission) as well as mission management and operations. The Canadian Space Agency (CSA) contributes CROME based on Earth-orbiting heritage through industry partner MDA Corporation. The Jet Propulsion Laboratory (JPL) provides AMCS and WAVE based on heritage instruments in orbit around Mars and Earth respectively. The Applied Physics Laboratory (APL) provides a MAVRIC based on existing Mars systems. Our diverse science team is comprised of leaders in the field from throughout the US, Canada and Europe.

References: [1] Byrne et al. (2009) *Ann. Rev. Earth Planet. Sci.* [2] Jakoksky and Haberle (1992), In: *Mars,* Arizona Press [3] Schorghofer and Aharonson (2005), *JGR* [4] Malin et al. (2001) *JGR* [5] Thomas et al. (2009) *Icarus* [6] Phillips et al. (2011) *Science* [7] Leighton and Murray (1966) *Science* [8] Head et al. (2003), *Nature* [9] McCleese *et al*. (2016), *International Mars Polar Conference, Iceland*. [10] Kleinböhl et al. (2016) *3rd Int. Workshop on Inst. for Planetary Missions*. [11] Read et al. (20018) *Plan. Space Sci.*

EVOLUTION OF SEASONAL ICE IN REYNOLDS CRATER AND PROMETHEI RUPES FROM CTX AND CRISM. W. M. Calvin[1], K. D. Seelos[2], [1]Dept. of Geological Sciences and Engineering, University of Nevada, Reno, 1664 N. Virginia St., MS 172, Reno, NV 89557 (wcalvin@unr.edu), [2]Johns Hopkins University Applied Physics Laboratory, 11100 Johns Hopkins Road, Laurel, MD 20723, (kim.seelos@jhuapl.edu).

Introduction: The "cryptic region" is a large area in the retreating southern seasonal cap of Mars that develops a low albedo, but retains the cold temperature of CO_2 ice in equilibrium with the atmosphere [1]. Calvin et al. [2] observed the seasonal retreat in four Mars Years (MY 28 to 31) using MARCI and found the large-scale boundary of this area was similar in all MY, with many small scale variations from year to year. Why the cryptic area occurs where it does and not throughout the retreating seasonal cap remains puzzling and not easily explained by elevation, deposition, or topography and may depend on subsurface or surface properties.

While there have been a number of coordinated campaigns by MRO imaging and spectral instruments to observed small, localized regions as they evolve with season [3-8], we noticed several regional scale phenomena in MARCI mosaics at ~2 km/pixel that we wished to explore at higher spatial resolution using CTX (~6 m/pix) and CRISM (up to 18 m/pix). The hemisphere opposite the cryptic region ("anti-cryptic") develops redder-hued material as compared to the classic low albedo cryptic region. Near the margins of the cryptic area there is a complex interplay of dark (presumably sand), red (dust), and retreating frost. MARCI data show clear defrosting of crater rims well within the seasonal cap boundary over Reynolds Crater (Figure 1).

Observations: Based on the MARCI seasonal views, new CTX and CRISM acquisitions were requested for Reynolds and a second nearby crater (Figure 2; 74ºS, 160ºW and 73ºS 156ºW), Main crater (75ºS, 312ºW), the boundary of Promethei Rupes (79ºS, 304ºW), and regions in Dorsa Argentea over the "anti-cryptic" area that retains seasonal frost very late. CTX observations of these 6 regions were acquired in MY 34 approximately every 5 of Ls from 180º to 280º, followed by every 10 to 20 of Ls up to 360º in order to monitor seasonal changes in color, albedo and terrain evolution. These observations for Reynolds crater are summarized in Table 1. CRISM color observations were made at the same time, primarily multi-spectral visible data (MSV; 90 channels at ~ 90 m/pix) to relate color evolution to changes seen in CTX. In addition to MSV data acquired in coordination with the CTX images in Table 1, there are an additional 20 observations in both MSV and FRS (full spectral resolution ~ 18 m/pixel) modes.

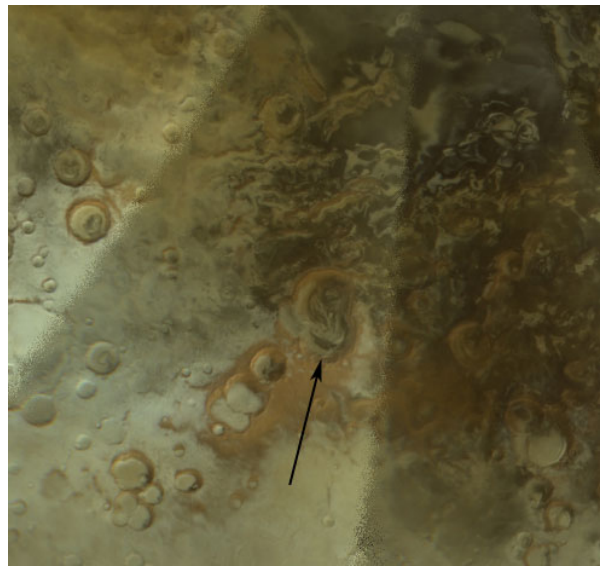

Figure 1: Close up of a MARCI mosaic at Ls 208º. The arrow points to Reynolds crater. Note the difference in color from the crater rim and areas below the crater to interior deposits and terrain above and right that has the characteristic low albedo associated with the "cryptic" terrain. Seasonal ice is also apparent throughout the scene and the region is well within the seasonal cap boundary.

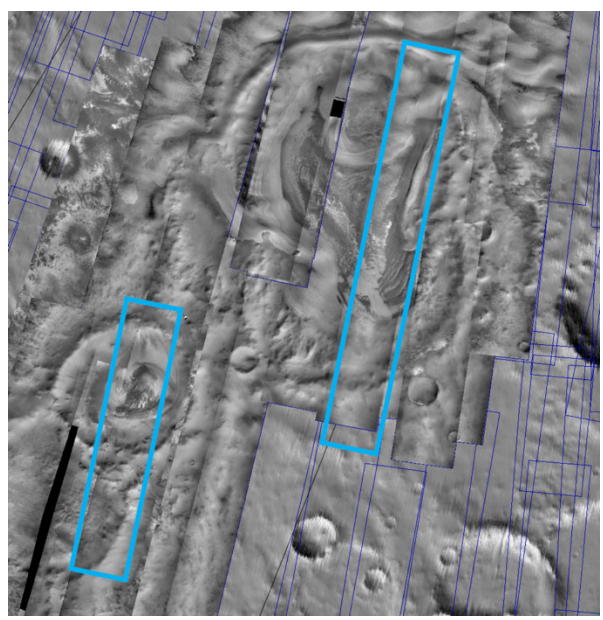

Figure 2: Approximate CTX footprints selected for seasonal repeat coverage over Reynolds and an adjacent crater at 74ºS 160ºW and 73ºS 156ºW.

Analysis: Unexpectedly, a large, planet-encircling dust storm began in early June, 2018, just at the beginning of this imaging campaign. This flattened contrast in CTX images, but most were clear enough to observe the evolution of seasonal frost patterns. As noted by [9], the dust storm did not cause enhanced or early retreat of the seasonal cap. Instead, as observed in CTX data, the MY 34 dust storm appears to have increased CO_2 deposition over Reynolds crater perhaps due to surface cooling from increased opacity that lead to deposition as frost sublimated from lower latitudes. We also observe that steep scarps or slopes retain seasonal frost the longest. Local equator-facing slopes initiate venting, and albedo feedback propagates seasonal frost retreat which allows dark covered material to sublimate faster, as also noted by Schmidt et al. [10]. Late season brightening is observed over Reynolds and Promethei Rupes, as also seen over other sites [7]. It has been suggested that solar heating will cause the surficial dust grains to sink into the remaining seasonal ice [6]; however removal of a surface layer of dust by local winds also seems likely, based on processes observed in the north [11].

Figure 3 illustrates albedo evolution in Reynolds crater from Ls 180º, before the dust storm, to Ls 307º, with no seasonal ice present. We have noted many large bright-dark boundaries and patterns are preserved and new jet events occur in the regions that were brightest at Ls 180º [12]. We will present the evolution of these regions and comparison to concurrent CRISM data. Through analysis of additional imagery we hope to better constrain local effects on seasonal cap sublimation and processes that contribute to development of the cryptic terrain in one location, rather than throughout the south seasonal cap.

References: [1] Kieffer et al. JGR-Planets, 105, p. 9653, 2000. [2] Calvin et al., Icarus, 292, p. 144, 2017. [3] Kieffer et al. Nature, 442, p. 793, 2006. [4] Hansen et al. Icarus, 205, p. 283, 2010. [5] Thomas et al. Icarus, 205, p. 296, 2010. [6] Portyankina Icarus, 205, p. 311, 2010. [7] Pommerol et al. JGR, 116, E08007, 2010JE003790, 2011. [8] Pilorget et al. JGR 118, p. 2520, 2013. [9] Calvin et al. AGU, P43J-3860, 2018. [10] Schmidt et al. Icarus, 200 p. 374, 2009. [[11] Calvin et al. 49th LPSC, #2455, 2018. [12] Calvin and Seelos, 50th LPSC, #2913, 2019.

Table 1: CTX Observations over Reynolds Crater

Cryptic terrain monitoring in Reynolds Crater	Ls
K05_055418_1054_XI_74S159W_180523	180
K05_055484_1054_XI_74S159W_180528	183
K06_055629_1054_XI_74S159W_180609	190
K06_055695_1054_XI_74S159W_180614	193
K06_055840_1047_XI_75S159W_180625	199
K06_055906_1066_XI_73S160W_180630	202
K07_055972_1042_XI_75S158W_180705	205
K07_056051_1054_XI_74S159W_180712	210
K07_056117_1065_XI_73S160W_180717	213
K08_056460_1066_XI_73S160W_180812	229
K08_056671_1057_XI_74S159W_180829	239
K09_056882_1064_XI_73S160W_180914	250
K09_057014_1054_XI_74S159W_180925	257
K10_057159_1054_XI_74S159W_181006	264
K11_057779_1054_XI_74S159W_181123	293
K12_058056_1052_XI_74S159W_181215	307
K13_058346_1054_XI_74S159W_190106	319

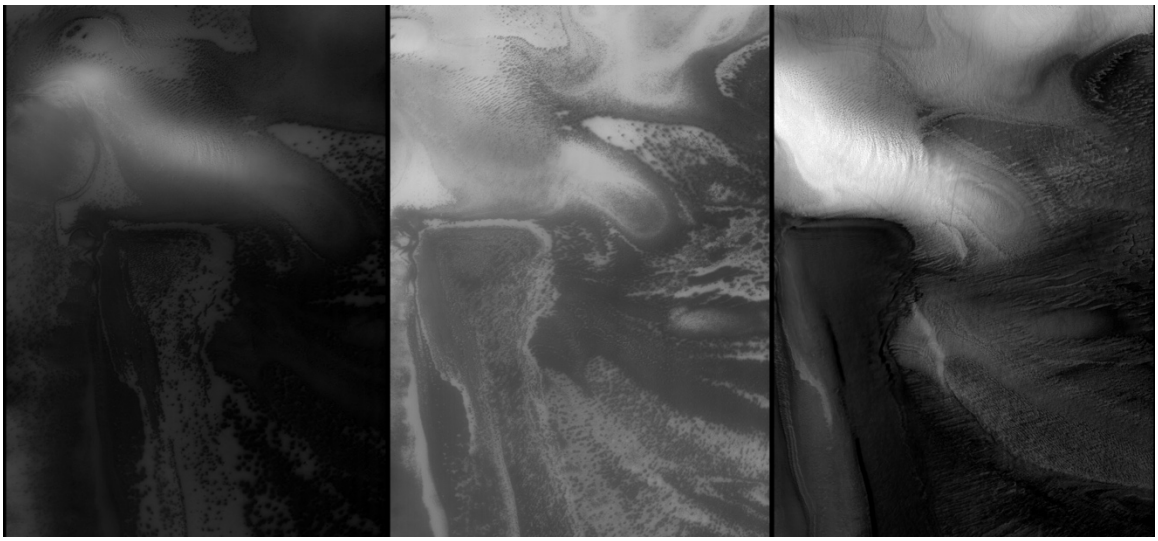

Figure 3: CTX images of albedo pattern evolution in Reynolds crater from Ls 180º, 205º, and 307º (left to right, portions of K05..180523, K07..180705, and K12..181215). Calibrated 8-bit data with a linear stretch on each. The right most panel is completely devoid of seasonal ice and shows relative topographic features associated with longer seasonal ice retention or earlier ice removal.

HYPERSPECTRAL MAPPING OF THE MARTIAN SOUTH POLAR RESIDUAL CAP USING LABORATORY ANALOGUES AND ORBITAL IMAGERY. J.D. Campbell[1], B. Schmitt[2], O. Brissaud[2], J-P. Muller[1]
[1]Imaging Group, Mullard Space Science Laboratory, Holmbury St. Mary, RH5 6NT, UK. Email: Jacqueline.campbell.16@ucl.ac.uk, [2]l'Institut de Planétologie et d'Astrophysique de Grenoble, France

Abstract: We present our research on hyperspectral characterization of the Martian South Polar Residual Cap (SPRC), with a focus on the search for organic signatures within the dust content of the ice. The SPRC exhibits unique CO_2 ice sublimation features known colloquially as 'Swiss Cheese Terrain' (SCT). These flat floored, circular depressions are highly dynamic, and may expose dust particles previously trapped within the ice in the depression walls and partially on the floors.

Here we identify suitable regions for potential dust exposure on the SPRC, and utilise data from the Compact Reconnaissance Imaging Spectrometer for Mars (CRISM) on board NASA's Mars Reconnaissance Orbiter (MRO) satellite to examine shortwave infrared spectra of dark regions to establish their mineral composition and evolution over time, compare the results to laboratory analogues, and assess whether there might be any spectral signatures indicative of Polycyclic Aromatic Hydrocarbons (PAHs).

Laboratory experiments have generated new spectra for PAHs relevant to Mars, and established their detectability limits within SPRC analogues. Whilst no conclusive evidence for PAHs has been found, depression rims are shown to have a higher water content than regions of featureless ice, to exhibit changes in dust content as they evolve, and there are indications of magnesium carbonate within the dark, dusty regions.

Introduction: Dynamic features have increasingly been observed on Mars; repeat observations starting with the Mariner missions of the 1960s [1] have indicated the Martian Surface exhibits a range of interesting changing surface processes. In particular, the polar caps exhibit significant change over time in addition to seasonal changes in ice coverage. On board MRO is an imaging spectrometer, CRISM [2] attaining spatial resolutions of ~20m and spectral resolutions of 6nm, which can be employed to analyse compositional properties of the Martian surface. The south polar cap of Mars consists of a permanent 400km diameter layer of solid CO_2, around 8m thick, overlaying water ice [3].

Swiss Cheese Terrain (SCT) is an unique surface feature found only in the SPRC. Its characteristic appearance (shown in Figure 1) is thought to be caused by seasonal differences in the sublimation rates of water and CO_2 ice [4]; scarp retreat through sublimation may expose dust particles previously trapped in the SPRC which can then be analysed using CRISM.

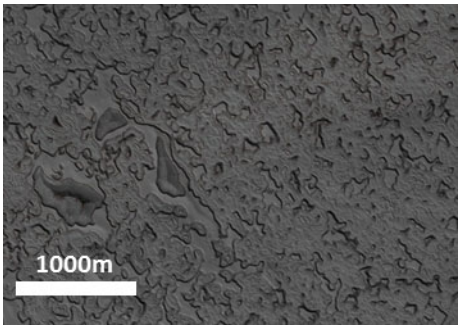

Figure 1: SCT sublimation features (CTX: B08_012572_0943_XI)

Polycyclic Aromatic Hydrocarbons: PAHs are a group of chemical compounds consisting of benzene rings of hydrogen and carbon [5] and are considered to be important in theories of abiogenesis; the search for organic molecules on Mars is important in ascertaining Mars' past conditions, and current habitability [6].

PAHs are abundant throughout the universe, and have been found to coalesce in space within dust clouds, [7] and have been detected on two of Saturn's icy moons, Iapetus and Phoebe as well as on comets [8]. The delivery of complex organic compounds to established, habitable planets via bolide impact is a very important concept in astrobiology. The ability to identify PAHs could provide a critical tool in the search for putative locations for extra-terrestrial organisms.

To date, the hypothesised connection of Martian Swiss Cheese Terrain and the presence of PAHs has not been systematically examined.

Methods: Initially, only Full Targeted Resolution (FRT) CRISM products have been considered for study to try to maximise spatial resolution (~20m/pixel) of small-scale SCT features. The CRISM Analysis Tool (CAT) plugin for ENVI software was used to process the CRISM scenes with corrections for photometry, atmosphere, image artefacts, and to generate summary products. Spectral summary products based on multispectral parameters are derived from reflectances for each CRISM observation that can be used as a targeting tool to identify areas of mineralogical interest for further analysis [9]. Region of Interest

(ROI) band thresholds were used to identify the strongest 10% of CO_2 and H_2O ice signatures from each scene (Figure 2, left), and then ROIs of a minimum of 25 pixels chosen from the same across-track region of the scene as the dark-rim features to provide local 'pure' ice spectra. These samples were then used to carry out correction to remove the overwhelming effects of ice spectral signals on dust rim spectra. summary products [9] were utilized to create RGB composite images of regions of interest to identify spectral differences around dust rims (figure 2, right). Spectra for specific rim features with strong carbonate overtone responses, corrected for ices, were then analysed and compared to laboratory spectra for Martian mineralogy and PAH signatures.

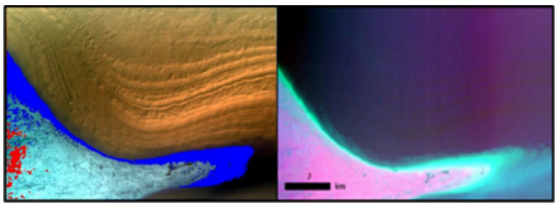

Figure 2: Left: 'True colour' visualisation of Site 1 from CRISM bands R = 230 G = 75 B = 10. Strongest 10% spectral responses for ices shown in red (CO2) and blue (H2O). Right: False colour visualisation of Site 1 using Pelkey (2007) summary products R = 1435 (CO2 ice) G = 1500 (H2O ice) B = BDCARB (carbonate overtones)

Laboratory experiments were performed to constrain the detectability limit of PAHs, and to establish PAH spectral features at wavelengths other than the well-known absorption feature at 3.29 µm. There is currently no existing published evidence of PAH detection within CO_2 ice features. The site of the laboratory experiments was the "Cold Surface Spectroscopy" facility (CSS) at the Institut de Planétologie et Astrophysique de Grenoble (IPAG) Grenoble, France using the spectro-gonio radiometer and its CarboN-IR environmental cell, which have been specifically developed for studying planetary analogues.

In addition, both unsupervised classification and comparison with laboratory analogue spectra is used to ascertain end member ratios and look at compositional changes over time, and the relationship between SCT morphology and dust content.

Results: The detectability limit of PAHs was established within SPRC analogues, end member spectra have been established for all components of interest, and new diagnostic absorption features for PAHs have been recorded at a number of wavelengths.

There are clear spectral differences between dust rims and non-rim regions, with indications that the initial stages of SCT pit formation result in lower dust content on pit rims as the scrap walls collapse, with an increase in dust content as the fully formed pits become more circular and retreat laterally, leaving behind concentrations of dust. No in-situ evidence of PAHs has been observed, but this work provides the necessary baseline spectra, detectability limits and understanding of pit formation relating to dust content, to improve interpretation of orbital data, and will form the basis for continuing research of dynamic features on Mars in order to detect organic material, and contribute to the search for habitable environments on Mars.

References:

[1] NASA (2015) http://science.nasa.gov/missions/marinermissions [2] Murchie et al. (2007) JGR, doi:10.1029/2006JE002682 [3] Vita-Finzi, C. (2005) Planetary Geology, 146-159. [4] Tokar et al., (2003) GRL, 30, 1677, 13. [5] Carey, F.A. Organic Chemistry, 398-423 [7] Vita-Finzi, C. (2005) Planetary Geology, 146-159. [6] Benner, S.A. et al. (1998) PNAS, 96,6,2425-2430 [7] Allamandola, L.J. (2011) EAS, 46,305-317 [8] Cruikshank. D.P. et al. (2008) Icarus, 193, 334-343 [9] Pelkey, S.M.et al. (2007) JGR, doi:10.1029/ 2006JE002831

Additional Information: Part of the research leading to these results has received partial funding from the European Union's Seventh Framework Programme (FP7/2007-2013) under iMars grant agreement n° 607379; MSSL STFC Consolidated grant no. ST/K000977/1 and the first author is supported by STFC under PhD studentship no. 526933.

SPECTRAL VARIATION BETWEEN SOUTH POLAR RESIDUAL ICE DEPOSITS IN MARS YEARS 28 AND 29. S. F. A. Cartwright[1], W. M. Calvin[1], and K. D. Seelos[2], [1]Dept. of Geological Sciences and Engineering, University of Nevada—Reno, 1664 N. Virginia St., MS 0172, Reno, NV 89557 (scartwright@nevada.unr.edu), [2]Johns Hopkins University Applied Physics Laboratory, 11100 Johns Hopkins Road, Laurel, MD 20723

Introduction: The south polar layered deposits (SLPD) of Mars constitute a ~4 km high dome of dusty water ice layers that have long been thought to represent a record of past climatic variation [1]. The portion of the SPLD that sits above an elevation of ~2 km retains a bright, meter to tens-of-meters deposit of CO_2 ice throughout the year (Fig 1). In addition to a number of unique erosional features on its surface [2], small exposures of water ice have been observed around the margins of the SPLD's CO_2 ice veneer, though it is unclear whether they constitute an uppermost layer of the SPLD or annealed seasonal water ice [3, 4]. Determining the detailed compositions and grain sizes of ice and dust mixtures that make up the upper portion of the SPLD may illuminate the formation mechanisms of those erosional features and, more broadly, the climate record of the SPLD.

The best equipped dataset to help constrain those attributes are the targeted observations of the Compact Reconnaissance Imaging Spectrometer for Mars (CRISM) [5], which has captured hundreds of hyperspectral visible-to-near-infrared observations of the SPLD at spatial resolutions up to 18 m/px. Here we use four such observations (Fig. 1, Table 1) to compare the distribution of CO_2 and water ice at early and late solar longitude (L_s) in Mars Years 28 and 29 in preparation for detailed spectral modeling of grain size and composition.

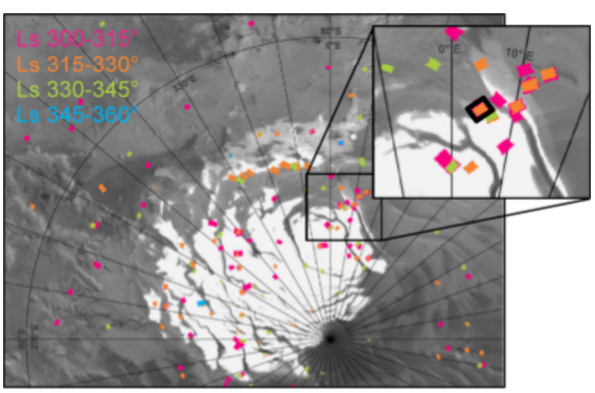

Figure 1: Mars Orbiter Camera (MOC) albedo map of the south polar region, overlaid with CRISM image footprints colored by L_s. The study region covered by observations in Table 1 is centered at 85.6° S, 6.3° E and outlined within the inset.

Table 1: Observational metadata for the four CRISM observations used in this work.

Observation	L_s (°)	Mars Year	Ref. Code
FRT00006EC9	288.82	28	E28
FRT00008354	330.68	28	L28
FRT00011936	227.06	29	E29
FRT00014639	321.78	29	L29

Methods: The four CRISM targeted observations were processed using the CRISM Analysis Toolkit (CAT) 7.4 plugin for Harris Geospatial ENVI 5.5 image analysis software [6]. Targeted Reduced Records (TRR3) downloaded from the Planetary Data System were converted to CAT file format before Lambertian photometric and volcano scan atmospheric corrections were applied. The resulting spectral cubes were then map-projected and georeferenced to FRT00006EC9 using 15 tie points distributed across the scene.

Due to its clear differentiation of several apparent units, FRT00008354 was used to define a collection of 33 regions of interest (ROIs) in and around the study region's residual CO_2 ice-covered mesas (Fig. 2). These ROIs capture dark and light portions of erosional pit floors and the light halos that surround them, different portions of the mesas themselves, and dark and light ice exposures elsewhere in the scene, including a reticulated debris field.

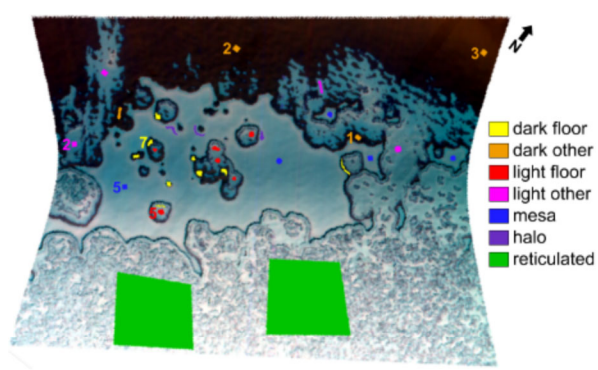

Figure 2: FRT00008354 (RGB = 2.52, 1.50, 1.07 µm) overlaid with ROIs color-coded by type. Note the flat mesas eroded into "swiss cheese terrain" by a number of pits. Numbers reference ROIs compared in Figure 3.

Averaged spectra of the ~20–50 pixels comprising each ROI were calculated for each of the four images, allowing for a direct comparison of spectral differences not only across distinct units in the study region, but also across two seasons in two Mars Years. These first-order evaluations of compositional difference will be used to guide further investigation with unmixing models by Kieffer and others [7, 8] that will constrain differences in grain size and dust/ice abundance.

Initial Results: *Inter-annual comparisons:* Averaged spectra for ROIs covering light pit floors, mesa tops, and other light exposures in late L_s observations show strong CO_2 ice signatures varying only in relative albedo (Fig. 3A), with a significant 10% increase being found in L29 (see Table 1 for corresponding observation ID for this and other reference codes). ROIs covering dark exposures outside the mesas in both late L_s observations show a marked difference in average spectra: while L28 shows a consistent strong water ice signature, in L29 those ROIs display varying degrees of apparent water ice with CO_2 (Fig. 3B).

Intra-annual comparisons: ROIs for light pit floors show elevated water ice content compared to early L_s observations in each year, as evidenced by broadening of the absorption at 1.5 µm. Similarly, there is a pronounced difference between dark exposures in early and late L_s, with dark exposures in pit floors and elsewhere shifting from strong CO_2 ice signatures in E28 to water ice in L28 (Fig 3C).

ROI spectra in mesa tops show greater depth of CO_2 absorption features compared to ROIs capturing the higher albedo halos that surround erosional pits, indicating a possible difference in grain size. Spectral signatures of the large ROIs covering the reticulated debris field in the lower portion of the study region (Fig. 2) indicate slight differences in water content between early and late L_s in both years.

Discussion: The observed intra-annual differences between early and late L_s observations are as expected: seasonal CO_2 frost present in southern spring obscures water ice signatures that may be visible by the time frost has been removed in late southern summer (e.g., Fig. 3C). This frost cover is expected to persist up to L_s = 320–340°, meaning the observed inter-annual differences between L28 and L29 (Fig. 3A, B) may hint at processes shifting that cutoff, such as enhanced removal following the MY 28 dust storm and/or increased deposition during the winter of MY 29 [9, 10]. Comparison of spectral modeling results across additional study areas and L_s values (Fig. 1) will help constrain the thickness and yearly retreat of seasonal CO_2 ice, allowing the nature of underlying water ice deposits to be more accurately characterized.

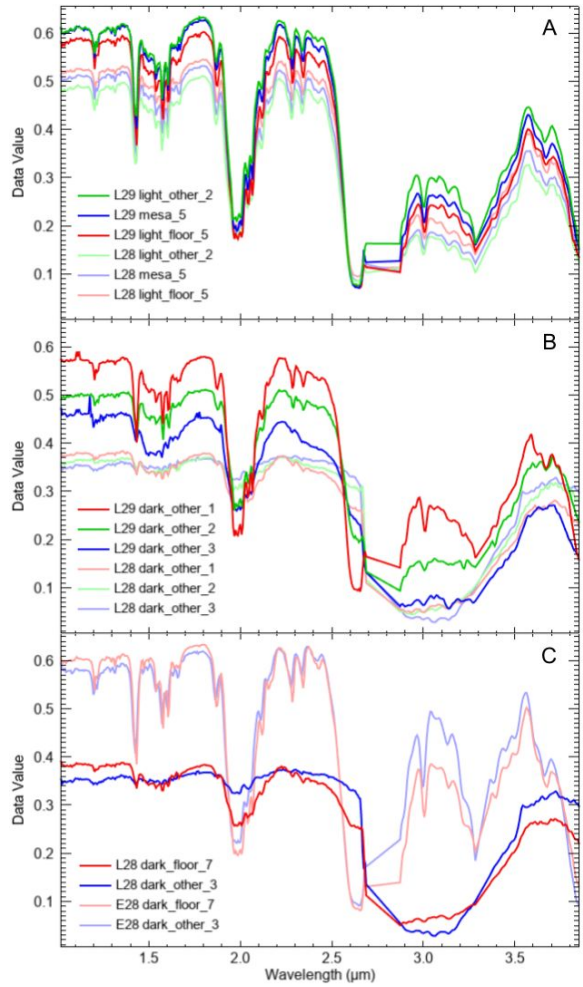

Figure 3: Plots of averaged ROI spectra showing comparisons between A) various light-toned exposures in late L_s observations for MY 28 and 29, B) dark exposures outside mesas in late L_s observations for MY 28 and 29, and C) dark pit floors in mesa interiors and dark exposures elsewhere in early and late L_s for MY 28. Line color links ROIs while opacity differentiates timeframes. See Table 1 for observation IDs corresponding to shorthand reference codes and Figure 2 for the location of numbered ROIs.

References: [1] Byrne (2009) *Annu. Rev. Earth Planet. Sci., 37,* 535–560. [2] Thomas et al. (2009) *Icarus, 203,* 352–375. [3] Douté et al. (2007) *Plan. & Space Sci., 55,* 113–133. [4] Montmessin et al. (2007) *JGR, 112,* E08S17. [5] Murchie et al. (2007) *JGR, 112,* E05S03. [6] Morgan et al. (2009) https://pds-geosciences.wustl.edu/missions/mro/CRISM_Workshop_090322_CAT_MFM.pdf [7] Kieffer et al. (2000) *JGR, 105,* 9653–9699. [8] Lapotre el al. (2017) *JGR, 122,* 983–1009. [9] Calvin et al. (2017) *Icarus, 292,* 144–153. [10] Piqueux et al. (2015) Icarus, 251, 164–180.

CO_2 ICE AND MGS-1 MARS GLOBAL SIMULANT : EXPERIMENTAL WORK TO RECREATE DARK SPOT EVOLUTION ACTIVITY AND SELF-CLEANING PROCESSES OBSERVED BY CaSSIS.

C. Cesar[1] , A. Pommerol[1], C. Herny[1], C.J. Hansen[2], G. Portyankina[3] and N. Thomas[1], [1]Physikalisches Institut, Universität Bern, Switzerland (camila.cesar@space.unibe.ch), [2]Planetary Science Institute, St. George, Utah, USA, [3]University of Colorado, Boulder, CO, USA.

Introduction: Combined observational data from CaSSIS and experimental work in our IceLab facilities would lead to a better understanding of CO_2 driven processes in Martian polar regions. A previous CaSSIS acquisition was thought to be odd compared to similar observations, showing yellow and green spots, the reflectance profiles over these features display variations in the PAN filter consistent with each other, NIR and RED filters differ in trends with the spots colours [1]. At first, time evolution and light scattering effects were believed to be producing this range of colours, composition was of course another candidate. Lately, several images with yellow and green colouring have been found in CaSSIS database and it is thought to be due to a specific filter combination (PAN-NIR-RED) but the origin of the reflectance variations is yet to be discover. Our goal is to experimentally identify the processes behind the reflectance variations which may be linked in some ways to the temporal evolution of spots.

Motivations: The self-cleaning process, showed in figure 4a and 4b of [2], is one of the main theory behind spots' evolution. The spots are first deposited after jets have erupted from overpressure at the base of the slab - leaving spiders as remnant on the surface [3], they then sink slowly into the slab, gets covered by fresh CO_2 frost/snow until fully covered (fig.1). A few experiments on dust ejection from CO_2 ice caps have been done [4], we are aiming to experiment on the consequences of such events. Moreover a study of Richardson crater [5] showed the presence of water content in small quantities but still with significant changes in reflectance, this might be also the case in the region we are focusing on and induce those yellow and green colouring (fig.2), although this water content might be difficult to reproduce in the laboratory since it is the order of a few ppm.

Experimental Setup: Using the SCITEAS chamber setup [6], we designed a simple experiment involving CO_2 ice and the newest Martian analogue MGS-1. The analogue is powdered arbitrarily on top of an industrial CO_2 Slab which is then illuminated with a Sun simulator with a power range up to 300W. A CCD Camera records, in the visible range, the sublimating ice and the sinking grains (Fig.3).

For comparison purposes, CaSSIS filters can be added physically on the camera and/or virtually into the acquired images. To obtain more significant results, we use the Optical Coherence Tomography Planetary Ultra-cold Samples (OCTOPUS), which is a system to image sample surfaces in 2D or 3D, to get a quantitative overview of the sinking grains – such as the sinking rate and the depth.

Results and Discussion: Our first test runs have been successful so far, the data acquired is still qualitative. We clearly see the grain sinking into the CO_2 slab while it sublimate. The goal is to quantify this process in a reproducible way and with various setups, including spot shapes, analogue distribution and illumination conditions. Further results will be presented at the conference.

References: [1] Cesar C. et al. (2019) *9th ICM,* Abstract #6253. [2] Kieffer H. et al. (2006) *Nature*, 442, 793-796. [3] Hansen et al. (2010) *Icarus 205,* 283–295. [4] Kauffman E., and Hagermann A. (2017) *Icarus 282,* 118–126. [5] Gardin E. et al. (2010) *JGR* 115-E6. [6] Pommerol A. et al. (2015) *PSS 109-110*, 106-122.

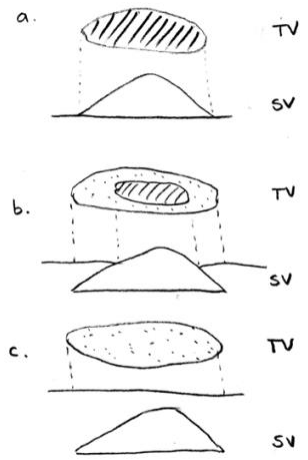

Figure 1 : Sketch of self-cleaning process. (a) Top View and Side View of a full spot on CO_2 ice slab. (b) On the TV of a partially covered spot, the central part appears darker with a "light halo" surrounding it. (c) Remnant halo from a completely covered spot.

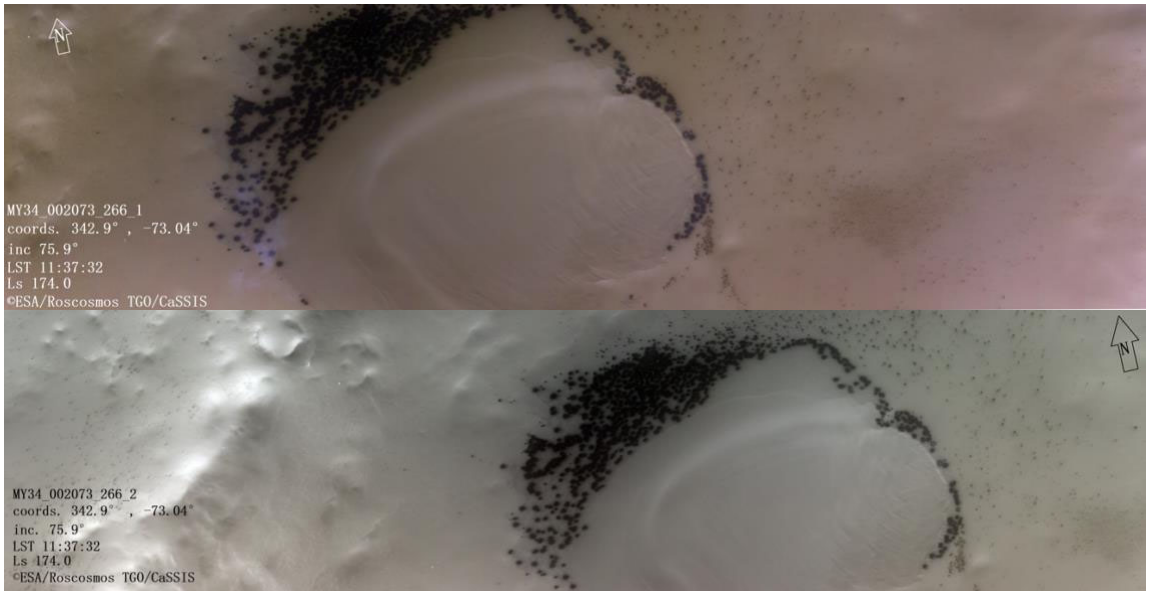

Figure 2 : CaSSIS stereo acquisition 2073_266 taken on May 11th 2018 at 18:56:54. (Top) stereo 1 with PAN RED BLU filters showing mostly dark blue spots, a few light blue, and small red ones, and what seem to be a cloudy feature . (Bottom) stereo 2 with PAN RED NIR showing respectively dark, grey and yellow spots, the cloudy feature seem faded and is present only in the PAN filter.

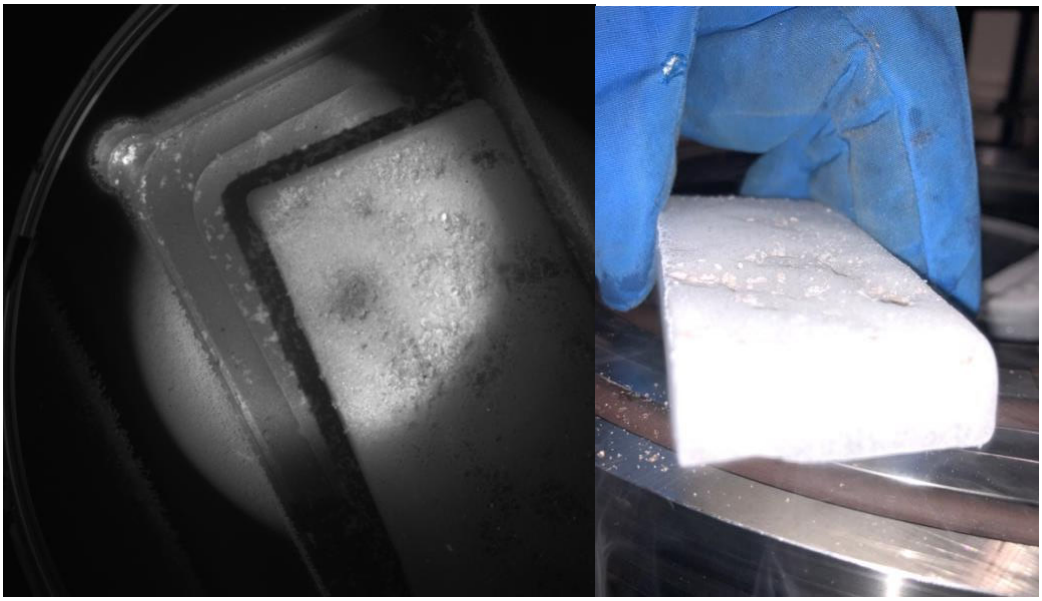

Figure 3 : (Left) Top view of the CO_2 slab during the test run. (Right) Side view of sinking areas after the experiment.

RATES AND TRENDS OF CIRCUM-POLAR AEOLIAN DUNE EVOLUTION. M. Chojnacki[1], J. Bapst[2], I. B. Smith[3], and K. E. Herkenhoff[4]. [1]Lunar and Planetary Lab, University of Arizona, Tucson, AZ (chojan1@pirl.lpl.arizona.edu), [2]Jet Propulsion Laboratory, California Institute of Technology, Pasadena CA, [3]York University, Toronto, Ontario, Canada, [4]U.S. Geological Survey, Flagstaff, AZ.

Introduction: The north polar region of Mars displays a range of ongoing seasonal and annual surface processes that constantly reshape the local landscape. Recognized in the last decade as a prominent region for active bedform movement (*1–3*), dunes surrounding the polar layered deposits (PLD) and residual cap also display the greatest migration rates and fluxes ~50% greater than on average for Mars (11.4 vs. 7.8 $m^3 m^{-1} yr^{-1}$)(*4*). These higher values are despite a limited sediment state caused by seasonal autumn/winter CO_2/H_2O ice accumulation that restricts dune migration for most of the year by reducing interaction with wind. Sand becomes ice-cemented while winter-time CO_2 ice buries dunes and then slowly sublimes through the Northern spring/summer until bedforms are "frost free" and mobile by summer (*2*, *5*). Some ice-cemented bedforms do not appear to regain mobility and are deposited into the geologic record.

The purpose of this work is to quantify and characterize major elements of polar landform evolution, such as sand dune formation, bedform dynamics, and deposition of sand into the polar sedimentary record.

Datasets and methods: The main dataset utilized to assess aeolian activity at a global scale consists of images acquired by the High Resolution Imaging Science Experiment (HiRISE) camera (0.25–0.5 m/pix)(*6*). Bedform dynamics were assessed with image orthorectification from stereo-photogrammetry (*4*, *7*).

Sand sources through proto-dune development: The steep (>30°), heavily fractured PLD cliffs commonly avalanche in Spring (L_s 8 - 48°), as observed by HiRISE (*8*). Variably sized (10-70 m) blocks of the PLD and basal unit, liberated by thermally-driven expansion and contraction, cascade onto lower slopes (*9*, *10*). With greater frequency in the spring and summer, smaller mass-wasting events of the basal unit (BU) occur a major source of dune and ripple-forming sand (*10*).

BU sand sources emanate from the cliffs and travel downwind in several forms (**Fig. 1d**). Sand may develop into ripple patches or larger nascent proto-dunes (e.g., dome dunes, sand streamers) then migrate downwind until sand supply is sufficient to form fully-developed dunes or broad sand sheets (**Fig. 1b**). These proto-dunes can migrate up to 2-4X faster (~2 m/Earth year) than mature dunes in similar locations, due to their smaller sizes and the relatively unencumbered atmospheric flow that drives them. Alternatively, we see evidence that suggests large amounts of sand saltates across bedrock surfaces downwind of BU sources without forming bedforms until entering the erg system (**Fig. 1d**). Proto-dunes which are variable in width (20-100 m) have sediment fluxes on the order of 10 $m^3 m^{-1} yr^{-1}$. These values are generally higher than the estimated erosion rates of some polar scarps (~0.3 m^3 per Mars year per meter along one scarp) (*11*).

Circumpolar sand dune activity and sediment fluxes: The most active dune regions on Mars occur within ergs of Olympia, Abalos, Siton, and Hyperborea Undae (**Fig. 1a**). Sand fluxes are greatest at: 1) the upwind edge adjacent to some of the steepest (>30°) PLD/BU scarp exposures, and 2) in mid-erg locations where >50 m-tall mega-dunes migrate. Numerous 20-30 m-tall dunes translate at relatively high rates (~1 m/yr) tangentially away from the poles and steered zonally by Coriolis-force directed winds (12). Moderate sand fluxes are observed along distal locations of the southern erg margin where multiple wind regimes converge (*4*, *5*, *12*).

A variety of atmospheric and geologic processes interact and modify polar dunes. Mesoscale model simulations indicated that spring and summer katabatic winds are driven by the retreat of the seasonal CO_2 and increasingly large thermal and albedo (15-25%), along with topographic variations between the ergs and polar cap (*12*, *4*). Periods of frost-free sand (late spring – end of summer) also coincide with the timing of peak of water vapor (*13*, *14*) and dust-laden storm frontal events (*15*). The apparent correlation of these processes with periods of highest sand movement is being investigated. Seasonal CO_2 ice appears to contribute to up to 20% of the local sand movement by forming large slipface alcoves that develop as the result of overburden along dune crests (**Fig. 1c**)(*4*, *16*). This apparently unique martian process occurs in the autumn or winter possibly related to CO_2 snowfall (*16*).

Aeolian deposition into the polar stratigraphic record: The deposition and storage of sandy materials take a variety of forms and in numerous polar locations. Sand pathways adjacent to PLD lower flanks show stabilized mature duneforms under meters of water ice deposits (*1*, *5*, *17*). Other central erg sites show dunes with limited mobility and subdued lee faces, indicating a lack of sand transport. These trends are due to restrictive boundary conditions (e.g., lower winds, greater frost), that may lead to further deposition and sand storage. For example, inter-dune areas of Hyperborea and Olympia Undae show aeolian cross-strata under migrating barchans (*5*, *18*). Craters on the southern edges of the polar

erg also show evidence for aeolian deposition. Louth crater, for example, has migrating dunes where active sand-ice deposition is occurring (**Fig. 1e**), although water-ice mounds appear to be in equilibrium (*19*). Over ~6 Mars years of observations ice-cemented aeolian strata can be observed at Louth to be deposited at 0.18 m/yr if stacked vertically these rates over time would result in nearly ~200 m per kyr. These examples forming under the modern climate may be similar to the large deposits of water ice and sand beneath Olympia Planum which formed under past climates (*17*).

Conclusion and future direction: The north polar circumpolar erg shows the highest rates of sand dune formation, migration, deposition, and sediment fluxes on Mars indicating the current polar climate is quite conducive to a very active sedimentary cycle. Future efforts will utilize additional constraints from the Mars Polar Climate Database and seasonal trends obtained from various MRO data (*12*, *20*). This will include determining the predominant sand flux orientation(s) from dunes to be compared with mesoscale modeling and better constrain the dominant wind direction(s) per season.

Acknowledgments: This research effort for M.C. was supported in part by NASA MDAP Grant NNH14ZDA001N.

References: [1] Bourke, M. et. al. (2008) *Geomorph*. 94, 247–255N. [2] Hansen, C. et. al. (2011) *Science*. 331, 575–578. [3] Bridges, M. (2011) *Geology*. 40, 31–34. [4] Chojnacki M. et al. (2019) *Geology,* 10.1130/G45793.1. [5] Ewing R. et al. (2010) *JGR Plant. 115, E08005* (2010). [6] McEwen A. et al. (2007) *JGR Plant. 112,* E05S02. [7] Chojnacki M. et al. (2018) *JGR Plant.* 123, 468–488. [8] Russell P. et al. (2008) *GRL.* 35, L23204. [9] Byrne S. et al. (2011) *Mars 8*, Abs. #1257. [10] Russell, P. et al. (2014) *Mars 8*, Abs. #1373. [11] Fanara et al. (2019) *Icarus*, 113434. [12] Smith I. & A. Spiga (2017) *Icarus*. 308, 188–196. [13] Pankine A et al. (2009) *Icarus*. 204, 87–102. [14] Brown A. et al. *Icarus*. 277, 401–415 (2016). [15] Wang, H et al. (2009) *Icarus*. 204, 103–113. [16] Diniega S. et al. (2018) *Geol.Soc.Lond.*, 467, 95-114. [17] Nerozzi S. et al. (2019) *GRL.* 46, L082114. [18] Brothers S. et al. (2018) *Icarus*. 308, 27–41. [19] Bapst J. et al. (2018) *Icarus*. 308, 15–26. [20] Calvin W. et al. (2015) *Icarus*. 251, 181–190.

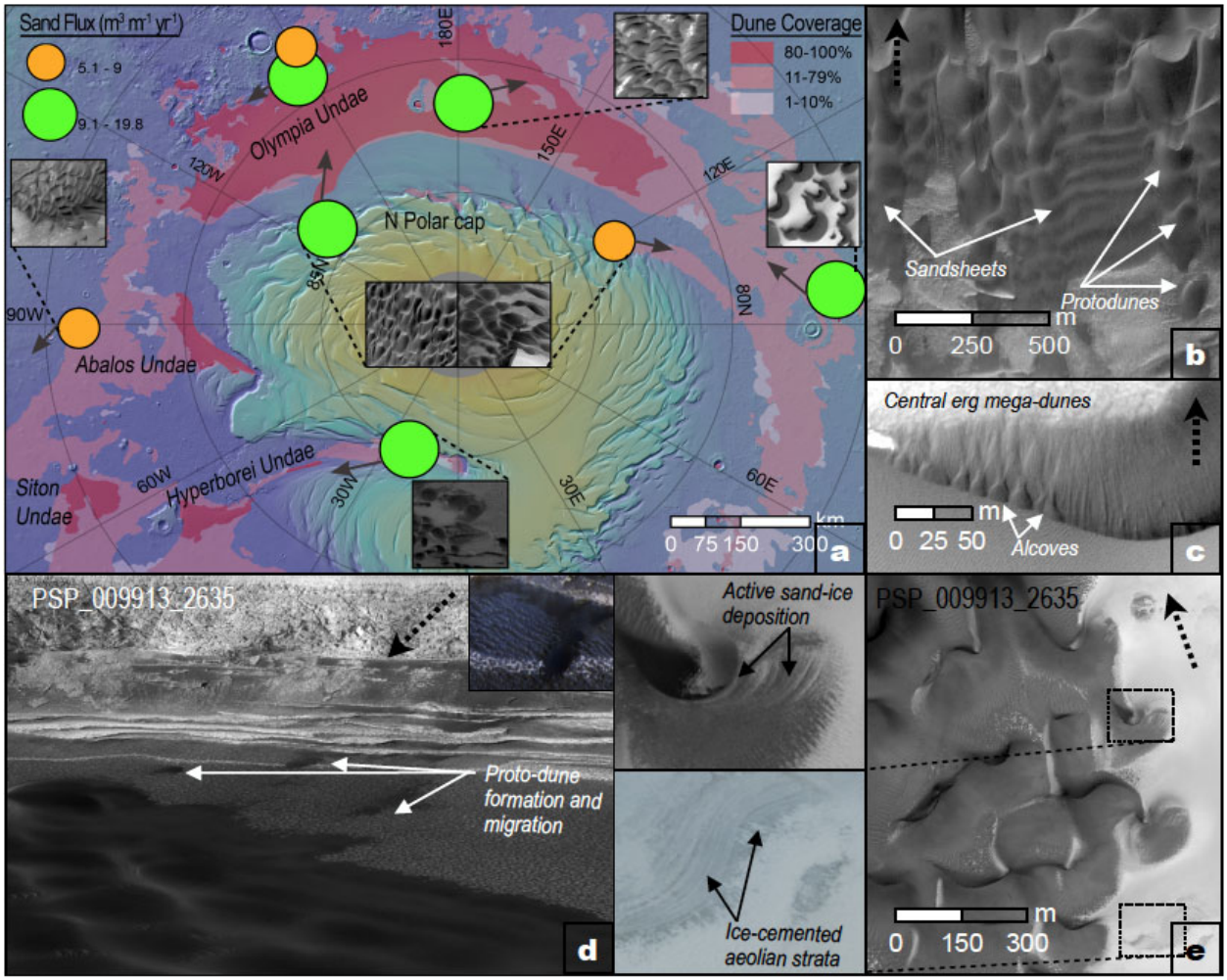

Figure 1. a) Sand flux measurements of polar dune fields (graduated circles) and their distribution (red polygons). Average dune migration vectors are represented by black arrows for each dune field. Inset HiRISE images are ~2-km-wide. b) Proto-dunes and Olympia Undae. c) Alcoves that form on steep lee-faces. d) Oblique view of polar scarps where basal units layers source proto-dunes (inset upper right), which eventually develop into dunes (1b). Scene is ~1.1-km-wide. e) Louth crater where dunes slowly migrate and deposit sands and ice into the crater floor units. Insets are ~170-m-wide.

The Comparative Distribution of Flowing and Non-Flowing Icy Material in the Nereidum Montes; Mars J. L. Collins-May[1], J. R. Carr[1], M. R. Balme[2], S. Brough[1], C. Gallagher[3], N. Ross[1] A. J. Russell[1], [1]Geography Politics and Sociology, Newcastle University, UK (j.collins-may@newcastle.ac.uk) [2] School of Physical Sciences, The Open University, UK, [3] UCD School of Geography, University College Dublin, Ireland

Summary: The aim of this work is to investigate whether there are significant topographical differences in the locations of flowing versus non-flowing deposits of ice in the Nereidum Montes. These results have implications for understanding Martian paleoclimate, as flowing deposits of ice should have formed in preferential locations for ice to accumulate, where deposits reach the required thicknesses to be able to flow.

Introduction: An abundance of features exist in the mid-latitudes of Mars (30°-60°) [1] that appear to be primarily composed of water ice [2]. Surface ice on Mars is currently unstable at the surface below 60° latitude [3], so the persistence of ice in the mid-latitudes indicates the climate must have been significantly different from today when these deposits were emplaced within the last few hundreds of millions of years [4-5]. This climatic shift might have been driven by an increase in Mars's mean obliquity [5], mobilizing ice from the polar regions to the mid-latitudes.

A subset of these mid-latitude icy deposits display morphological characteristics typical of downslope flow of ice on Earth, such as diverting around obstacles, lobate termini and arcuate surface ridges [6]. These flowing landforms are collectively known as Viscous Flow Features (VFF), [6] and are theorized to have developed during one or multiple high obliquity periods, possibly as layers of icy mantling materials built up to sufficient thicknesses to begin to flow [6]. Therefore, VFF should be located in more preferential areas for ice to form and survive than non-flowing icy deposits.

Determining which factors control the accumulation of enough ice to begin to flow and form a VFF is crucial to understanding the paleoclimate of Mars and how it is impacted by orbital excursions [7].

In this work, we compare the distribution of VFF and non-flowing icy material across several topographic variables that influence the development of glacier ice on Earth. These are: latitude, longitude, elevation, surface slope, relative relief and aspect.

Study Area: The Nereidum Montes mountain range, which forms the northern rim of the Argyre Impact Basin, is particularly well suited for this study [8]. This site has a relatively low latitude (34°S to 50°S), close to the latitudinal limit of surface ice deposits. The climate at these latitudes is harsh for ice deposits to exist in, due to greater insolation compared to higher latitudes. Therefore any ice deposits in the Nereidum Montes are located in the most favorable locations for ice, so areas with VFF should have more easily distinguishable characteristics than areas with non-flowing ice. The Nereidum Montes also possesses a large range in longitude (~40°), elevation (~8500 m), surface slope (0° to 49°), relative relief (~3500 m) and aspect, which is crucial for an analysis how these factors may control where VFF features form rather than non-flowing ice deposits.

Methods: We mapped all VFF in the Nereidum Montes at a scale of 1:25,000 using ConTeXt Camera (CTX) [9] imagery. Deposits with surface textures similar to VFF but lacking indications of flow, were mapped as Non-Flowing Icy Bodies (NFIB). The elevation, slope, relative relief and aspect of VFF and NFIB were then extracted from MOLA DEM [10] data.

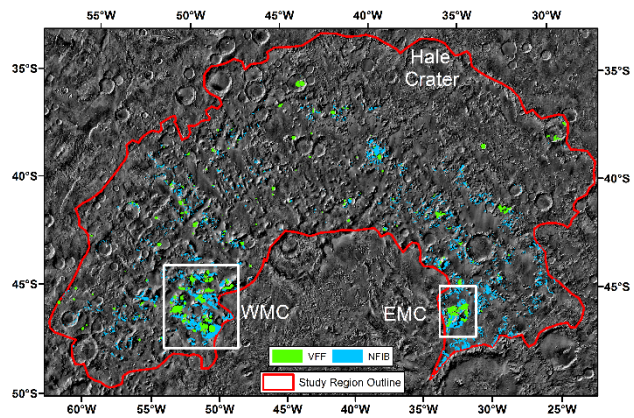

Figure 1: THEMIS Daytime Infrared imagery overlain with the mapped VFF and NFIB. Also highlighted is the location of two mountainous regions exhibiting large concentrations of VFF and NFIB, the Eastern Mountain Cluster (EMC) and the Western Mountain Cluster WMC).

Results & Discussion: Our mapping reveals that more VFF and NFIB is located at higher latitudes in Nereidum Montes than lower ones (Fig. 1). NFIB is more prevalent than VFF at almost all latitudes (Fig. 1), so increased ice survival at higher latitudes does not appear to promote the formation of VFF over NFIB. There are longitudinal patterns in the distribution of VFF and NFIB, with both types being the most prevalent in two regions of the Nereidum Montes that

we term the Eastern Mountain Cluster (EMC) and Western Mountain Cluster (WMC) (Fig. 1). However, VFF are much more common in the WMC than the EMC (Fig. 1).

The clearest differences between non-flowing and flowing icy material are in surface slope (Fig. 2). NFIB deposits tend to have lower surface slopes than VFF do, with a clear peak in abundance at 12°. The surface slope distribution of VFF material is more consistent across the range of surface slope values than NFIB, and almost all of the mapped material with a surface slope of over 30° is VFF material. This may reflect a difference in internal dynamics between VFF and NFIB deposits.

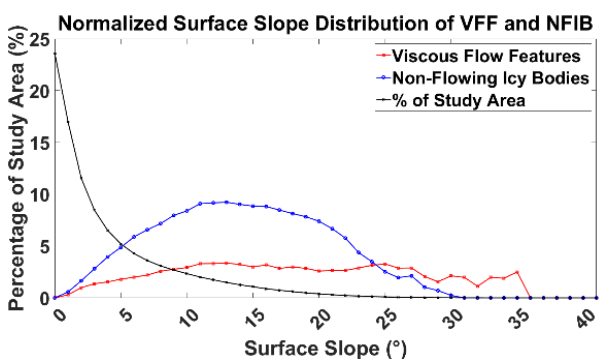

Figure 2: The surface slope distribution of VFF and NFIB in 1° bins.

Increasing relative relief promotes greater surface coverage by icy material overall, with no icy material found in locations with less than 300 m of relief. However, NFIB material is more common than VFF in the majority of relative relief bins present at the study site (Fig. 3). Though VFF coverage at 3500 m to 3600 m of relative relief is 100%, this bin is composed of one pixel and may not be representative of the actual relationship. Therefore, increasing relief does not appear to promote the development of VFF over NFIB.

Aspect also influences the distribution of icy material (Fig. 4). Icy material has a clear preference for southerly aspects, with very little material facing northwards. This is anticipated, as south facing aspects reduce direct insolation in the southern hemisphere of Mars. Though southerly aspects appear to be the most preferential for the formation or survivability of ice, this factor does not appear to drive the formation of more VFF than NFIB, as NFIB covers more of the Nereidum Montes than VFF in every aspect direction.

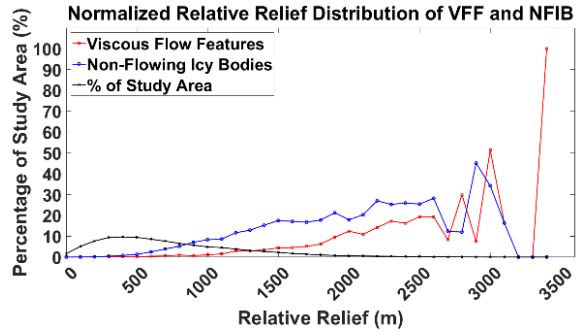

Figure 3: The relative relief distribution of VFF and NFIB in 100 m bins.

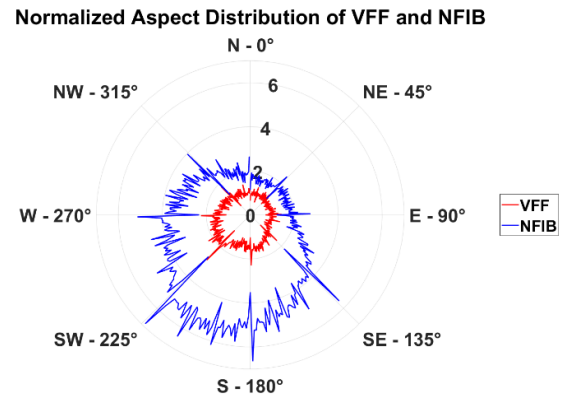

Figure 4: The aspect distribution of VFF and NFIB in 1° bins.

Overall, topography influences the presence of VFF and NFIB in similar ways, supporting the idea that VFF are formed or preserved by the same conditions that NFIB deposits are. The broadly similar distribution of VFF and NFIB also suggests that VFF are composed of the same material as NFIB. However, while topography plays a role in determining where icy material survives overall, the formation of VFF over NFIB is likely due to other factors. An example may be wind patterns, driving the deposition of more ice in certain locations.

References: [1] Brough et al (2019), *EPSL,* 507, 10-20 [2] Holt et al., (2008) *Science*, 322, E5905, 1235-1238 [3] Head et al., (2005) *Nature,* 434, E7031, 346-351 [4] Levy et al., (2010) *Icarus*, 209, I2, 390-404 [5] Forget et al., (2006), *Science*, 311, E5759, 368-371 [6] Milliken et al., (2003), *JGR; Planets,* 108, I6, 1-11 [7] Levy et al., (2014) *JGR: Planets*, 119, I10,2188-2196 [8] Banks et al., (2008) *JGR:Planets*, 113, I12, 1-20 [9] Malin *et al.,* (2007) *JGR: Planets*, 112, I5, 1-25 [10] Smith et al., (2001) *JGR: Planets*, 106, I10, 23689-23722.

DETECTION LIMITS FOR CHIRAL AMINO ACIDS USING A POLARIZATION CAMERA. C. W. Cook[1], S. Byrne[1], D. Viola[2], C. Drouet d'Aubigny[1], J. Mikucki[3], [1]Lunar and Planetary Laboratory, University of Arizona, Tucson, AZ 85721 (clairec@lpl.arizona.edu), [2]NASA Ames Research Center, Mountain View, CA 94035, [3]Department of Microbiology, University of Tennessee, Knoxville, TN 37996

Introduction: The detection of biosignatures on a planetary surface is of significant scientific interest. Martian ice deposits (especially long-lived ice in the South Polar region) may preserve biosignatures by shielding them from UV radiation and slowing the rate of oxidative reactions common in the martian regolith [1]. High enantiomeric excesses are one such biosignature that a future mission that excavates subsurface ice could test for. Enantiomers are each of the two non-superimposable mirror image configurations of chiral molecules. In biological materials on Earth, the ratio of the L enantiomer to the D enantiomer of amino acids is high, while in abiotic materials, the two are found in approximately equal amounts [2].

High enantiomeric excesses in samples can be detected by their polarizing effects on transmitted light. The optical rotation of a molecule is the angle by which plane-polarized light is rotated when it passes through a sample of the molecule in solution. The two enantiomers of a chiral molecule will have optical rotations with equal magnitude and opposite sign. For abiotic mixtures of two enantiomers, the optical rotations will roughly cancel out. However, in biogenic samples, a net change in optical rotation may be imparted. Polarimetry has thus been proposed as a biosignature detection method [3-5] .

Here, we assess the potential of polarization measurements, specifically optical rotation, to quantify enantiomeric abundances. We determine the minimum concentration of amino acids that can be detected using this approach. Given that in-situ samples would likely include mixtures of several amino acids and other compounds such as salts, we also determine the effect of mixtures of amino acids and salts on the optical rotation.

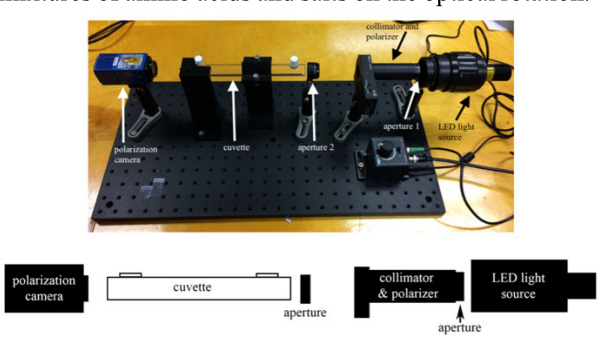

Figure 1: Picture and diagram of the optical set-up. From left to right: PolarCam, cuvette, aperture, collimator and polarizer with aperture on the end, LED.

Methods: The experimental set-up is shown in Figure 1. An LED light source is collimated and directed through a polarizer to create plane-polarized light, followed by a cuvette holding the sample, and the collimated beam is analyzed by a polarization camera (4D Technology's PolarCam Snapshot Micropolarizer Camera).

PolarCam uses a wiregrid polarizer array which contains a pattern of polarizers with 0, 45, 90, and 135 degree polarizations that together form a super pixel that is repeated over the array (Figure 2).

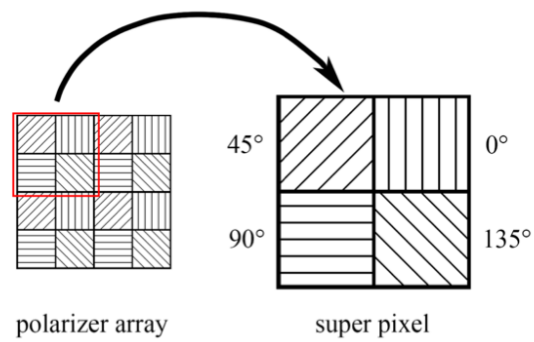

Figure 2: Diagram of a portion of the polarizer array and the arrangement of a single super pixel, based on [6].

We investigated two amino acids: serine (with a specific optical rotation at 590 nm of -6.83° [7]) and phenylalanine (with a specific optical rotation at 590 nm of -35.1° [8]). At shorter wavelengths, the specific optical rotation is higher [9] so we measured the optical rotation at 490 nm in addition to some measurements at 590 nm. Solutions of a single amino acid were measured for a range of enantiomeric abundances. In addition, some measurements were made with mixtures of serine and phenylalanine, with varying enantiomeric abundances. To determine the effect of salts on the optical rotation, measurements were also made with sodium chloride (NaCl) or magnesium sulfate heptahydrate ($MgSO_4 \cdot 7H_2O$) added to the amino acids. In each case, the stock solution with the amino acid(s) dissolved in water was serially diluted to produce solutions for a range of concentrations. Control measurements of pure water were taken before and after sample measurements.

For each sample and control measurement, we found the Angle of Linear Polarization (AoLP) by combining elements of each super pixel, then the average AoLP over all super pixels on the detector. We mitigated systematic errors which caused the AoLP to drift over time, by linearly interpolating between the AoLP for the

controls taken before and after the sample measurement to find what the control AoLP would be at the time the sample measurement was taken. We then subtracted the AoLP of the sample from this control AoLP to get the optical rotation of the sample. Figure 3 shows an example of the optical rotations obtained in this way for phenylalanine.

As concentration is reduced, the optical rotation shrinks to the detection limit and subsequently becomes noise with as many positive as negative results. Similarly as enantiomeric excess is reduced, larger concentrations are required for detection until the abundance of L-enantiomers is 50% (at which point these amino acids are undetectable with this method regardless of their concentration). We take the detection limit for optical rotation as the lowest measured concentration for which 1) the optical rotation plus or minus its error bars never crosses zero, 2) the optical rotation has the expected sign, and 3) every higher-concentration measurement satisfies conditions 1 and 2.

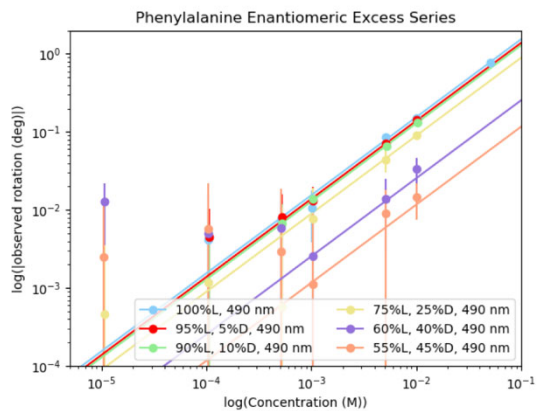

Figure 3: Absolute value of optical rotation of phenylalanine for various L-enantiomer abundances and concentrations. Curves shown are linear fits to the data points, passing through (0,0).

We also measured the optical rotations of three bacteria samples: *Marinobacter gelidimuriae* isolated from subglacial brine from Blood Falls, Antarctica [10], as well as a sample we denote Schw_1, from the glacial surface at Blood Falls, Antarctica, and a sample we denote Easton_1, isolated from snowpack on Easton Glacier, WA, USA.

Results: The detection limit for serine for 100% L is 0.005 M (moles/liter), decreasing to 0.05 M for 45% L. For phenylalanine, the detection limit for 100% L is 0.0005 M, decreasing to 0.01 M for 45% L.

As expected, the concentration detection limit for lower enantiomeric abundances is higher. In addition, detection limits for solutions with some L-enantiomer abundance and the equivalent D-enantiomer abundance are generally the same, as expected.

The optical rotations of the mixed amino acids are consistent with a linear combination of the optical rotations of the components. As expected, because phenylalanine has a higher specific optical rotation, the solutions with a higher proportion of phenylalanine have a higher optical rotation and lower detection limit. Adding salts does not significantly affect the optical rotation.

For concentrations $>10^6$ cells/mL, the optical rotation of *Marinobacter gelidimuriae* is detectable and negative, as one would expect for bacteria containing a majority of amino acids with negative optical rotations. Schw_1 and Easton_1 were detectable at $\sim 10^8$ cells/mL, but unusual results were found at lower concentrations, possibly indicating that the errors were large and the method was not effective at lower concentrations.

Discussion: Using this instrument, solutions with enantiomeric abundances 5% apart (corresponding to enantiomeric excesses 10% apart) are rarely distinguishable through their polarization effects. Even when they are, the concentrations at which they are distinguishable are more than an order of magnitude higher than the detection limits, meaning that even if an amino acid were detected at the detection limits that we found, the enantiomeric excess could not necessarily be determined to a high accuracy.

Biosignature detection via its polarizing effect on transmitted light offers a convenient and fast method to evaluate icy samples for more detailed analysis. However its detection thresholds are relatively high compared to other methods such as gas chromatography-mass spectrometry with chirality analysis.

References: [1] Lasne J. et al. (2016) *Astrobiology, 16*, 977-996. [2] Kvenvolden K. (1973) *Space Life Sciences, 4,* 60-68. [3] Sparks W. B. et al. (2005) *Astrobiology, 5,* 737-748. [4] Thaler T. L. et al. (2006) *Astrobiology, 6,* 901-910. [5] Kothari N. et al. (2008) *Astrobiology, 8,* 1061-1069. [6] Brock N. et al. (2011) Proc. *SPIE 8160,* 81600W. [7] Budavari S. (ed.) (1989) *The Merck Index*, 1341. [8] O'Neil M. J. (ed.) (2006) *The Merck Index*, 1255. [9] Polavarapu P. L., Covington C. L. (2015) *Physical Chemistry Chemical Physics, 17*, 21630-21633. [10] Chua M. (2018) *Microbiology Ecology, 94*, fiy021.

Proxy records of frost: Frost-driven geomorphic changes on martian sandy slopes. Serina Diniega[1], Candice J. Hansen[2], Ganna Portyankina[3]. [1]Jet Propulsion Laboratory, California Institute of Technology, Pasadena, CA, USA (serina.diniega@jpl.nasa.gov), [4]Planetary Science Institute, [3]LASP, University of Colorado, Boulder.

Introduction: Over the last ~decade, many small-scale geomorphological changes within martian sandy slopes have been identified and studied, occurring on ~annual timescales. In some sites where the timing of activity has been constrained to a portion of a Mars year, the formation of features has been tied to periods when frost is accumulating or sublimating. This, together with other data such as spatial distribution of the features, strongly suggests that *martian CO_2 frost and ice, especially when interacting with a granular surface, is an effective and primary geomorphic agent* (at least during the present and recent Amazonian) and should be considered, with wind and impacts, when interpreting martian geomorphology.

This work will summarize current results and ongoing studies of martian landforms observed to be active over seasonal-to-decadal-timescales and hypothesized to have activity connected to the accumulation and/or sublimation of seasonal frost (updated since the 2018 Amazonian Climate Wkshp). These types of studies are vital if we are to improve our ability to interpret these landforms as proxy markers of specific environmental conditions and thus use them to learn more about the Amazonian and present-day martian climate.

The landforms:

- Active martian **gullies** (Fig. 1) were first observed within the southern mid-latitudes, on both dune and rocky slopes [1-3], with present-day changes in alcove, channels, and aprons. The activity timing within the southern mid-latitudes has been constrained to late winter/early springtime, suggesting a connection to springtime sublimation-driven or initiated processes [4-6].
- *Superficially* similar features have been observed in the northern polar [7-10] and mid-latitude [11] dune fields. However, alcove formation within the north polar erg occurs before spring sublimation begins [13-15], possibly during early autumn [15]. Additional differences from the southern gully activities are found in the feature sizes and shapes, and locations of activity in subsequent winters, suggesting that the north polar alcoves may form through a different process [12].
- **Linear gullies** are long (up to 2 km), narrow channels that run downslope and are relatively uniform in width, ending in circular depressions referred to as terminal pits. Activity is tied to early spring, their location on pole-facing sandy slopes, and their general morphology [13,14] is consistent with a model of subliming CO_2 ice blocks sliding down the sandy slopes [14].
- New meters-scale **dendritic troughs**, carved into the surface, have been found in some polar, sandy regions and have been observed to be growing annually, likely due to scouring from sand [15]. The formation process is consistent with erosion by sublimation-induced gas jets fed by sub-ice gas flow [16,17]. Over time, this type of activity may form the araneiform terrain (AKA spiders) in the south polar region [18,19], with longer timescales not necessarily requiring the presence of sand.
- New **furrows** appear annually along the crests and margins of many dunes when the seasonal frost disappears [20]. Erosion of these features is also thought to be driven by cryoventing, with vents occurring where thermal and slope conditions change, leading to a weaker ice layer [21].

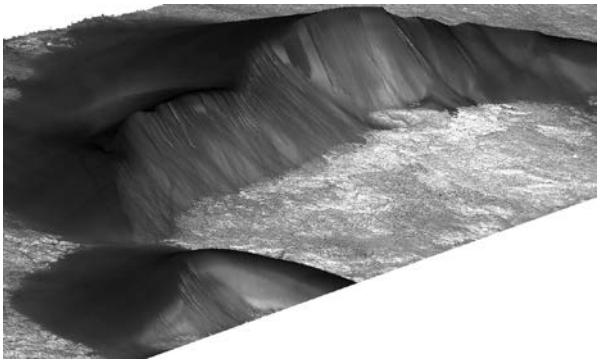

Figure 1. *Active dune gullies extend downslope on this megabarchan at the edge of Kaiser Crater dune field (46.8°S, 20.1°E). These are massive features (on a very large dune – 750 m tall), and some exhibit repeat activity over multiple Mars years. DTM was generated from PSP_006899_1330 and PSP_006965_1330.*

The drivers:

In this and many previous works, we have focused on CO_2 frost and ice as this volatile makes up 96% of the martian atmosphere [22]; accumulates on the martian surface in significantly greater amounts than water frost/ice (e.g., compare [23] with [24]); and – when information is available – coincides better with the timing of surface landform activity. Solid CO_2 can interact with the martian surface via these forms:

- As the autumn season cools, transient (diurnal) frost can condense on the martian surface. Such frost has been observed in low latitudes [25] and laboratory experiments have shown it can induce at least small-scale mass-wasting within granular material at or below the angle of repose [26].

- Seasonal frost accumulates within latitudes poleward of ~30d [27], with depths increasing up to tens of centimeters in the polar regions [23].
- As winter progresses, the CO2 frost anneals into denser slab ice [28].
- In the spring, blocks of CO_2 ice are cold-trapped in alcoves while ice on the slipface sublimes. If these ice blocks break free, they slide over the warmer exposed dark sand. Such blocks have been observed on the martian surface [e.g., 4]; terrestrial field experiments have shown that such blocks can easily 'hovercraft' down dune slopes, carving out a track [14,29]; and laboratory experiments under martian winter-time conditions show that stationary subliming blocks can create pits [20].
- Snowfall also occurs in the polar regions [30] and may influence some large-scale mass-wasting activity observed on north polar dunes [31].

Several CO_2-frost driven mechanisms have been proposed as possibilities for this present-day martian surface activity [e.g., 6,14,18,31-6], but the exact drivers/process(es) are still under investigation.

Implications for the martian landscape: Features such as martian gullies, linear gullies, and spiders/troughs/furrows are found over a range of latitudes [20,37-8] and are likely to reflect current or recent local-scale environmental conditions. Examining where different landforms are found may indicate where different types of solid CO_2 can be found on Mars, and what this implies about the martian volatile cycle.

References [1] Diniega et al. (2010) *Geology* **38** (11): 1047-1050. [2] Dundas et al. (2010) *Geophys. Res. Lett.* **37**: L07202. [3] Malin et al. (2006) *Science* **314**: 1573–1577. [4] Dundas et al. (2012) *Icarus* **220**: 124-143. [5] Dundas et al. (2015) *Icarus* **251**: 244-263. [6] Dundas et al. (2018) *Geo. Soc. London* **SP467**, #5: [7] Hansen et al. (2011) *Science* **331**: 575-578. [8] Horgan & Bell (2012) *Geophys. Res. Lett.* **39**: L09201. [9] Hansen et al. (2015) *Icarus* **251**: 264-274. [10] Diniega et al. (2018) *Geo. Soc. London* **SP467**, #6. [11] Widmer & Diniega (2018) *LPSC 49*, 1651. [12] Diniega & Dundas (2018) *LPSC 49*, 2244. [13] Morales et al. (2017), *49th DPS Mtg*, 400.01. [14] Diniega et al. (2013), *Icarus* **225**(1): 526-537. [15] Portyankina et al. (2017) *Icarus* **282**: 93-103. [16] Keiffer et al. (2000) *JGR* **105**(E4), 9653-9699. [17] Kieffer (2007) *JGR* **112**(E8): E08005. [18] Piqueux et al. (2003) *JGR* **108**(E8): 5084. [19] Hansen et al. (2011) *Icarus* **205**(1): 283-295. [20] Mc Keown et al. (2017), *Nature: Scientific Reports* **7**: 14181. [21] Bourke (2013), *LPSC 44*, 2919. [22] Kieffer et al. (1992), *in* Mars, *edit* Kieffer et al.: 1-33, Univ. of Ariz. Press, Tucson. [23] Kelly et al. (2007), *JGR* **112**(E3): E03S07. [24] Vicendon et al. (2010b), *JGR* **115**: E10001. [25] Piqueux et al. (2016), *JGR Planets* **121**: 1174-1189. [26] Sylvest et al. (2018), *GRL* **43**: 12363-12370. [27] Schorghofer et al. (2006), *Icarus* **180**: 321-334. [28] Matsuo & Heki (2009) *Icarus* **202:**90. [29] McElwaine et al. (2018) *LPSC 49*, 2174. [30] Hayne et al. (2014), *Icarus* **231**: 122-130. [31] Hansen et al. (2018), *LPSC 49*, 2175. [32] Pilorget & Forget (2016) *Nature Geoscience* **9**: 65–69. [33] Hugenholtz (2008) *Icarus* **197**: 65–72. [34] Ishii & Sasaki (2004), *LPSC 35*, 1556. [35] Ishii et al. (2006) *LPSC* 37, 1646. [36] Hoffman (2002) *Astrobiology* **2**: 313–323. [37] Harrison et al. (2015) *Icarus* **252**: 236-254. [38] Pasquon et al. (2016) *Icarus* **274**, 195-210.

Acknowledgements: We thank the JPL/Caltech Education Programs for enabling student contributions as well as HiRISE and JMARS for images and data analysis tools. Much of SD's and her interns' dune-alcove work was supported by MDAP grant NNN13D465T.

	Locations	Timing	Type of frost	Mechanism
Dune-gullies	S mid-lats	After spring sublimation starts	Seasonal frost	Sublimation leading to destabilization of the slope
Dune-alcoves	N polar and mid-lats	Early autumn, just after first frost?	Diurnal/early seasonal frost? Early snowfall?	Deposition on/within top layer and destabilization?
Linear gullies	S mid-lats	After spring sublimation starts	CO2 ice blocks	Sublimation exposing slope and breaking ice layer, block sliding down
Dune furrows	N polar + S polar and mid-lats	After sunrise in early spring?	Seasonal slab ice layer	Cryoventing due to solid-state greenhouse effect, and related CO_2 gas flux erosion under the ice slab
Araneiforms	70S-90S excl. perm. SPC	After sunrise in early spring		

FREQUENCY AND MORPHOLOGICAL CONSEQUENCES OF MARTIAN GULLY ACTIVITY. C. M. Dundas[1], [1]U.S. Geological Survey, 2255 N. Gemini Dr., Flagstaff, AZ 86001, USA (cdundas@usgs.gov).

Introduction: The origin of recent gully landforms has been one of the key debates in Mars science over the last two decades, with important implications for habitability and climate. At the time of discovery, gullies were interpreted as evidence for groundwater release [e.g. 1-4]. Subsequent analysis favored melting of snow or near-surface ground ice [e.g. 5-9]. Either of these hypotheses implies the frequent occurrence of near-surface liquid water in geologically recent time, although they markedly diverge in their climate implications: regular melting and runoff implies surface conditions much wetter than the present cold desert.

However, the discovery of ongoing activity in gullies [10] has significantly changed this picture. Early observations of seasonality [11-13] have developed into strong evidence that seasonal CO_2 frost is the major driver of current flows in gullies [14]. This has lent new support to the hypothesis that CO_2 frost-driven flows are not merely a secondary process, but are in fact the primary and perhaps the only cause of gully formation [e.g. 15-17]. Distinguishing between these three hypotheses is thus fundamental for Mars climate science and habitability: CO_2-driven gully formation points to a cold, dry recent climate with limited scope for near-surface habitability. By contrast, wet models are more promising for life, and melting of snow or ice would have strong implications for recent climate.

Survey of Gully Activity: Extensive repeat image coverage from the High Resolution Imaging Science Experiment (HiRISE) enables the detection of new flows in gullies. Previous surveys have demonstrated widespread activity, including formation of many of the morphologies once attributed to liquid water [16-17]. This work presents an extension of that survey for non-dune gullies encompassing additional data. This accomplishes several objectives: detection of new examples provides more case studies of the largest, rarest events which have the greatest geomorphic impact, and expands the set of gullies empirically shown to be active. It also provides a stronger data set for comparison with models for the distribution and properties of gully activity under various scenarios.

Results: At the time of writing, activity has been documented at 22% of 514 southern-hemisphere monitoring sites with long-baseline HiRISE coverage, in most cases with before-and-after HiRISE images. (For these purposes, one site is treated as one set of overlapping HiRISE images. Sites may be adjacent and include variable numbers of gullies.) Among the subset of sites examined by [17], the portion with observed activity has risen from 20% to 25% with the addition of more monitoring data. Many sites, and some individual gullies, have been active repeatedly.

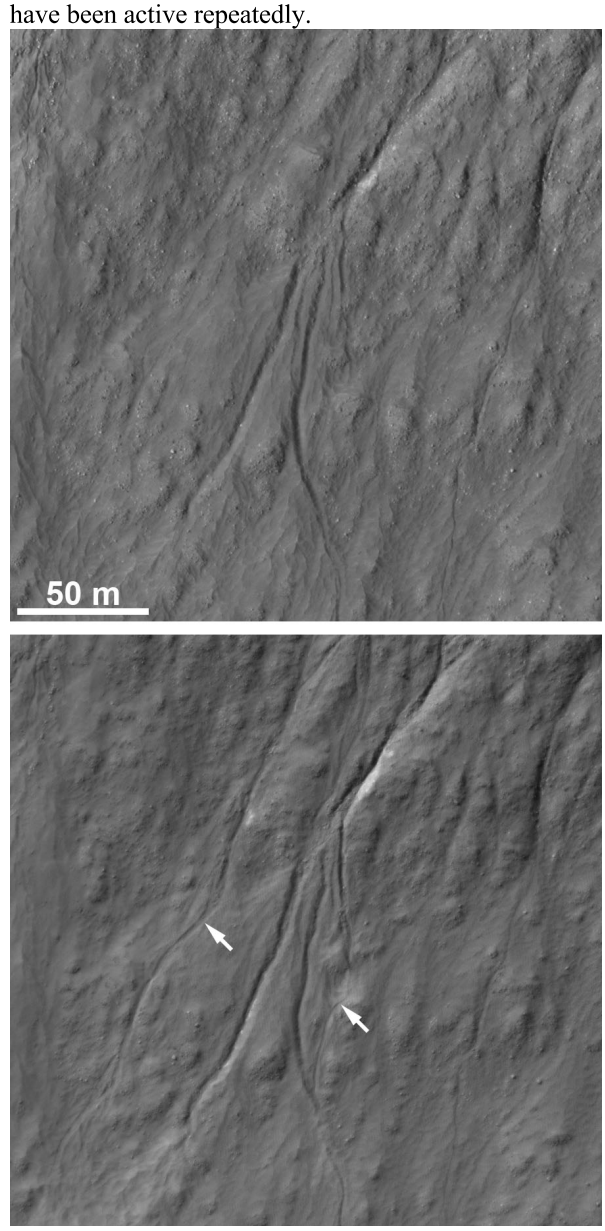

Figure 1: Example of a gully flow event with significant incision of multiple channel segments (arrows). HiRISE images PSP_003094_1430 and ESP_050538_1430. North is up and illumination is from the left.

The properties of individual flow events are highly varied. Their deposits can be brighter or darker than the surroundings, and roughly half have minimal albedo contrast. Most (>80%) reshape the morphology within the channel at scales visible to HiRISE, although the

extent varies greatly, ranging up to debris-flow-like deposits that transport boulders and are likely >1 m thick. Morphology within channels is commonly reworked, with local incision and deposition of lumpy bar-like deposits. Less commonly, the outer edges of sinuous curves are modified, altering the channel sinuosity.

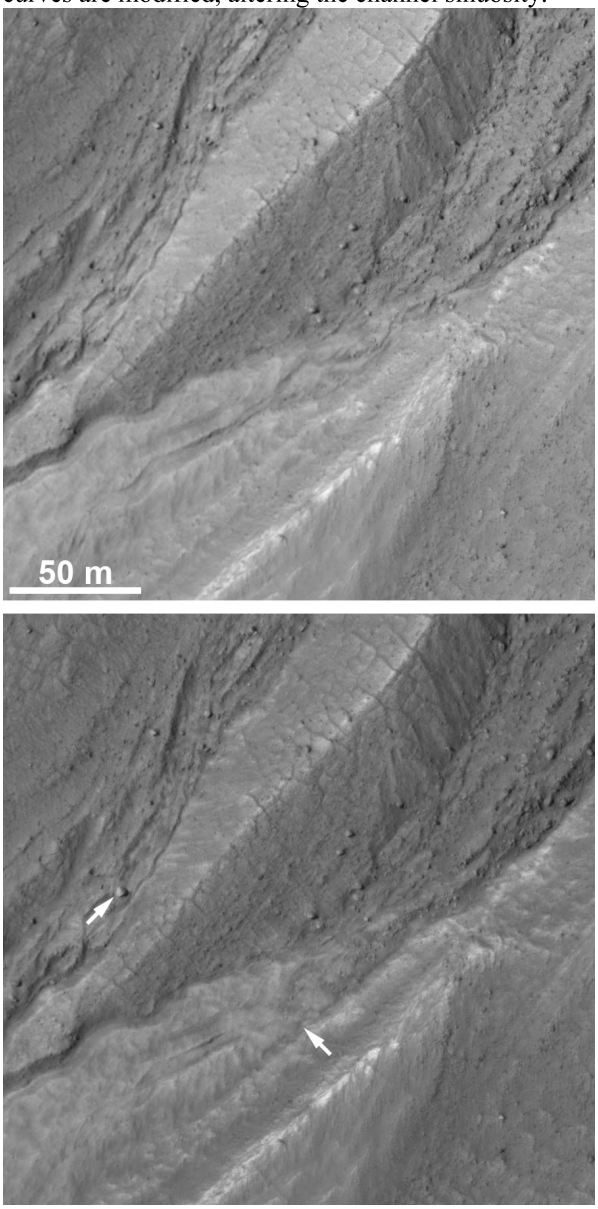

Figure 2: Multiple flow events have occurred in this gully system. At left, note movement of a ~5 meter boulder. At right, deposition has infilled part of the channel system (arrow), while erosion occurred up-slope. HiRISE images ESP_013941_1420 (top) and ESP_057839_1420 (bottom). North is up and illumination is from the left.

Discussion: The geomorphic effect of current activity in gullies is significant. As channel extension and burial is not uncommon, and flows frequently rework the interior morphology of channels, the fine-scale features of gullies represent the effects of modern processes in most cases.

The increase in percentage of active sites at previously surveyed locations is due to two factors: longer time baselines, and the acquisition of more monitoring images that closely match the lighting and viewing geometry of older data. This both improves detections in new images and permits recognition of changes that were present in older data but not readily observable; only events considered definite are included, and manual surveys of poorly matched images can miss subtle changes. Both of these factors indicate that the observed activity rate is a lower bound. The substantial increase in activity detected at the sites from [17] demonstrates that these effects are important. This has both scientific and operational implications: further acquisition of well-matched data is productive, and over a long time baseline, it is likely that a large fraction of gully sites will show activity. This supports the hypothesis that gully formation is ongoing via CO_2 frost processes, as the process is occurring under the cold dry modern climate. While the Martian climate system has varied over time, gullies should not be used as evidence for past liquid water, and variations in gully activity over time may reflect variations in the CO_2 cycle.

Complete results from the survey will be presented at the conference. In future work, these results will be used in conjunction with topographic data to constrain the fluidization of gully flows and compare the new flow slopes with the overall topography of gullies [cf. 18-19].

Acknowledgments: This work was funded by NASA MDAP 80HQTR19T0087.

References: [1] Malin M. C. and Edgett K. S. (2000) *Science*, 288, 2330-2335. [2] Mellon, M. T. and Phillips R. J. (2001) *JGR*, 106, 23,165-23,180. [3] Gaidos E. J. (2001) *Icarus*, 153, 218-223. [4] Hartmann W. K. (2001) *SSR*, 96, 405-410. [5] Costard F. et al. (2002) *Science*, 295, 110-113. [6] Christensen P. R. (2003) *Nature*, 422, 45-48. [7] Balme M. R. et al. (2006) *JGR*, 111, E05001. [8] Dickson J. L. and Head J. W. (2009) *Icarus*, 204, 63-86. [9] Williams K. E. et al. (2009) *Icarus*, 200, 418-425. [10] Malin M. C. et al. (2006) *Science*, 314, 1573-1577. [11] Harrison T. N. et al. (2009) *AGU Fall Meeting,* abstract #P43D-1454. [12] Dundas C. M. et al. (2010) *GRL*, 37, L07202. [13] Diniega S. et al. (2010) *Geology*, 38, 1047-1050. [14] Dundas C. M. et al. (2012) *Icarus*, 220, 124-143. [15] Hoffman N. (2002) *Astrobiology,* 2, 313-323. [16] Dundas C. M. et al. (2015) *Icarus*, 251, 244-263. [17] Dundas C. M. et al. (2017) *GSL Spec. Pap.*, 467, 67-94. [18] Kolb K. J. et al. (2010) *Icarus*, 208, 132-142. [19] Gulick, V. C. et al. (2019) *GSL Spec. Pap.*, 467, 233-265.

Geologic Investigation of a Debris-covered Mountain Glacier in Argyre Basin, Mars: Implications for Past Climate and History of Non-Polar Ice. M.R. El-Maarry[1,2], X. Diot[3], [1]Birkbeck, University of London, Malet Street, department of Earth and Planetary Sciences, WC1E 7HX, London, UK, [2]University College London (UCL), London, UK. [3]Sogetrel Telecommunications, Nancy, France.

Introduction: Glacier-like forms (GLFs) are a particular class of ice-rich landforms that occupies the mid-latitudes of Mars [e.g., 1–4]. They appear to be concentrated around the 40º–55º latitude range in both hemispheres [3,4]. Within these latitudinal bands, GLFs are observed to occur primarily in regional clusters including the fretted terrain in Arabia, NE Tharsis and NE Elysium, circum Argyre (particularly northern Argyre), and circum Hellas (particularly east and west of the basin) [3]. Here we present results from an ongoing geological investigation of what we interpret to be a debris-covered mountain glacier in the Argyre basin. The glacier system displays 1) multi piedmont-like terminal lobes, 2) gullied cirque-like source regions, 3) flows reaching ~35 km with an elevation drop reaching nearly 2 km from source to terminus, and 4) periglacial modification of surface materials indicative of near-surface ice. A better characterization of this landform may provide clues regarding the formation and evolution of non-polar ice on Mars, particularly during periods of high obliquity.

Geologic Setting: The glacier is located along the inner eastern rim of Argyre basin, which suggests that the hosting mountain is an erosional remnant of the basin's rim materials [e.g., 5]. The mountain has an elevation of ~3250 m and rises ~4250 m above the surrounding terrains to the east, and more than 6000 m above the Argyre floor to the west. It displays a wide mesa-like flat top more than 20 km across along its longest axis with steep (22–30°) sides that have developed into cirque-like alcoves. Two prominent alcoves face NE and NW and their walls are highly dissected by narrow depressions resembling gullies. The mountain displays 3 distinct lobes that appear to flow from the base of the cirques trending NE, NW, and SW, among other minor flows, while a lobate debris apron extends to the SE. The lobes travel for tens of km gently sloping (generally 2–4°) downhill where they terminate with sharp lobate boundaries.

Observations: We created a CTX mosaic for the study region and georeferenced it to an HRSC DTM to extract morphometric information on flow directions and influence of surrounding topography. In addition, the glacier system is covered by a number of HiRISE images, which provide a spatial resolution of 0.25–0.5 cm/pixel. Below we present a number of notable observations.

Paleo-accumulation regions: The source region for many of the flows appears to be the central mountain.

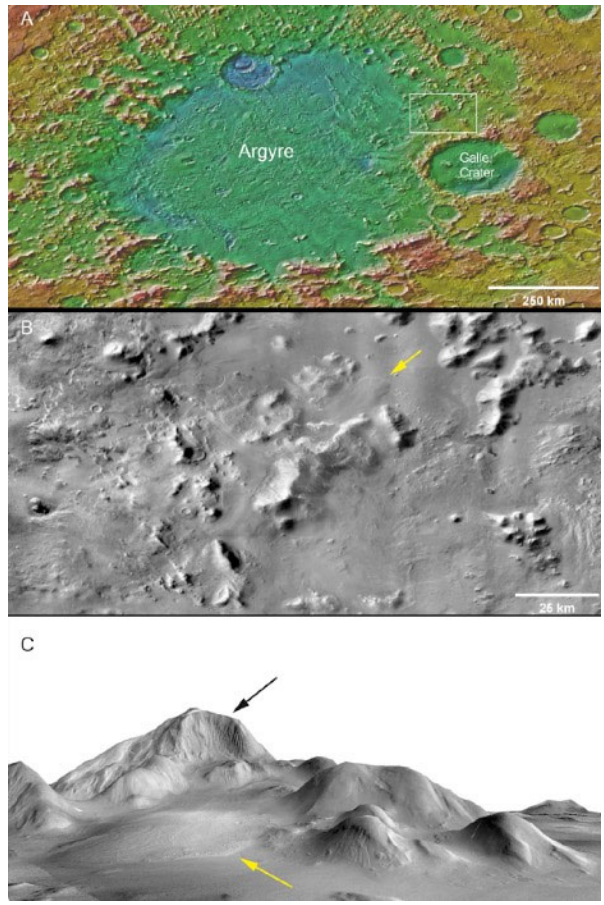

Fig. 1. Glacier-like landform (GLF) in Eastern Argyre. [A] Context view using THEMIS Day IR map with colorized MOLA elevation of Argyre basin overlaid. The study region is enclosed in a white box. [B] THEMIS Day IR mosaic of the GLF . Yellow arrow points to one of the prominent lobes as well as the approximate direction of the perspective view shown in panel C. [C] Perspective view from the east with a vertical exaggeration of 3. Yellow arrow points to the prominent eastern lobe while the black arrow points to the large eastern cirque-like alcove with multiple narrow dissected depressions interpreted as gullies, and shown in Fig. 2 in more detail.

Near the top, large cirque-like structures are visible that show extensive networks of gullies of variable widths and cross cutting relationships suggesting multiple, and varying, erosion cycles through time. Many of the drainage systems appear to originate from quasi-

linear ridges, which are closely aligned with each other at the top of the mound (Fig. 2). We interpret these ridges to be the paleo-boundaries (possibly ancient till deposits) between the drainage systems and past ice deposits at the mountain top, which contributed to the drainage systems.

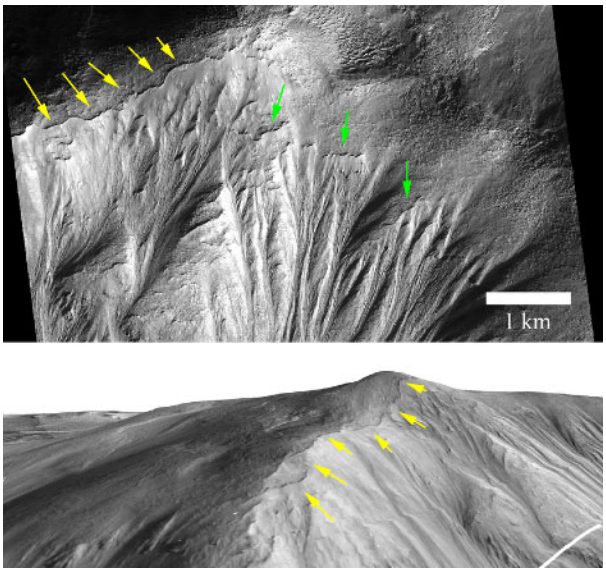

Fig. 2. [Top] HiRISE image covering the top of the eastern cirque shown in Fig. 1c. Extensive gullies are visible in this image with many appearing to originate from narrow linear ridges (arrows). Yellow arrows point to a prominent set shown in perspective view in the bottom panel. Green arrow point to other isolated examples. [Bottom] Perspective view covering the top of the eastern cirque (no vertical exaggeration). Yellow arrows show the ridges shown in the top panel that are aligned with the cliff top and mark the regions where many of the gullies in the eastern alcove appear to originate from.

Fractures and gullies: On the western slopes of the central mountain, a number of distinctive gullies show deep alcoves, terminal fan-shaped deposits, and transverse fractures that cut through the gully system (Fig. 3). This type of transverse fractures that are quasi normal to the general slope suggest long-term modification following the gullies formation, which could be a result of periglacial modification, volatile loss, slowly flowing ice, or a combination of these processes.

Surface periglacial modification: High resolution images covering multiple locations in the glacier system show that the surface is pervasively modified showing patterned grounds, which we interpret to be seasonal thermal contraction polygons. In areas of pronounced slopes, surface patterns appear to be addition-

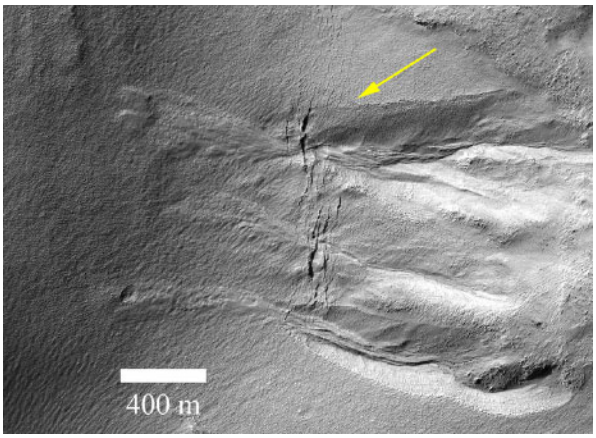

Fig. 3. Part of a HiRISE image showing a well-defined gully system with wide alcoves, fan shaped deposits, and transverse fractures dissecting the system.

ally aligned with these slopes with fractures that are transverse to the slope direction showing preferential widening. Such locations are likely preferential zones for volatile loss. In certain cases, the fractures widen to create wide troughs (Fig. 4). We plan to present these findings, among others, in the meeting in more detail and discuss implications to past climates and history of non-polar ice on Mars.

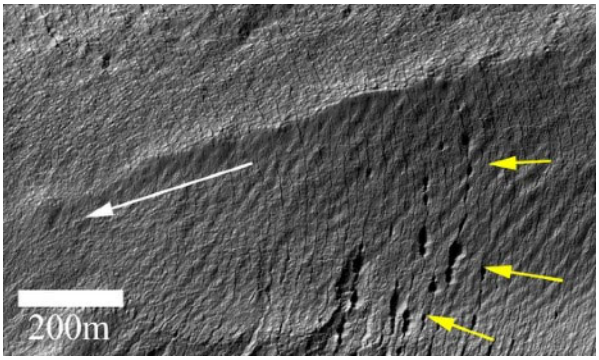

Fig. 4. Part of a HiRISE image covering the surface of one of the western lobes of the glacier system showing the pervasive patterned ground indicative of near surface ice. Note the preferred orientation of the surface pattens in response to the local slopes. White arrow shows the direction of the regional downslope. Yellow arrows show examples of widening troughs.

References: [1] Arfstrom, J., and Hartmann, W.K., (2005), *Icarus, 174*, 321–335. [2] Head. J.W. et al. (2010), *EPSL*, 294, 306–320. [3] Souness, C. et al. (2012). *Icarus, 217,* 243–255. [4] Hubbard, B. et al. (2014), *Cryosphere, 8,* 2047–2061. [5] Dohm, J.M. et al. (2015), *Icarus,* 253, 66–98.

QUANTIFYING NET ANNUAL POLAR DEPOSITION RATES OF WATER ICE AND DUST ON MARS AT VARIOUS OBLIQUITIES WITH THE NASA/AMES LEGACY MARS GLOBAL CLIMATE MODEL.

J. A. Emmett[1] and J. R. Murphy[2], M. A. Kahre[3], [1]New Mexico State University Department of Astronomy (jeem9157@nmsu.edu), [2]New Mexico State University Department of Astronomy (murphy@ad.nmsu.edu), [3]NASA Ames Research Center (melinda.a.kahre@nasa.gov)

Introduction: The polar layered deposits (PLD) are ~3 km-thick surface deposits in Mars' North and South polar regions comprised of layers of water ice and dust in various mixtures, which are thought to record astronomically-forced climate variations over the past 1's–10's of Myrs [3]. Understanding the formation mechanisms of layers is critical to the interpretation of this climate record.

Methods: *Models.* We utilize the NASA/Ames Legacy Mars Global Climate Model (MGCM) [2] to investigate the sensitivity of annual rates of water ice and dust surface deposition in the polar regions to various obliquity parameters and surface water ice distributions plausibly characteristic of the past ~5 Myrs (the inferred age of the NPLD) [3]. The MGCM utilizes fully interactive dust lifting schemes [2], infinite global sourcing of dust, and infinite sourcing of water where surface water ice reservoirs are specified. The radiative effects of water vapor and suspended dust are considered, but are currently neglected for water ice.

MGCM-derived polar deposition rates produced under specified obliquity and water source locations are then ingested into a time-marching integration model to simulate layer formation during a recent low-eccentricity epoch spanning ~1.7-1 Myrs ago [3].

MGCM Simulations. Paleoclimate simulations employ obliquities ranging from 15°-35° and initial surface water ice source locations consisting of various combinations of polar ice caps and middle latitude surface water ice reservoirs (glaciers). We here focus upon two surface water ice source prescriptions: Simultaneous north and south ice caps poleward of 77.5° N/S (representing a post-low-obliquity epoch characterized by polar accumulation [5]), and surface water ice between 37.5-42.5 N and S (representing a post-moderate obliquity epoch characterized by middle latitude glaciation [5]).

To investigate polar processes under present-day climate conditions, a simulation utilizing present orbit parameters and a source distribution defined by the morphology of the present-day NRC was analyzed.

Results: *Paleoclimate Simulations.* Zero eccentricity simulations that employ simultaneous north and south polar ice caps generally predict an annual north-to-south exchange of water ice. Annual loss/gain in the north/south results from polar summertime surface

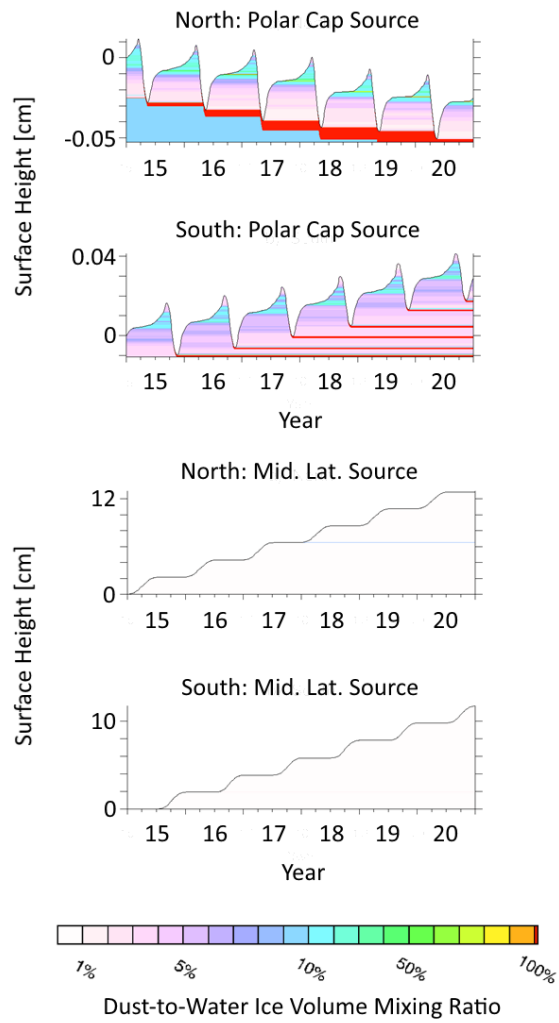

Figure 1: Five-year evolution of the polar water ice and dust deposits under 25° obliq., zero eccen., polar cap source and middle latitude source conditions.

pressure-temperature conditions favoring greater sublimation in the north. The 15° and 30° obliquity scenarios exhibit a south-to-north exchange. At 15°, this is due to the presence of perennial CO_2 ice caps and the relatively late recession of the north's CO_2 cap edge (late exposure of water ice). At 30°, this is due to a southern summer dust event that enhances total downward radiative flux upon the south cap in that season. The magnitude of the annual cap-to-cap water ice exchange increases with increased obliquity from ~1e-5 cm/yr (15°) to ~0.1 cm/yr (35°). The polar surfaces accumulate dust at all obliquities, primarily as dust

cores nucleated by snow particles. Polar dust deposition increases with increased obliquity from ~1e-4 cm/yr (15°) to ~1e-2 cm/yr (35°) due to increased wind stress lifting (increased temp. gradient) along the more latitudinally-extensive seasonal CO_2 cap edges.

Zero eccentricity simulations that employ simultaneous north and south middle latitude glacial deposits predict rapid annual polar water ice accumulation at the expense of the middle latitude ice. Polar accumulation (and middle latitude loss) of water ice increases with increased obliquity from ~1 cm/yr (15°) to ~3 cm/yr (35°). The polar surfaces accumulate dust at all obliquities, primarily as dust cores. Polar dust deposition rates decrease from ~3e-3 cm/yr (15°) to ~1e-3 cm/yr (35°) as increasing overlap between the extensive seasonal CO_2 caps and the middle latitude surface water ice deposits reduces cap-edge wind stress lifting.

Present-Day Simulation. The present-day simulation predicts an annual migration of water ice from the periphery of the modern north residual water ice cap towards the cap interior (poleward of 77.5° N) at ~0.01 cm/yr but no annual water ice accumulation in the south. Both polar regions accumulate dust at 0.001 cm/yr, resulting in ~15% dust northward of 77.5° N.

A Model of PLD Growth and Layer Formation at Low-Eccentricity. Over the period spanning 1.7-1 Myrs ago, a subset of integration model simulations are capable of accumulating a northern surface deposit at a time-averaged rate close to that estimated for the NPLD's recent and long-term accumulation history (~0.5 mm/yr) [4]. Such integration model simulations:

- Are characterized by persistent north and south polar caps, and exhibit a long-term transfer of water from the south cap to the north cap.
- Like [1], accumulate two types of dust-rich layers per obliquity cycle in the north:

1) A ~30 m-thick layer containing ~20% dust forms at high obliquity when both NPLD water ice deposition and dust deposition are high.
2) A 2 cm-thick dust lag deposit forms at low obliquity when water ice is annually removed from the NPLD (and transferred to the SPLD).

Discussion: Integration model results suggest that a south cap-to-north cap exchange of water could sustain NPLD accumulation at ~0.5 mm/yr under low-eccentricity conditions, and produce ~30 m layers reminiscent of observed NPLD stratigraphy [3].

The inability of these zero eccentricity GCM models to form or retain middle latitude glacial deposits at any obliquity suggests, like [4], that excursions to low-eccentricity epochs may act as interglacial periods.

This work predicts instability of the SPLD under present-day conditions but has identified plausible paleoclimate scenarios conducive to annual accumulation of SPLD water ice, providing possible insight into its estimated >10 Myr age.

The polar deposition of dust primarily in the form of snow nuclei suggests that the microphysical coupling of water ice and dust may have a considerable impact on PLD formation processes and composition.

Acknowledgements: This work has been supported by NESSF Grant # NNX16AP37H

References: [1] Hvidberg, C.S. et al. (2012) *Icarus* 221(1). [2] Kahre M.A. et al. (2006) *JGR* 111(6). [3] Laskar J. B. et al. (2007) *Nature,* 419. 375-77
[4] Madeleine J.B. et al. (2009) *Icarus* 203(2). 390-405
[5] Mischna M.A. et al. (2003) *JGR* 108(6). 405-19

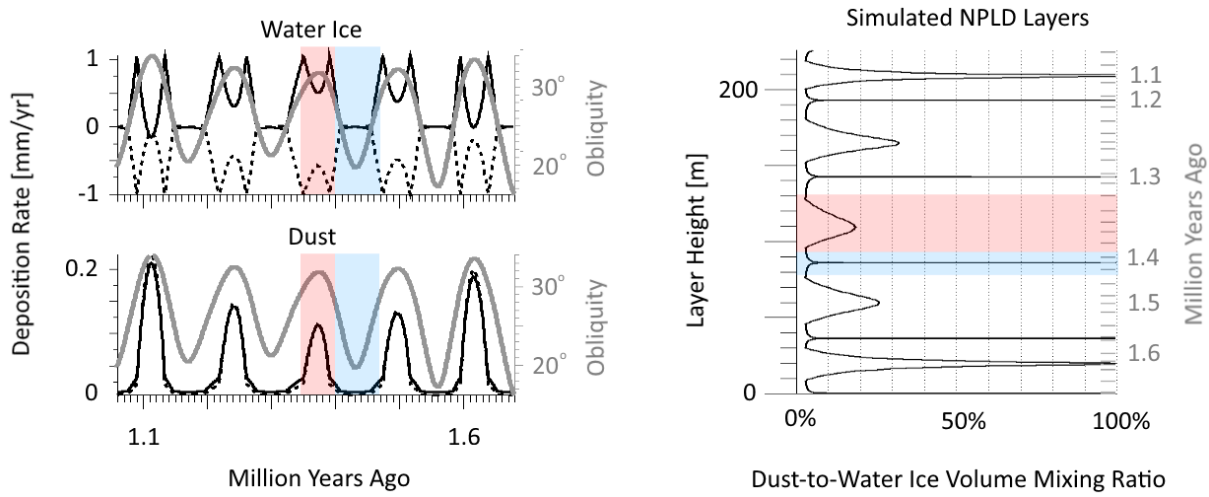

Figure 2: Results of an integration model simulation initialized with 1.5 km-thick north and south polar ice caps yielding a time averaged simulated NPLD accumulation rate of 0.35 mm/yr **(left)** Simulated net water ice and dust deposition rates vs time (solid = NPLD, dashed = SPLD) with superimposed obliquity history (gray). **(right)** Resulting simulated NPLD stratigraphy. Pink/Blue strips highlight the two described layer types.

A DUAL ARCHITECTURE FOR SUBSURFACE ACCESS TO MARS VOLATILES DEPOSITS. B. Glass[1], J. Goordial[2], V. Parro[3], S. Seitz[1], D. Bergman[4], J. Eigenbrode[5], A. Dave[1] and A. Rogg[1], [1]NASA Ames Research Center, Moffett Field, CA 94305, USA (brian.glass@nasa.gov), [2]University of Guelph, Guelph, ON N1G2W1, Canada, [3]Centro de Astrobiología (CSIC-INTA), 28850, Torrejón de Ardoz, Spain, [4]Honeybee Robotics, Altadena, CA 91001, USA, [5]NASA Goddard Space Flight Center, Greenbelt, MD 20771, USA.

Introduction: Building upon our increased knowledge and understanding on Mars polar regions, including the structure of volatiles deposits, direct in-situ access and drilling into Mars polar regions in the near surface and subsurface will be necessary to better understand Mars polar environmental processes, climate history, and potential astrobiology. Characterizing surface polar layers while searching for any biomarkers preserved in Mars polar volatiles is the focus of the Icebreaker follow-on to Phoenix, currently proposed to NASA's Discovery program [1]. In mid- and lower-latitude regions with non-polar ice deposits, in situ subsurface exploration also will be desirable for both astrobiology and in the search for accessible resources for further exploration.

Sampling and drilling in situ near-surface volatiles and near-surface stratigraphy and soil composition at the Martian polar and other volatile-bearing regions will allow us to address issues of past climate history, study volatile reservoirs and replenishment, and present-day surface processes. ExoMars in 2020-21 will sample to 2m, but is not designed to drill icy materials and will go to lower latitudes [2]. Phoenix in 2007 attempted to explore the Mars polar near-subsurface, but its arm and scoop were only able to scratch the surface as they were not able to penetrate the harder ice-cemented layers found at 20-30cm depth [3]. The proposed Icebreaker Discovery mission would return to the Phoenix region but would go deeper, with a 1m rotary-percussive drill as well as an arm and scoop for sample transfer and surface studies [4].

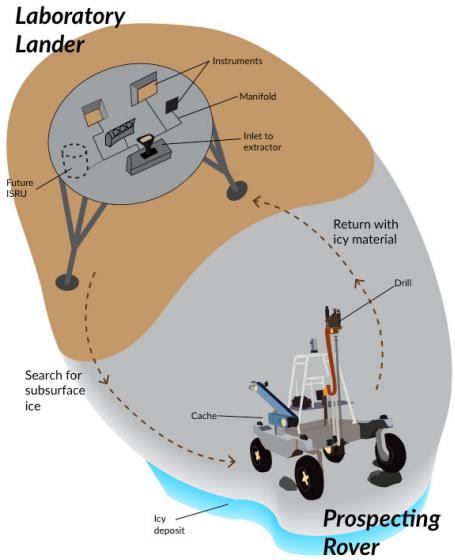

Figure 1. Concept sketch of dual-platform field operations for volatiles exploration.

Past NASA-supported drill technology prototypes have over the past 15 years developed robotic software and hardware capable of hands-off remote drilling and sample acquisition, tested both at terrestrial analog sites and in thermal vacuum chambers, with the Honeybee Trident drill design under current consideration for both Icebreaker and lunar prospecting [5]. This and prior prototypes have been tested within NASA's PSTAR program for in situ drilling and exploration for astrobiology and hence the search for near subsurface biomarkers. The current Atacama Rover Astrobiology Drilling Studies (ARADS) project has demonstrated in Chile a robotic Trident drill and sample transfer arm on a rover, acquiring samples from depths to 1m and transferring these to other instruments onboard the rover [6].

Approach: Practically, however, in recent years we have seen from both Curiosity and from the Mars 2020 Rover designs that, even on a large rover chassis, it is difficult to accommodate and support an array of in-situ instruments with suitable resolution in addition to materials acquisition and processing. And outside Mars polar regions, an immobile Phoenix/InSight or Icebreaker-class lander runs an additional mission-critical risk of landing on a no-ice dry spot, given the patchiness in subsurface ice believed to exist at Mars mid- and lower latitude sites. And constraining all Mars astrobiology or volatile-reservoirs studies to Phoenix (polar) latitudes (viz. Icebreaker) does not provide enough data points from diverse Mars locations, including the lower and mid-latitude regions most likely to host eventual human explorers.

An issue with robotic sample return to Earth is that it requires multiple Mars launch cycle opportunities. In typical terrestrial field science, field samples are gathered and classified in the field, but then brought back to a laboratory facility for detailed analysis. Likewise, resource industries prospecting on Earth typically take borehole samples, but return these to a lab for detailed analysis, rather than cart around a mobile facility.

A recent NASA white paper on accessing subsurface ice [7] addresses these polar science architectural issues regarding studying ices, biomarkers and life detection (both for their own sake and as a precursor to human

exploration of Mars) and advocates (in parallel with sample return to Earth) a dual in-situ architecture with a highly-capable in-situ stationary "laboratory lander" platform for sample processing and analysis tended by a mobile, drilling "prospecting rover." The prospecting rover, similar in some respects to the lunar VIPER or Resource Prospector concepts, would locate subsurface ice, drill and capture volatile samples, then return these to the "lab-lander" for handoff for analysis and processing. As shown in **Fig. 1**, this smaller "ice prospecting rover" would locate, sample, image and retrieve ice-bearing samples, bringing them to a stationary base -- a "lab lander" platform where the detailed analysis or processing would be done. Sample transfer from a "fetch" rover to a lander is similarly an issue for Mars Sample Return. Developing mission simulations using both a rover and a static platform allows side-by-side testing to find which operations are optimized by use on which platform.

Proposed Project and Polar Analog Site: The proposed Mars Analog Research Architecture Combining Acquisition, Delivery and Analysis (MARACADA) project would develop an example of this dual rover-lander ice-sampling architecture. This project approach will bring together an existing PHX/InSight lander mockup (**Fig. 2a**) as its "lab lander" together with an existing rover/drill from ARADS (**Fig. 2b**). The "lab lander" will host and integrate current mission-capable instruments to demonstrate the science and exploration architecture.

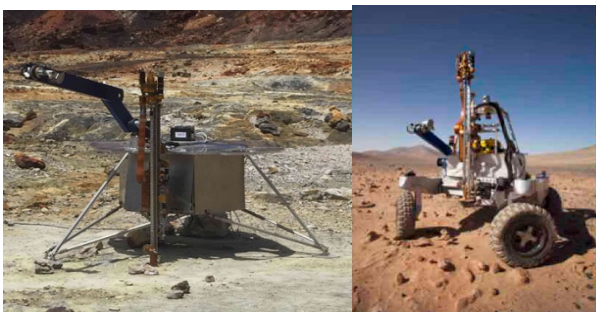

Figure 2. (a) PHX/InSight lander mockup with Ice-breaker drill in June 2017 tests (b) ARADS rover/drill.

These would be deployed and tested at the Haughton impact structure (75.4N, 89.8W), a Mars-analog field site in the Canadian Arctic. Haughton contains continuous permafrost developed on a variety of impact-related outcrops i.e., massive melt breccia deposits, intra-crater paleolacustrine deposits, and fluvioglacial deposits [8]. Haughton Crater's "Drill Hill" is located on a 150m-thick deposit of this impact fallback breccia, with evident periglacial structures and intermittent clear subsurface ice layers found typically within 1m of the surface [9]. MARACADA will develop the white paper's dual-platform exploration architecture by doing actual sampling and science operations with the lab-lander and prospecting rover at locations of interest within the Haughton Crater region.

Early Testing: Prior to MARACADA or similar tests at analog sites, the existing ARADS drilling rover together with local in-situ processing was demonstrated in September 2019 during the ARADS field tests in the Atacama Desert. While this was not a polar analog site,

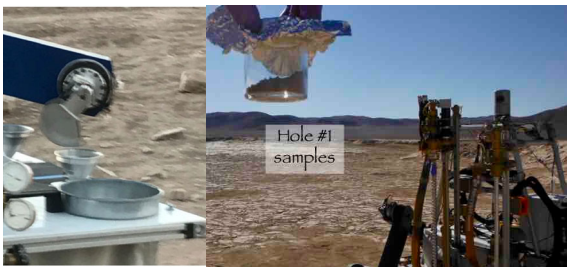

Figure 3. Drilled sample caching for later transfer for off-rover "lander" analysis, in Sept. 2019 Atacama tests.

it allowed for field experimentation with the drilling, acquisition and onboard caching (see **Fig. 3**) of subsurface samples, then used in local in-situ analysis (chromatography and the LDCHIP immunoassay instrument) not on the ARADS rover, as it traversed. Adding sample caching to the nominal onboard instrument sample distribution forced repetitive cleaning after every manual cache transfer from the rover (**Fig. 3**), to avoid contamination of the onboard instruments and drill by humans manually retrieving samples from the rover. Implementation of MARACADA's automated sample cache transfer (rover to lab-lander) would obviate this need in future tests.

Conclusions: A dual robotic architecture for in-situ prospecting and analysis of subsurface samples holds promise for future exploration of polar volatiles and other shallow subsurface deposits on Mars, as well as potentially supporting the study and exploitation of volatile reservoirs at mid-latitude sites. Following a an internal NASA near-surface volatiles exploration study, work has begun to implement and test this dual approach at Mars analogs. Technology development issues (such as autonomous surface docking and robotic cache transfer) developed in support of a dual volatiles-exploration mission architecture will also be relevant to similar issues associated with Mars sample return.

References: [1] McKay, C. et al. (2013) *Astrobiology*, 334-353. [2] Vago, J. et al. (2015) *SSR*, 518-528. [3] Arvidson, R.E. et al. (2009) *JGR Planets*, 114(E1). [4] Glass, B. et al. (2013) *JFR*, 192-205. [5] Bergman, D. et al. (2016) *ASCE Earth & Space*. [6] Glass, B. et al. (2019) *AbSciCon*. [7] Eigenbrode, J. et al. (2017) unpublished SMD white paper. [8] Osinski, G.R. and Lee, P. (2005) *Meteoritics & Planet. Sci.*, 1887-1899. [9] Glass, B., et al. (2016) *6th Mars Polar Sci. Conf.*

ATMOSPHERIC PHENOMENA OBSERVED BY OMEGA/MEX OVER HIGH LATITUDES. B. Gondet, J.-P. Bibring, Y. Langevin, Institut d'Astrophysique Spatiale, Université Paris-Sud, Orsay, France, (Brigitte.gondet@ias.u-psud.fr),

Introduction: Since the beginning of the mission (January 2004) OMEGA, the VIS-NIR hyperspectral imager onboard Mars Express has acquired regular high latitudes observations in conjunction with others instruments (HRSC, PFS, SPICAM and VMC) in nadir and limbs modes. Atmospheric phenomena are observed detected at different Ls, altitude, locations and local time,. This constitutes an important database largely unexploited at this point. We will present examples of detections concerning clouds, dust and emissions, and identify themes of potential collaborations.
H2O and CO2 ices evolution will be also discuted in this meeting by Yves Langevin.

Examples of available observations:

All observations of the spatial distribution of clouds and dust, either lateral of vertical, come with compositional spectral measurments covering the 0.4 to 5.1 microns range for most observations. All the pictures below are RG (500nm, 700nm and 900nm) with the same normalisation

Gravity waves [1], [2] are observed at 2 periods: Ls~310° (fig1) and LS~35° fig (3,4).

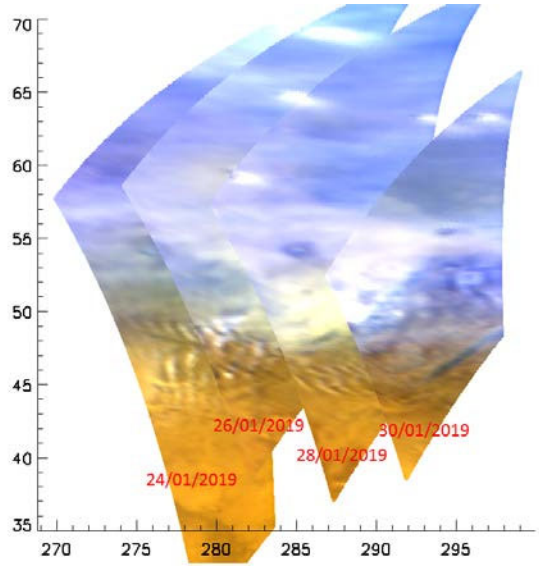

Fig 1: Gravity waves observed at Ls 310°(2019). The altitude of the clouds are ~80 kms (Thanks to the shadow of the clouds)

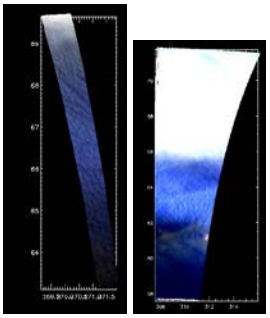

Fig 2 and Fig 3 Gravity waves obsersed at LS 35° (2019 and 2005).

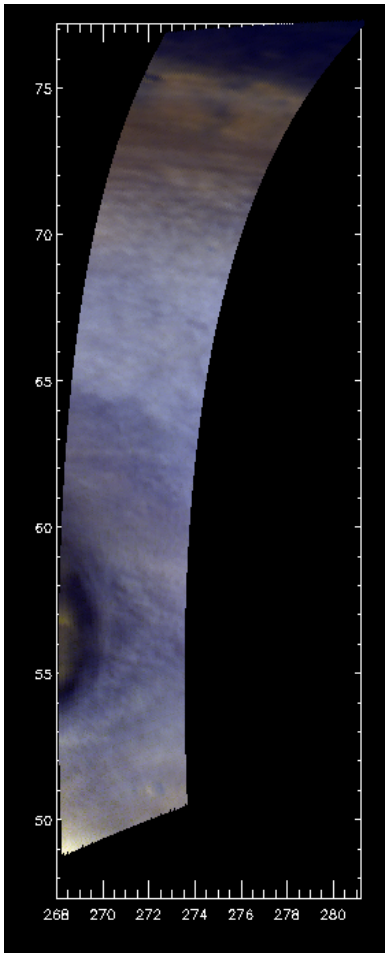

Fig 4: double Vortex (2018). This vortex as been also observed by VMC and HRSC ([3])

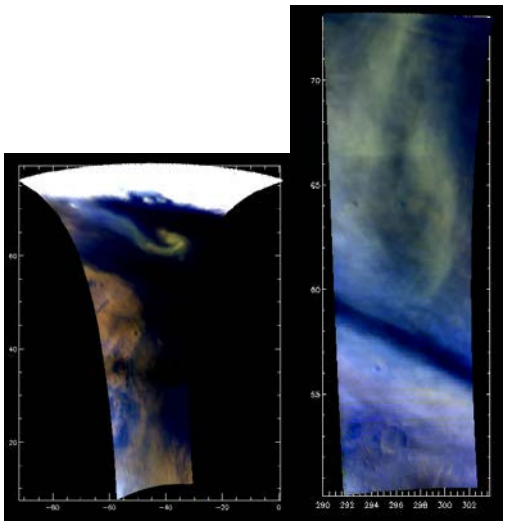

Fig 4 and fig 5: dust storms at high altitude

References:

[1] Hauchecorne, A.. *Geophys. Res. Lett.*, 14, 933– 936 [2] Spiga, A. *GR*L *Volume 39, issue 2*, [3] Sánchez-Lavega, A. *Journal of Geophysical Research: Planets, Volume 123,*

Discussion and Conclusion:

OMEGA measurements gathered over more than 16 years offer an opportunity to explore the yearly variability of the Martian atmosphere over the north latitudes, with sufficient time sampling or spatial coverage to put constrains on several aspects of the atmospheric dynamic. OMEGA still provides unique aerosols compositional characterization capabilities that enable detailed analyses of CO2 clouds and other poorly known high altitude aerosols layers. Ongoing and upcoming collaborations with the Martian atmospheric community will further reveal the richness of this dataset for atmospheric studies.

The Apparent Lack Of Wet-Based Glaciation Fingerprints On Mars. A. Grau Galofre.[1], K. X. Whipple[1], P.R. Christensen[1], G.R. Osinski[2], A.M. Jellinek[3], S.M. Chartrand[4] [1]School of Earth and Space Exploration, Arizona State University, Tempe, AZ, US (agraugal@asu.edu), [2]Institute for Earth and Space Exploration / Dept. Earth Sciences, University of Western Ontario, London, ON, Canada, [3]Department of Earth, Ocean, and Atmospheric Science, University of British Columbia, Vancouver, BC, Canada [4]School of Environmental Science, Simon Fraser University, BC, Canada

Introduction: Large-scale continental glaciations on Earth, such as the ones occurred during the last glacial maximum 20,000 years ago, modified extensively the landscape of the mid and high latitudes. Upon retreat, ice sheets exposed a scoured landscape sculpted by glaciation, with landforms such as lineations, striae, drumlins, moraines, water pockets, eskers and sinous channels (Figure 1). Most of the terrestrial ice was generally wet-based (basal ice is at or very close to the melting point), with the possible exception of the very high latitudes where ice was frozen to the ground (cold-based) for much of its history. The Canadian Arctic preserves an exceptionally rare landscape that is result of extensive, mostly cold-based glaciation, with episodes of melting [2].

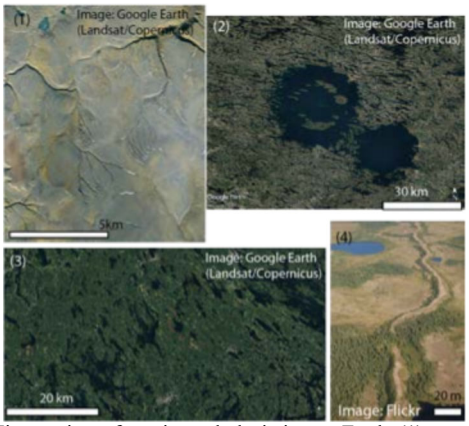

Fig 1. Fingerprints of continental glaciation on Earth. (1) mega-scale lineations (Quebec). (2) Scouring marks and striae (Finland). (3) Esker (Labrador). (4) Subglacial channels (Nunavut).

Whereas during its history Mars has also been extensively glaciated [3,4, 5, 6], the record of extensive interaction between ice and landscape is much more limited. This problematic lack of glacial erosion signs, particularly those attributed to erosion by wet-based glacial masses in analogy to terrestrial large-scale glaciation, has historically led to the hypothesis that Martian glaciation was largely cold-based [5,7]. However, the discovery of extensive eskers and esker fields around the southern polar cap [4,8] as well as examples dating from the Amazonian period [9,10] in the mid latitudes challenge the hypothesis that Martian ice masses were always frozen to the ground.

Objective: We interrogate the dynamics of wet-based glaciers on Mars using the framework of terrestrial glaciology [11], and consider the different mechanisms of drainage of a wet-based ice sheet [11,12]. We field observations from the Canadian high Arctic (Axel Heiberg Island [12]) to justify that the localized melting of mostly cold-based ice sheets results in channels and eskers, not in scouring patterns, lineations, and moraines (Figure 1). We present preliminary results that show that under lower temperature and gravity conditions, glacial masses adapt their basal water drainage to develop efficient, dendritic systems of subglacial channels, of which eskers are sedimentary remnants. The fingerprints of Martian wet-based glaciation may have been fundamentally different than in terrestrial ice sheets.

Theory framework: Water accumulated under thick ice is confined under large pressures and strong gradients, which tend to drive it away from thicker ice regions and towards the ice margin. When basal meltwater cannot drain efficiently, it tends to accumulate in poorly connected pockets of water (cavities), where water pressure builds up, partially opposing the weight of the ice itself and leading to lubrication of the ice mass. This process results in the acceleration of the glacier or ice sheet, which now slides as a block under its own weight (Figure 2). The process of glacial sliding is the most common response on Earth to water accumulation at the base, and leads to landscapes sculpted by the abrasion of ice sliding and scouring the ground (Figure 1).

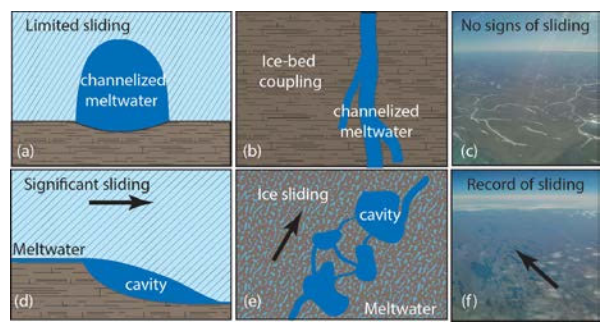

Fig. 2. The drainage of wet-based ice sheets. Upper line shows the formation of subglacial channels and efficient drainage, and effect on the landscape. Bottom line shows inefficient drainage (poorly connected cavities) and its effects on the landscape.

The other scenario occurs when water accumulated under the ice can drain efficiently. This is the case when channels form beneath the ice (subglacial), establishing a well-connected network of drainage pathways. The establishment of these channels drains the pressurized water before lubrication effects can happen, slowing or halting the sliding of ice. The landscape attributed to a scenario where subglacial

channels dominate over sliding consists on subglacial channels etched on the ground, sometimes intertwined with depositional landforms such as eskers, with no signs of sliding, scouring, moraines, etc [1,2] (Figure 1).

Preliminary results: We interrogate the effects of the lower Martian gravity on the glacial sliding velocity of Martian ice masses (keeping all other parameters the same for comparison with terrestrial glaciers) and present the preliminary results in figure 3. Comparing Earth (blue line) and Mars (red line), we can see how sliding rates are a factor ten slower on Mars than Earth, before taking into account glacial hydrology.

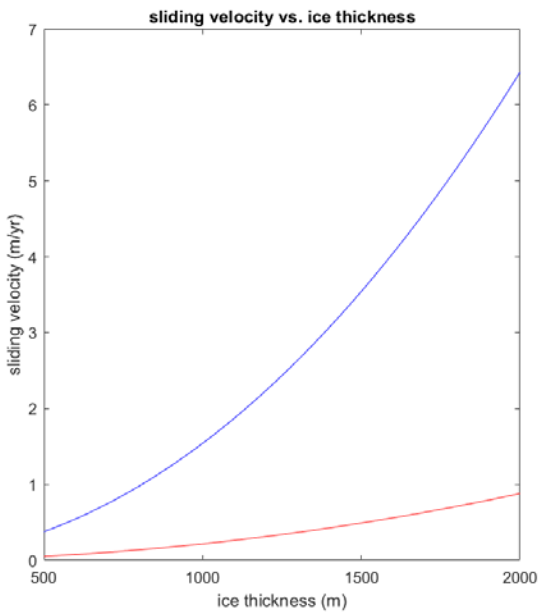

Fig. 3: Preliminary results showing glacial sliding velocity on Earth (blue curve) and Mars (red curve) before considering the effect of the lower gravity on drainage efficiency (work in progress)

Field observations: We present fieldwork results from a campaign in Axel Heiberg island to support the theoretical remarks and model results. Axel Heiberg is located in the Canadian Arctic Archipelago (Figure 4), and preserves two ice caps: the Muller ice cap (north) and the Stacie ice cap (south). The island topography is steep and rugged at the western side, where extensive alpine and piedmont-style glaciers terminate in deeply incised U-shaped valleys and fjords. The eastern side, on the contrary, displays shallower slopes and outwash plains (Figure 4). Whereas it is impossible to scale for the Martian gravity using terrestrial analogues, this effect can be captures in the slope: steeper slopes will have a stronger downhill gravitational stress component, shallower slopes will see a smaller effect. Axel Heiberg offers an ideal, dynamic analogue scenario that allows us to visualize the effects of 'gravity' on ice landscape evolution.

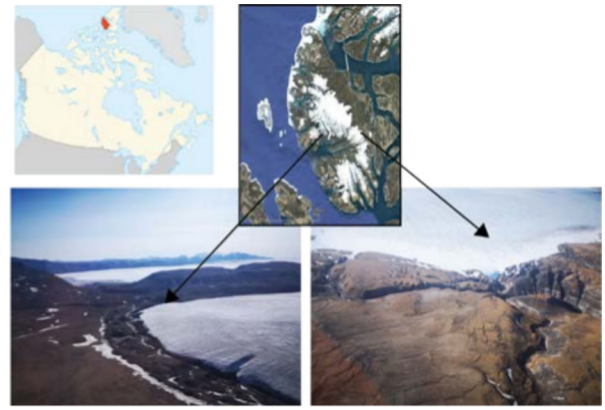

Fig.4. Context for the field observations site in Axel Heiberg Island, showing the western and eastern sides and glacial terminations. Bottom left: Push moraine (western terminus of Stacie ice cap). Bottom right: Orthoimage showing subglacial channels (eastern terminus of Stacie ice cap)

As expected from the theory summarized before, steeper slopes (as a proxy for higher gravity) lead to the onset of faster sliding. On the western side of the island, the typical glacial landscapes form, including scouring marks, moraines, and outlet glaciers. On the eastern side, ice sheets terminate in lobes with no evidence for push moraines. Channels emerge from underneath the ice sheets carrying meltwater.

Conclusions: Preliminary results from applying the framework developed for terrestrial glacial sliding and glacial hydrology show that sliding may be heavily inhibited on Mars owing to its lower gravity. Preliminary analysis from field observations suggest that the same ice sheet in shallower slopes (proxy for lower gravity) displays differences on the basal drainage system, yielding sliding and typical signs of wet-based glaciation to the west of the Stacie and Muller ice caps, Axel Heiberg Island, and subglacial channels on the east of these ice caps. The search for the same large-scale glacial landforms that formed on Earth under continental-scale wet-based ice sheets may be unjustified for Mars.

References:

[1] Grau Galofre, A. et al. (2018), TC, *12*(4), 1461. [2] Dyke, A. (1999). *Quaternary Science Reviews*, *18*(3), 393-420. [3] Kargel, J. S., and Strom, R. G. (1992) *Geology*, *20*(1), 3-7. [4] Head III, J. W., and Pratt, S. (2001). JGR *Planets*, *106*(E6), 12275-12299.
[5] Fastook, J. L., and Head, J. W. (2015). *PSS*, *106*, 82-98.
[6] Levy J.S., et al. (2014) JGR Planets *119*(10), 2188-2196.
[7] Wordsworth R. (2016) Ann. Rev. EPS *44*, 381-408. [8] Kress, A.M. and Head J.W. (2015) PSS *109*, 1-20. [9] Gallagher C. and Balme M. (2015) EPSL *431*, 96-109. [10] Butcher, FEG et al. (2017) JGR planets *122*(12), 2445-2468.
[11] Cuffey, K. M., and Paterson, W. S. B. (2010). *The physics of glaciers*. Academic Press. [12] Schoof, C. (2010) *Nature*, *468*(7325), 803.

STRATEGIES FOR REMOTELY DETECTING CHLORINE SALTS ON MARS. J. Hanley[1], Z. Bandelier[2], C. Murphy[3,2], R. Carmack[4], B. Horgan[4]. [1]Lowell Observatory, Flagstaff, AZ (jhanley@lowell.edu); [2]Northern Arizona University, Flagstaff, AZ; [3]Amherst College, Amherst, MA; [4]Purdue University, West Lafayette, IN.

Introduction: NASA's Phoenix lander provided a unique insight into the regolith of the North Polar Region of Mars through its Wet Chemistry Lab (WCL) analysis. Ions in solution were measured by a sensor array of electrochemically based ion-selective electrodes (ISE). WCL detected a variety of ions, in particular chloride (Cl^-) and perchlorate (ClO_4^-) [1-3]. It is also possible that chlorate (ClO_3^-) was present but masked by the signal of perchlorate [4].

Chlorine salts may also play a role in the mechanical properties of the regolith, as well as the stability of subsurface water. High soil cohesion was encountered at the Phoenix landing site making sample analysis challenging; such cohesion may result from hydrated salts and eutectic brines bonding grains together at their contacts by wetting, or from dehydrated salts crystallizing at grain contacts. Changes in hydration state with time (such as diurnally or seasonally) may then result in correlated changes in cohesive properties with time [5].

The presence of chlorine salts at the Phoenix landing site is important for understanding the geological and chemical history of the North Polar Region, as the presence of chlorine salts can help us infer the chemistry and stability of any water/ice that may be or has been present. This is because chloride, perchlorate, and chlorate salts can all suppress the freezing temperature of water significantly, in some cases with a eutectic temperature down to ~204 K [4, 6, 7]. They also slow down the evaporation rate, extending the lifetime of the liquid water solution. Positively identifying the various chlorine salts, especially their cation-anion pair and hydration state, will allow us to further understand the results from the WCL experiment, and more importantly to assess the stability of water (whether liquid or solid) at the Phoenix landing site. Previous detections of perchlorate and chlorate hydrates in Recurring Slope Lineae (RSL) [8] have been suggested to be instrument artifacts [9, 10]. Here we present strategies and discuss limitations for detecting chlorine salts through VNIR remote sensing spectroscopy.

Methods: Although we know that chlorine salts exist on the surface at the Phoenix landing site, we do not know what their original hydration state or cation-anion pair was (e.g. $Ca(ClO_4)_2.4H_2O$ vs $NaClO_4$ anhydrous vs $Mg(ClO_3)_2.6H_2O$ vs NaCl, etc.). The biggest challenge to positively identifying and distinguishing these salts through remote sensing is that many hydrated salts look very similar in the near-infrared, even when comparing to sulfate salts [11]. We have developed routines specifically for identification and mapping of variations in the wavelength locations of absorption band minima in CRISM spectra [12]. We have begun to apply these routines in order to identify chlorine salts in our specified CRISM images [13].

The majority of CRISM analyses use spectral indices, however, these indices are not able to differentiate between spectrally similar minerals. For example, the SINDEX measures the convexity at 2.3 µm due to sulfate absorptions at 1.9/2.1 µm (poly/mono-hydrated sulfates) and 2.4 µm. This index, though, will also be positive for any hydrated mineral with a fall off toward 2.5 µm, like kaolinite. Likewise, hydrated minerals are often identified using the CRISM BD1900R parameter, which finds the average depth of absorption between 1.91-1.94 µm relative to ~1.86/2.12 µm; yet, this parameter is non-specific to a particular hydrated mineral.

To aid in identification of oxychlorine salts, we created a rubric of VNIR spectral parameters that can be used to help tell the salts apart from other common Martian minerals. Lab spectra of 33 common Martian minerals [14] were compared to spectra collected by [11] of oxychlorine salts to determine the best combination of spectral parameters to most uniquely

Name	Parameter	Formulation	Kernel Width	Rationale	Caveats
BD2130	2.14 µm ClO_4-H_2O feature band depth*	$.5 * \left[1 - \frac{R2120}{a * R2030 + b * R2190}\right] + .5 * \left[1 - \frac{R2140}{a * R2030 + b * R2190}\right]$	R2030:5 R2120:3 R2140:3 R2190:5	Hydrous perchlorates	Orthopyroxene Alunite Gypsum Kaolinite Margarite
BD2220	2.2 µm Cl-O combination or overtone feature band depth*	$1 - \frac{R2220}{a * R2140 + b * R2320}$	R2140:5 R2220:3 R2320:5	Oxychlorine salts	Nontronite Talc Zeolite

Table 1. *Newly created spectral parameters. Formulation is based off of Viviano-Beck et al. [14]. R#### is the reflectance at given wavelength, kernel width is the number of channels over which the median of the reflectance was taken in order to reduce residual noise when applied to CRISM data.*

detect oxychlorine salts. Two new spectral parameters, BD2130 and BD2220, were created to calculate band depths of spectral features specifically found in oxychlorine salts. Band depths were calculated using the process described in [14] and are shown in Table 1.

The common minerals and the oxychlorine salts were run through selected existing parameters (BD1400, BD1435, BD1750_2, BD1900_2, BD1900-R2, BD2100_2, BD2210_2, BD2300, MIN2250 & SINDEX2) as well as the two newly created parameters in order to see which of the old parameters highlighted (passed a threshold value of > 0.01) the oxychlorine salts and which common minerals were highlighted by the new parameters. With this data we were able to create a rubric for which combination of parameters could be turned into a browse product like those in [14] capable of separating out oxychlorine salts: Hydrated Perchlorate (HPC) and a new Hydrated (HYD2). Our test sites have been Columbus Crater and the Phoenix landing site.

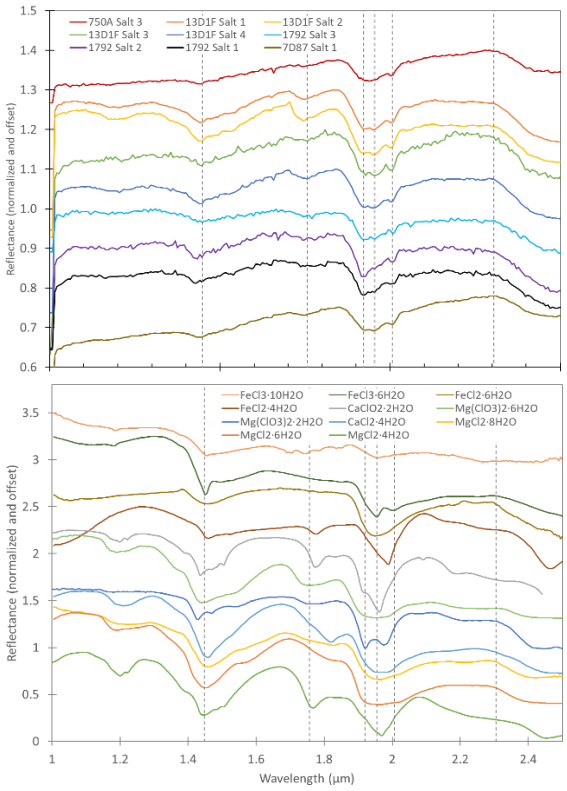

Figure 1. *Top: CRISM spectra of potential salts taken from various images in Columbus Crater, Mars. Bottom: Reference laboratory spectra [11] with similar features as potential salts from (top).*

Results: The new parameters we used in this study, BD2130 and BD2220 did not detect regions with definite absorptions at the desired wavelengths. Using PHS in ENVI helped by locating phyllosilicates which have similar absorption features to the feature highlighted by BD2220. Areas could be found where only BD2220 was highlighted in PHS and most parameters in HPC and HYD2. BD2130 did not highlight many areas in many of the CRISM images. There was a large amount of noise in the BD2130 image, which made finding regions that were actually highlighted difficult. BD2130 would often be darkest in the brightest areas of HYD2 and HPC.

Despite their flaws, these parameters did lead to the identification of many spectra that have features suggestive of chlorine salts (Figure 1). Some spectra, including those in FRT_13D1F and HRL_62B6, had absorption features close to 2.22 microns. While it is uncertain whether they are due to chlorine salts, clays, or other minerals, finding this feature is an important step. We will continue to test BD2130 in other locations, as other images in Columbus Crater and beyond could show chlorine salts through the use of this parameter.

Implications: Our new parameters aim to improve our ability to identify chlorine salts and differentiate between hydrated and anhydrous phases. [6] discovered an artifact that appears in CRISM data due to improper atmospheric corrections near 1.9 and 2.1 µm. This artifact could have caused false positives for perchlorate bands, and may be responsible for previous detections of perchlorates. Since our method of detection does not rely on the 2.1 µm band alone, it should be able to compensate for issues with this region of the spectrum. Proper identification of these salts would give insight to the history of brines on Mars. Salts present could lower the freezing point of a liquid they are interacting with such that liquid water could persist under present day Martian conditions. This would increase the possibility for life to persist in near-surface environments on Mars.

If these salts are in the presence of near-surface ice, they will serve to suppress the sublimation rate, as well as encourage liquid formation by lowering the freezing temperature. In the polar summer, the temperatures were such that a eutectic liquid solution of $Mg(ClO_4)_2$ could exist for most of the day. This has implications for the long term stability of liquid water and ice in the polar regions of Mars.

Acknowlegements: This work is funded by MDAP #NNX16AJ51G.

References: [1] Hecht, M.H. et al. (2009) *Science, 325,* 64-67. [2] Kounaves, S.P. et al. (2009) *JGR, 114,* E00A19. [3] Kounaves, S.P. et al. (2010) *GRL, 37,* L09201. [4] Hanley, J. et al. (2012) *GRL, 39,* L08201. [5] Hanley, J. et al. (2014) *LPSC,* #2879. [6] Altheide, T. et al. (2009) *EPSL, 282,* 69-78. [7] Chevrier, V.F. et al. (2009) *GRL, 36,* L10202. [8] Ojha, L. et al. (2015) *Nature Geosci, 8,* 829-832. [9] Leask, E.K. et al. (2018) *GRL, 45,* 12,180-12,189. [10] Vincendon, M. et al. (2019) *Icarus, 325,* 115-127. [11] Hanley, J. et al. (2015) *JGR, 120,* 1415-1426. [12] Horgan, B. et al. (2013) *LPSC,* Abstract #3059. [13] Carmack, R. et al. (2019) *LPSC,* Abstract #1701. [14] Viviano-Beck, C.E. et al. (2014) *JGR, 119,* 2014JE004627.

DYNAMIC SEASONS ON MARS – POLAR IMAGES AND INVESTIGATIONS. C. J. Hansen[1], K.-M. Aye[2], S. Diniega[3], P. Hayne[2], A. McEwen[4], G. Portyankina[2], M. E. Schwamb[5], [1]Planetary Science Institute, 1700 E. Fort Lowell, Tucson, AZ 85721, cjhansen@psi.edu; [2]LASP, University of Colorado, Boulder, CO 80303; [3]Jet Propulsion Laboratory / California Institute of Technology, Pasadena, CA 91109; [4]University of Arizona, Tucson, AZ 85719; [5]Astrophysics Research Centre, Queen's University Belfast, Belfast BT7 1NN, UK.

Introduction: The activities associated with seasons on Mars are arguably the most dynamic processes in Mars' current climate. Multiple investigations are underway, enabled by multi-year datasets. We will highlight the status of a few of these polar areas of research.

The Mars Reconnaissance Orbiter (MRO) has been in orbit for 7 Mars years observing the changes in the seasons, and inter-annual variability. With the High Resolution Imaging Science Experiment (HiRISE) on MRO we have the advantage of routinely pointing off-nadir to get repeat imaging of dynamic processes, and a high signal-to-noise ratio that enables imaging when the sun is low on the horizon [1]. The MRO Mars Climate Sounder (MCS) retrieves atmospheric temperature profiles and detects snowfall by combining limb observations which detect clouds, with measurements of the brightness temperature [2], which reveals ongoing or recent snowfalls [3].

Spring sublimation and surface modification: In the fall snowstorms and direct condensation deposit a layer of seasonal CO_2 frost on the surface [3, 4]. Over the winter the frost anneals to ice [5] setting the stage for action in the spring. The Kieffer model [described in detail in 6] postulates that when the sun rises in the spring sunlight penetrates the impermeable translucent ice and warms the ground below. The ice sublimates from the bottom and gas is trapped under increasing pressure, eventually rupturing the ice and escaping. Entrained particulates fall onto the top surface of the ice in fan-shaped deposits. Throughout the Mars year the transport of CO_2 into and out of the atmosphere drives winds, and the seasonal fans, like windsocks, mark its direction as spring progresses.

Gas escaping from under the seasonal ice layer entrains surface material, eroding channels into the surface [8]. The nature of the surface erosion is in part controlled by the friability of the surface. Furrows on dunes form in one Mars spring [9, 10]. Erosion, aided by sand, has been observed to form "spiders" (araneiform) in just a few Mars years [11]. Mature araneiform terrain development may take thousands of years [12]. A wide variety of configurations of troughs has been observed – the escaping CO_2 gas will find the path of least resistance [13, 14], as shown in Figure 1.

The Planet Four citizen science project (www.terrains.planetfour.org) is using MRO Context Imager (CTX) images to map out where araneiform terrain has been carved in the south polar region to improve our correlation of terrain-types with its formation [15]. Why don't we see araneiform terrain in the north polar regions, (other than furrows on dunes)? Is it due to the nature of the surface, or that the winter conditions are different due to Mars' elliptical orbit?

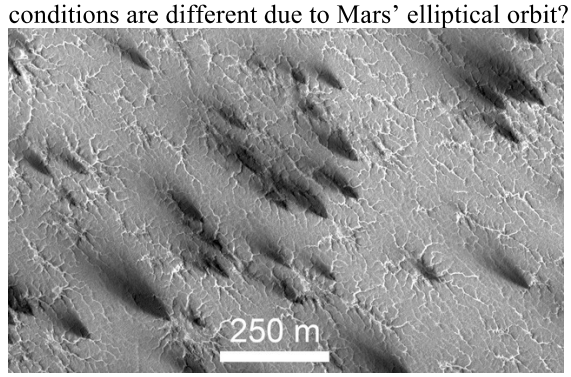

Figure 1. Image ESP_055604_0930, taken at 86.9S / 170.5E, L_s 188.9, shows araneiform terrain under a conformal coating of CO_2 ice with seasonal fans on top.

Fall frost condensation and alcove formation: HiRISE images of the north polar erg in the fall and spring show the development of new alcoves on the dunes [15]. Comparison of our standard sites in different Mars years shows considerable variability in how many new alcoves form over one Mars winter and how large they are (see Figure 2).

A single MY32 image taken in the fall after the first bright frost appears shows that the formation of the alcoves appears to be connected to the onset of frost condensation. It is difficult to image the dark dunes as polar night falls and the polar hood forms so we have just a few images to compare to the MCS data. The MCS data show that there is inter-annual variability in exactly when the CO_2 begins to condense, the amount of time between condensation and the first snowfall, and how great the first snowfall is at a given site. These are factors that could influence the stability of the dune brink – for example, a significant amount of ice build-up would armor the dune against fierce autumn winds and may stabilize it against a later mass loading of snowfall that otherwise could oversteepen the slope. New images of alcove formation in MY33-MY34 are being analyzed for three sites, planned after the discovery from the single MY32 image that fall was the important timeframe. We are also

collecting data at more sites, but it will take a few Mars years to develop a record for alcove formation at the new sites.

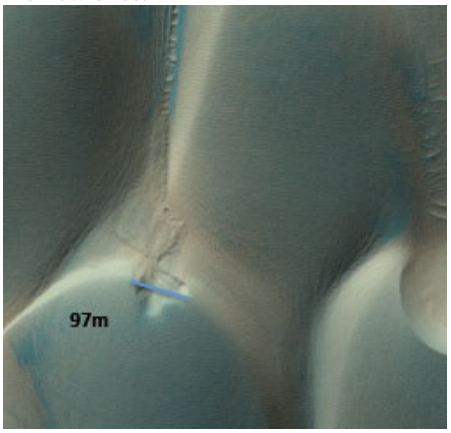

Figure 2. A large new alcove was observed at a site known informally as "Buzzel" in ice-free image ESP_036387_2640 at 84N / 233E acquired in MY32. There were more large new alcoves in this Mars year than other years, at the same site.

Interannual Variability: Atmospheric conditions appear to influence alcove formation on the north polar erg. In the southern hemisphere dust storms are implicated in the timing, number and size of the seasonal fans that appear on the seasonal cap.

The Planet Four citizen science fans project volunteers outline fans in HiRISE image cutouts (http://www.planetfour.org). We now have a catalog of seasonal fans for multiple Mars years [16]. The catalog allows us to quantify differences in Mars years with metrics as a function of time such as numbers of fans, sizes of fans, area covered, and orientation (which tells us about the local wind direction).

In years with preceding dust storms (both global and regional) fans emerge earlier in spring. As shown in Fig. 3 they are smaller and there are more of them. Global dust storms do not occur every Mars year but regional dust storms do. These storms are categorized as "A", "B", and "C"-type storms, differentiated primarily by when they begin and their latitudinal extent [16]. Pronounced regional "A"-type dust storms took place in late spring in MY 29 and MY32 [16], suggesting that regional storms could also play a role in lofting dust into the atmosphere that in turn influences the seasonal activity in the subsequent spring. With the hypothesis that both global and Type A regional dust storms affect seasonal activity, we would expect an increase in the number of fans in MY29, following the global dust storm of MY28; in MY30 following the intense type A storm in MY29; and in MY33 following the Type A storm in MY32 [17].

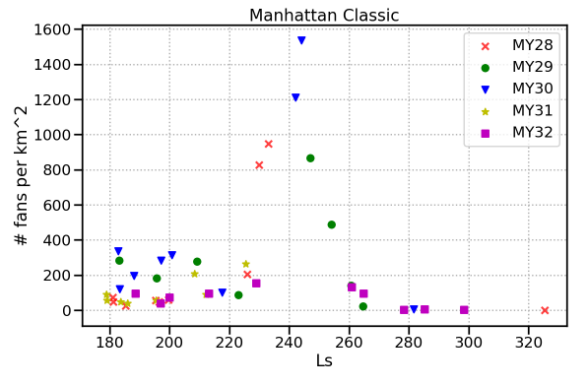

Figure 3. Early in spring the number of fans in MY29 and MY30 are clearly higher than other Mars years.

Summary: Multi-year datasets are enabling investigations of dynamic processes that go beyond being a snapshot in time. While combining datasets that provide different points of view to the same phenomena are important for short-term studies, this is crucial for understanding long-term relationships between short-, long-term and transient phenomena. These correlation studies with the use of extended datasets are instrumental for understanding the physics behind dynamic processes that repeat yearly for decades.

Acknowledgments: This work was funded in part by MDAP grant NNN13D465T and in part by the Mars Reconnaissance Orbiter project managed by the Jet Propulsion Laboratory / California Institute of Technology.

References: [1] McEwen, A. S. et al. (2007) *JGR* 112, E05S02. [2] Hayne, P. O. et al. (2012) *JGR* 117, E8. [3] Leighton, R. B. and B. C. Murray (1966) *Science* 153, 136-144. [4] Hayne, P. O. et al. (2014) *Icarus* 231, 122-130. [5] Matsuo, K. and K. Heki (2009) *Icarus*, 202, 90-94. [6] Kieffer, H. H. (2007) *JGR* 112, E08005. [7] Piqueux, S. et al. (2003) *JGR* 108, E8. [8] Bourke, M. and A. Cranford (2011) *Fifth International Conference on Mars Polar Science,* Abstract #6059. [9] Hansen, C. J. et al. (2013) *Icarus* 225, 881-897. [10] Portyankina, G. et al. (2017) *Icarus* 282, 93-103. [11] Piqueux, S. and P. Christensen (2008) *JGR* 113, E06005. [12] Hansen, C. J. et al. (2010) *Icarus* 205, 283-295. [13] Thomas, N. et al (2010) *Icarus* 205, 296-310. [14] Schwamb, M. E. et al. (2018) *Icarus* 308, 148-187. [15] Hansen, C. J. et al. (2011) *Science* 331, 575-578. [16] Aye, K.-M. et al. (2019) *Icarus* 319, 558-598. [17] Kass, D., et al., (2016) *GRL* 43:6111. [18] Hansen, C. J. et al. (2019) *LPSCXXXXX* Abstract # 3110.

HIRISE OBSERVATIONS OF RECENT PHENOMENA IN THE NORTH POLAR REGION OF MARS. K. E. Herkenhoff[1], S. Byrne[2], C. M. Dundas[1], N. F. Baugh[2], and M. A. Hunter[1], and the HiRISE Science Team, [1]U. S. Geological Survey Astrogeology Science Center (2255 N. Gemini Dr., Flagstaff, AZ 86001; kherkenhoff@usgs.gov), [2]University of Arizona Lunar and Planetary Laboratory.

Introduction: The High Resolution Imaging Science Experiment (HiRISE) on the Mars Reconnaissance Orbiter (MRO) has observed the north polar region of Mars during 8 summer seasons. Here we summarize analyses of the north polar data, focusing on active and recent processes including evolution of steep scarps in the north polar layered deposits (NPLD), bright and dark crossing streaks, and the north polar residual cap (NPRC).

Full-resolution HiRISE images are up to 20,000 monochrome pixels (~6 km) wide with color data in the central 4000 pixels [1]. Such HiRISE images of the north polar region at scales of ~30 cm/pixel show morphologic details and reflectance variations indicative of currently- or recently-active processes. The observations discussed here highlight the importance of both long- and short-term monitoring of north polar targets to further our understanding of time-variable phenomena in this region.

Steep Scarps: Initially recognized in Mars Global Surveyor data, steep scarps in the NPLD have been repeatedly observed by HiRISE. These scarps occur where the dark, basal unit is exposed to erosion, undercutting the more competent, overlying NPLD and causing mass wasting. Previous studies found that such rock falls occur primarily during late summer through early winter, and that the volume of wasted material is difficult to estimate [2]. Thermoelastic modeling indicates that extensional stresses are greatest in winter [3], generally consistent with the HiRISE observations.

Determination of the NPLD erosion rate at these steep scarps is complicated by differences in illumination and viewing geometry between HiRISE images of the rock falls. Planning repeat observations with nearly-identical observational geometry was difficult until we developed software to identify future opportunities for imaging targets with lighting and viewing geometry that is similar to a previously-acquired image. This new tool was used during the northern summer of Mars Year (MY) 34 to acquire images that, when paired with images taken earlier in the MRO mission with similar observational geometry, are better suited to measuring changes due to mass wasting. An example of such an "exact-match" image pair that includes clear evidence for wasting along a steep NPLD scarp is shown in Figure 1. The binned MY 28 (2006) image shows blocks at the base of the scarp that fell before the image was acquired; many of these blocks do not appear to have changed significantly in the 6 Mars years before the unbinned MY 34 (2018) image was taken, but blocks disappear in other areas.

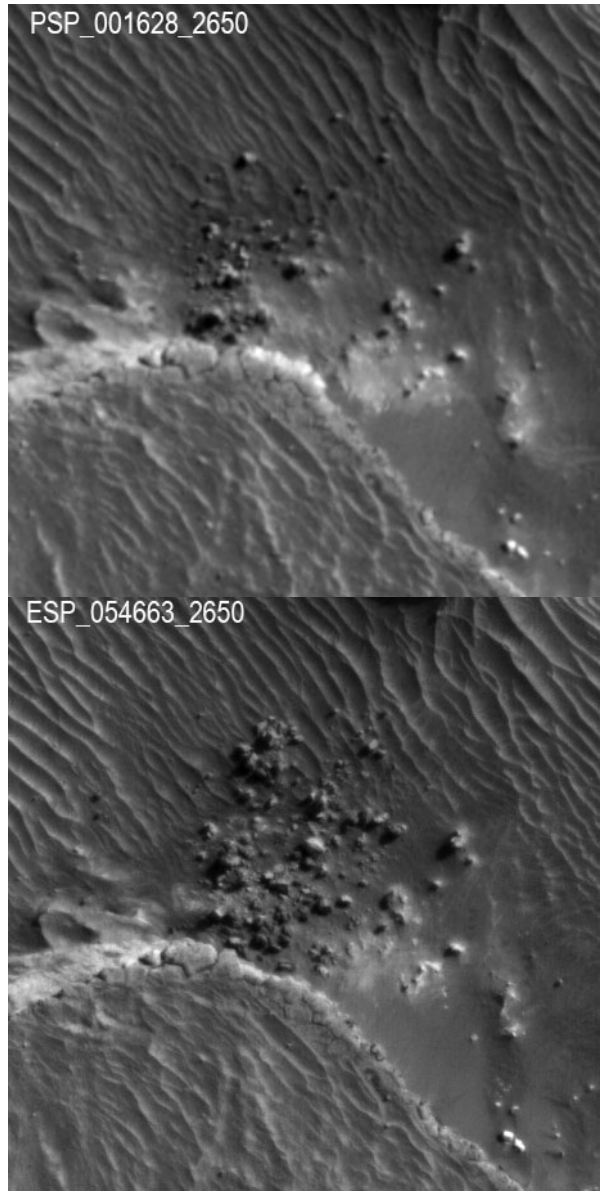

Figure 1. Subframes of red HiRISE images of a steep scarp in the north polar layered deposits at 85.1°N, 237°E. Illumination from upper right, area shown is about 147 m square. Top: PSP_001628_2650, acquired on 1 December 2006 (Mars Year 28, binned 2x2), L_s = 143.6°. Bottom: ESP_054663_2650, acquired on 25 March 2018 (Mars Year 34), L_s = 149.0°.

Another image of this scarp, ESP_019284_2650, was acquired in MY 30 at L_s = 144.6° and shows that a section of the scarp had already failed by that time. Blocks that appear near the base of the scarp in the MY 28 image were marked using ArcMap so that new blocks could be easily recognized in the later images: some of the older blocks have disappeared, as seen at other NPLD block falls. New blocks were outlined in each of the MY 30 and 34 images and their area measured. The lengths of shadows cast by 6 large blocks were measured in ESP_054663_2650 (solar incidence = 72.7°) and used to estimate the height of each block. The heights are similar to the radii of spheres having the same cross-sectional area as the blocks (standard deviation = 45 cm or 1.4 pixels), so we calculated the volume of each block as that of a half-sphere with the same radius as a circle having the same area as the block. The 0.02 to 37 m^3 range of block volumes derived using this approach is similar to that found along a similar NPLD scarp [4]. Ignoring unresolved blocks, the minimum volume of new blocks measured in ESP_019284_2650 is 538 m^3 and that of new blocks in ESP_054663_2650 is 1468 m^3. These volumes correspond to mass wasting rates of 0.08 and 0.1 m^3 per MY per meter along the NPLD scarp or 0.09 m^3 per MY over the 6 Mars Year span of these observations, somewhat less than the 0.3 m^3 per MY per meter rate found at another NPLD scarp [4]. We plan to make similar measurements at other locations where NPLD block falls have been observed in order to better constrain the average NPLD erosion rate.

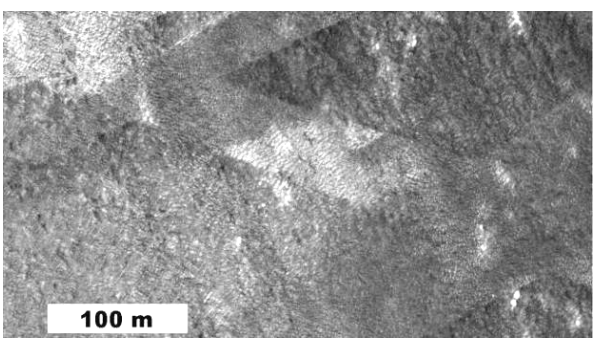

Figure 2: Subframe of red HiRISE image PSP_009273_2610, acquired at L_s = 100.3 in MY 29, showing complex streak superposition at 80.8°N, 330.6°E.

North Polar Streaks: Bright and dark streaks have been observed at the periphery of the north polar residual cap (NPRC) by previous Mars orbiters and were the target of repeated HiRISE observations. The complex interactions between overlapping bright and dark streaks in some of these HiRISE images (Fig. 2) indicate that formation of the streaks involves processes more complex than simply the emplacement of dark veneers. Bright and dark streaks are seen to evolve during the northern summer, evidence for active eolian redistribution of frost and perhaps darker (non-volatile) dust or sand. HiRISE color images do not include the area shown in Figure 2, but part of this area was imaged in color during MY 30. This and other color images of similar streaks show the red/blue ratio of the bright streaks is consistent with partial frost cover. While the color and albedo of the streaks are observed to change during the summer season and interannually, the surface texture does not, suggesting that mobility of dark, non-volatile material has a negligible effect on the underlying topography. The sharp boundaries of the streaks are similar to those seen along slope streaks in dust [5], perhaps formed by advancing clouds of saltating particles.

Residual Ice Cap: The NPRC on Mars has long been known to be composed of water ice [6]. Relatively dark patches observed within the NPRC during the summer indicate that the cap is thin or transparent in places. Counts of craters in MRO Context Camera (CTX) and HiRISE images indicate that the NPRC is accumulating at a rate that might result in observable changes in crater morphology during the MRO mission [7]. HiRISE and CTX images of the NPRC show few fresh craters. Therefore, a campaign of HiRISE observations of four NPRC targets near 87°N latitude (the maximum latitude of the MRO ground track) was initiated during the Martian northern summer of MY 29 (2008) and continued through the summer of MY 34. The images acquired during this campaign, with nearly nadir viewing geometry and similar solar azimuth, have been searched for evidence of current redistribution of NPRC material. Only minor albedo changes (no topographic changes) are observed in these areas. MY35 imaging is planned to continue to search for significant changes.

Summary: HiRISE and other MRO data show evidence for multiple types of ongoing activity in the north polar region, consistent with the apparent youth of the NPRC surface [7]. The latest HiRISE images of recently-active features will be shown and discussed at the conference.

References: [1] McEwen, A. S. *et al*. (2007) *JGR* **112**, doi:10.1029/2005JE002605. [2] Russell, P. S. *et al*. (2014) Eighth Internat. Conf. on *Mars,* abstract #1257. [3] Byrne, S. et al. (2014) Eighth Internat. Conf. on *Mars,* abstract #1373. [4] Fanara, L. *et al*. (2019) *Icarus* doi:10.1016/j.icarus.2019.113434 (in press). [5] Toyota, T. *et al*. (2011) *Planet. Space Sci*. **59**, 672-682. [6] Jakosky, B. M. and Haberle R. M. (1992) In *Mars* (H.H. Kieffer *et al.,* Eds.), pp. 969-1016. Univ. Arizona Press, Tucson. [7] Landis, M. E. *et al*. (2017) *LPSC* **XLVIII**, abstract #1588.

WIND TUNNEL EXPERIMENTATION OF ICE PARTICLES TRANSPORT IN MARTIAN-LIKE ENVIRONMENT C. Herny[1] , J. Merrison[2], J. Iversen[2], Z. Yoldi[3], M. Bordiec[4], S. Carpy[4], O. Bourgeois[4], and N. Thomas[1], [1]Physikalisches Institut, Universität Bern, Sidlerstrasse 5, 3012 Bern, Switzerland (clemence.herny@space.unibe.ch), [2]Departement of Physics and astronomy, Aarhus University, Ny Munkegade 120, 8000 Aarhus C, Denmark, [3]Niels Borh Institute, Tagensvej 16, 2200 København N, Denmark, [4]Laboratoire de Planétologie et Géodynamique - UMR CNRS 6112, Université de Nantes, 2 rue de la Houssinière - BP 92208, 44322 Nantes Cedex 3, France

Introduction: The transport of ice by wind plays a major role in the surface mass balance of polar caps [1, 2]. Ice can be redistributed by wind due to (1) transport of ice particles and/or (2) transport of water vapour associated with sublimation/condensation. On Mars, although the low atmospheric density is less favorable for the transport of particles than on Earth, both dust and sand have been observed to be transported by wind [3,4]. Despite ice Aeolian landforms have been observed at the surface of the North Polar Cap of Mars [2, 5, 6], ice particle transport has not been directly observed on the Martian surface. Similarly, no laboratory studies of snow/ice particle transport under Martian-like conditions (even at pressure lower than 1000 mbar) have been attempted thus far due to the complexity of the material. In this study we performed experiments of ice particle transport in a wind-flow under low temperatures and low pressures. From the experiments, threshold shear velocity of water ice particle transport is retrieved for different pressures and particle shapes and sizes in order to evaluate the plausibility of ice particle wind-driven transportation at the surface of Mars.

The North Polar Cap of Mars: The Martian atmosphere is thin (7 mbar), cold (220 K) and dry (< 80 µm-pr) [7]. These conditions favored ice sublimation/condensation processes. The polar caps are made of a mixture of ice and dust. Spectral analyses [8, 9] suggested the optical grain sizes to vary between 10 µm to about 2000 µm for the seasonal frost and surface of the perennial North polar cap. But, the mechanisms of ice deposition are not well established. It can potentially come from vapour condensation directly onto the surface [9] or from snow fall [10]. This will affect the shape and size of ice particles and degree of ice sintering, which all influence the shear velocity threshold. The North polar cap experiences a permanent katabatic wind regime [11] with a typical friction shear velocity u_* about 0.2 m.s^{-1}. The complex interactions between the cryosphere and the wind leads to the formation of Aeolian features at different scales [2, 5, 6].

Wind tunnel experiments: We performed experiments using the environmental wind tunnel AWTSII at Aarhus University. It is a cylindrical vacuum chamber, housing a recirculating wind tunnel about 8 m long, 2 m wide and 1 m high [12]. The facility can achieve a turbulent boundary layer flow at both low temperature and low pressure. The ice samples were produced by crushing ice blocks (irregular and angular shape particles) and by using the Setup for production of Icy Planetary Analogues (SPIPA, spherical shape particles) [13]. The ice samples were sieved (125 - 250 µm, 250 - 500 µm, 500 - 2000 µm) as a monolayer on a sample plate (20 cm x 20 cm) cover with volcanic regolith (125 µm). The fan speed was increased by steps (shear velocity $u_* = 0$ to 2 m.s^{-1}) and the wind flow characterized by laser Doppler anemometry. The removal of ice particles was monitored by webcam**.** We performed the experiments for the different particle shapes and sizes for 4 different air pressures; 40, 100, 500 and 1000 mbar. The air temperature was maintained low (~-25°C) close to the sample plate to prevent the ice melting, sublimating and sintering.

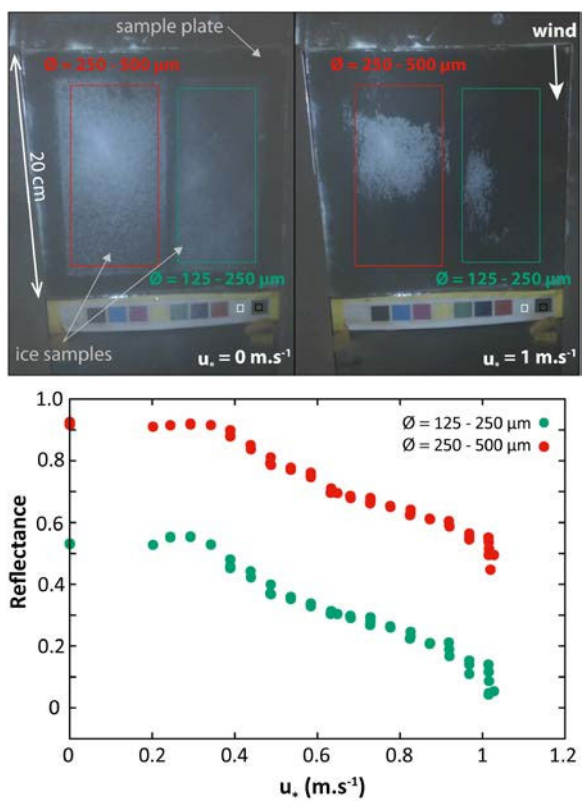

Figure 1: Images of the ice samples (SPIPA) evolution from $u_* = 0$ m.s^{-1} (up left, beginning of the experiment) to $u_* = 1$ m.s^{-1} (up right, end of the experiment). Two ice samples, with different particles sizes (125 – 250 µm and 250 – 500 µm respectively on the right and on the left) are observed side by side. For both grain sizes, ice particles have been removed by wind. The wind comes from the top to the bottom of the images. The experiment is performed at P = 500 mbar and T ~-25°C. A color bar is placed near the sample plate to calibrate the reflectance of the regions of interest defined on the ice samples (green and red boxes). The reflectance decreases as the shear velocity increases for both ice particles sizes (lower plot). The estimated threshold shear velocity in both case is about 0.4 m.s^{-1}.

Threshold shear velocity calculation: The threshold shear velocity was determined from analysis of acquired images. When bright ice particles are removed from the dark volcanic regolith sample plate, the reflectance of the surface decreases (Fig. 1). Black and white reference targets are placed close to the sample plate in the field of view of the webcam. The reflectance evolution of a region of interest (ROI) on the sample plate is calculated as follow:

reflectance = (ROI – black target)/
(white target – black target)

The reflectance serve as a proxy for ice mass removal. For each image the reflectance is linked to the corresponding shear velocity. In the case of Fig. 1, the reflectance is constant until a certain wind speed and then decreases. To determine the threshold shear velocity u_{th}, we set the threshold reflectance at 10% decrease from the first image at $u_* = 0$ m.s^{-1}.

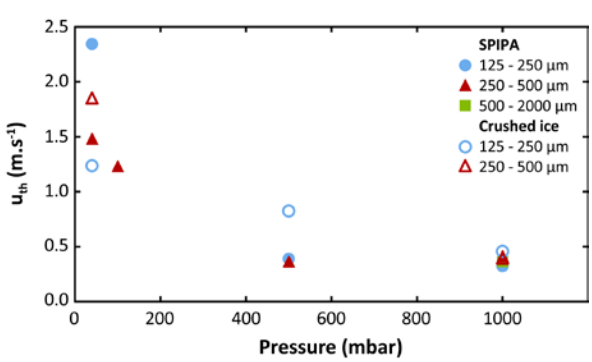

Figure 2: Threshold shear velocity evolution with wind tunnel air pressure for different ice particles production and sizes.

Results: Figure 2 shows preliminary results of the threshold shear velocity evolution with air pressure for different grain sizes and shapes. The averaged value obtained at 1000 mbar, u_{th} = 0.4 m.s^{-1}, is consistent with theoretical and experimental calculation of ice/snow at terrestrial condition [14, 15], from 0.3 m.s^{-1} to 0.6 m.s^{-1} for range of ice particles sizes selected, supporting our set-up reliability. The shear velocity increases significantly as the pressure decreases. The ice grain shapes and sizes appear to have a influence at lower pressure while no significant effect is highlighted at terrestrial pressure. However more replicates should be perform at low pressures to better characterized u_{th}.

Conclusion and future work: We have performed for the 1st time experiments of ice particles transportation at low pressure in a planetary wind tunnel. These preliminary results show an increase of threshold shear velocity as the pressure decreases. The conclusions should be reinforced with additional measurements and then be scaled to Martian gravity in order to conclude about the likeliness of transport of ice particles by wind at the surface of Mars. In case results reveal that the transport of ice particles under Martian condition is unlikely, we plan to experimentally explore the second hypothesis of ice mass redistribution which is the transport of water vapour associated with sublimation/condensation that is also thought to have a strong influence on the polar caps of Mars [16, 17].

References: [1] Das I. et al. (2013) *Nature Geoscience*, *6*, 367-371. [2] Howard A. D. (2000) *Icarus, 144,* 267-288. [3] Cantor B. A. et al. (2010) *Icarus, 208,* 61-81. [4] Bridges B. A. et al. (2012) *Geology, 40,* 31-34. [5] Smith I. B. and Holt J. (2010) *Nature, 465,* 450-453. [6] Herny C. et al. (2014) *EPSL*, *403*, 56-66. [7] Pankine A. A. et al. (2010) *Icarus*, *210*, 5871. [8] Langevin Y. et al. (2005) *Science*, *307*, 1584-6. [9] Appéré T. et al. (2011) *JGR : Planets*, *116*, E05001. [10] Spiga A. et al. (2017) *Nature Geoscience*, *10*, 652-657. [11] Spiga A. et al. (2011) *PSS*, *59*, 915-922. [12] Holstein-Rathlou C. et al. (2014) *Am. Met. Society*, *31*, 447-457. [13] Pommerol A. et al. (2019) *Space Sci. Rev., 215*. [14] Shao Y. and Lu H. (2000) JGR, *105*, 437-443. [15] Clifton A. et al. (2006) *JoG*, *52*, 585-596. [16] Herny C. et al. (2016) 6th MPSC, Abstract #6075. [17] Bordiec M. et al. (2018) ICAR X.

Acknowledgements: This work has been fund by Europlanet (Europlanet 2020 RI has received funding from the European Union's Horizon 2020 research and innovation program under grant agreement No 654208). This work has been supported by the University of Bern. This work has been carried out within the framework of the NCCR PlanetS supported by the Swiss National Science Foundation.

TERRESTRIAL BRAIN TERRAIN AND THE IMPLICATIONS FOR MARTIAN MID-LATITUDES. S. M. Hibbard[1], G. R. Osinski[1], E. Godin[1] and A. Kukko[2], [1]University of Western Ontario (1151 Richmond St, London, ON N6A 3K7, shibbard@uwo.ca), [2]Finnish Geospatial Research Institute (Helsinki, Finland).

Introduction: Periglacial features, such as polygonally patterned ground and brain terrain, are widely distributed across the mid-latitudes of Mars [e.g. 1-5]. The origin of polygonally patterned ground and its relationship to ice on both Earth and on Mars remains debated, although a wide range of possible terrestrial analogues have been documented [e.g. 2]. However, very little is known about the origin of so-called brain terrain and suitable Earth analogues have not been identified.

Brain terrain occurs in the mid-latitudes of Mars and is characterized by an anastomosing complex of ridges and troughs arranged in a brain-like pattern (Fig. 1). There have been only a handful of studies on brain terrain; most workers suggest it is periglacial in origin [1,5,6] but its relationship with ice is unknown. The leading hypothesis suggests dry periglacial processes cause localized sublimation of the ice-bearing latitude dependent mantle (LDM) [1].

We recently identified a landform, referred to here as terrestrial brain terrain (TBT), in the Canadian High Arctic [7]. In this study, we report on further occurrences of TBT documented in summer 2019 that may provide insight into brain terrain formation mechanisms on Mars.

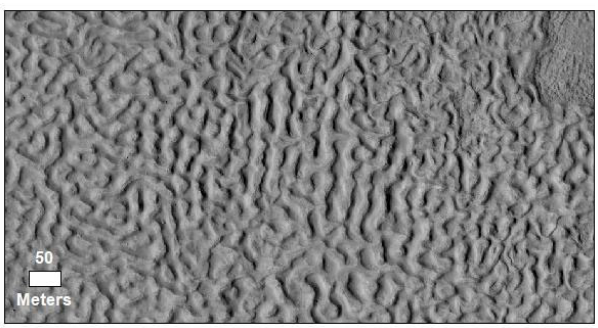

Figure 1: *Example of brain terrain on gently sloping lobate debris apron (LDA) moraine in Protonilus Mensaeat 40°N. HiRISE image ESP_045507_2200.*

Terrestrial Brain Terrain: Since our first identification of a possible terrestrial analogue for martian brain terrain at Dundas Harbor on Devon Island, Nunuvut, Canada [7], we have discovered several other sites on Axel Heiberg Island in our 2019 field season (Fig. 2). These landforms have strikingly similar morphological characteristics to Martian brain terrain. TBT is characterized by a sinuous network of ridges and troughs that form amorphous to well-defined open or closed circles (Fig. 2). We are now continuing our search across the Canadian Arctic by mapping out their distribution using high resolution World Imagery (down to 30 cm resolution).

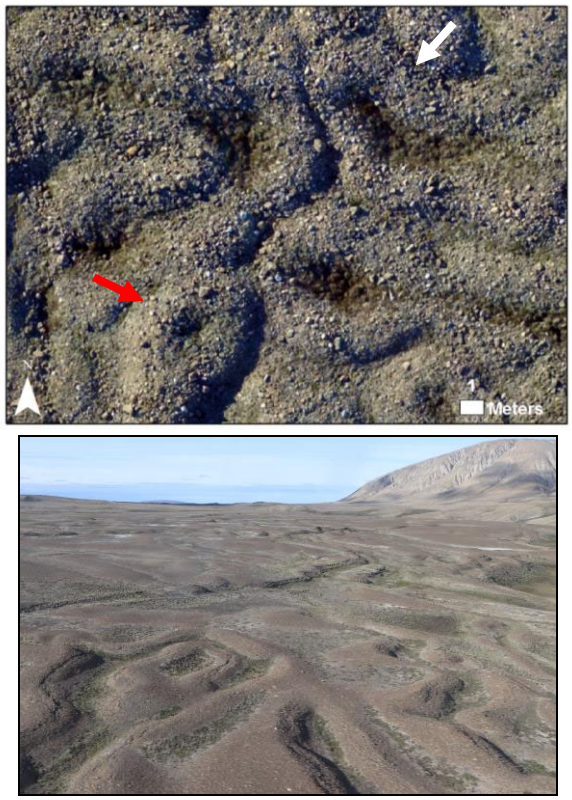

Figure 2: *Top: Example of terrestrial brain terrain (TBT) on gently sloping glacial till moraine in Dundas Harbor, Devon Island. Amorphous (white arrow) to well-defined (red arrow) open and closed circular features. Bottom: TBT field view on Axel Heiberg Island on gently sloping glacio-fluvial plains material.*

Field Methods. We collected a combination of drone imagery (Using DJI Phantom 3 and DJI Mavic Pro), sediment samples, ground penetrating radar (GPR; using Sensors and Software 250 Noggin) and laser scanning (using AkhkaR4DW Backpack mobile laser scanning system) of TBT in the Arctic 2018 [7] and 2019 field seasons.

Observations. Initial observations made by [7] included TBT in an active periglacial environment forming in cobbley glacial till on a gentle slope of 9°. The presence of relatively fresh axial cracks on ridges, minimal grain sorting, and absence of massive ice are also notable observations.

We have found similarities in scale, morphology, grain size and depositional environment in the additional 4 sites identified in the 2019 field season. All

sites have similar ridge width (1 2 m) and height (< 2 m). In some cases, open or closed ridges are much more localized or isolated (Fig. 3c). TBT consistently occurs in larger grained, cobbley material either in glacial till or glacio-fluvial deposits. All TBT occurrences are on gentle slopes less than 10°. Multiple sites also show thermal contraction cracks of polygons cross cutting TBT (Fig. 3) suggesting TBT formation may predate polygon formation.

Figure 3: *Aerial image examples of terrestrial brain terrain on Axel Heiberg Island (a, b) and Devon Island (c). Thermal contraction polygons (arrows).*

Possible Formation Mechanisms. As we continue to process data from the 2019 field season, we are currently exploring two potential end-member hypotheses for the formation of TBT:

(1) TBT formed periglacially through stone circle sorting and solifluction processes [cf., 7]. The presence of relatively fresh cracks in the ridges of TBT suggests differential uplift in the ridges and a possible mechanism for post-depositional sorting. Thermal cracking cross cutting TBT may indicate more than one periglacial process is occurring. This would indicate that TBT is a currently active periglacial phenomenon. More field experiments can be done to test hypothesis. The installation of long term rods to measure ground uplift across a series of ridges and troughs could give us rate and direction of uplift [e.g. 8].

(2) TBT formed due to glacial processes, such as differential melting of an ice-cored moraine or a type of kettle and kame topography. Polygonal cracking would then have come later during the present-day periglacial-dominant conditions overprinting any glacial deposits. This would suggest TBT formed in the past when conditions were icier.

A combination of these two processes is also being considered.

Implications for Mars: Brain terrain can be found across the LDM in the mid-latitudes of Mars. It can be found on concentric crater fill [1], at the base of LDA (Fig. 1), and on flat-lying plains [5]. Two hypotheses for brain terrain formation have been proposed both of which are periglacial in nature. (1) Frost heave mechanisms similar to stone circle sorting processes [6], and (2) Differential interstitial ice sublimation of LDM material [1,5]. These hypotheses suggest brain terrain forms under either strictly wet or dry periglacial processes.

Although TBT is not fully understood, it is morphologically similar to Martian brain terrain and occurs in the cold polar desert environment in the Canadian High Arctic. If TBT is a presently active periglacial landform, then it is forming under wet periglacial conditions, suggesting brain terrain on Mars may be a relict landform.

TBT may be the first appropriate terrestrial analogue and continued studies on TBT may help us better understand brain terrain on Mars.

References: [1] Levy J. S. et al. (2009a) *Icarus, 202,* 462-476. [2] Levy J. S. et al. (2009b) *JGR, 114*. [3] Balme M. R. and Gallagher C. (2009) *EPSL, 285,* 1-15. [4] Zanetti M. et al. (2010) *Icarus, 206*, 691-706. [5] Williams N. R. et al. (2017) *LPS XLVIII,* Abstract #2852. [6] Dobrea E. Z. N. et al. (2007) *7th Intl. Conference on Mars*, Abstract #3358. [7] Hibbard S. H. and Osinski G. R. (2019) *LPS L*, Abstract #2126. [8] Hallet B. and Prestrud S. (1986) *Cambridge, 26*, 81-99.

Experimental Heat Transfer Supporting Simulated Water Well Performance on Mars. Stephen J. Hoffman[1], James H. Lever[2], Alida D. Andrews[3], and Kevin D. Watts[4]. [1]The Aerospace Corporation, 2525 Bay Area Blvd., Houston, Texas 77059; stephen.j.hoffman@nasa.gov. [2]U.S. Army Cold Regions Research and Engineering Laboratory, 72 Lyme Rd, Hanover, NH, 03755; james.lever@erdc.dren.mil. [3]The Aerospace Corporation, 2525 Bay Area Blvd., Houston, Texas 77059; alida.andrews-1@nasa.gov. [4]NASA Johnson Space Center, 2101 E NASA Pkwy, Houston, TX 77058; kevin.d.watts@nasa.gov.

Introduction: Current theory holds that Mars once had abundant water flowing on its surface, but now there is a general perception that this surface is completely dry [1]. Several lines of research have shown that there are sources of potentially large quantities of water ice at many locations, including regions considered as candidates for future human missions [2]. Recent discovery of exposed water ice scarps in Martian mid-latitudes [3] has bolstered the evidence for massive amounts of almost pure water ice in some of these regions.

These favorable indications of massive quantities of water have initiated studies of potential changes to human Mars missions if a means can be devised to make this water available to these crews [4]. One such approach relies on mechanical drills to access the water ice through overlying debris and then using a technique known as a Rodriguez Well to melt the ice, store the resulting water in a subsurface ice cavity until needed, and then pump the water to the surface for use [5]. The Rodriguez Well technique has been used in terrestrial polar regions since the early 1960's and has been supplying fresh water to the Amundsen-Scott South Pole Station since 1995.

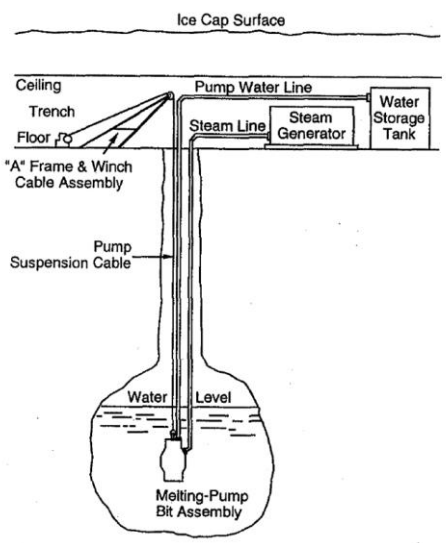

Figure 1. 1960's era Rodriguez Well [5].

Previous planning work in this area utilized a computer simulation to predict the performance of the Rodriguez Well [5]. While the basic approach used in this model is appropriate for a similar well on Mars, several parameters must be changed to correctly model the Martian environment. Parameters used in this model that are related to heat transfer between water and the atmosphere as well as between ice and the atmosphere are empirically derived. Consequently, experiments simulating a pool of water in the Martian environment are required to determine appropriate heat transfer values if this simulation is to be used in support of future Mars missions.

Simulated Mars Environment: An experiment was set up at the NASA Johnson Space Center, with the assistance of the U.S. Army's Cold Regions Research and Engineering Laboratory, to measure these heat transfer coefficients under Mars surface environmental conditions. These tests were carried out in a small bell jar, with a chamber measuring roughly 2 feet (61 cm) in diameter and 2 feet (61 cm) tall. An internal cooling shroud connected to a Julabo™ chiller allowed gas temperatures as low as -40 C.

Figure 2: NASA JSC Two-Foot Bell Jar [NASA]

The experiment used a pool of water in an insulated dewar ensuring that heat loss would only be from the top of the water pool. A resistance heater was held in the water pool and was connected to a resistance temperature detector (RTD), also in the water pool, in a feedback loop to maintain a specified water temperature: either 1° C or 2° C. The power used by the heater was a measure of the heat transferred from the water to the gas. A load cell under the dewar measured the mass

loss of water due to evaporation. The interior of the chamber was instrumented with RTDs and thermocouples at various locations, heat flux sensors at the chamber wall, a pressure transducer for gas pressure, and a relative humidity sensor. A camera and LED light source were used to monitor for ice formation on or in the dewar.

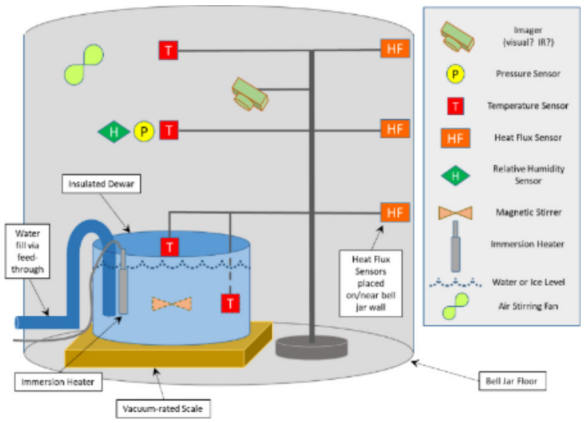

Figure 3. Experiment Setup

Experiment Test Points: Natural convection, driven by evaporation and heat flow from the pool, governs the flow regime inside a Rodriguez Well. The experiment was operated at several test points to gather data from which heat transfer coefficients and water evaporation rates could be derived. For all tests, the chamber was filled with essentially pure CO_2. Two insulated hemispherical dewars, one 11.4 cm (4.5 in) in diameter and the other 15.2 cm (6.0 in) in diameter, were used to hold the water pool, allowing tests at two different water-pool surface areas. Two gas temperature points (-20° C and -40° C) and several gas pressures, ranging from 1000 mbar (750 torr) to 8 mbar (6 torr) were used to gather these data. Test conditions were chosen to learn whether the experimental work of Bower and Saylor [6] that related natural-convection flow properties to evaporation rates in terrestrial conditions, via dimensionless Rayleigh and Sherwood numbers, could be extended to Mars surface conditions. In all, 12 combinations of pressure, temperature, and water pool diameter were used in this experiment.

Initial results: Tests at all 12 test points have been completed and data are being evaluated. Quantitative results for convective mass and heat transfer and the degree of correlation with Bower and Saylor will be an outcome of these evaluations. However, one clear outcome from the tests is that a water pool representative of a Rodriguez Well can be created and maintained at 1° C to 2° C under Mars surface pressure and temperature conditions.

Conclusion: Favorable indications of massive quantities of water on Mars have initiated studies of potential changes to human Mars missions. Using a technique known as a Rodriguez Well to melt the ice, store the resulting water in a subsurface ice cavity until needed, and then pump water to the surface for use is one potential means to effect these changes. A computer simulation of the Rodriguez Well in a terrestrial environment is one of the engineering tools being used to characterize the performance of this type of well on Mars. An experiment at the NASA Johnson Space Center is gathering data for convective heat transfer and evaporation rates at Mars surface conditions so that this computer simulation can be properly modified to predict performance on Mars. While quantitative results await processing, tests have indicated that a pool of water can be maintained at 1°C to 2° C while at Mars surface temperatures and pressures.

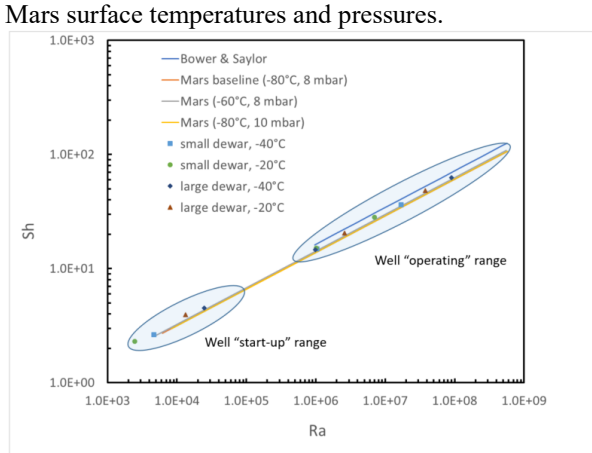

Figure 4. Anticipated Results Plotted With Bower and Saylor Results.

References: [1] Di Achille, G. and Hynek, B.M., (2010) "Ancient Ocean on Mars Supported by Global Distribution of Deltas and Valleys," *Nature Geoscience, 3* (7), 459–463. [2] Beaty, D.W., et al., (2016), "The Possible Strategic Significance of Mid-Latitude Ice Deposits to a Potential Future Human Mission to Mars," Sixth Mars Polar Science Conference, Abstract #6059. [3] Dundas, C. M., et al., (2018) "Exposed subsurface ice sheets in the Martian mid-latitudes," *Science 359*, 199–201. [4] Hoffman, S.J., et al., (2017) "A Water Rich Mars Surface Mission Scenario," IEEE Aerospace Conference 2017, Big Sky, MT, IEEE Paper 2422. [5] Lunardini, V. J. and Rand, J., (1995) "Thermal Design of an Antarctic Water Well," US Army Cold Regions Research and Engineering Laboratory, Special Report 95-10. [6] Bower, S.M., and Saylor, J.R., (2009), "A study of the Sherwood–Rayleigh relation for water undergoing natural convection-driven evaporation," *International Journal of Heat and Mass Transfer 52*, 3055–3063.

SAND, SUN, ICE, WIND, DUST, AND TIME: AN UPDATED HISTORY OF PLANUM BOREUM, MARS.

J. W. Holt, [1]Lunar & Planetary Laboratory, University of Arizona, jwholt@arizona.edu

Introduction: Our understanding of the composition and geologic history of Planum Boreum (PB), Mars has grown extensively due to a wealth of data from recent and ongoing missions including Mars Reconnaissance Orbiter (MRO) and Mars Express (MEX), building on an extensive compilation of previous studies [1]. In particular, radar stratigraphy obtained by the Shallow Radar (SHARAD) [2] on MRO has provided a new context for interpreting high-resolution imagery, morphology, and spectral data. This review synthesizes our current understanding of the long-term evolution of Planum Boreum, starting with the cavi portion of the basal unit (BU) and moving through the overlying north polar layered deposits (NPLD), with significant updates since a review at the Sixth Mars Polar Science Conference [3]. Since then, advances have been made in constraining the composition and structure of the cavi, its relationship to earliest NPLD deposition, and the dust content of layers in the NPLD that give rise to radar reflections.

Cavi: The BU, an informal designation, consists of the Rupēs unit overlain by the aeolian cavi unit [1]. The cavi, long considered to be a roughly 50/50 mixture of sand and ice with aeolian cross-bedding, has been shown to contain transitional aeolian parasequences that stack towards a pure water–ice deopositional environment, allowing the cavi and NPLD to be interpreted as a single, orbitally-forced sequence [4]. New SHARAD mapping and analyses have determined that cavi internal structure at the highest latitudes likely consists of thick (tens of meters) layers that alternate between nearly pure ice and more concentrated sand, likely dune fields that preserved the ice through periods of higher insolation [5]. The ice layers are interpreted as remnants of former polar caps predating the NPLD [5]. Furthermore, both the extent of cavi and its bulk ice content are both larger than previously thought, ranging from nearly 90% water ice at the highest latitudes observed, to approximately 60% in Olympia Planum based on SHARAD analyses [5], with bulk ice content confirmed by MRO gravity studies [6].

Cavi to NPLD: The transition from cavi to NPLD is gradational [1], and new mapping with SHARAD shows that the uppermost cavi and lowermost NPLD were in fact contemporaneous at different locations within PB [7], supporting an earlier interpretation based on outcrops alone [1]. This cavi-to-NPLD transition took place on a surface that was highly nonuniform and asymmetric about the pole [8,9], although BU morphology and structure are contiguous with that of Olympia Undae. Earliest accumulation of NPLD was likewise nonuniform, with a separate accumulation center forming a proto Gemina Lingula [7].

Composition: While bulk composition of the NPLD has been constrained by radar to be ~95% water ice [10], subhorizontal radar reflectors within the NPLD have long been assumed to arise from stratigraphic variations in dust content that modulate the dielectric properties of the layers [11,12]. Recent results combining SHARAD data with modeling have shown that this is a reasonable assumption, and reflection strength is highly sensitive to layer thickness. Observed reflectors in the uppermost NPLD are consistent with so-called "marker beds" that are meters thick [13]. Furthermore, constraints on dust content and thickness for individual layers can be obtained from SHARAD using this methodology [14], with vertical profiles and geographic distributions possible. Typical layer thicknesses resulting from this analysis are 2 - 4 m, and dust contents lie the 10% - 50% range [14]. This provides a new way to test paleoclimate models that grow NPLD with dust incorporated into the dynamics [e.g., 15].

Flow and Melt: Although ice flow has previously been proposed as a significant factor in shaping the gross morphology of Gemina Lingula [16-17], the analysis of internal radar stratigraphy including a 3-dimensional flow model [18] does not support that interpretation, nor does the presence of buried troughs within Gemina Lingula [19]. Likewise, there is no evidence yet identified in radar stratigraphy to support basal melting of NPLD from enhanced geothermal flux, or brittle deformation on large scales. Furthermore, sedimentary structures indicate that aeolian processes have played a dominant role throughout NPLD history, both within the basal unit [4] and in the uppermost NPLD during the onset and evolution of the spiral troughs [20-22].

Spiral Troughs: The spiral troughs of the NPLD are unique windows into surface/atmosphere interactions that exert strong controls on the morphology of Planum Boreum. Stratigraphic structures indicate the first appearance of the spiral troughs out halfway through NPLD accumulation, and their subsequent migration concurrent with new deposition [20]. This finding and the unique inter-trough stratigraphy supports an origin with katabatic winds as a critical driver [21]. All major characteristics of the troughs can be explained in the context of repeating katabatic jumps, otherwise known as cyclic steps [22], wherein lateral transport of material is an important process.

Accumulation History: Stratigraphy within the NPLD indicates the dominance of processes that are sedimentary in nature; therefore we use large-scale stratigraphic unconformities to define the major depositional sequence boundaries. At least three large-scale depositional sequences are preserved, each of which is bounded by an erosional event. The lower of these depositional units was mapped across Planum Boreum to reveal the early appearance of Chasma Boreale [23]. A higher unconformity found in the saddle region east of Chasma Boreale indicates a later period of regional erosion. In both instances, the lateral extension of reflectors bounding these unconformities are conformal under the main lobe of Planum Boreum, indicating that these erosional epochs may have been relatively short-lived and limited in extent. Evidence does, however, exist for significant retreat of the NPLD margin in the region of Gemini Scopuli prior to the most recent episode of deposition.

Overall, the stratigraphy indicates a relatively simple accumulation history, with continuous deposition in the center of the deposits and either two or three large- scale (but relatively brief) hiatuses interrupting deposition and creating erosional surfaces in the lower latitudes of Planum Boreum. The youngest spiral troughs initiated above the upper unconformity, but some are older, indicating that conditions required for trough formation are not necessarily connected to erosion events or sudden changes in accumulation.

Links to climate modeling: Paleoclimate modeling can link changes in orbital parameters to atmospheric conditions and surface temperatures in order to predict the temporal and spatial patterns of ice accumulation. One such model, (MAIC-2; [24]), estimates global surface-ice mass balance for the past 10 Myr. This model uses as input the periodic changes in insolation derived from predictions of Mars' orbital parameters [25]. Due to mean obliquities higher than ~35° prior to ~5 Ma, large polar ice deposits do not accumulate prior to ~4 Ma in this model. The model was modified to include only the volume of NPLD as mapped using SHARAD data. Significantly, the model predicts three large-scale erosional events that interrupt relatively continuous accumulation in the past 4 Ma, largely consistent with the accumulation and erosional events observed in the radar stratigraphy.

The most recent of these events was further studied by mapping a stratigraphic unconformity in the uppermost NPLD [26]. Following a depositional hiatus (and possible erosion), an increase in accumulation is evident from steeper trough migration paths [20] and layering that drapes the entire surface. This event is most confidently tied to the most recent shift in obliquity at 370 ka [25, 27]. The quantity of ice accumulated after this unconformity (including an equivalent package at the south pole) is within a factor of two of that predicted to have moved from the mid-latitudes to the poles poles [26], so for the first time we are beginning to match observations of ice accumulation to global climate models for specific periods in Mars' past.

Conclusions: The stratigraphy of Planum Boreum contains a rich record of deposition, erosion, aeolian processes and compositional variations. Significant challenges remain to fully link the observations to climate modeling, but the observed radar stratigraphy is consistent with a simple model predicting northern polar ice growth since 4 Ma. Aeolian processes have exerted a strong role in shaping the surface, from the cavi/NPLD transition until the present day where we can observe surface/atmosphere interactions at work.

The dynamics of dust entrainment, transport, and deposition are important areas of future work to further refine the correlation between modeled ice deposition and observed layer stratigraphy at the outcrop level [15, 28]. Accumulation patterns observed with radar can provide further constraints for mesoscale climate modeling of ice deposition and ablation in the north polar region [29] and may allow for the interpretation of radar reflectors throughout the NPLD as a climate signal linked to orbital forcing, which could yield the next leap in our understanding of polar processes on Mars.

Acknowledgements: This work was supported by the MRO project, and NASA grants NNX10AO26G, NNX11AL10G, and NNX15AM52G. SHARAD is provided and operated by the Italian Space Agency.

[1] Tanaka, K.L. et al. (2008), *Icarus*, 196. [2] Seu, R. et al. (2007) *JGR*, 112. [3] Holt, J.W. (2016), *6th Mars Poar Conf.* [4] Brothers, S.C. et al., (2018), *Icarus,* (308). [5] Nerozzi, S. and Holt, J.W., (2019), *GRL*, 46(13). [6] Ojha, L. et al. (2019) *GRL*, 46, 8671-8679. [7] Nerozzi, S. and Holt, J.W., (2018), *Icarus*, 46(308). [8] Putzig N. E. et al. (2009) *Icarus*, 204. [9] Brothers, T.C. et al. (2015), *JGR,* 120. [10] Grima, C. (2009), *GRL*, 36. [11] Phillips, R.J. et al. (2008) *Sci- ence*, 320, 1182. [12] Nunes, D.C. and Phillips, R.J. (2006) *JGR*,111. [13] Lalich, D. and J.W. Holt (2016), *GRL*, 44(2). [14] Lalich, D.E. et al. (2019), *JGR* 124(7). [15] Hvidberg, C.S. et al. (2012), *Icarus*, 222(1). [16] Fisher, D.A. (2000), *Icarus*, 144, 289-294. [17] Winebrenner et al. (2008), *Icarus*, 195. [18] Karlsson, N.B. et al. (2011) *GRL* 38. [19] Smith, I.B. and J. W. Holt (2015), *JGR*, 120. [20] Smith, I.B. & Holt, J.W. (2010) *Nature* 465. [21] Howard et al. (1982) *Icarus* 50. [22] Smith, I. B. et al., (2013) *JGR* 118(9), 1835–1857. [23] Holt, J.W. et al. (2010), *Nature* 465. [24] Greve et al. (2010), *PSS*, 58. [25] Laskar, J. et al. (2002), *Icarus* 170. [26] Smith, I.B. et al. (2016), *Science*, 352. [27] Levrard, B. et al. (2007), *JGR,* 112. [28] Becerra et al., (2016), *JGR*, 121(8). [29] Nerozzi et al., (2019), *LPSC*, Abs. 2854

The Role of Regolith in the D/H Variation on Mars from the Poles to the Equator. R. Hu[1,2], [1]Jet Propulsion Laboratory, California Institute of Technology, Pasadena, CA 91109, renyu.hu@jpl.nasa.gov, [2]Division of Geological and Planetary Sciences, California Institute of Technology, Pasadena, CA 91125.

Summary: The regolith on Mars exchanges water with the atmosphere on a diurnal basis and this process causes significant variation in the abundance of water vapor at the surface. While previous studies of regolith-atmosphere exchange focus on the abundance [1,2,3], recent in-situ experiments and remote sensing observations measure the isotopic composition of the atmospheric water [4,5,6]. We are therefore motivated to investigate isotopic water exchange between the atmosphere and the regolith and determine its effect on the deuterium to hydrogen ratio (D/H) of the atmosphere. We model transport of water in the regolith and regolith-atmosphere exchange by solving a transport equation including regolith adsorption, condensation, and diffusion. The model calculates equilibrium fractionation between HDO and H_2O in each of these processes. The fractionation in adsorption is caused by the difference in the latent heat of adsorption, and that of condensation is caused by the difference in the vapor pressure. Together with a simple, bulk-aerodynamic boundary layer model, we simulate the diurnal variation of the D/H near the planetary surface. We find that the D/H can vary by 300 – 1400‰ diurnally in the equatorial and polar locations, and the magnitude is greater at a colder location or season. The variability is mainly driven by adsorption and desorption of regolith particles, and its diurnal trend features a drop in the early morning, a rise to the peak value during the daytime, and a second drop in the late afternoon and evening, tracing the water vapor flow into and out of the regolith. The predicted D/H variation can be tested with in-situ measurements. As such, our calculations suggest that stable isotope analysis is a powerful tool in pinpointing regolith-atmosphere exchange of water on Mars.

Model: We construct a one-dimensional model to simulate transport of isotopic water in the Martian regolith and boundary layer. It has a thermal diffusion module, a water transport module, and a boundary layer module. The model includes the isotope fractionation effects of adsorption, condensation, and molecular diffusion. The water transport module includes water vapor, adsorbed water, and condensed water in the regolith. Adsorption and condensation are assumed to be in equilibrium [2]. The diffusion equation for water includes the effects of soil porosity, tortuosity, and both molecular and Knudsen diffusion regimes [7]. For the eddy diffusion coefficient and the rate of mass transfer between the atmosphere and the soil, we use the bulk aerodynamic method [8], with the surface temperature, the near-surface atmospheric temperature, and the wind speed as input parameters. These parameters are either measured in situ, or calculated by global circulation models. We use typical values for the thermal inertia, the particle size, the specific surface area, the adsorption isotherm, and the surface roughness length in the model, and explore sensitivity of the results to these parameters.

Regolith adsorption fractionates water because the latent heat of adsorption of HDO is higher than that of H_2O. Ref. [9] conducted experiments of water transport in JSC Mars-1, a commonly used Martian regolith analog, and measured the effective diffusivities of H_2O and HDO under temperatures, pressures, and the background atmosphere corresponding to Mars. Because the ratio between the effective diffusivity is the inversed ratio between the adsorption coefficient, we fit the effective diffusivity data of Ref. [9] to an Arrhenius form for use in the model. We also include the fractionation factor between vapor and ice caused by the vapor pressure isotope effect [10].

Model Testing. We test the water transport model and compare model results with the relative humidity measurements made in situ by Curiosity's REMS instrument [11]. In particular, we obtain the REMS recalibrated data of relative humidity, air temperature, surface temperature, and wind speed from the Planetary Data System (PDS) for two 10-day periods. We pick an initial amount of water so that the resulting water column in the atmosphere matches the value measured by Curiosity's ChemCam instrument in each season [12].

We confirm that the model results are consistent with the measured relative humidity and absolute humidity. Most of the variation in the relative humidity is caused by the variation of the temperature; however, the measured absolute humidity features a rise by a factor of 2 – 3 after sunrise. This feature is well captured by the model. We consider this exercise a bona fide test because for a fixed water column, should there be major errors in the model, the nighttime humidity would depart substantially from the data. The modeled variation of the surface water abundance is also consistent with the existing 1D and mesoscale 3D models [13,14], and follows the typical patterns of diurnal water exchange on Mars [2].

Result: The modeled D/H diurnal variation in a polar location (i.e., the Phoenix landing site) is shown in Fig. 1. We use the Mars General Circulation Model (MGCM) outputs [15] for the surface temperatures and the wind speed, and choose the starting atmospheric D/H so that the resulting δD matched with telescopic measurements [5]. The D/H variation is mainly driven by the regolith-atmosphere exchange coupled with the fractionation in regolith adsorption. Surface condensation causes an additional variation. Since the fractionation factor is larger at a lower temperature, the magnitude of the variation is larger for a colder season. The D/H variation is ~1400‰ at the surface during the season of aphelion. The magnitude of the D/H variation is sensitive to the fractionation factor of adsorption. The uncertainty in the fractionation factor causes to the D/H variation's magnitude to change by ~50%.

To study more generally the diurnal variation of D/H at various latitudes and seasons, we model equatorial and mid-latitude locations, and the results are shown in Fig. 2. The diurnal variation follows a similar trend as the driving forces for the variation are regolith adsorption and desorption, and their coupling with the boundary layer. The adsorbed water is enriched in HDO compared to the water vapor. As a result, when there is a flux from the regolith to the atmosphere, we see an increase of the near-surface D/H (i.e., the midday rise), and when there is a flux from the atmosphere to the regolith, we see a decrease of the near-surface D/H (i.e., the morning and evening drop). In the evening when regolith-atmosphere exchange is weak, the near-surface D/H gradually returns to the diurnal average due to mixing in the atmosphere.

In all, the results indicate that the D/H variation traces the exchange flux. Measuring the diurnal variation of D/H in water on Mars's surface with sufficient precision will thus provide a new indicator for the regolith-atmosphere exchange of water.

References: [1] Flasar F. M. and Goody R. M. (1976) *Planet. Space Sci., 24,* 161–181. [2] Zent A. P. et al. (1993) *J. Geophys. Res., 98,* 3319–3337. [3] Savijärvi H. (1995) *Icarus, 117,* 120–127. [4] Webster C. R. et al. (2013) *Science, 341*, 260–263. [5] Villaneuva G. L. et al. (2015) *Science, 348*, 218–221. [6] Vandaele A. C. et al. (2019) *Nature, 568*, 521–525. [7] Mellon M. T. and Jakosky B. M. (1993) *J. Geophys. Res. Planets, 98*, 3345–3364. [8] Sutton J. L. et al. (1979) *J. Atmos. Sci., 35*, 2346–2355. [9] Moores J. E. et al. (2011), *Icarus, 211*, 1129–1149. [10] Lamb K. D. et al. (2017), *PNAS, 114*, 5612–5617. [11] Gómez-Elvira J. et al. (2012), *Space Sci. Rev., 170*, 583–640. [12] McConnochie T. H. et al. (2018), *Icarus, 307*, 294–326. [13] Savijärvi H. et al. (2019), *Icarus, 319*, 485–490. [14] Steele L. J. et al. (2017), *Icarus, 289*, 56–79. [15] Forget F. et al. (1999), *J. Geophys. Res., 104*, 24155–24175. [16] Smith M. D. et al. (2009), *J. Geophys. Res. Planets, 114*, E2.

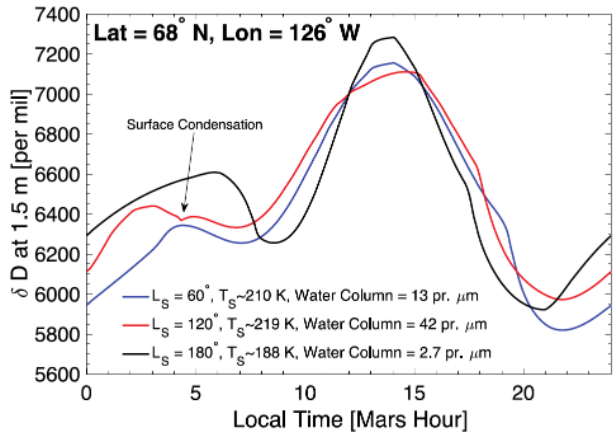

Fig. 1. Modeled diurnal variations of D/H in the province of the Phoenix landing site. The variation at the surface is up to ~1400‰ at the season of aphelion. The L_S=120° model has surface condensation that causes a small dip in the D/H curve.

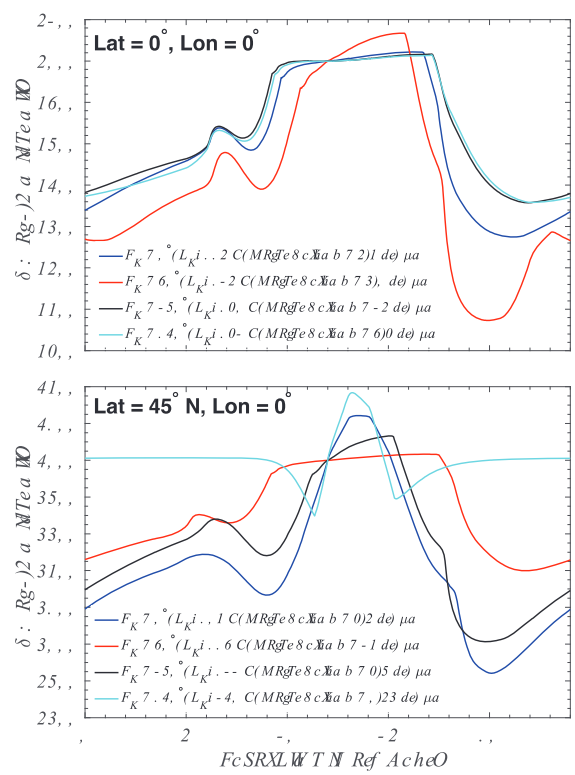

Fig. 2. Modeled diurnal D/H variations at the equatorial and mid-latitude locations of Mars. Labels show the mean surface temperature and the atmospheric water column, which we make to match with orbital remote sensing [16] by adjusting the initial water loading. The magnitude of the D/H variation is greater for a lower surface temperature, except when condensation occurs.

SURFACE PATTERNS OF TERRESTRIAL ICE SHEETS – FROM IN-SITU TO SPACE OBSERVATIONS. [illegible]

Introduction: [illegible]

Surface patterns and weather: [illegible]

[illegible]

Discussion: [illegible]

References: [illegible] *Icarus,* [illegible]

[illegible]

RDS N 1 ES P TU T1 N RMLOF UI D N 1 S UL1 O IAD-a 1 UDS T VTLOF 1 TDOTP S -: 1 TDC S P : P UIA 1 RRDOC1 F D J. C. Johnson[1,2,3], P. A. Johnson[1,3], and A. A. Mardon[2,3], [1]Faculty of Engineering, University of Alberta (email: jcj2@ualberta.ca), [2]Faculty of Medicine and Dentistry, University of Alberta (email: paj1@ualberta.ca) [3]Antarctic Institute of Canada (103, 11919-82 Str. NW, Edmonton, Alberta CANADA T5B 2W4; email: aamardon@yahoo.ca)

Intrnductinm While the martian regolith predominates its geography, the permafrost has been receiving growing attention with the speculation of an abundance of subsurface ice. Permafrost is ubiquitous across latitudes on Mars. Viking Mission data indicates the permafrost thicknesses range from 3.5 km at the equator to 8 km at the polar caps. Similar to terrestrial conditions, Ice-I comprises the predominant subsurface ice and is thought to be the predominant water source in permafrost.

Rresemce nf shrnuded oerl bfrnst ice-wbter. Spectroscopic data obtained from the Mariner Missions as well as the Viking Landers 1 and 2 [1], which has shown that the absorption spectra of the polar caps were not significantly different from the spectra observed for ordinary ice on earth, has been used to conjecture the presence of water-ice on Mars. In addition, Martian temperatures are cool enough to provide the necessary stability for the permanent presence of water-ice. The gas chromatograph/mass spectrometer data [1] further suggested the presence of water in the soil materials sampled from the Martian surface while the video evidence of the episodic appearance of frost and snow were captured. While a substantial proportion of water remains in an unfrozen state that is distributed throughout the pore space in terrestrial conditions, the proportion of ice to unfrozen water is likely higher due to its dependence on temperature and solute concentration. Considering the tight correlation between the search for water and the search for extraterrestrial life, the drilling, collection, and cultivation of permafrost microorganisms in Mars represents an interesting avenue of exploration.

N icrnnrgbnisl Tbl oking. While the survival of microorganisms over extended time periods may be curbed by ionizing radiation-induced damage to chromosomal DNA, studies completed in Siberian permafrost on microbial strains of *Psychrobacter cryohalolentis* and *Psychrobacter arcticus* have revealed that this may not be the case on Mars. The presence of perchlorates in the regolith, silicates in Martian dust, and heavy radiation make the discovery of organisms highly unlikely. Nevertheless, ancient permafrost could still represent a historical sink for micro-organic life. If so, sampling areas such as the cratered southern highlands between 60 and 80°S at about 180°W indicates an area considered to be the oldest, best preserved ice-rich permafrost on Mars.

N ndek fnr Rerl bfrnst Tbl oking Unnk While Smith and McKay (2005) have extensively described models for aseptic drilling, this is described with the outdated assumption that the organisms that may have once existed are dead by radiation. However, supposing that life still exists, we propose a novel way to detect signatures of life that have been developed for the regolith that could be extended to these areas.

A series of sensors have been used for microorganism detection. Coupled with traditional chemicals employed for the detection of signatures of life, Kasas *et al.* has designed sensors to detect the nano-vibrations created by the metabolic activities of microorganisms. While operations based on core drilling are essential noting the pure depth of theses caps, more precision-based excavation requires more controllable, maneuverable tools that incorporates such sensors. Here, we propose the development of a robotic arm that can integrate these sensors and be used in conjunction with the drill. This can enable excavators to tap into various other methodologies for sampling including borings, test pits, and natural exposure sampling.

The basic specifications for the robotic appendage would be similar to other remote manipulation systems such as the Canadarm. Specifications for the sensor terminus include 1) a cantilever array that contains several different sensors paired with corresponding linker molecules; 2) a suitable sample loading mechanism and preservation capsule; 3) matched physical properties of the cantilever (i.e. spring constants) to match the gravitational field of Mars.

S eferemces.

[1] Anderson D.M. (1985) Subsurface Ice and Permafrost on Mars. *Ices in the Solar System*. 156: 565-581
[2] Amato, P., Doyle, S.M, Battista, J.R. and Christner B.C. Implications of subzero metabolic activity on long-term microbial survival in terrestrial and extraterrestrial permafrost. (2010) *Astrobiology* 10(8): 789-98.
[3] H.D.Smith and C.P. McKay. (2005) Drilling in ancient permafrost on Mars for evidence of a second genesis of life. *Planetary and Space Science* 53(12): 1302-8. [4] Kasas, S., Ruggeri, F. S., Benadiba, C., Maillard, C., Stupar, P., Tournu, H., and Longo, G. (2015). De- tecting nanoscale vibrations as signature

of life. *Proceedings of the National Academy of Sciences of the United States of America*, 112(2), 378–381.

APPLICATION AND CONSIDERATIONS FOR NANOSCALE VIBRATION REMOTE SENSING TECHNOLOGY FOR DETECTION OF MICROORGANISMS IN THE MARTIAN POLAR REGIONS. P. A. Johnson[1,2], J. C. Johnson[1,2] and A. A. Mardon[2], [1]University of Alberta (email: paj1@ualberta.ca) [2]Antarctic Institute of Canada (103, 11919-82 Str. NW, Edmonton, Alberta CANADA T5B 2W4; email: aamardon@yahoo.ca)

Introduction: The possibility of life on Mars is a largely explored field of space research. A promising area of interest are the polar ice caps along with regions characterized by surface frost and water ice glaciers, particularly because the presence of water in itself, is known to be key to life, although there are several hypotheses suggesting the feasibility of extraterrestrial extant life with a source of energy and stable environmental conditions alone. We hereby describe a novel remote-sensing probe and design considerations for its use in Martian topography and climate conditions.

Remote sensing probe: Traditionally, remote-sensing techniques rely primarily on elemental composition analyses for identification of biomarkers that can discriminate the presence of microorganisms. One concern is that the use of Earth's signature of life criteria for Mars is limited. We have previously described the use of soil sampling with nano-scale vibration sensors for remote sensing and on-site detection of microorganisms [1]. This technology utilizes nano-vibrations created by the metabolic activities of microorganisms to detect the presence of life. It additionally allows for the combination of dynamic and chemical information to identify and characterize life. Moreover, its application extends from regolith and rocks to ice and permafrost, which means it has the potential to identify life in close proximities and within the polar regions of Mars.

Design considerations: With the geographical distinctions characterizing the polar ice caps and glaciers however, it is essential for us to make several modifications to the existing technology. First and foremost, the technology should be resistant to malfunction in colder temperatures. This can be achieved through the use of thermally protective material in design. Reinforced carbon-carbon, LI-900 silica ceramic coating, and insulation tiles are examples of materials which can be utilized for this thermal protection. Our group has also previously examined design considerations for motor units of space probes and unmanned aerial vehicles for use in Mars missions [2]. We would like to extend these considerations for remote-sensing probes as well. These considerations include: (i) power considerations, (ii) high climb and loiter speed, (iii) data-link bandwidth capabilities. (iv) navigation, (v) rotor use in Mars' gravitational field, and (vi) emergency considerations including loss of contact with ground control.

References: [1] Johnson J.C. *et al.* (2019) Soil sampling with nanoscale vibration sensors for on-site detection of microorganisms. *Mars Extant Life: What's Next?*. Abstract #5079 [2] Johnson J.C. *et al*. (2019) Design considerations to tailor unmanned aerial vehicles for martian geoclimatic condition. *American Research Journal of Humanities and Social Sciences*, 5(1), 1-2.

WATER ICE CLOUD FEEDBACKS OVER THE NORTH POLAR RESIDUAL CAP AT MODERATE OBLIQUITY. M. A. Kahre[1] (melinda.a.kahre@nasa.gov) and R. M. Haberle[1] (robert.m.haberle@nasa.gov), [1]NASA Ames Research Center, MS 245-3, Moffett Field, CA, 94035.

Introduction: Several global climate modeling studies have now shown that water ice clouds can warm the surface 10s of K at moderate obliquities [1,2,3]. Significant greenhouse warming occurs because the predicted clouds are optically thick, the cloud particles are large enough to efficiently interact with infrared radiation, and the clouds either form at or are transported to high altitudes where the atmosphere is cold. Radiative-dynamic feedbacks play a critical role in producing the conditions needed for a strong cloud greenhouse. Two feedbacks have been identified: one involves atmospheric warming by clouds aloft at lower latitudes. These clouds are generally associated with the global Hadley circulation. The second feedback involves clouds that form over the North Polar Residual Cap (NPRC) during summer. These clouds are more closely associated with the regional polar circulation. We focus here on the second of these feedbacks with the goal of understanding the details of the interactions between sublimation, cloud formation and transport in the north polar region. We show that these feedbacks strongly control the wetness of the atmosphere and the strength of the cloud greenhouse at moderate obliquity.

Methods: We use the NASA Ames Legacy Mars Global Climate Model [4], which is supported by the Agency's Mars Climate Modeling Center, to investigate radiative-dynamic feedbacks by water ice clouds in the north polar region at moderate obliquity. We present two simulations at 30° obliquity: one with radiatively active clouds and one with radiatively inert clouds. With the exception of modifying the obliquity, the version of the model used here is identical to that presented in [4]. We note that the dust forcing in both of these simulations is based on observations from MY 24 [5]. In these simulations, permanent ice reservoirs do not form outside of the north polar region, indicating that the North Polar Residual Cap (NPRC) is stable and the water cycle is closed.

Results and Discussion: As summarized in Table 1, clouds significantly impact the climate at 30° obliquity. While radiatively active clouds increase the planetary albedo over the case with inert clouds, they also increase the annual mean surface temperature by 15 K.

	A_p	T_e (K)	T_{se} (K)	T_e-T_{se} (K)	T_g (K)
Active	0.34	202	226	24	219
Inert	0.26	208	216	8	204
A-1	.08	-6	10	16	15

Table 1: Planetary Albedo (A_p), effective temperature at the top of the atmosphere (T_e), effective surface temperature, greenhouse power (T_e-T_{se}), and surface temperature (T_g) for the case with radiatively active clouds and the case with radiatively inert clouds.

During NH summer, the radiatively active cloud case produces clouds that grow thick, warm the surface, and enhance sublimation relative to the simulation with radiatively inert clouds (Figure 1). This occurs because clouds extend to high altitudes over the NPRC (Figure 2) and radiate to space at a cold temperature, forcing the surface to warm. The sublimation flux increases due to the warmer surface, which in turn increases the wetness and the cloudiness of the polar atmosphere. Feedbacks with the circulation in the polar region help transport vapor and clouds up high (not shown).

It is notable that the strongly positive feedback between cloud formation and sublimation results in a significantly wetter and cloudier atmosphere (Figure 3), which in turn drives a strong cloud greenhouse. The atmosphere nearly an order of magnitude wetter due to radiative-dynamic feedbacks associated with water ice clouds.

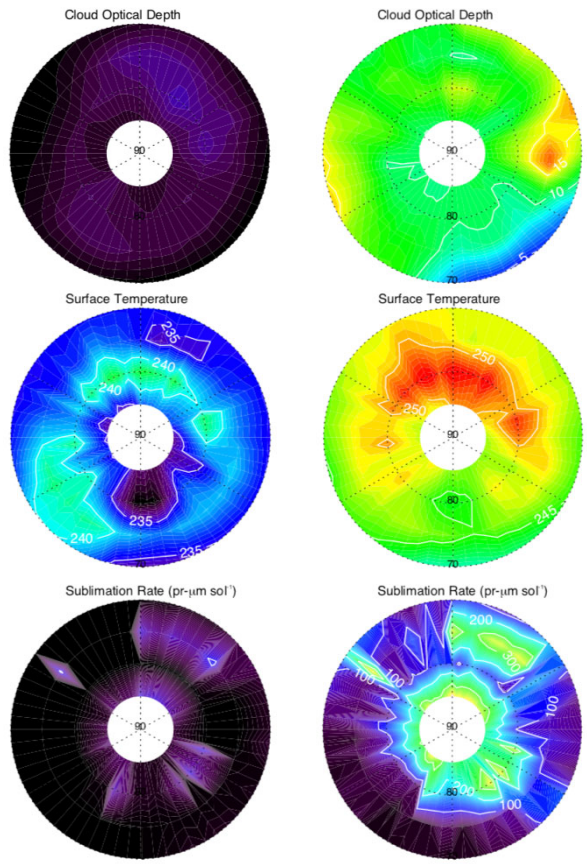

Figure 1: North polar 10-sol average cloud optical depths (top panels), surface temperatures (middle panels) and sublimation rates (bottom panels) at L_s 90 for the inert cloud case (left panels) and the radiatively active cloud case (right panels).

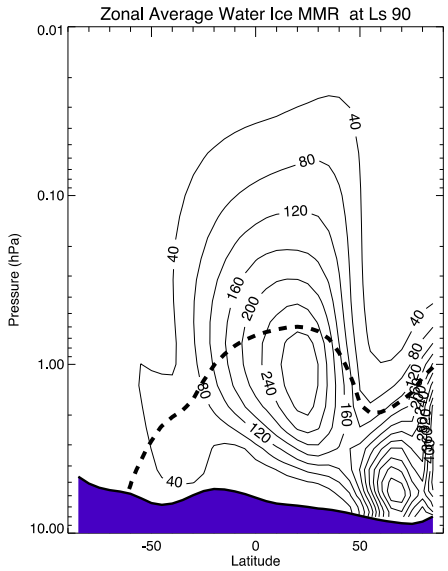

Figure 2: 10-sol zonal average water ice cloud mass mixing ratio (10^{-6} kg kg^{-1}) at L_s 90. The dashed line denotes where the cumulative top-down optical depth is unity.

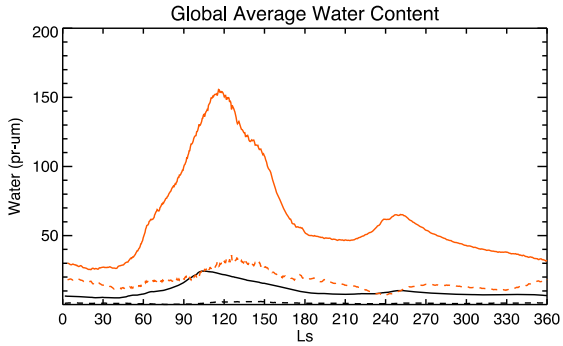

Figure 3: Global mean water vapor (solid lines) and water ice (dashed lines) for the case with radiatively active clouds (orange lines) and the case with radiatively inert clouds (black lines).

Summary and Conclusions: We have drawn attention to the clouds that form over the north residual cap during summer and their importance to the character of the water cycle. In our simulations they warm the surface and increase the water sublimation rates, which enhances the cloudiness over the cap and changes the circulation and the transport of water from the high latitudes. This strongly positive feedback significantly increases the cloudiness of the atmosphere and thus the effectiveness of the cloud greenhouse. A key aspect of this feedback is the ability of the polar circulation to transport moisture to high altitudes. A preliminary analysis of our model suggests that the regional polar circulation is complicated and that several of its components are involved. This highlights the importance of realistically simulating clouds over the NPRC, which has been challenging for modeling groups for current day Mars. Future modeling efforts will involve utilizing the NOAA/GFDL cubed-sphere dynamical core, which will allow for higher resolution simulations with a grid that does not have the converging meridian problem that all latitude/longitude grids exhibit. This should allow us to better diagnose the nature of the polar feedback and its ability to influence the global water cycle.

References: [1] Haberle R. M. et al. (2012) LPSC. [2] Kahre M. A. et al. (2018) COSPAR. [3] Madeleine J-B. et al., (2014) GRL, 41, 4873-4879. [4] Haberle R. M. et al. (2019) Icarus, 333, 130-164. [5] Montabone, L. et al. (2015) Icarus, 251, 65-95.

AN EXPERIMENTAL SETUP TO STUDY CO_2 ICE IN A SIMULATED MARTIAN ENVIRONMENT.

R. Karimova[1] and I. B. Smith[1,2], (rushana@yorku.ca) York University, 4700 Keele St, Toronto, ON M3J 1P3 Canada, [2]Planetary Science Institute, Denver, Colorado 80401.

Introduction: CO_2 constitutes the North and South Polar Seasonal ice caps [1] and the perennial South Polar Residual Cap (SPRC) [2]. Massive deposits of CO_2 ice were also found buried in the South Polar Layered Deposits using SHARAD data [3, 4]. CO_2 processes are closely related to major geomorphological features at extreme latitudes, such as pits, fingerprint terrain, jets, dunes, and polygonal throughs [5, 6, 7, 8]. There are numerous observations of the ice from remote sensing instruments; however, there is not sufficient data under laboratory conditions in order to unambiguously interpret the remotely-sensed data [9]. Better constraints of the CO_2 ice optical, mechanical, and crystalline properties under Martian conditions could help answer the questions regarding its role in the past and current climate, it's role in affecting the surface features we observe, and the ice's long-term unexpected stability in the SPRC.

We have created an experimental setup to investigate the formation, behavior and optical properties of CO_2 ice under such conditions at York University. We create CO_2 ice and record some variability of textures similar to ones reported by [9] and are further expanding our capabilities to conduct experiments under more precise pressure-temperature conditions, and time-scales for ice deposition more realistic for Mars.

Current experimental setup: The setup consists of a 50-liter cylindrical stainless-steel vacuum chamber, evacuated by a dual-stage rotary vane vacuum pump to pressures of on the order of magnitude of 1 torr. CO_2 gas is then introduced into the chamber, where an aluminum plate is simultaneously cooled by liquid nitrogen (LN2) flowing in copper tubing. The formation of the ice on the plate is recorded using a generic USB camera and a USB digital microscope under 50 to 100 times magnification.

We created CO_2 ice during 10 to 20-minute runs and observe surface and interior changes.

During the entire experiment, as ice deposits, the pressure within the chamber continues to decrease. Our setup is not yet sensitive enough to monitor the pressure closely, but this capability is being installed presently.

Preliminary results: During each run, a transparent, approximately five-millimeter-thick layer of CO_2 ice grew within 2-10 minutes (Fig. 1a). During growth, the ice rapidly fractured in polygonal patterns (Fig. 1b). The numerous fractures annealed within seconds, healing the ice to be transparent again, while more, new fractures continued to form each second (Fig. 2). The process of fracture, heal, fracture, heal takes <5 seconds and repeats numerous times in the experiment.

After reaching a steady state with no more slab ice growth, the surface accumulates very small grains that are highly reflective and not transparent (Fig. 1c). This ice has a different texture that appears more porous, with finer crystal size. In some instances, instead of this uniform frost layer, separate larger crystals form on the transparent ice. This texture was also reported by [9]. A thin non-transparent layer drapes over these crystals, within 15 to 20 seconds, while still preserving their distinct shape (Fig. 3).

Upon completion of the experiment, in some runs we see "bubbling" during venting the chamber before the sublimation of the ice. Another type of recorded activity was the formation of singular pits in the top frost layer, potentially, due to the escape of sublimated CO_2 gas from the bottom layer.

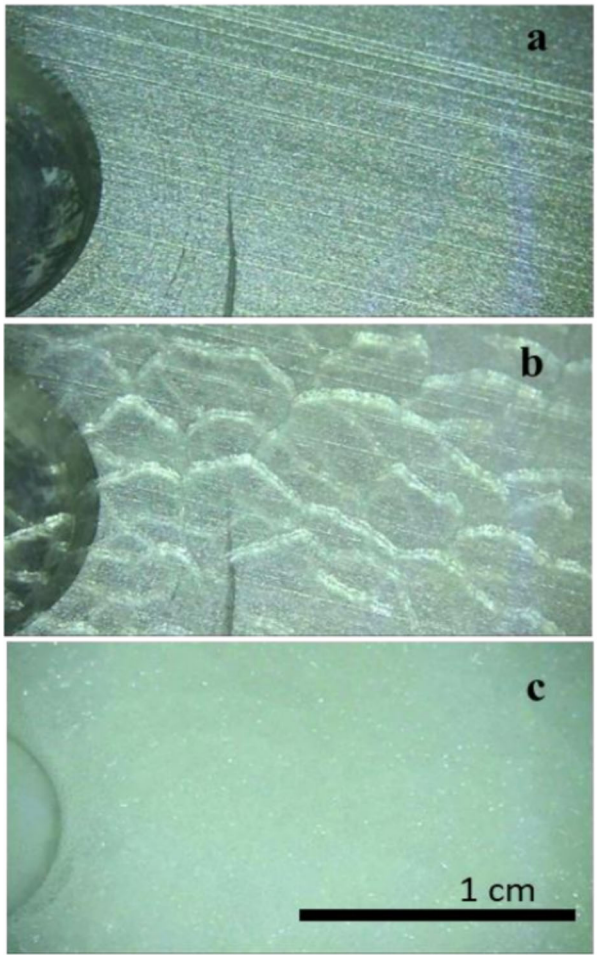

Figure 1 (a) Transparent CO_2 ice; (b) Fracturing of ice; time interval between photos is one second (c) fine non-transparent frost, image taken 108 seconds later.

Interpretation: The prominent fracturing during slab ice deposition is likely caused by strong thermal gradients between the cooled plate and the ambient atmosphere in the chamber, where temperatures are not yet modulated. CO_2 ice healing has been reported previously [9, 10], but the mechanism isn't fully understood.
The different textures of the created CO_2 ice are likely the result of different formation conditions. These texture variations occur as the CO_2 gas pressure drops with time and the temperature increases as the ice surface increases in distance from the plate.

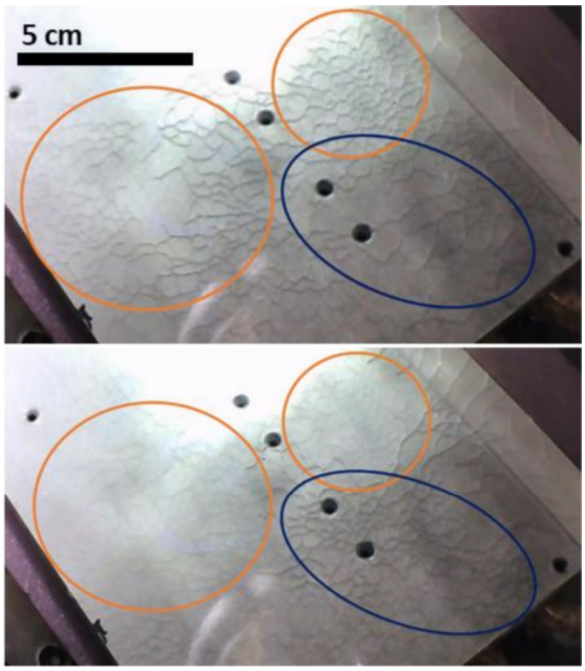

Figure 2 Annealing of fractures on transparent CO_2 ice. Orange: areas of healed fractures; blue: area of new fractures. Time interval between pictures is 2 seconds

Further steps: We continue to improve the setup to better approximate Martian conditions and monitor temperature and pressure. The improvements include more precise gas independent pressure measurement, automated CO_2 gas flow control for creating precise constant pressure, temperature regulation in the form of a cooling shroud and platen system to reduce temperature gradients by cooling the gas above the forming ice. These would allow a slow-rate ice accumulation at larger thicknesses. A further step is to incorporate UV and IR spectrometers to record the surface reflectance of the ice, since there are gaps in laboratory measurements of spectral characteristics of CO_2 ice [11]. One of our main goals is conducting a quantitative analysis of the behavior of the CO_2 ice under various insolation conditions, which could shed light on some current phenomena on Mars, such as the possible differences between visibly dark and bright CO_2 ice areas, as well as the relationship between the formation and persistence of the ice and its albedo.

Acknowledgements: We thank Adrianna van Brennen for her work in assembling the experimental system, which made this work possible.

References: [1] Leighton, R. B., & Murray, B. C. (1966). Science, 153(3732), 136-144. [2] Paige, D. A., and Ingersoll, A P. (1985). Science 228.4704: 1160-1168. [3] Phillips, R. J., et al. Science 332.6031 (2011): 838-841.[4] Bierson, C. J., et al. Geophysical Research Letters 43.9 (2016): 4172-4179. [5] Thomas, P. C. et al., (2000). Nature, 404(6774), 161. [6] Portyankina, G., Hansen, C. J., & Aye, K. M. (2017). Icarus, 282, 93-103. [7] Hansen, C. J., et al., (2015). Icarus, 251, 264-274. [8] Kieffer, H. H., (2007). JGR: Planets 112.E8. [9] Portyankina, G., et al. (2019) Icarus 322: 210-220. [10] Philippe, S., (2016). (thesis) [astro-ph.CO]. Université Grenoble Alpes. [11] Hendrix, A. R., D. L. Domingue, and K. S. Noll. The Science of Solar System Ices. Springer, New York, NY, 2013. 73-105

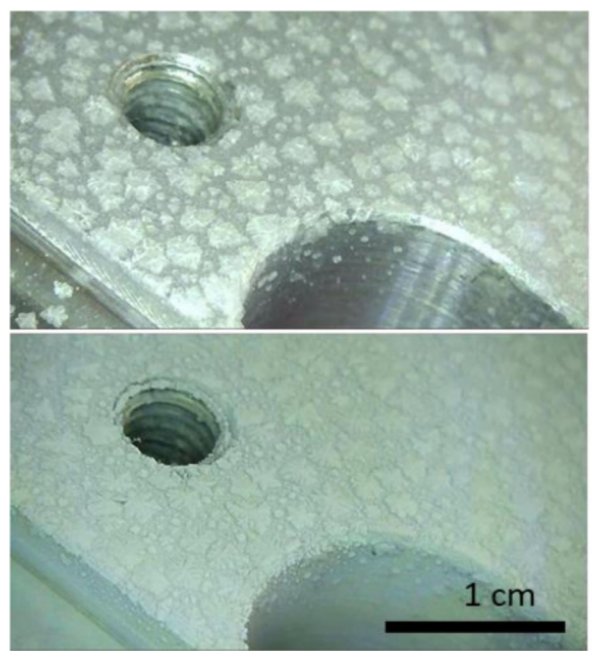

Figure 3 CO_2 ice crystals described by [9] form and then are covered by frost growth. Time interval: 22 seconds

INTERHEMISPHERIC DIFFERENCES IN CO_2 SUPERSATURATION AND CO_2 GAS DEPLETION IN MARS' POLAR WINTER ATMOSPHERE FROM MARS CLIMATE SOUNDER OBSERVATIONS.

A. Kleinböhl[1], D. M. Kass[1], S. Piqueux[1], P. O. Hayne[2], and K. Noguchi[3], [1]Jet Propulsion Laboratory, California Institute of Technology, Pasadena, CA, [2]Laboratory for Atmospheric and Space Physics, University of Colorado, Boulder, CO, [3]Nara Women's University, Nara, Japan. (Armin.Kleinboehl@jpl.nasa.gov)

Introduction: Temperatures in the martian lower atmosphere commonly reach the frost point of CO_2 in polar winter conditions [1,2]. Temperature retrievals using data from the Mars Climate Sounder (MCS) reveal that temperatures in the south winter polar region repeatedly drop several K below the frost point of CO_2. In contrast, temperatures in the north polar winter region tend to be very close to the CO_2 frost point. Temperatures below the CO_2 frost point indicate supersaturation of the atmosphere with respect ot CO_2. This can occur due to a lack of condensation nuclei, or due to condensation nuclei being very small, leading to large contact angles and low nucleation efficiencies [3]. Depressed temperatures in polar winter can be caused by the removal of CO_2 from the atmosphere through condensation, resulting in an atmosphere that is depleted in gaseous CO_2 and enhanced in non-condensables like N_2 and Ar. The reduced CO_2 mixing ratio reduces the condensation temperature and requires a colder atmospehre for a given degree of supersaturation. We evaluate differences in the temperature structure between the north and south polar winter atmospheres with respect to CO_2 supersaturation and CO_2 gas depletion.

MCS Instrument and Retrievals: The Mars Climate Sounder [6] is a passive infrared radiometer onboard Mars Reconnaissance Orbiter (MRO), which views the martian atmosphere in limb and on-planet geometries. It has five mid-infrared, three far infrared, and one broadband visible/near-infrared channels. Each spectral channel uses a linear detector array consisting of 21 elements, which provides -10 to 90 km altitude coverage with 5 km vertical sampling when pointed at the Mars limb.

Profile retrievals from MCS radiance measurements use a modified Chahine method together with a Curtis-Godson approximation in the radiative transfer [7] and employ a single-scattering approximation to account for scattering in the limb radiative transfer [8].

This study is enabled by retrievals with a 2D radiative transfer scheme for orbital limb emission measurements in the infrared [9], which describes horizontal gradients using consecutive limb measurements by MCS in the forward direction along the orbit track. The lines-of-sight of these limb views overlap significantly, allowing the characterization of horizontal gradients for a particular measurement through information from its neighboring measurements.

Retrievals of temperature use the MCS mid-infrared channels A1, A2, and A3 that cover frequencies within the 15 µm gaseous absorption band of CO_2. Aerosol extinction retrievals are based on limb measurements in channel A4, centered on a water ice absorption feature at 12 µm, and channel A5, covering an absorption feature of Mars dust around 22 µm. We note that channel A5 is also sensitive to CO_2 ice occurring in the lower atmosphere of the winter polar regions. Atmospheric CO_2 ice in these regions is characterized by large particle sizes, leading to an extinction spectrum that is comparatively flat over a large range of infrared wavelengths [10]. For this analysis dust spectroscopic parameters are used [8]. Comparisons indicate that the use of dust vs. CO_2 ice spectroscopic parameters has virtually no influence on the result of the temperature retrieval.

Results: Figure 1 shows examples of profile retrievals of temperature in the core of the southern polar vortex at L_s=130°-135°. Temperatures at pressures over ~20 Pa (below ~20 km altitude) are consistently below the CO_2 frost point calculated for a 95% mixing ratio of CO_2 (black dashed line). On average the temperature profiles in the lower atmosphere parallel the frost point with a separation of about 4 K.

Figure 2 shows the temperature development in the south polar region over the course of the winter. The temperature rapidly drops below the CO_2 frost point. Aerosol measurements suggest that CO_2 ice forms al-

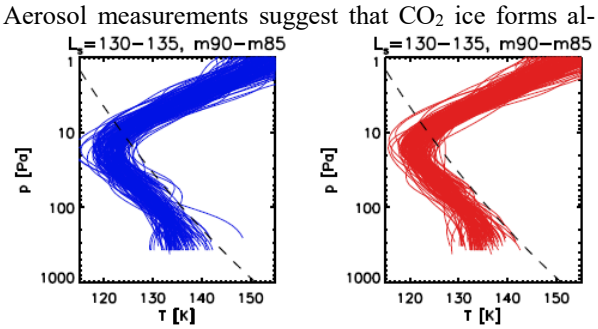

Figure 1: Retrieved temperature profiles from MCS observations in the south polar region on the nighttime (left) and daytime (right) parts of the MRO orbit between 90°S and 85°S in Mars Year 33. The dashed line indicates the CO_2 frost point.

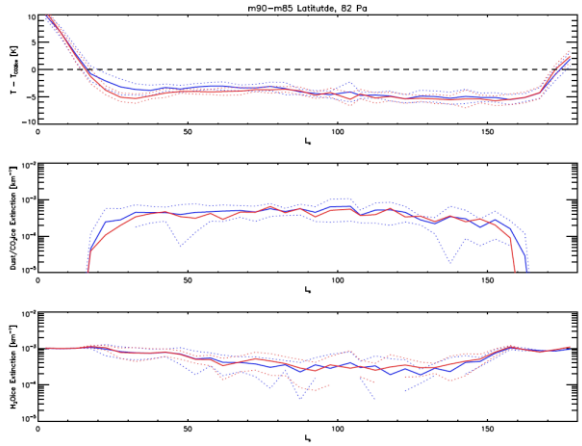

Figure 2: Averages of retrieved temperatures with respect the CO_2 frost point (top), carbon dioxide ice extinction (retrieved as dust extinction, center) and water ice extinction (bottom) vs. L_s from MCS measurements at a pressure level of 82 Pa (~12 km altitude) between 90°S and 85°S in Mars Year 33. Colors indicate measurements on the nightside (blue) and dayside (red) parts of the orbit.

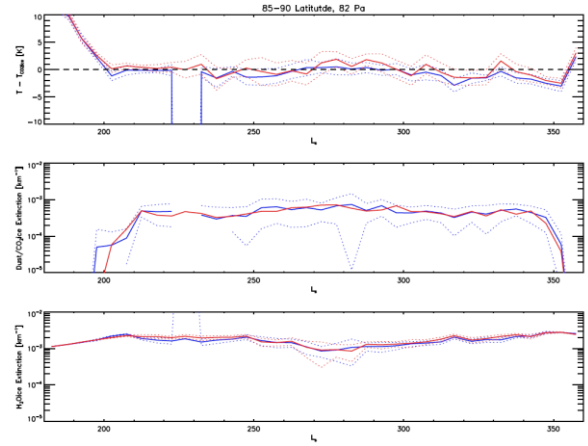

Figure 3: As in Figure 2 but between 85°N and 90°N in Mars Year 32.

most immediately at the beginning of the winter, likely aided by water ice as condensation nuclei, which is present at extinction levels around 10^{-3} km^{-1}. The temperature depression below the frost point is about 4 K at the beginning of the winter. It is unlikely that widespread depletion of CO_2 has taken place already at the beginning of the winter, suggesting that the temperature effect is caused by supersaturation. The observed temperature depression corresponds to a supersaturations in the order of 1.8. This is somewhat higher than suggested by model calculations and laboratory measurements [11,12] but in family with reanalyses of radio science temperature measurements [13].

Towards the end of the winter the temperature dips up to ~5 K below the frost point. After L_s=160° only little CO_2 ice opacity is observed anymore (Figure 2). We assume that part of this temperature depression is caused by the depletion of CO_2 gas due to CO_2 frost formation on the surface [14] and CO_2 ice formation in the atmosphere followed by sedimentation. It is unlikely that the temperature depression is solely caused by this effect as this would suggest unrealistically low CO_2 mixing ratios in comparison to previous measurements [4,5]. Assuming a supersaturation at the same levels as observed in the beginning of the winter, the observed additional temperature depression can be explained by CO_2 depletion corresponding to about a six-fold enhancement in N_2 and Ar, in family with the enhancement derived from γ-ray spectroscopy [4,5].

Figure 3 shows the same information as Figure 2 but for the north polar winter in Mars Year 33. In contrast to the south polar region, temperatures in the north stay very close to the CO_2 frost point, and only dip below by 1-2 K towards the end of the winter. This indicates that neither widespread supersaturation nor CO_2 depletion of significant magnitude were present, suggesting that the polar vortex in the north is less isolated than in the south. Water ice extinctions in the north polar region are with 2-3•10^{-3} km^{-1} somewhat higher than in the south. The higher availability of water ice particles as condensation nuclei likely contributes to the lack of supersaturation in the north polar region. In terms of CO_2 depletion, the observed behavior is consistent with results from γ-ray spectroscopy, which finds little enhancement of non-condensables at northern high latitudes [4,5].

Acknowledgments: We thank P. Patel for initial analyses on this topic. This work was performed at the Jet Propulsion Laboratory, California Institute of Technology, under contract with the National Aeronautics and Space Administration. © 2019, California Institute of Technology. Government sponsorship acknowledged.

References: [1] McCleese, D. J. et al. (2008) NGeo, 1, 745-749. [2] McCleese, D. J. et al. (2010) JGR, 115, E12016. [3] Wood, S. E., (1999), PhD thesis, UCLA. [4] Sprague, A. L. et al. (2004) Science, 306, 1364-1367. [5] Sprague, A. L. et al. (2012) JGR, 117, E04005. [6] McCleese, D. J. et al. (2007) JGR, 112, E05S06. [7] Kleinböhl, A. et al. (2009) JGR, 114, E10006. [8] Kleinböhl, A. et al. (2011) JQSRT, 112, 1568-1580. [9] Kleinböhl, A. et al. (2017) JQSRT, 187, 511-522. [10] Hayne, P. O. et al. (2012) JGR, 117, E08014. [11] Määttänen, A. et al. (2005) JGR, 110, E02002. [12] Glandorf, D. L. et al. (2002) Icarus, 160, 66–72. [13] Noguchi, K. et al. (2014) JGR, 119, 2510–2521. [14] Piqueux, S. et al. (2019) this conference.

□ □s □□□ □□□y □□□w□ □v □u□s □u□□u□□□□p □ □p□□u□□ut w□□□□t p□ p □p□□ p□p□□w

J.P. Knightly[1], J. Tullis[1], J. Dixon[1], V.F. Chevrier[1], [1]Space and Planetary Sciences, University of Arkansas, 1 University of Arkansas, Fayetteville, AR 72701, jknightl@uark.edu

□□□□□□□□□□□**h** Patterned ground and polygonal features identified across the Martian mid- to high-latitudes share similarities in surface and subsurface morphology to terrestrial patterned ground [1, 2, 3]. While subsurface water ice was detected by Phoenix, freeze-thaw processes as seen on Earth were not observed. It has been hypothesized that under a warmer environment during periods of high obliquity, freeze-thaw may be possible, which carries important implications regarding the nature of liquid water on Mars in the recent past [4, 5, 6]. Thermal contraction is thought to be possible under present Mars surface conditions, although there are few accessible terrestrial analogs [7].

Determining if patterned ground on Mars is presently active or relic will help to constrain the dominant formation mechanism. This can be accomplished in part by working with existing HiRISE data in conjunction with terrestrial photogrammetry of patterned ground, incorporating both active and relic sites without present-day active layers.

t □□□□□□□□□**h** Two field sites were selected to study the micromorphological characteristics of relic patterned ground: a previously characterized relic patterned ground site in the Uinta Mountains in Utah [8] and an uncharacterized patterned ground site located in the Westfjords of Iceland (Fig. 1).

The genesis of hummocky patterned ground in Utah is estimated to have occurred during the Last Glacial Maximum (LGM) [8]. The selected survey locations are in an alpine tundra on a 3720 m elevation plateau that was surrounded by valley glaciers but remained ice-free during the LGM. While alpine permafrost is predicted to exist in the Uinta Mountains today, none has been observed at the site.

Alpine patterned ground in the Westfjords consists of sorted circles and hummocky terrain at 600 m elevation. In-situ measurements revealed a similar temperature profile as observed in the Utah patterned ground (Table 1). As with the Utah site, patterned ground in the Westfjords is situated on a mountain plateau that would have been surrounded but not covered by valley glaciers during the LGM. The subarctic location, presence of nearby active patterned ground at elevations above 800-900 m [9], and the proximity of the site to the Drangajökull ice cap 60 km away suggests that the relative inactivity of the site is a more recent condition.

A DJI MavicPro unmanned aerial vehicle (UAV) was used to rapidly image each site at altitudes ranging from 7.6 to 85 m above ground surface along programmed transects. A series of 7 flights were conducted at different locations across the Uinta Mountains site and 14 flights were conducted across the Westfjords site. Flight locations were chosen to collect a representative sample of the types of patterned ground observed at each site.

Agisoft Metashape/PhotoScan was then used to generate orthoimagery and digital terrain models (DTM) that were imported into ESRI ArcGIS and used to further characterize the micromophology of each site. Results were compared to DTM's of the Phoenix landing site to make predictions regarding the present activity of Martian patterned ground.

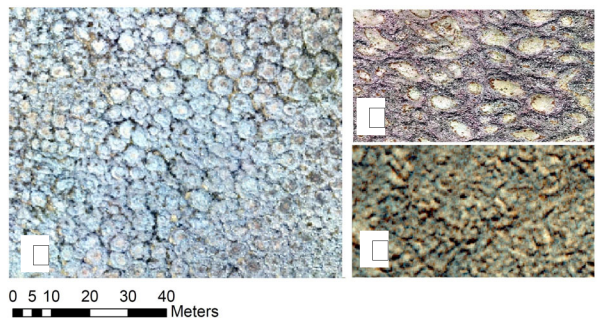

v □□□□ **T**: UAS-acquired orthoimagery of patterned ground in (a) Iceland, (b) Utah, and (c) HiRISE image of patterned ground at Phoenix landing site.

Patterned Ground Characteristics				
Site	**Depth to Water Ice (m)**	**0.5m Temp (°C)**	**Avg. Feature Area (m^2)**	**Sorting**
Westfjords, Iceland	NA	5.47	9.11	Well sorted
Uinta Mountains, Utah	NA	4.37	70.6	Poorly sorted
Devon Island, Canada	0.6[10]	1.25[10]	23.54	Well sorted
Phoenix Landing Site	0.05[3]	NA	50.67	Well sorted

NA = Not available or not applicable

□□□□□**Th** Selected characteristics of patterned ground in Iceland, Utah, and the Phoenix landing site. Characteristics of active patterned ground on Devon Island [10] for reference.

□□□□□□**h** The micromorphology of terrestrial and Martian patterned ground sites were compared by examining their average dimensions, slope, aspect, and surface roughness. Slope and aspect were derived using the respective spatial analyst tools in ArcGIS. Surface roughness was derived by calculating the standard deviation of height in the raster DTM for each site.

Selected physical characteristics are detailed in Table 1. The average slope of the Iceland and Utah sites

are similar at around 16 degrees and the Phoenix landing site has an average slope of 2 degrees. The aspect of all sites lies between 183-199 degrees (to the south-southwest), demonstrating a strong solar influence in patterned ground evolution among all possible modes of formation. Surface roughness is tabulated in Table 2 and visualized in Fig. 2. The surface roughness across all sites averages between 1.0×10^{-4} m and 2.0×10^{-4} m, with the Phoenix landing site trending closer to the roughness of the Utah site.

Surface Roughness				
Site	**Min**	**Max**	**Mean**	**Standard Deviation**
Iceland Sorted Circles	-0.827	0.825	0.000207	0.193
Utah Patterned Ground	-0.929	0.922	0.000133	0.139
Phoenix Landing Site	-0.814	1.000	0.000101	0.124

U Summary of surface roughness of height in meters between relic terrestrial patterned ground and the Phoenix landing site.

t h The work conducted through this scope is the first step in developing a litmus test that can determine patterned ground activity using morphological indicators derived from existing and future HiRISE imagery in tandem with higher resolution terrestrial data collected via UAV of previously understudied relic sites. The collection of very high resolution terrestrial datasets allows for the establishment of baseline metrics across the spectrum of patterned ground types. These terrestrial baselines can be compared to lower resolution HiRISE data by converting terrestrial data to spatial resolutions that better correlate with HiRISE products from which predictions can be made regarding Martian patterned ground.

The results suggest there are some similarities between terrestrial relic patterned ground and the Phoenix landing site, however a larger survey of sites is needed. In order for this litmus test to be the most effective, additional field work will be conducted at terrestrial field sites where permafrost and seasonal active layers are present. Although they are remote, sites where thermal contraction is possible are desirable in the long term.

p h Europlanet 2020 RI has received funding from the European Union's Horizon 2020 research and innovation program under grant agreement No 654208.

h [1] Lucchitta B.K. (1983) *Permafrost 4th Int. Conf. Proceedings, 744-749*. [2] Mangold N. (2005) *Icarus 174 336-359*. [3] Shaw A. et al (2009) *JGR 114, E00E05*. [4] Nakamura T. and Tajika E. (2003) *GRL 30 (13), 1685*. [5] Kreslavsky M.A. et al (2005) *PSS 56, 289-302*. [6] Soare R.J. et al (2014) Icarus 233, 214-228 [7] Levy J.S. et al (2008) *Antarctic Science 20 (6), 565-579*. [8] Munroe J. S. (2007) *Arctic, Antarctic, and Alpine Research 39 (4), 578-591*. [9] Etzelmüller B. et al (2007) *Permafrost and Periglacial Processes 18, 185-199*. [10] Knightly J.P. et al (2019) *LPS L*, Abstract #2181.

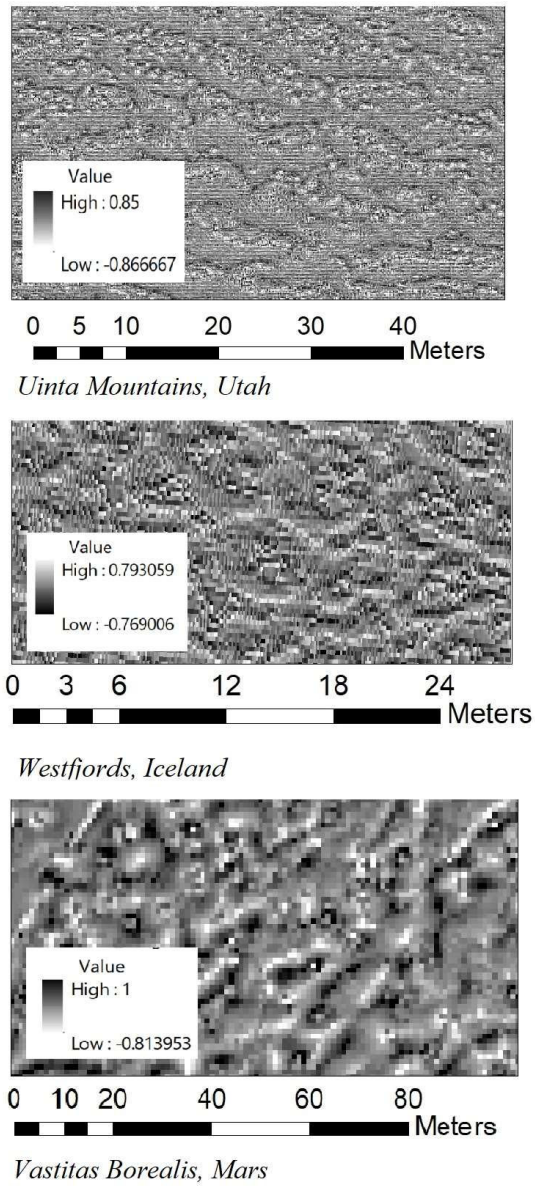

v U Surface roughness raster images of relic terrestrial patterned ground and the Phoenix landing site.

GCM SIMULATIONS OF THE MARTIAN WINTER POLAR ATMOSPHERE AND CO_2 SNOWFALLS: DEPENDENCE OF HORIZONTAL RESOLUTION AND RADIATIVE EFFECTS OF CO_2 ICE CLOUDS.

T. Kuroda[1], [1]Department of Geophysics, Tohoku University (6-3 Aramaki-aza-Aoba, Aoba, Sendai 980-8578 Japan, tkuroda@tohoku.ac.jp).

Introduction: In the winter polar atmosphere of Mars, the warming of upper atmosphere occurs due to the adiabatic heading enhanced by the Hadley cell [1,2]. With a solstitial global dust storm, the warming becomes even stronger [3]. Also, the seasonal CO_2 polar cap is formed by the CO_2 ice particles which are formed in the atmosphere and falls on the surface, as well as the CO_2 ice condensed directly on the surface. We have reproduced that the CO_2 snowfalls in northern winter polar atmosphere were strongly modulated by the cold phases of transient baroclinic waves, making the snowfalls rather periodic, and also that the accumulation of the snowfalls had spatial dependences using a Mars Global Climate Model (MGCM) [4]. In this presentation, further MGCM investigations about the properties of the winter polar atmosphere and CO_2 snowfalls on Mars, especially about the dependence of horizontal resolution and radiative effects of CO_2 ice clouds, will be shown.

Model description: The DRAMATIC (Dynamics, RAdiation, MAterial Transport and their mutual InteraCtions) MGCM used in this study has been developed on the dynamical core of CCSR/NIES/FRCGC MIROC with a spectral solver for the three-dimensional primitive equations [5]. For the application to Mars, radiative effects of gaseous CO_2 and airborne dust has been implemented as well as realistic surface parameters (topography, albedo, thermal inertia and roughness) [6].

A simple scheme representing the formation and sedimentation of CO_2 ice clouds has been implemented into the MGCM, in which we assume the particle size of CO_2 ice clouds to be ~50 μm near the surface [4]. The formed clouds can be transported also by advection. The definition of the spatial dust distribution is based on the MY26 dust scenario [7] and traditional assumption of vertical profile [8]. The non-LTE effect is not considered in the radiative effects of CO_2 molecules.

Three kinds of horizontal resolution are set for the MGCM simulation; T21 (or 5.6° × 5.6° grid interval), T63 (1.9° × 1.9°) and T106 (1.1° × 1.1°). The vertical grid consists of 53 σ-levels with the top of the model at ~90 km.

Sensitivity of the horizontal resolution: Figure 1 shows the 30-sols (L_s=270°-289°)-averaged zonal-mean temperature and CO_2 ice cloud mixing ratio for T21, T63 and T106 simulations. As seen, the polar warming becomes stronger with higher resolution, due to the enhancement of northward wind velocity by the resolved gravity waves in the model [9]. The distributions of the mean amount of CO_2 ice clouds differ between T21 and T63, while they are similar between T63 and T106, possibly due to the change of the mean structure of temperature. Note that the quantitative cloud amount in the upper atmosphere might not realistic because the model does not include a non-LTE parameterization of the cooling by CO_2 molecules, which should result in the overestimation of cooling.

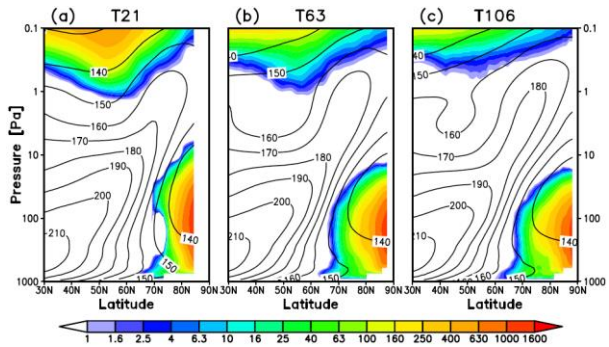

Figure 1: Latitude-altitude cross-sections of zonal-mean temperature (in K, contour) and mixing ratio of CO_2 ice clouds (in ppm of mass, shades) averaged in L_s=270°-289° (30 sols) for (a) T21, (b) T63 and (c) T106 simulations.

Figure 2 shows the north polar projections of mean CO_2 ice cloud mixing ratio at 50 Pa (~25 km altitude) and accumulation rate of surface CO_2 ice in winter (for the same period as in Figure 1). Signals of CO_2 ice clouds are seen only in the north of ~70°N, while the CO_2 ice accumulation is seen in the north of ~55°N, which shows that the formation of seasonal CO_2 ice cap in 55°-70°N is mostly due to the direct condensation on the surface. The amount of CO_2 ice clouds and surface CO_2 ice accumulation are larger in T21, in comparison with T63 and T106 simulations. In the polar atmosphere the kinetic and potential energy due to the harmonics of total wavenumber $21 \leq s \leq 60$, which are resolved in T63 but not resolved in T21, tend to dominate [10]. It is a possible reason for the discrepancy, and further investigations about the effects of those harmonics would be shown in the presentation.

In the T63 and T106 simulations, the distribution of mean CO_2 ice clouds at 50 Pa has the structure of

zonal wavenumber 1 with the peak of ~120°E (as indicated also in Fig.2a of [4]). The peak longitudes of the surface accumulation differ from that, possibly due to the vertical differences of peak temperature induced by stationary planetary waves (see also Fig.3 of [4]). The simulated structures in T63 and T106 are similar, but T106 reproduces also smaller features. In the presentation, results of the southern winter polar region and comparisons with those of the northern polar region (displayed here) will also be shown.

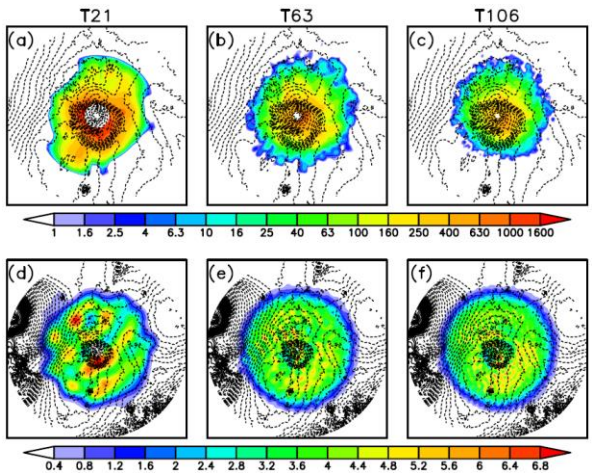

Figure 2: Polar projections (0° longitude at the bottom) of CO_2 ice distributions for the northern polar region averaged in L_s=270°-289° (30 sols). The left (a,d), center (b,e) and right (c,f) columns show the results of T21, T63 and T106 simulations, respectively. Shades represent (a-c) the mixing ratio of CO_2 ice clouds (in ppm of mass) and (d-f) the accumulation rate of surface CO_2 ice (in kg m^{-2} sol^{-1}). Dotted contours represent the topography. The edge latitudes of the plots are 60°N for (a-c) and 40°N for (d-f).

Sensitivity of the radiative effects of CO_2 ice clouds: Figure 3 shows the preliminary results of the longitude-altitude cross-sections of 3-sols-averaged temperature and CO_2 ice cloud mixing ratio at ~80°N and L_s~280° in T21, comparing between the results of radiatively-passive and active CO_2 ice clouds. The refractive index of CO_2 ice clouds is taken from [11] for the radiatively-active calculation. Note that only the infrared radiation should be effective because of the polar night.

As seen, with the radiatively-active clouds, the atmospheric temperature decreases in a few Kelvins, and correspondingly the cloud thickness becomes ~10 times larger than the radiatively-passive cloud case. Note that the results are still preliminary, so further investigations and updated results would be shown in the presentation.

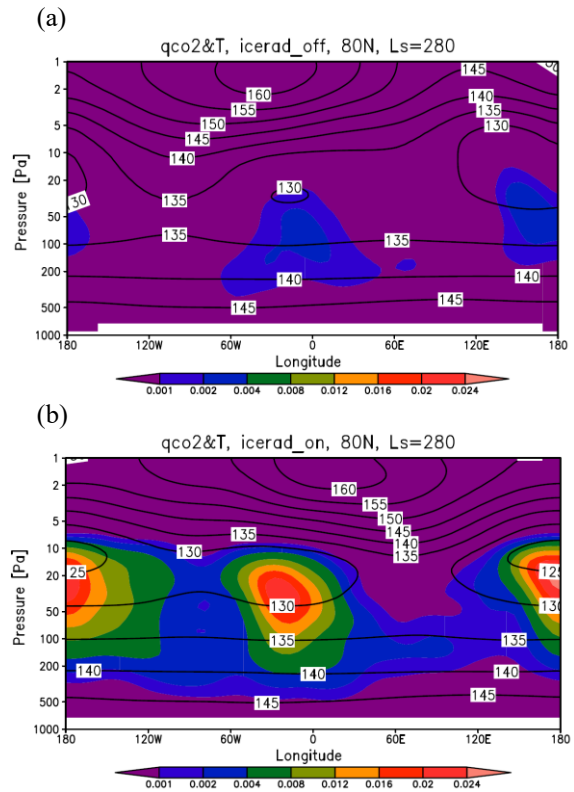

Figure 3: Longitude-altitude cross-sections of 3-sols-averaged temperature (in K, contour) and mass mixing ratio of CO_2 ice clouds (shades) at ~80°N and L_s~280° with T21 horizontal resolution, for (a) radiatively-passive and (b) radiatively-active CO_2 ice clouds.

References: [1] Heavens, N.G. et al. (2011) *JGR, 116,* E01010. [2] Medvedev, A.S. and Hartogh, P. (2007) *Icarus, 186,* 97–110. [3] Kuroda, T. et al. (2009) *J. Meteor. Soc. Japan, 87,* 913–921. [4] Kuroda, T. et al. (2013) *GRL, 40,* 1484–1488. [5] K-1 Model Developers (2004) *K-1 Tech. Rep., Univ. of Tokyo, 1,* 1–34. [6] Kuroda T. et al. (2005) *J. Meteor. Soc. Japan, 83,* 1–19. [7] Montabone, L. et al. (2015) *Icarus, 251,* 65–95. [8] Conrath, B.J. (1975) *Icarus, 24,* 36–46. [9] Kuroda, T. et al. (2015) *GRL, 42,* 9213–9222. [10] Kuroda, T. et al. (2016) *JAS, 73,* 4895–4909. [11] Warren, S.G. (1986) *Appl. Opt., 25,* 2650–2674.

Advances In The Use Of Radar Reflectivity As A Climate Proxy In The North Polar Layered Deposits.

D. Lalich[1], M. Raguso[2], V. Poggiali[1], and A. Hayes[1], [1]Cornell Center for Astrophysics and Planetary Science, dlalich@astro.cornell.edu [2]California Institute of Technology

Introduction: The North Polar Layered Deposits (NPLD) are a formation of nearly pure water ice layers [1] up to 2 km thick and 1000 km across roughly centered on the north pole of Mars, in the Planum Boreum region. Although their precise age is unknown, it is likely no more than four million years old based on orbitally forced climate models [2, 3]. In addition to layering visible in outcrop imagery, the Shallow Radar (SHARAD) instrument on the Mars Reconnaissance Orbiter (MRO) has detected many subparallel reflectors within the NPLD [4]. Reflectors are organized into four groups or "packets," separated by reflection-free zones. The exact source of these reflectors is a matter of debate, but they are generally thought to result from variations in dust content with depth [4, 5]. Previous work linked layers and reflectors to orbitally-forced insolation cycles, implying that reflectors could act as a climate proxy for late Amazonian Mars [6, 7, 8, 9].

One hypothesis for the source of radar reflectors is that they are caused by the so-called "marker beds" identified in outcrop stratigraphy [8, 10]. Marker beds are thin layers characterized primarily by their relative resistance to erosion, which implies that they have a different composition than the surrounding ice. Previous research has failed to conclusively link specific marker beds to radar reflectors, but has shown that some genetic link is likely [10].

By assuming SHARAD reflectors are caused by an enhancement in dust content within marker bed layers, Lalich et al. [11] were able to use reflectivity measurements to place constraints on layer composition. However, they were forced to make a number of simplifying assumptions and limited their analysis to ten small study sites around the NPLD. In this work we seek to extend that analysis through a combination of more extensive reflector mapping, the consideration of other types of reflector-causing stratigraphy, and the application of recently developed SHARAD processing techniques.

Data and Study Area: Radar data were acquired using the SHARAD instrument on MRO. SHARAD is an orbital radar sounder that uses an 85 μs chirped pulse centered at 20 MHz with a 10 MHz bandwidth. SHARAD has a cross-track resolution of 3-6 km and an along-track resolution of 0.3-1 km achieved using synthetic aperture processing [12]. It has a nominal range resolution of 8.4 meters in water ice.

In addition to standard radargrams, we also make use of data produced using a processing technique known as "super resolution," which has recently been adapted for SHARAD [13]. Combined with targeted interference suppression, we are able to enhance the range resolution of SHARAD by a factor of three, and increase the signal-to-noise ratio by ~3 dB [13]. Previously, uncertainty in subsurface layer thickness hindered efforts to use SHARAD reflectivity as a proxy for ice composition [11], and analysis of "split chirp" radargrams suggested that what appeared as single reflectors in SHARAD data might instead be the result of multiple thin layers [14]. Using super resolution radargrams, we can place tighter constraints on layer thickness and more accurately discriminate between individual reflectors, dramatically increasing our ability to interpret reflectivity measurements.

For this work we have selected the "saddle region" of the NPLD as our study area. The region's flat topography virtually eliminates lateral clutter which can sometimes make SHARAD radargrams difficult to interpret. Our selection also facilitates comparisons to previous studies, which also focused on the saddle region [11, 15]. Unlike those previous studies, we aim to extend our analysis beyond the top packet of reflectors (~500 m depth) and therefore explore a longer period of time.

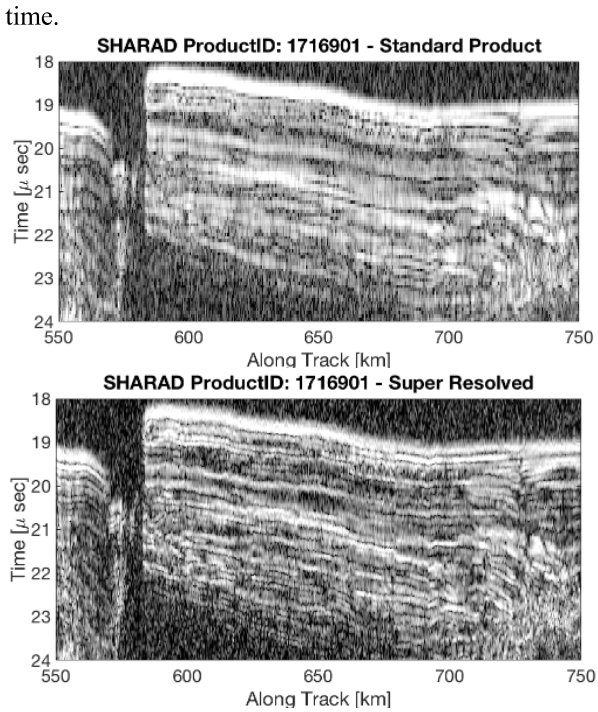

Figure 1: Top: Standard SHARAD radargram over the saddle region. **Bottom:** Same observation with super resolution processing.

Measuring SHARAD Reflectivity: Reflectivity for each mapped reflector is measured using a modified version of the method from Lauro et al. [16]. Assuming equal surface and subsurface roughness and negligible slope, reflectivity can be calculated using the ratio of the power reflected by a subsurface reflector (P_{ss}) to the power reflected at the surface (P_s):

$$R_{ss} = \frac{P_{ss}}{P_s}\frac{R_s e^{2\delta kz}}{(1-R_s)^2} \quad (1)$$

Where R_s is the surface reflectivity, δ is the loss tangent, k is the wavenumber, and z is the depth to the subsurface reflector. In keeping with previous work [11], surface reflectivity is not assumed to be constant over the mapped area. Instead, we will use a previously generated map of SHARAD surface reflectivity to determine the local surface reflectivity at each radargram trace [17]. For δ we adopt the bulk value calculated by Grima et al. [1].

Using Reflectivity to Constrain Composition: To first order, the radar reflectivity of a material is dependent on its permittivity. In practice, however, SHARAD is not able to resolve individual layer interfaces, and thus observed reflectivity is also dependent on layer thickness and/or the total number of layers responsible for a single resolvable reflector. In order to use SHARAD to estimate layer composition, Lalich et al. [11] assumed that reflectors were caused by single marker beds, modeled reflectivity as a function of marker bed thickness and dust content, and then compared measured reflectivities to their model. We will follow the same basic procedure for this study. However, while there is some evidence linking marker beds and SHARAD reflectors, it is still possible that at least some reflectors are caused by multiple layers too thin to resolve even using super resolution processing [14].

To account for this, we will use a new model for estimating subsurface reflectivity (and thus composition) that allows for multi-layer scenarios [18]. While it would normally be unrealistic to consider every possible permutation of reflector-causing layer sets, the super resolution data discussed earlier will allow us to limit the likely scenarios to a manageable number.

Future Work: While the saddle region makes for an ideal first study area, reflectivity can vary substantially over the NPLD [11, 15]. In the future, expanded radar mapping could help disentangle the effects of local and mesoscale climate conditions from the global signal present in the polar cap. Layered ice deposits are also present outside the PLD themselves, notably in Korolev crater. Similar reflectivity analyses of these deposits could reveal much about the Martian polar and global climate systems.

Integrating radar and visible stratigraphy could also enhance scientific returns from each dataset. Previous efforts to match reflectors with specific outcrop layers were unsuccessful [10], but it is possible that a similar effort may yield better results with the advent of super resolution processing.

References: [1] Grima, C. et al. *GRL 36,* (2009). [2] Levrard, B. et al. *JGR: Planets 112,* (2007). [3] Greve, R., & Mahajan, R.A., *Icarus 174,* (2005). [4] Phillips, R. J. et al. *Science 320,* (2008). [5] Byrne, S. *Annual Review of Earth and Planetary Sciences 37* (2009). [6] Cutts, J. A. & Lewis, B. H., *Icarus 50*, (1982). [7] Toon, O.B. et al., *Icarus 44*, (1980). [8] Hvidberg, C. S. et al., *Icarus 221*, (2012). [9] Becerra, P. et al. *GRL 44,* (2017). [10] Christian, S. et al., *Icarus 226*, (2013). [11] Lalich, D.E. et al. *JGR: Planets 124* [12] Seu, R. et al. *JGR: Planets 112* (2007). (2019). [13] Raguso, M.C. et al. *IEEE 5th Workshop on Metrology for Aerospace* (2018) [14] Campbell, B.A. & Morgan, G.A. *GRL 45* (2018) [15] Lalich, D. & Holt, J.W. *GRL 44* (2016). [16] Lauro, S.E. et al., *Icarus 219*, (2012). [17] Grima, C. et al. *Icarus 220,* (2012). [18] Born and Wolf *Principles of Optics* (1980).

SOUTH POLAR LAYERED DEPOSITS NEAR-SURFACE PROPERTIES INFERRED FROM A DATED IMPACT CRATER. *= #5 # <JWWR&! 1 #B# = L5 ` NW! 9#: # 4 J^KJ[(! @#? # 8 JbWV&! B# 2 b[WV! 3 #= # 4 ^WWJ\) ! B#B# B^]JXW! 1 # 2 [R]XW! ; #5 # 8 NTNVQXOO' #&<JKXJ]X]b OX] 1]VX\YQYRL JWWBYJLN@Qb\RL\! DWR_N\R]b XO3 XUX]JMK! 2 X^UWN! 3 ? VJ[PJ[N#LJWWR 0 U\Y#LXUX]JMK#NM^ ! ' <^WW[JWW@LJWYJ[b <JKX]J]X]b! DWR_N\R]b XO1 [RXWW! C^L" \XW! 1 G! (:N @LXY^UBXW<JKX]J]X]b! 3 JUOX]WB 9W]R]^]N XO CNLQWXUXPb! @J\JMNW! 3 1 !) 1 \]]XPNXUXPb BLRNWLN 3 NWN! DB7 B! 6 UP\]JOO 1 G! *: XQWXWBYJLN3 NWN! 8 X^\]XW! CF #*

Introduction: *= J[\f @XU[<JbNM 4 NYX\R\ @<4 \ LXW]JRW]JW]JUR RWP LU^N]X MNLRVQYRWP = J[\f LURV J]N QR]X]b#@]N_BX^\ \]^MRN QJ_N MNNL]NM[NL^[" [RWP YJ]]NYW RW]QN JU]NYW]RWP UbN\ XORLN JWWMN\] HNP#! & ' I JWWM V JMN N]RV J]N XO]QN JLL^V ^U]BXW [J]N [NZ^R]NM]X [NYURL]N]QNV HNP#! (!) I# ? [KR]JU MJ]J QXV \N_NJU= J[\ bNJ[\ QJ_N V JMN \RPWROLJW Y[XP[N\ RWLXW]]JRWRWP]QN RWYN"JWW^JU_J[B]BXW RW]QN \N]\XWU3 ? , RLN JWWMX]QYN TNb LXW]XU XW]QN VJ\\ KJUWLN XO]QN @<4 \ HNP#! *I# 6[XV]QYVJU VXMNRWP JWWMVJ[]BWXKUZ^Rb VXMNU! R] JYYNJ[\ ^WRNUb]QJ]]QN L^[[NW > X]Q @<4 >@<4 LX^UM QJ_N\^[_RNMKNbXWM* = b[KNOX]N]QNY[N\NW H-"- I!]QX^PQ L]J]N JPN N]RVJ]N OX]]QN BX^]Q @<4 B@<4 \^[OJLNJ[N//* = b[H-"&&#*

= ^UBXUN URWN XO N_BNNLN RWRLJ]N]QN B@<4 OX]VNMRWU[PNMNX\R]BXWUN_NW\ ` R]Q UXWP NX\BXW" JUQB]^\N# CQN N RWLU^MN \]]J]RP[JYQRL [NU]BXWQR\ QXV PNXUXPRL VJYYRWP H&' I JWWM \LJ[Y Y[X]/^\BXW JWUb\R H&( I! JWWM]QN QRPQN K^UT M^\] LXW]NW ]QJW ]QN>@<4 ! J\ RWON[NMQXV P[J_Rb H&) I# 3 QJ[JL]NR:" RWP ]QN ^YYN VN]N\ XO]QN B@<4 ` RUQNUY MN]NVRWN]QN MNY]Q JWWMLXV YX\R]BXW XO]QN B@<4 \^KURV J]BXW UP! JWWM]QNNOX[N]QN UNWP]Q XO]QN B@<4 f\ L^[[NW JLL^V ^U]BXWQB]^\ JWWM\^YYX]]]QNX]MN\ XOV JPWR']^MNXUMN \^[OJLNJPN]QJW]QN>@<4 #

E N[NYX]] RWON[NMB@<4 \^[OJLNY[XYN]]RN QXV JWXK\N_NMWN RVYJLJ L]J]N! d& V RWMBVN]N! MN]NL]NMKN` NNW 3 XW]Na] 3 JVN]J 3 CF XK\N_J"]BXW JLZ^R]NMRV:^Ub JWWBN]NVKN ' %& J] d- &#*e B!) & 5 # E NRWON J VRWV^V d(V MNNY K^[BXM\^K" URV J]BXWUP MNYX\R]J]]QR UXLJ]BXW#

SPLD impact crater features: *E QRUN]QN MN]NL"]BXW XO M]NM NHP#! J KNOX]N JWWMJQN RVYJLJ RVJPN \^JUb QXV 3 CF! LXW]]JRWRWP]QN OX]VJ]BXW]RVN RVYJLJ N_NW\ QJ\ KNNWLXV V XWRV]QN M^\]b [NPBXW XO= J[\ H&*! &+I!]QR R]QNO]\] MKL^V NW]NMMN]NL]BXW XOJ WN ! M]NMRVYJLJ XW]QN B@<4 # CQR d& V RV" YJLJ ` J\ RVJPNMKb 8 BA9B5 RW? LJXKN ' %& 6RP^]N & JQN MN]NL]BXWKb 3 CF RWBN]NVKN#*

CQN OR\] 8 BA9B5 XK\N_J]BXW XO]QN LJ]N XL" L^[[NM QRUN3 ? , QX\] ` J\ \]RUY[N NW 6RP^]N &! UNQ YJWNU# <RPQN YJ]LQN LJWKN\NNWJMBLNW]X M]T NSNLJJ ` QRLQ LX^UM KN LJ^\NM Kb NSNLJJ VJ]N]BU \LX^[RWP]QN\^[OJLN# ? _NJUW]QN LJ]N NSNLJJ [N\NV" KUN]QJ] XORVYJLJ RWX RLN'QNN]J[PN\ RW]QNNZ^J]X" [BU[NPBXW XO= J[\ H&+"&-I#*

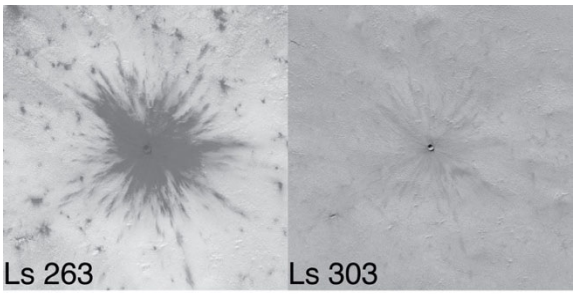

Figure 1. The ~18m diameter new impact crater in two HiRISE images (ESP_057152_0985 & ESP_057970_0985), one with (left) and without (right) seasonal frost coverage.

CQN @<4 \ J[NRLN]RLQ' JWWMJ] J]NVYN]J]^[N` QN ]QN NONL]R_N bRNUM\]]NWP]Q V Jb LJ^\N\b\]NVJ]RLJUb U[PN MBVN]N L]J]N\ LXVYJ[NM]X RVYJLJ\ RWX XWb URQRL VJ]NBUHNP#! & I# CQN d& V MBVN]N XO]QR L]J]N R ` RQRW]JWPNXO]QN MBVN]N\ XORLN'NaYX\RWP VRMU]R]^MN L]J]N\ d' ") V RWWR_RMJUL]J]N\ H&, I JWWMWN ! M]NMLJ]N\ d' "() V H&- I# E QRUN]QN NR XWb XWN L^[[NW NaJVYUN]QN M]NM B@<4 RVYJLJ MBVN]N R WX] \RPWROLJWb U[PN]QJW X]QN\ RWX URQRL]J[PN\ JWWMKN bN RWLJ]N]QJ]]QN B@<4]J[" PN\]]NWP]Q_J[RN M]JVJ]RLJUb QXV]QNVRMU]R]^MN [NPBXW XO= J[\#

CQN NUN_J]BXWY[XORUN QXV J 8 BA9B5 MPRLJU]N" [JRWVXMNU 4 C= 6RP^[N' \QX` ]QJ] ]QR L]J]N QJ\ J \RVYUN KX` U\QJYN JWWMULT\ ]XYXP[JYQRL ONJ]^[N \^PPN]R_N XO JW NONL]R_N \]]NWP]Q MRONNWLN RV]QN ^YYN ON VN]N\ XO]QN\^[OJLN HNP#! ' %# CQN L]J]N QJ\ J MNY]Q]X'MBVN]N [J]BX MB4 XOd%&&*'%&&-# CQN VNJW MB4 XO M]NM RVYJLJ\ JUUY[RVJ]b L]J]N\ X] Y[RVJ]b L]J]N LU^\]N\ RWX URQRL]J[PN\ R d%# (! ` RQ J U[PN[JWPN H&-I# 4 J^KJ[ N JU# H&-I LJUL^U]NM ]QN VJaRV^V MB4 [J]BX OX] J YJ[JKXUL L]J]N ` RQ ` JUU J] J MbWJVRL JWPUNXO[NYX\NXOd(*e ` X^UMKN d%&, *# CQN WN B@<4 RVYJLJ MB4 [J]BX JWWMRW]NBX] VX]YQXUXPb J[N LXWR]NW ` RQ J Y[RVJ]b RVYJLJ L]J]N RWX\RWPUNNONL]R_N\]]NWP]Q]J[PN#*

Persistent dark ejecta and implications for grain size: *5_NWJQN]QN\^[[X^WWRWP]N[JRWQJM MNQX\]NM 6RP^]N &!]QN RWWY! LXW]RWX^\ NSNLJJ XO]QR L]J]N [NVJRWNM M]T LXVYJ[NM]X]QN MNQX\]NM B@<4 \^[OJLN# CQR LX^UMKN LJ^\NMKb J P[JRW\R:N MRONNWLN KN` NNW]QN NSNLJJ KUWN]N JWWM]QN\^[" [X^WWRWP]N[JRW# E QRUN X]QN OJLJX\ URN\^[OJLN*

[X^PQWV\ X[LXV YJL]RXWLX^UMLXW[RK^]N]X]QR! QYN ` NY[RV J[RU NaYUX[NP[JRV\ R:NJ\ J LJ^\N#

*9WX[MY[ ]X N]RV J]N]QN P[JRV\ R:N MRONYNVLN KN']` NNVNSNLJJ JWM\ ^[[X^WRWP\! ` N QR\ ] LJUL^UJ]NMJW J_YJPN 9%6 _JU^N QXV]QN 8 RA9B5 RV JPN RV[NY[N' \NVJ]R_N\ NLJRXW XO]QN MJ[T NSNLJJ JWM\ ^[[X^WRWP! ^WONLJNM B@<4 \^[OLN 6RP^[N (# CX RVYNY[N]QN N9%6 [N^U\ RV]NYV\ XOP[JRV\ R:N ` N^\NMJ [JMR' J]R_N ][JWON VXMNUQXV H&! XY]RLJULXW]JW\ OX[ = J[\ M^\] QXV H' I JWM= RV\ LJ]]NYRWP ]QNXb# E N J\\^VN ]QN YJ[]RLUN\ R:N'MR][RK^]RXWOXUX` \ J VXMR' ORMPJVV J MR][RK^]RXWH(I#CQN VXMNU9%6 _\#VXMN [JMR\ R YUX]NMRV6RP^[N(# 9WX[MY[ ]X [NYURLJ]N]QN MRONYNVLN RV VN]\^[NM9%6!]QN NSNLJJ ` X^UMQJ_N]X LXW]JRV\ URPQ]Ub U[P]Y MV\] YJ[]RLUN ]QJW ]QN \^[" [X^WRWP MNQX]NMB@<4 \^[OLN# CQR \^PPN]\ ]QJ] U[P]Y'P[JRWNMM\] ` J\ Y[NON]NY]RJUb Y[N]N_NM YX\" \RKUb J\ \VJUN]Y YJ[]RLUN ` YN[NVX_NMKb ` RWM#

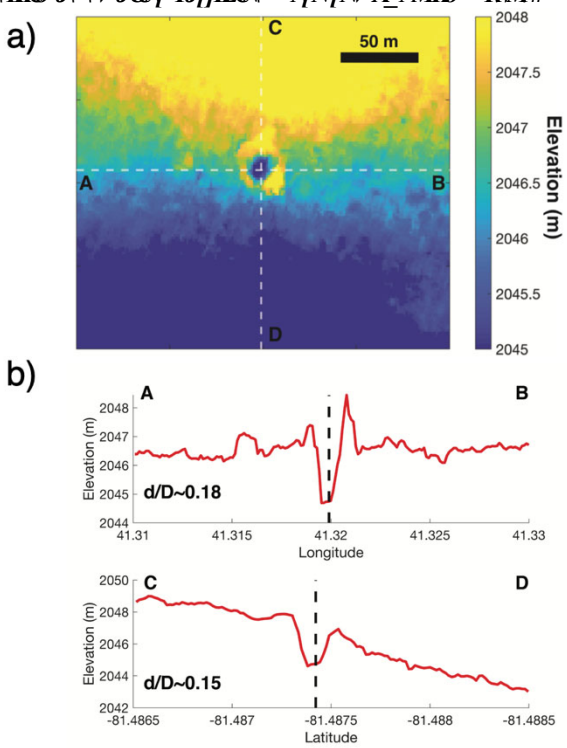

Figure 2. a) The HiRISE DTM (north is up) and b) depth profiles showing the calculated depth/diameter ratio for the new, dated SPLD impact.

Could there have been water ice in the ejecta blanket?: *E N TWX` ]QJ] ]QN K^UT @<4 J]N ]RLQ RV ` J]N RLN]QN RLN \]JKRUb VXMNU RWRLJ]N R_\QX^UM KN Y[N]NY]J]\QJUX` MNY]Q WN]] ]QN YXUN HNP#! ') I# CQX^PQ N]]Ub \^VVN LXUX] RV JPN \QX` J \VJUU KU^N J]N]!]QR L]J]N MKN WX] QJ_N J K]RPQ NSNLJJ KUJWN UR]N]QX\NJ] VRMU]R_^MN HR, I# E N N]RV J]NM]QN ` J]N \^KURV J]RXW[J]N]X MN]NVRWNROJ ` J]N RLN NSNLJJ UbN LX^UM QJ_N \^KURV J]NM KN` NNW L]J]N OX]V J]RXWJWMRV JPRWP Kb 3 CF VJa#d' VXW]Q JWM 8 RA9B5 VJa#d( VXW]Q #4 ^[RWP ]QR ]RV N 3 ? ' QX\] ` J\ Y[N]NY JWM URNUb ORaNM]QN\^[OLN]NV YN]J]^[N J] d&*%; #1 VJaRV ^V XOd*%!- %µV V" XO` J]N RLN LX^UM QJ_N\^KURV J]NM KNOX[N]QN L]J]N ` J\ RV JPNM Kb 3 CF JWM 8 RA9B5 # CQN]NOX[N! \^KURV J]RXW ` X^UM QJ_N XWb NONL]R_NUb [NVX_NM UR]UN ` J]N RLN QXV]QN NSNLJJ#*

E N ` RU[NOWN ]QN N N]RV J]N ^\RWP = J[\ 3 URV J]N BX^WWN = 3 B MJ]J JWM N]RV J]N ]QN [N^U]RWP RLNS]NPXUQ VRaRWP [J]RK OX] ]QN ^YYN ON VN]N\ XO ]QNB@<4 #ANPJ[MN\ XO^WLN]JRW]RN RV]QR \^KURV J" ]RXW QX` N_N!]QR L]J]N NaYX\NMO[UN\ ` J]N RLN]QJW]QX\NJ]]QNV RMU]R_^MN HR, I#

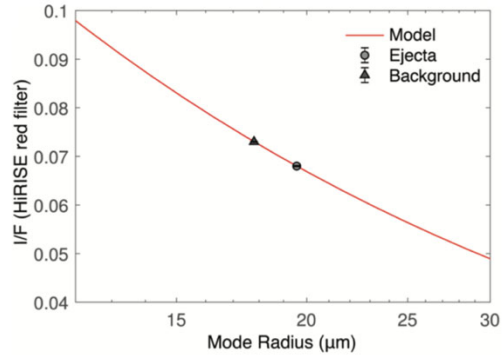

Figure 3. I/F calculated in the HiRISE red filter wavelength range for different particle sizes. Statistical uncertainties in the I/F measurement are small compared to uncertainties in the model, and are smaller than the symbols plotted above.

Acknowledgements: *CQN J^]QX]\ ` RQ]X]QJWT]QN= J[\ ANLXWWR\ JWLN? [KR]N Y[XSNL] JWM 8 RA9B5]NJV! RWLU^MRWP]QN 8 RCBS3 9@@ XWLb LUN M^[RWP RV" JPRWP!]QN 8 RA9B5 4 C= UK! JWM 4 JWRNUAXKRWXW#*

References: [1] Milkovich, S.M., et al. *JGR*, 2005. **110**(E1). [2] Becerra, P., et al., *JGR:Planets,* 2016. **121**(8) [3] Fishbaugh, K.E. and C.S. Hvidberg, *JGR,* 2006. **111**(E6). [4] Hvidberg, C.S., et al*., Icarus*, 2012. **221**(1) [5] Piqueux, S., et al., *Icarus*, 2015. **251** [6] Jakosky, B.M., et al., *JGR: Planets*, 1995. **100**(E1). [7] Laskar, J., et al., *Nature*, 2002. **419**. [8] Levrard, B., et al., *JGR:Planets* 2007. **112**(E6). [9] Koutnik, M., et al, *JGR: Planets*, 2002. **107**(E11) [10] Herkenhoff, K. and J.J. Plaut, Icarus, 2000. **144**(2) [11] Landis, M.E., et al., *Amazonian Climate Workshop.* LPI Contributions, 2019. **2089**. [12] Kolb, E.J. and K.L. Tanaka, *Mars,* 2006. [13] Becerra, P., et al., *GRL*, 2019. **46**(13): p. 7268-7277. [14] Zuber, M.T., et al., *Science,* 2007. **317**(5845) [15] Malin, M.C., et al.,. *Science*, 2006. **314**(5805). [16] Daubar, I.J., et al., *Icarus,* 2013. **225**(1) [17] Dundas, C.M., et al., *JGR:Planets*, 2014. **119**(1) [18] Daubar, I.J., et al., *JGR:Planets*, 2014. **119**(12) [19] Landis, M.E., et al., *GRL*, 2016. **43**(7). [20] Quaide, W.L. and V.R. Oberbeck, *JGR*, 1968. **73**(16). [21] Wiscombe, W.J. and S.G. Warren, *J. of Atm. Sci.*, 1980. **37**(12). [22] Wolff, M.J. and R.T. Clancy, *JGR:Planets*, 2003. **108**(E9). [23] Hayne, P.O., et al., *JGR:Planets*, 2012. **117**(E8). [24] Mellon, M.T., et al., *Icarus*, 2004. **169**(2): p. 324-340

OBSERVATIONS OF THE POLAR CAPS OF MARS BY OMEGA/MEX IN THE VISIBLE RANGE.

Y. Langevin[1] and B. Gondet[1], [1] Institut d'Astrophysique Spatiale, Univ. Paris Saclay / CNRS (yves.langevin@ias.u-psud.fr)

Introduction: The OMEGA imaging spectrometer on board Mars Express has been observing the Martian surface and atmosphere since January 2004. The observations so far cover 16 years, more than 8 Martian years. Observations of polar caps can only be performed by OMEGA when the sun is high enough above the horizon, during local spring and summer. The orbit of Mars Express is highly elliptical (300 km x 10500 km), with a precession motion of the line apsides by 360° every 1.6 years. The local time decreases by ~ 1 hour / month due to the combined effects orbit plane precession and Mars orbital motion. Contrary to sun-synchronous orbiters (e.g. MRO), this means that observations at the same Ls for successive Martian years are obtained at quite different spatial resolutions (from 300 m to 11 km/pixel) and local times (secondary to L_s for lighting at high latitudes).

The OMEGA image cubes initially covered a wavelength range from 0.37 µm to 5.09 µm with three channels: "VIS" channel (96 spectral bands from 0.36 - 1.05 µm); "C" channel (128 spectral bands from 0.93 µm - 2.7 µm); "L" channel (128 spectral bands from 2.53 µm - 5.09 µm). The "C" and "L" channels rely on a cryo-cooler for bringing the temperature of the detector down to its operational range (~ 80 K). The "C" cooler became non-operational in June 2010, far beyond its expected lifetime. In January 2016, functional issues were encountered when operating the "L" channel, so that most recent OMEGA observations have been implemented with the "VIS" channel alone.

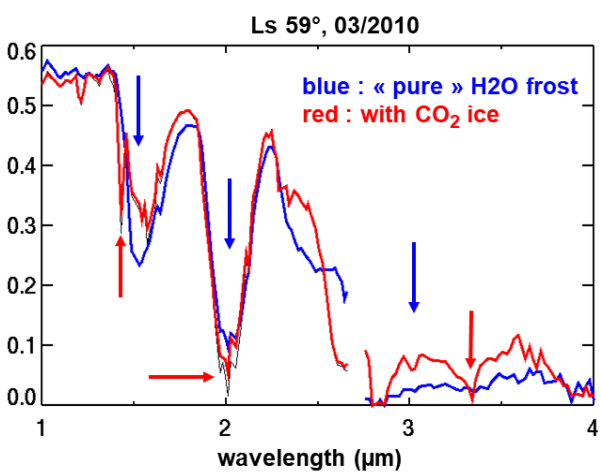

Fig. 1: signatures of H_2O frost and CO_2 ice observed by OMEGA in 2010 with the "C" and "L" channel.

Evolution of instrumental capabilities: The three successive configurations of OMEGA (all three channels until June 2010, then "VIS" + "L" until January 2016 then "VIS") have a major impact on the capability for identifying ice-covered areas, for discriminating between CO2 ice and H2O ice and for obtaining information on particle size. As shown in Fig. 1, CO_2 ice and H_2O ice present major absorption bands in the "C" and "L" channels (contrary to the "VIS" channel). One can still rely on "VIS" albedo for identifying ice-covered areas as most have reflectance higher than 50%, to be compared to ~ 45% for dust-covered areas. Observations of ice-covered areas with all three channels are available during more than 3 Martian years, and seasonal cap processes are relatively stable from Martian year to Martian year. This made it possible to identify spectral ratios in the "VIS" range with diagnostic capabilities between bright dust, H_2O ice and CO_2 ice, in particular the ratio between 0.506 µm and 0.618 µm (see Fig. 2).

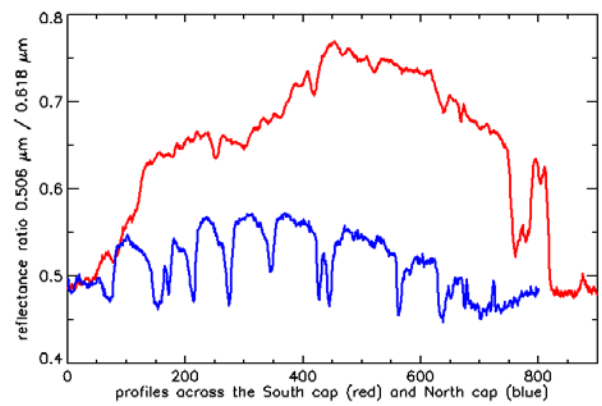

Fig. 2 profiles of the 0.506 µm / 0.618 µm ratio across the south cap (dominated by CO_2 ice) and North cap (dominated by H_2O ice). Bluer regions correspond to ice covered regions as identified from absorption features in the "C" and "L" channels.

Caution is however needed when using "VIS" spectral ratios as there can be a major impact of aerosols in this spectral range. Furthermore, one also needs to check for high albedo as dark terrains can be much bluer than dust-covered bright terrains. While the initial capabilities cannot be restored, an extended time coverage is of interest for investigating the stability of polar processes and the impact of specific global dust storms (2007, 2018) on polar processes.

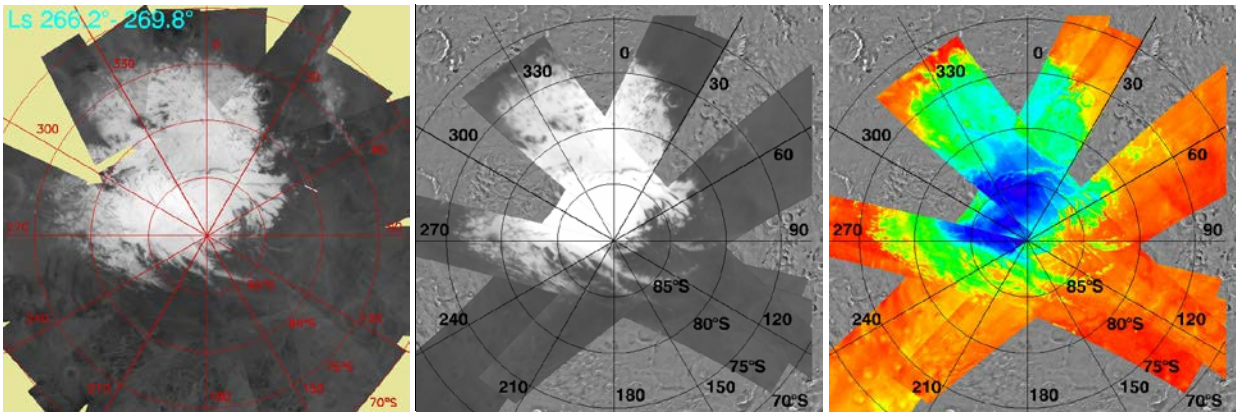

Fig. 3, left: albedo at 1.3 µm ("C" channel) of the South seasonal cap shortly before the summer solstice in 2005 (from [1]); center: albedo at 0.615 µm ("VIS" channel) in the same Ls range (266 -269°) in 2018; right: ratio 0.508 µm / 0.618 µm (from redder to bluer) in 2018. Slight mismatches in overlap result from different incidences.

Results: ***Retreat of the South seasonal cap;*** 6 "VIS" cubes obtained from October 10 to October 15, 2018 made it possible to obtain a near comprehensive map of "VIS" albedo and spectral slope shortly before the summer equinox with a resolution of 2.5 km/pixel. The center and right panels show the consistency between albedo and slope for identifying ice (CO_2 ice in that L_s range). The extent of the south seasonal cap is remarkably similar to that observed at a higher resolution (1 km/pixel) in 2005 (left panel) both for the main cap and for outliers, with a few minor discrepancies (e.g. more extended frost deposits in 2018 at 90°E and 120°E). This is of interest as the 2018 observations were obtained a few months after a major global dust storm, while there was no global dust storm in 2005. The last stages of the retreat are also quite similar in 2005 and 2018 (Fig. 4). The impact of such events in terms of high latitude dust deposition (which would promote sublimation) seems to be minimal.

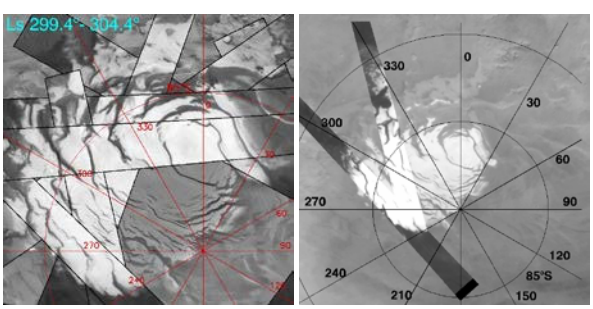

Fig. 4: last stages of the retreat (Ls 300-305°) in 2005 (left, 1.3 µm) and in 2018 (right, 0.615 µm)

Observations of the North perennial cap: cubes obtained from high altitude in December 2017 (Ls 101°) provide extended coverage at low resolution (8 km/pixel) shortly after the sublimation of seasonal frost. They demonstrate that combining albedo and slope information is required when dark terrains are present, as they are nearly as blue as large-grained water ice. The low albedo and reddish "VIS" spectral slope of the region at 60°E, 80° - 85° N indicates that it is significantly more contaminated by dust end of 2017 than in 2005 ([2],[3])

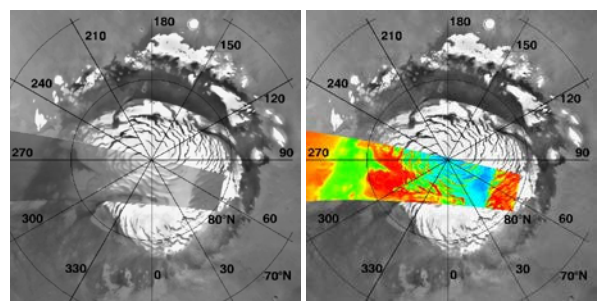

Fig. 5: albedo at 0.615 µm (left) and "VIS" spectral slope of the North cap at Ls 101° end of 2017.

Conclusion: The "VIS" channel observations can be used for extending time coverage over more than 8 Martian years, using earlier OMEGA observations with more extended spectral coverage for confirmation of the validity of the selected spectral criteria in the "VIS" range. Several 100 cubes are available per Martian year at N and S high latitudes, which make it is possible to compare evolutions with or without major dust storms.

References:

[1] Langevin Y. et al., 2007, JGR, **112**, E08S12 ; [2] Langevin Y. et al., 2005, Science **307**, p. 1581-1583 [3] Apperé T. et al. (2011) JGR **116**, E05001

PHLEGRA MONTES: CANDIDATE LANDING SITE WITH SHALLOW ICE FOR HUMAN EXPLORATION. A.S. McEwen[1] S.S. Sutton[1], A.M. Bramson[1], S. Byrne[1], E.I. Petersen[1], J.S. Levy[2], M.P. Golombek[3], N.R. Williams[3], N.E. Putzig[4] [1]LPL, Univ. Arizona, [2]Colgate Univ., [3]JPL, Caltech, [4]PSI.

Introduction: Human exploration and settlement of Mars is of interest to SpaceX [1] as well as NASA, ESA, and CNSA (China). H_2O is essential for drinking, growing food, and producing oxygen and hydrogen, but avoiding polar regions is important to keep temperatures moderate and for solar power. MRO/HiRISE working with JPL has been imaging candidate landing sites for SpaceX. This effort is focused on the northern mid-latitudes because of low altitudes, the known presence of shallow ice down to 39°N [2], and milder winters than the southern middle latitudes. Human Mars landers will likely target flat landing sites (slopes <5°) that are relatively free of large boulders and dust.

Based on topographic data and HiRISE images, two regions stand out as most promising: Arcadia Planitia and Phlegra Montes (Fig. 1). Arcadia Planitia is especially flat and has extensive apparently boulder-free areas. Phlegra Montes probably also has dozens of acceptable areas (>200 m diameter) plus other advantages. In the Phlegra Montes there are Noachian and Hesperian terrains likely to provide diverse materials in addition to regolith and ice, and there are hills that provide north- and south-facing slopes. Shallow ice is stable down to lower latitudes on pole-facing slopes [3], and surface temperatures are higher on equator-facing slopes. A landing site on a flat area near north- and south-facing slopes might be ideal.

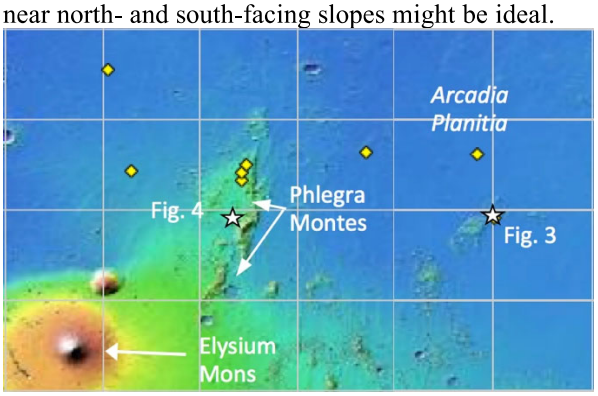

Figure 1. Location map on color-coded altimetry from 20–60° N, 140–200° E. Yellow diamonds indicate ice-exposing impacts [2]. Locations of Figs. 3 and 4 are marked with white stars.

Geology of Phlegra Montes: This 1,400 km long set of elevated features extends from 30-52° N and 160-170° E. The large-scale topography is that of asymmetric linear-to-arcuate ridges interpreted as nine major and several minor thrust-fault structures [4]. The hills are heavily modified by glacial flow landforms, some of which have radar-sounding returns interpreted as nearly pure ice under a debris layer [5–8]. The bedrock composition is poorly known because of Amazonian modification, but basaltic compositions have been detected in nearby Erebus Montes [9].

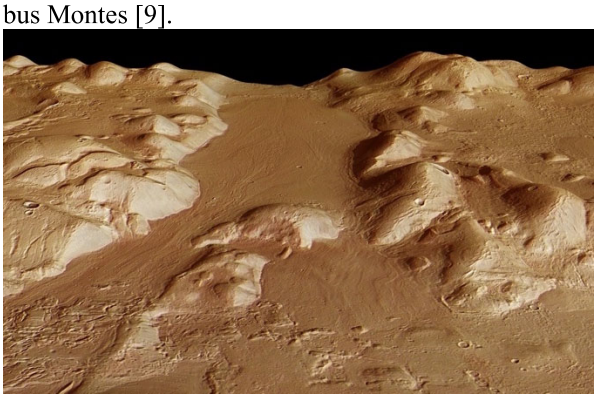

Figure 2: HRSC perspective view of a portion of southern Phlegra Montes. ESA/DLR/FU Berlin. (http://www.esa.int/spaceinimages/Images/2011/12/Phlegra_Montes_in_perspective2

Evidence for Shallow Ice: Icy flow geomorphologies are ubiquitous in Phlegra Montes [10] (Fig. 2). One location has been interpreted to have had over 1 km ice thickness [11]. Remnant debris-covered glaciers in the Phlegra Montes have been estimated to contain tens to hundreds of km^3 of ice today [12]. Interpretation of eskers suggests wet-based glaciation occurred in southern Phlegra Montes [13]. The mid-latitude flow features are presently covered by at least a few meters and perhaps tens of meters of rocky debris [14]. However, there are recent impact sites exposing clean ice from <1 m depth near here [2], including one example at 39.1°N latitude (Fig. 3). Thermokarst features in this region have been identified equatorward of 30N [15] and are also interpreted as contemporary presence of ice. A recent study [16] has found a high consistency of ice across the Phlegra-Arcadia area using various datasets. Ice-exposing craters in the Phlegra-Arcadia region of Mars are typically found on terrain with ubiquitous polygonal pattern, few boulders and sometime near thermokarst landforms. Polygons of this size (≤10 m) form by thermal contraction cracking of ice beneath a thin layer of regolith [17]. Our working hypothesis is that nearby terrains with ~10 m scale polygons, or thermokarst landforms, have shallow ice today.

Boulders: The "Golombek rule" is that an acceptable landing site has zero boulders detected in full-resolution HiRISE images [18]. This rule is based on the fact that HiRISE boulder detection is complete at >1.5 m diameter, and given exponential extrapolation to 1-m diameter (typically 0.5 m high), even a single boulder detection could result in >1% chance of the lander failing due to a boulder. The SpaceX Starship is a very different landing system from past NASA landers, and the tolerance for boulders may differ, but are still best avoided.

Figure 3: New ice-exposing impact crater cluster east of Phlegra Montes (HiRISE ESP_029467_2195).

There are now >100 HiRISE images from 30-40° N and 160-166° E, about half at full resolution. (We are assuming that above 40°N is unacceptable due to low winter temperatures and the polar hood). Although this is extremely sparse coverage (<5%), there are at least 7 images showing large areas (>200 m) with no boulders and with polygons that may indicate shallow ice (Fig. 4). These areas have moderate to moderately-low thermal inertia [19], high albedo [20], and a low dust cover index [21] suggesting near surface materials are dominantly dry sandy soils with a thin coating of dust.

Slopes: MOLA data indicates regional (35-km) slopes range from 0-20° over Phlegra Montes; roughness mapping shows relatively low small-scale roughness typical of the middle to high latitudes [22]. Polygonal terrain at the Phoenix landing site is relatively smooth [17]. There are currently 5 good HiRISE stereo pairs over promising locations (that appear flat and are nearly boulder free); at least one digital terrain model (DTM) will be completed by the time of the conference.

Future Data Needs: Waiting for new impact events to confirm shallow ice at new sites from 30-40° N could take decades. A recent study [23] concluded that Polarimetric Synthetic Aperture Radar on a future Mars orbiter is needed to map the distribution of ice within the top few 10s of meters. Additional HiRISE-class images are needed in potential landing sites, including stereo coverage.

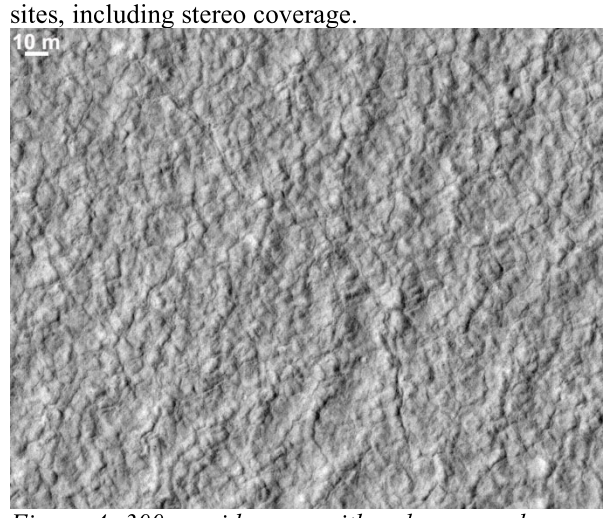

Figure 4. 300-m wide area with polygons and no resolved boulders, located at 38.7 N, 163.88 E. A DTM will be produced here to determine small-scale slopes. Portion of ESP_035362_2190.

References: [1] Wooster, P. et al. (2018) 42nd COSPAR Scientific Assembly, Abstract id. B4.2-31-18. [2] Dundas, C.M. (2014) JGR 119, 2013JE004482. [3] Aharonson, O. and Schorghofer, N. (2006) JGR 111, E11007. [4] Klimczak, C. et al. (2018) JGR-Planets 123, 1973-1995. [5] Holt, J.W., et al. (2008) Science 322, 1235–1238. [6] Plaut, J.J., et al. (2009) Geophys. Res. Lett. 36, L02203. [7] Safaeinili, A. et al. (2009), *LPSC XL*, #1988. [8] Petersen, E.I. et al. (2018) GRL 45, 11,595-11,604. [9] Rogers, D. and P.R. Christensen (2003) JGR 108, 5030. [10] Kress, A. et al. (2010) 41st LPSC, #1166. [11] Dickson, J.L. et al. (2010) E&PSL 294, 332-342. [12] Levy, J.S., et al. (2014). JGR, 119, 2188–2196. [13] Gallagher, C. and M. Balme (2015) E&PSL 431, 96-109. [14] Baker, D.M.H. and L.M. Carter (2019) Icarus 319, 745-769. [15] Viola, D., and A.S. McEwen, 2018, JGR, 123, 262-277. [16] Putzig, N.E. (2019) Ninth Int'l Conf. on Mars, Abstract #6427; swim.psi.edu. [17] Mellon, M.T. et al. (2008) JGR 113, E00A23. [18] Golombek, M.P. et al. (2008) JGR 113, E00A09. [19] Putzig, N. and M. Mellon (2007) Icarus 191, 68–94. [20] Christensen, P. et al. (2001) JGR 106, 23823–23871. [21] Ruff, S. and P. Christensen (2002) JGR 107, 5127. [22] Kreslavsky, M.A. and J.W. Head (2002) GRL 29, 14-1. [23] MEPAG ICE-SAG Final Report (*2019*), at http://mepag.nasa.gov/reports.cfm.

A Review of Martian CO2 Sublimation Processes and their Field and Laboratory Analogs. L.E. McKeown[1] and S. Diniega[2] and G. Portyankina3 and K.-M. Aye3 [1]Natural History Museum (l.mckeown@nhm.ac.uk) [2] Jet Propulsion Laboratory, Pasadena, CA, USA, LASP, 3University of Boulder, Colorado, USA

Introduction: The Martian surface is host to a diverse array of surface features that are widely attributed to the sublimation of volatiles – either in the present day or recent geological past. Atmospheric conditions even in the coldest environments on Earth are orders of magnitude different to those on contemporary Mars. Additionally, many sublimation-driven features on Mars are unlike anything seen on Earth. Therefore, understanding how sublimation drives the evolution of the Martian surface has until recently, relied heavily on remote-sensing and modelling efforts.

A new advent of laboratory experiments have offered an empirical perspective on the formation of Mars polar features, by simulating all but acceleration due to gravity on Mars. However, scaling issues introduce limitations that necessitate a multi-faceted approach. We review the laboratory and field analog work conducted to date in relation to Martian sublimation features, planned future experiments and we invite discussion on how else our understanding of the evolution of the Martian surface might benefit from laboratory and field analog approaches used to date. In addition, we review potentially sublimation-driven features on other planetary bodies and invite discussion on whether we can use analogs on Mars or Earth as natural laboratories.

Field Work: We review Terrestrial field campaigns conducted to explore analog processes of a putatively sublimation-driven nature. For example; a series of field campaigns in Utah and Arizona conducted to investigate the Sliding CO_2 Block Hypothesis in relation to linear dune gullies [1] were necessary to investigate whether sliding sublimating CO_2 blocks could erode channel morphologies and deposit lateral levées. We also discuss analog-based research using Terrestrial gullies (e.g. [2-5]) which provide a resource to investigate wet-based mass-wasting processes and highlight the need for Mars condition laboratory experiments to explore slope-destabilising sublimation feature formation under Martian conditions, of which only few campaigns have begun to investigate [e.g. 6, 7].

Laboratory Experiments: Laboratory experiments under Martian atmospheric pressure and polar temperature ranges have been integral to understanding the conditions under which active sublimation features on Mars form. For example, experiments investigating the nature of condensed ice morphologies are key to understanding the environments under which active dendritic troughs form in the present day on Mars [8]. Experiments simulating cryoventing under Mars conditions have provided a proof-of-concept of Kieffer's Hypothesis for araneiform formation [9]. Experiments under Earth conditions have even allowed us to provide a rough estimate of how much linear dune gully pits should widen with a given volume block of CO_2 [10]. Moreover, laboratory experiments under Mars conditions have revealed new exotic processes such as those instigated by metastable liquid water, which now must be considered in the context of Martian mass-wasting features [11, 6].

Conclusion: This abstract provides a non-exhaustive summary of recent empirical studies of extant processes on Mars and the advances made by this work in our understanding of the contemporary modification of the Martian surface. We present proposed next-step experiments on insolation-driven CO_2 sublimation in the context of araneiform development and we welcome and invite feedback on potential constraints – particularly from modellers. We collate key insights provided by laboratory and field studies of Martian sublimation processes, as well as related analog work on non-sublimation processes, with a view to inviting discussion among the community on how we can improve upon and utilize these methodologies going forward.

References:

[1] Diniega, S., Hansen, C.J., McElwaine, J.N., Hugenholtz, C.H., Dundas, C.M., McEwen, A.S., Bourke, M.C. A new dry hypothesis for the formation of martian linear gullies, Icarus, 225. 526-537, 2013

[2] Hartmann, W. K., Thorsteinsson, T, Sigurdson, F. Martian hillside gullies and icelandic analogs, Icarus, 162, 2, 2003

[3] Conway, Susan & Haas, T. & Harrison, Tanya & Carling, Paul & Carrivick, Jonathan. Martian gullies and their Earth analogues: Introduction. Geological Society, London, Special Publications, 2018

[4] Conway S., de Haas T. & Harrison T.N. Martian gullies: a comprehensive review of observations, mechanisms and the insights from Earth analogues. In: Martian Gullies and their Earth Analogues. Geological Society, London, Special Publications, 467, 2018

[5] Conway S.J., Butcher F.E.G., de Haas T., Deijns A.J., Grindrod P.M. & Davis J.M. 2018a. Glacial and

gully erosion on Mars: a terrestrial perspective. Geomorphology, 318, 26–57

[6] Raack, Jan; Conway, Susan J.; Herny, Clémence; Balme, Matthew R.; Carpy, Sabrina and Patel, Manish R. Water induced sediment levitation enhances downslope transport on Mars. *Nature Communications*, 8, 1151, 2017

[7] Sylvest, M. E., Conway, S. J., Patel, M. R., Dixon, J. C., and Barnes, A. (2016), Mass wasting triggered by seasonal CO_2 sublimation under Martian atmospheric conditions: Laboratory experiments, *Geophys. Res. Lett.*, 43, 12,363– 12,370

[8] Portyankina, G.; Merrison, J.; Iversen, J.J.; Yoldi Martínez de Mandojana, Zuriñe; Hansen, C.J.; Aye, K.-M.; Pommerol, Antoine; Thomas, Nicolas (2019). *Laboratory investigations of the physical state of CO 2 ice in a simulated Martian environment.* Icarus, 322, pp. 210-220. Elsevier 10.1016/j.icarus.2018.04.021

[9] L.E. Mc Keown, M.C. Bourke, J.N. McElwaine, M.E. Sylvest, and M.R. Patel. The
Formation of Araneiforms by Carbon Dioxide Venting and Vigorous Sublimation Dynamics Under Martian Conditions. *Under Review*

[10] L. E. Mc Keown, M. C. Bourke, and J. N. McElwaine. Experiments on Sublimating
Carbon Dioxide Ice and Implications for Contemporary Surface Processes on Mars.
Scientific Reports, 7:14181, 2017.

[11] M. Mass_e, S. J. Conway, J. Gargani, M. R. Patel, K. Pasquon, A. McEwen, S. Carpy,
V. Chevrier, M. R. Balme, L. Ojha, M. Vincendon, F. Poulet, F. Costard, and
G. Jouannic. Transport processes induced by metastable boiling water under martian
surface conditions. Nature Geoscience, 9, 2016.

LACK OF MELTWATER MAY PREVENT RADAR SOUNDING MEASUREMENTS OF SUPRAGLACIAL DEBRIS THICKNESS IN THE MARTIAN MIDLATITUDES. T. M. Meng, E. I. Petersen, M. S. Christoffersen, B. S. Tober, and J. W. Holt, [1]Lunar & Planetary Laboratory, University of Arizona (tmeng@email.arizona.edu)

Introduction: Lobate debris aprons (LDA) are among the purest reservoirs of water ice in Mars' mid-latitudes. Furrow and ridge morphology suggests viscous deformation akin to compressional features observed on terrestrial rock/debris-covered glaciers, where ice ablation is prevented due to an insulating debris layer[1-3]. Depth-corrected orbital radar sounding detections of LDA bases consistently constrain their bulk dielectric properties to that of cold, high-purity water ice with thicknesses on the order of hundreds of meters [4-6]. Due to their relatively low latitude, high purity, and large volume, LDA may be among the strongest candidates for targeting martian water and life resources for future exploration.

A significant challenge in targeting sites with low risk and high scientific return for mission planning is understanding the distribution of supraglacial debris thickness in relation to ice concentration. To date, no near-subsurface radar returns have been interpreted as reflections from a debris-ice contact; either the dielectric contrast is negligible or the contact is too shallow to distinguish from the side-lobes of the compressed pulse [7]. While the theoretical vertical resolution of SHARD is approximately 10 m for the dielectric permittivity of ice [8] and the lack of an internal reflection could signify relatively thin debris, a graded contact or surface scattering could also contribute to the non-detection of a debris layer upwards of 30 m thick.

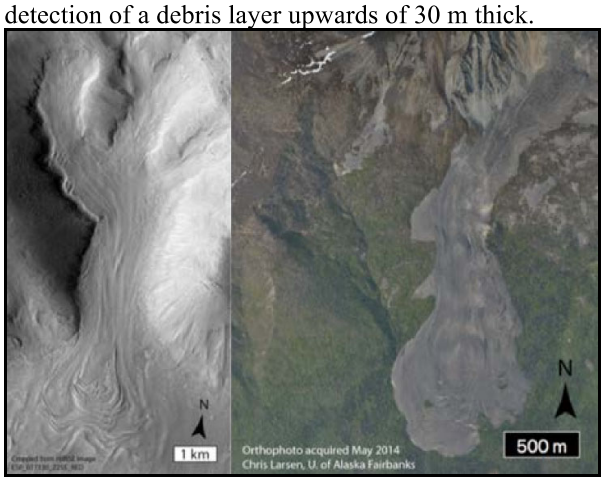

Figure 1: Rock glaciers observed on Mars with HiRISE (left) and in Alaska with airborne photogrammetry (right), showing analogous furrow/ridge morphology.

CTX and HiRISE imagery provide important information regarding the surface morphology of LDA, but terrestrial debris-covered glaciers are also active and accessible laboratories to study the processes that govern debris-layer evolution on Earth which can be used to infer the contributions of similar processes under Mars midlatitude conditions (Figure 1).

North American Analog Sites: We visited four ice-cemented/ice-cored rock glaciers (Gilpin Peak, Colorado; Galena & Sulphur Creek, Wyoming; Sourdough, Alaska) with the objective of using a Sensors & Software PulseEKKO ground-penetrating radar (GPR) to image glacier geometry and structure. These rock glaciers range from 34°N to 62°N latitude, and the minimum elevation decreases with increasing latitude from 3400 m to 500 m a.s.l. Although the interpreted origins of these rock glaciers range from glacial to periglacial [9, 10], we detected distinct near-surface reflectors which were interpreted as debris-ice contact at each site, both with winter snow cover and during the summer melt season. The upper bound on measured debris thickness from GPR is 5 m, and for all of the sites the mean thickness is approximately 2 m.

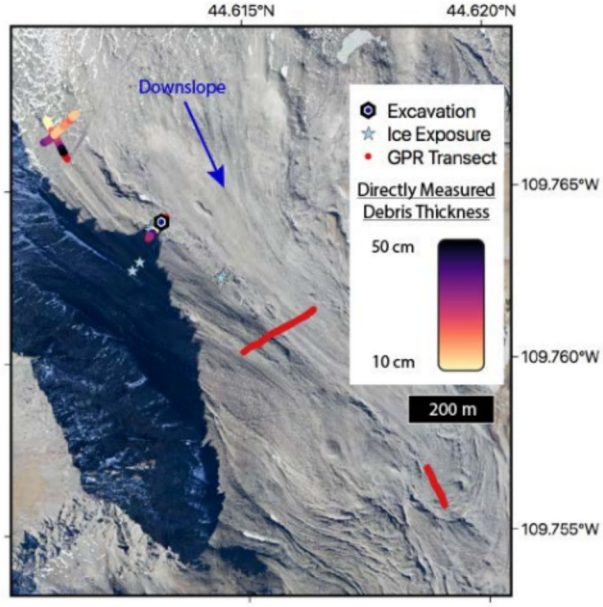

Figure 2: Map view of Sulphur Creek rock glacier showing locations of GPR surveys and directly sampled debris thicknesses along with subaerial ice exposures. Field data collected August 2019, aerial image acquired September 2016 .

Sulphur Creek Tie Point: The upper cirque of Sulphur Creek Rock Glacier provided the thinnest debris cover, which allowed for direct observation of the debris layer (Figure 2). We dug a trench near the location of a near-surface reflector truncation in the GPR data with the objective of tying the reflection to a physical contact (Figure 3). We excavated 90 cm before reaching glacial ice, and we split the section into four units depicted in Figure 4. This depth to ice, along with the two-way radio wave travel time of 17 ns, suggests a dielectric permittivity of 9, consistent with the observed wet sand. This estimate can constrain our other GPR measurements of debris thickness.

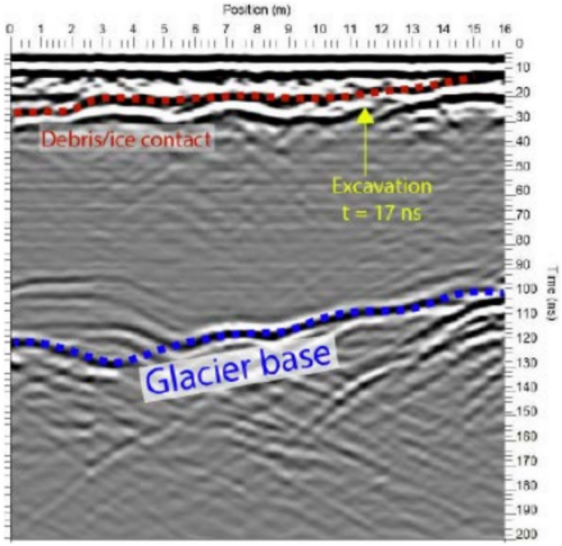

Figure 3: 200 MHz radargram showing the shallow debris-ice reflection that was investigated at the excavation site.

We observed inverse grading in the debris layer, and a notable characteristic of this section was the presence of meltwater and a layer of ice-cemented debris between the graded debris and glacial ice. Other shallow debris measurement sites showed consistent grading and a film of meltwater at the debris-ice contact. While mechanical grading that sorts smaller particles to the bottom of the debris layer could be accomplished by the movement of debris following viscous glacier deformation, the thin layer of ice-cemented debris and the film of liquid water could not have formed without invoking melt, which is an obvious difference between Earth and Mars surface conditions.

Challenges for Orbital Radar Sounding of Mars: Our observations of the debris layers on four North American rock glaciers provide constraints on the debris variability on local and regional scales, but they also warn of issues that may be encountered when exploring their martian analogs. The presence of liquid water in the active layer may be required to create the sharp dielectric contrast observed at the terrestrial sites, so with present-day conditions on Mars, we would not expect to see a strong near-surface reflection, but rather a dielectric gradient. Future radars with higher center frequency or larger bandwidth would aid in further investigation of debris thickness and stratigraphy by increasing spatial resolution.

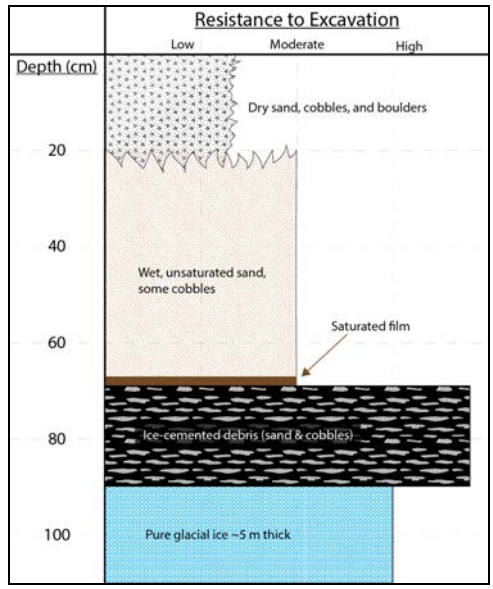

Figure 4: Stratigraphic column interpreted from the Sulphur Creek excavation site. Note the saturated film and ice-cemented debris providing a high-reflectivity contact.

As a corollary, if strong near-surface reflectors are observed on Mars in future missions, this could serve as an indicator that liquid water may have played a role in martian landscape evolution within the time scale of the extant glaciers. With currently available instrumentation, further study of debris layer variability should explore water vapor diffusion and model depths to ice stability for varying slope aspects, insolation, and grain size assemblages in tandem with morphological analysis of compressional ridges and furrows.

References:

[1] Head J. W. et al. (2010) *Earth & Planet. Sci. Letters, 294,* 306–320. [2] Baker D. M. H. et al. (2010) *Icarus, 207,* 186–209. [3] Levy, J. S. et al. (2014) *JGR: Planets, 119,* 2188–2196. [4] Holt J. W. et al. (2008) *Science, 322,* 1235–1238. [5] Plaut J. J. et al. (2009) *GRL, 36,* L02203. [6] Petersen E. I. et al. (2018) *GRL, 45,* 11595–11604. [7] Baker D. M. H. & Carter L. M. (2019) *Icarus, 319,* 745-769. [8] Seu R. et al. (2007) *JGR, 112,* E05S05. [9] Potter N. et al. (1998) *Geografiska Annaler, 80,* 251–265. [10] Degenhardt J. J. & Giardino J. R. (2003) *JGR: Planets, 108,* E4.

RECENT FORMATION OF ICE-RICH LATITUDE-DEPENDENT MANTLE FROM POLAR ICE RESERVOIRS. J. Naar[1], F. Forget[1], J.-B. Madeleine[1], E. Millour[1], A. Spiga[1],M. Vals[1], A. Bierjon[1], L. Benedetto de Assis[1], [1]Laboratoire de Météorologie Dynamique, UMR CNRS 8539, Institut Pierre-Simon Laplace, Sorbonne Universités, UPMC Univ Paris 06, 4 place Jussieu, 75005, Paris, France. (joseph.naar@lmd.jussieu.fr)

Introduction: Corroborating evidences in geomorphology and modeling has unveiled the presence of a subsurface latitude-dependent mantle (LDM) of water-ice-rich deposits down to 30° latitude in both martian hemispheres [1]. These layers appear to be less than ~ 2Myr and were possibly deposited as snowfall in response to climate change driven by shift in obliquity, similar to Earth glacial/interglacial periods [2].

However, martian climate models usually struggle to reproduce environmental conditions required to form LDM under recent paleoclimatic orbital forcing.

We present a new parametrization of ice/frost albedo which, along with radiatively active water-ice clouds (RAC), predicts ice accumulation rates in mid-latitudes compatible with deposition of a tens of meters-thick LDM under recent obliquities (several incursions to 35°).

Evolution of water stability regions with obliquity: Remnant glacial and periglacial geological features are observed at equatorial and mid-latitudes on Mars, a few tens of million years old. These landforms likely result from equatorward shift of water-ice stability with rising obliquity [3]. This tropical ice becomes unstable during low obliquity phases, and ice has been modeled to accumulates in high latitudes [4,5]. Yet, these former ice reservoirs are millions of years older than the LDM, likely formed during higher obliquity phases (~45°). The water source of the LDM is therefore not thought to be of low-latitude origin, but may be remobilized polar water-ice.

Water-ice clouds in recent paleoclimates: Water-ice clouds effects have a small effect on the present-day martian climate [6], corresponding to a ~25.2° obliquity. When obliquity shifts up to 35°, atmospheric humidity is enhanced by polar warming and water-ice cloud become a key element of martian climate [7,8].

Their radiative effect strongly warms the atmosphere, amplifies meridional circulation and water transport toward tropical latitudes. [7] showed that taking into account radiatively active clouds allow for mid-latitude ice deposits considering only polar caps as a water source in this obliquity regime. However, the accumulation of these ice deposits required the prescription of high atmospheric dust content to ensure its persistence during summer.

Frost and ice albedo: During recent high obliquity episodes up to ~35°, ice accumulates in mid-latitudes as frost. Frost should have a much higher albedo than perennial ice [9]. This was not taken into account in [7]. We improve the parametrization of ice albedo by decoupling older ice,with a canonical albedo of 0.35, and frost, whose albedo can reach 0.7. We find that it has a compelling influence regarding surface water stability and persistence over the years. High albedo inhibits sublimation in summer by lowering surface heating.

Paleoclimatic simulations: Using this refined parametrization, we perform climatic simulations at 35° obliquity with null eccentricity. The corresponding accumulation rates of ice are compatible with the setting of hundreds of meters of LDM down to ~45° latitude in both hemispheres and its persistence year by year (Figure 1). In the last ~2 Myr on Mars, obliquity has reached ~35° a dozen times, for approximately 1000 years each time [10]. Assuming an efficient preservation process, the accumulation rate is sufficient to form a hundreds of meters thick latitude-dependent mantle of ice-rich deposits. The latitudinal extension of the LDM down to 30° isn't represented in these simulations, but many orbital configurations remain to be explored with our model.

Future studies: These preliminary results are part of the "Mars Through Time" program. Scientific perspectives include understanding the formation of LDM, and more generally investigating recent paleoenvironments leading to the formation of geologically young glacial and periglacial landforms on Mars.

References:

[1] Head, J. W., J. F. Mustard, M. A., Kreslavsky, R. E. Milliken, and D. R. Marchant (2003), *Nature*, 426 (6968), 797–802. [2] Forget, F., Byrne, S., Head, J. W., Mischna, M. A., & Schörghofer, N. (2017), *Asteroids, Comets, Meteors-ACM2017*, 464-496. [3] Forget, F., Haberle, R. M., Montmessin, F., Levrard, B., & Head, J. W. (2006), *311*(5759), 368-371. [4] Levrard, B., Forget, F., Montmessin, F and Laskar, J. (2004), *Nature*, 431 (7012), 1072-1075. [5] Madeleine, J. B., Forget, F., Head, J. W., Levrard, B., Montmessin, F., & Millour, E. (2009), *Icarus*,

203(2), 390-405. [6] Madeleine, J. B., Forget, F., Millour, E., Navarro, T., & Spiga, A. (2012), *GRL*, *39*(23).[7] Madeleine, J. B., Head, J. W., Forget, F., Navarro, T., Millour, E., Spiga, A., ... & Dickson, J. L. (2014), *GRL*, *41*(14), 4873-4879. [8] Kahre, M. A., Haberle, R. M., Hollingsworth, J. L. and Wilson, R. J. (2019), Ninth International Conference on Mars, held 22-25 July, 2019 in Pasadena, California. LPI Contribution No. 2089, id.6303. [9] Navarro, T., Madeleine, J. B., Forget, F., Spiga, A., Millour, E., Montmessin, F., & Määttänen, A. (2014), *JGR: Planets*, *119*(7), 1479-1495. [10] Laskar, J., Correia, A. C. M., Gastineau, M., Joutel, F., Levrard, B., & Robutel, P. (2004), *Icarus*, *170*(2), 343-364.

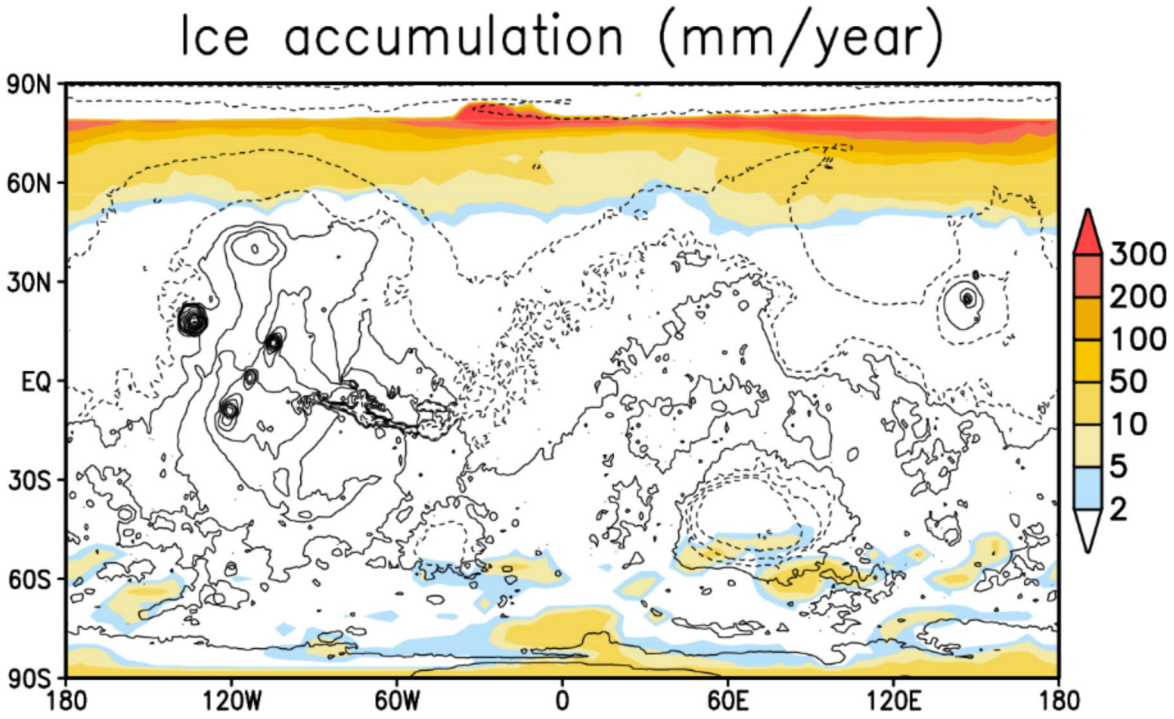

Figure 1 : Net accumulation of surface water ice (mm per year) at obliquity 35° and eccentricty 0 predicted by the LMD GCM assuming an ice frost albedo of 0.7. The model takes into account radiatively active clouds as in [8], and assumes a clear atmosphere all year long (dust opacity at 610 Pa set to 0.2).

THE EARLY HISTORY OF PLANUM BOREUM: AN INTERPLAY OF WATER ICE AND SAND. S. Nerozzi[1], J. W. Holt[2], A. Spiga[3], F. Forget[3], E. Millour[3], [1]Institute for Geophysics, Jackson School of Geosciences, The University of Texas at Austin, TX 78757 (stefano.nerozzi@utexas.edu), [2]Lunar and Planetary Laboratory, University of Arizona, Tucson, AZ, [3]Laboratoire de Météorologie Dynamique, Université Pierre et Marie Curie, Sorbonne Université, Paris, France.

Introduction: The Planum Boreum of Mars is composed of two main units: the North Polar Layered Deposits (NPLD), and the underlying basal unit (BU). The rich stratigraphic record of the NPLD is regarded as the key for understanding climate evolution of Mars in the last 4 My [1] and its dependency on periodical variations of Mars' orbital parameters (i.e., orbital forcing) [2-4]. Their initial emplacement represent one of the most significant global-scale migrations of water in the recent history of Mars, likely driven by climate change, yet its dynamics and time scale are still poorly understood. Recent studies revealed the composition, stratigraphy and morphology of the lowermost NPLD and the underlying BU (Fig. 1, 2; [5,6]). These findings depict a history of intertwined polar ice and sediment accumulation in the Middle to Late Amazonian, thus opening a new window into Mars' past global climate.

Here we present a summary of the latest findings on the climate-driven evolution of Planum Boreum, their significance in advancing the exploration of Mars, and new outstanding questions on Mars polar science. These studies are based on the integration of radar profiles and images acquired by the Shallow Radar (SHARAD, [7]) and the High Resolution Imaging Science Experiment (HiRISE, [8]) on the Mars Reconnaissance Orbiter, and the General Circulation Model (GCM [9]) developed by the Laboratoire de Météorologie Dynamique (LMD).

Former ice caps preserved with the cavi unit: The cavi unit is an aeolian deposit of basalt sand and water ice making up large portions of the BU. SHARAD signals penetrate through this unit revealing internal and basal reflectors. We use these detections to reconstruct the general stratigraphic structure of the unit, and obtain its bulk composition. Our exercise reveals substantial spatial variability in composition, with average water ice volume fractions comprised between 62% in Olympia Planum and 88% in its northern reaches beneath the NPLD. Similarly, internal reflectors occur more frequently closer to the pole and gradually disappear moving south. We hypothesize that the cavi unit is made of alternating ice and sand sheets, with water ice becoming prevalent towards the north pole (Fig. 2). Water ice accumulation models predict substantial ice growth during periods of low spin axis obliquity before the onset of NPLD deposition [10,11], with the thickest accumulation close to the north pole. In the models, this is soon

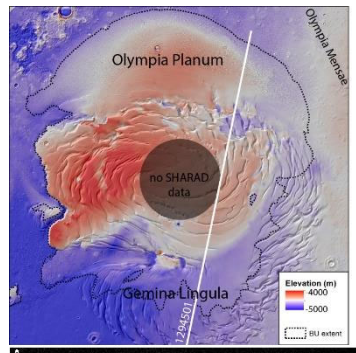

Figure 1: Topographic map of the BU and surrounding terrains revealed by SHARAD [6,7], with superimposed shaded relief of the present day Planum Boreum topography. The white line delineates the location of the SHARAD profile in Fig. 2.

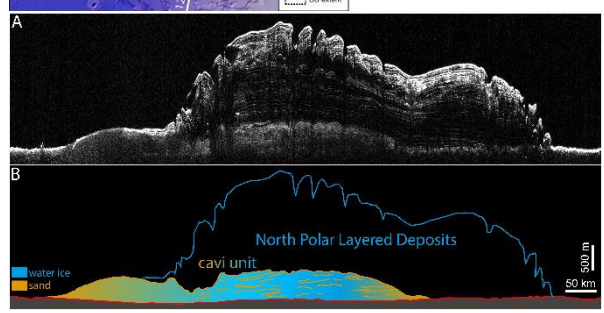

Figure 2: (A) SHARAD profile 1294501 depth corrected assuming bulk water ice composition (e=3.1 [10]), and (B) interpretation thereof [6]. The putative basal surface of the cavi unit is represented in red.

followed by complete loss through sublimation; however, models do not include a protection mechanism against sublimation. We hypothesize that aeolian sand sheets migrated from the margins of paleo-Planum Boreum, burying portions of the remnant ice sheet and thus preventing its complete sublimation. This hypothesis is supported by observations of sand mantles extending for 10s of km on top of thick water ice along visible outcrops and radar profiles of the lowermost NPLD [5,6]. Therefore, we argue that ice caps dating to Middle to Late Amazonian are not necessarily lost due to instability during high obliquity periods, but can be partially or wholly preserved within sand sheets underneath the NPLD. These ice deposits are detected by SHARAD and can be delineated in their spatial extent. Moreover, the high water ice fraction makes the cavi unit an important water ice reservoir, potentially the third largest on Mars after the two PLDs.

Newly mapped extent, stratigraphy, and morphology of the BU: Analysis of SHARAD profiles indicates that the BU extends over a larger area than previously thought. In particular, we detect the presence of cavi unit material extending underneath the NPLD from

the western edge of Gemina Lingula to a visible exposure in the eastern end of Olympia Undae, covering an area of over 120,000 km^2 (Fig. 1). HiRISE images taken over the outcrop location reveal sub-horizontal strata forming terraces and characterized by sinuous forms and cross strata. We interpret this as a cavi unit outcrop, that we can now place into the broader stratigraphic context of Planum Boreum based on SHARAD profiles. Similarly, we combined radar observations and HiRISE-based stratigraphic mapping of visible outcrops along the margins of Planum Boreum to delineate the extent and thickness of the Rupēs and cavi units.

Our radar-based topographic mapping also reveals a series of elongated depressions tens to hundreds of meters deep along the edge of the cavi unit. In some cases, the base of these depressions are flat and appear to continue as internal reflectors for hundreds of kilometers. We interpret these findings as further confirmation of the presence of alternating ice and sand sheets within the cavi unit, delineating sequences that exhibit different resistance to erosion. The location of the elongated depressions coincides with the presence and shape of the buried chasma observed by ref. [12], suggesting that the cavi unit was eroded in the same event that shaped the chasma. We detect similar features at other locations of the BU, suggesting that many other erosional events are recorded by the unit's surface morphology.

Reconstructing the initial NPLD accumulation: SHARAD-based analysis of the lowermost NPLD stratigraphy reveals that initial water ice accumulation was not uniform, but limited in extent and confined into two areas centered around the north pole and in the present Gemina Lingula region, confirming the existence of a proto-Gemina Lingula [12]. Likewise, subsequent ice accumulation was variable in extent. We use the newly acquired information on BU composition, topography and lateral extent to accurately constrain the initial conditions and parameter space for sensitivity experiments with the LMD GCM aimed at understanding the driving forces responsible of the initial accumulation of the NPLD, and its temporal evolution. In particular, we defined parameter sets of spin axis obliquity (15-40°, 5° steps), orbital eccentricity (0-0.12, 0.03 steps), perihelion precession (0-270°, 90° steps), and atmospheric pressure (current, +106% based on ref. [13]).

The GCM output reveals that both obliquity and eccentricity play key roles in driving the amount of water ice accumulation in Planum Boreum, with low obliquity and high eccentricity scenarios resulting in the largest ice growth. Obliquity also appears to control the latitude of ice accumulation, with low obliquity driving thick ice growth at ~60°N. Local topography appears to control longitudinal patterns of ice growth in all our simulations. We find a strong similarity of the latest GCM outputs with the isolated proto-Gemina Lingula deposit (Fig. 3) and present-day icy outliers of Olympia Mensae. This suggests that Olympia Mensae may be remnant of the migration of water ice from low to polar latitudes that resulted in the initial accumulation of the NPLD. Moreover, the formation of proto-Gemina Lingula may predate the accumulation of other NPLD units closer to the north pole.

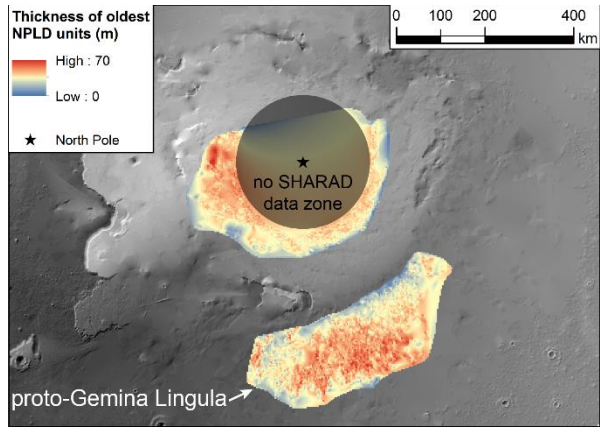

Figure 3: Earliest NPLD water ice accumulation in Planum Boreum as mapped by SHARAD [6].

Outstanding questions: Based on our latest findings in Planum Boreum, we delineate the following outstanding questions. How many episodes of past ice accumulation are recorded within the cavi unit? What is their precise age? What is the nature of western half of the BU, which is dominated by the Rupēs unit? Does this unit also record past polar ice accumulation events? Do younger unconformities in the NPLD follow a similar pattern of erosion/deposition, indicating long-term regional climate patterns?

Acknowledgments: This work was supported by NASA MDAP grant NNX15AM52G. SHARAD is provided and operated by the Italian Space Agency. The GCM was kindly provided by the Laboratoire de Météorologie Dynamique, UPMC, Paris.

References: [1] Cutts J.A. (1973) *JGR*, 78, 4231-4249. [2] Murray B.C. et al. (1973) *Science*, 180, 638-640. [3] Laskar J. et al. (2002) *Nature*, 419, 375-377. [4] Laskar J. et al. (2004) *Icarus*, 170, 343-364. Nerozzi, S. and Holt, J.W. (2018) *Icarus*. [6] Nerozzi, S. and Holt, J.W. (2019) *GRL*. [7] Seu R. et al. (2007b) *JGR, 112*, E05S05. [8] McEwen, A.S. et al. (2007) *JGR*, 112, E05S02. [9] Forget F. et al. (1999) *JGR, 104*, 155-176. [10] Levrard B. et al. (2007) *JGR, 112*, E06012. [11] Greve R. et al. (2010) *PSS, 58,* 931-940. [12] Holt J.W. et al. (2010), *Nature, 465*, 446-449. [13] Bierson C.J. et al. (2016) *GRL, 43,* 4172-4179.

IN-SITU MICROCT INSTRUMENT FOR THE NORTH POLAR LAYERED DEPOSITS OF MARS.

R. W. Obbard[1], P. Sarrazin[1,2], N. Vo[3], K. Zacny[4], S. Byrne[5]

1- SETI Institute, Mountain View CA, USA (213, 37 Dewey Field Road, Hanover, NH 03755; robbard@seti.org)
2- eXaminArt, LLC, Los Altos, CA, USA
3- Diamond Light Source, Didcot, Oxfordshire, UK
4- Honeybee Robotics, Pasadena, CA, USA
5- Lunar & Planetary Laboratory, University of Arizona, Tucson, AZ, USA

Introduction: Understanding the martian climate and how it has changed over its geologic history will contribute to our understanding of climate change on all terrestrial planets. The North Polar Layered Deposits (NPLD) are a multi-kilometer thick sequence of dusty-ice layers thought to contain a record of past states. Deciphering this polar record has been, and remains today, a major goal of Mars research [1].

We know that the dust-content of the NPLD is less than a few percent and that internal layers are contiguous across the entire deposit [2,3]. Sulfate and perchlorate salts have been detected within the PLD and are presumably co-deposited with silicate dust [4-6]. Internal layering has been imaged at high-resolution by MRO's High-Resolution Imaging Science Experiment (HiRISE) where it is exposed in the many troughs and scarps within the NPLD [7] and at low resolution by the Shallow Radar (SHARAD) instrument [3,8,9].

However, the resolutions of layer observations from remote sensing are too coarse and lack the detail needed to detail layer properties and infer climatic information. Fully deciphering the martian climatic record will require in situ high-resolution measurements at the surface that can resolve the properties such as such as dust content and distribution and porosity that may vary temporally and climatically.

Our current understanding of NPLD layers suggests that completely resolving annual layers over most of NPLD history will require 0.1mm vertical resolution. As most NPLD ice could be quite clean, characterizing the dustiness of polar layers requires much greater sensitivity than a few percent. We require dust detectability of 100 ppm by volume with a measurement accuracy of 100 ppm to characterize annual variations in periods of low dust activity. Porosity has important implications for layer deposition mechanism and is substantially preserved in terrestrial ice-sheets down to depths of decameters. Bramson et al. (2017) [10] recently found that substantial porosity can be preserved in mid-latitude martian ice over 10s of Myr – more than the expected age of the NPLD. Measurement of porosity vs. depth can constrain martian densification rates and climatic conditions at the time of deposition [11].

MicroCT is the most comprehensive technique to analyze the NPLD because it can provide high resolution (micron scale) information on densification, layer thickness and morphology, as well as particle size and type. A lander-mounted microCT system could provide much of the microstructural data we would seek from a PLD ice-sediment core, while avoiding the significant hurdles posed by bringing samples back to Earth.

Micro Computed Tomography.

Micro Computed Tomography (microCT) is a non-destructive technique for analyzing micron-scale internal features of a solid sample that could otherwise only be revealed by physically sectioning the material. Series of high-resolution radiographic images are collected at small angular steps, and a 3-dimensional model of the sample is computed.

Layering can be examined by particle size, shape, and relative atomic weight. MicroCT has been used extensively in the study of depositional processes in sedimentary rock [12] and ice [13,14].

Mars In Situ Tomography (MIST) System.

The Mars In Situ Tomography System is a miniaturized micro computed tomography (CT) instrument concept intended for deployment to the Mars North Polar Layered Deposits (NPLD) on a lander or rover. MISTS will provide in-situ 3D-reconstructions of ice cores, enabling the study of sediment distribution. The system consists of two subsystems, the CT instrument and a coring auger that interfaces with Honeybee Robotics' drilling system. The CT system is based on a cone-beam geometry with a simple architecture combining a microfocused X-ray tube, an X-ray image sensor and a core scanning stage.

Our objective is to design a miniaturized microCT system and associated X-ray transparent coring and breakoff tube for the TRIDENT drill and to develop/build and test prototype MIST components in a laboratory cold environment.

We have designed, developed and tested a functional breadboard tomography instrument and an ice-coring tool. The breadboard system was used to collect data from simulants and samples of manmade ice and

the resulting tomographs reconstructed with software that is being developed to accommodate the unique conditions imposed by the miniaturized system and its intended use.

Figure 1 shows a lander-based MIST system. The cone-beam geometry and simple architecture is shown in Figure 2. The breadboard system is based on opto-mechanical hardware, a commercial 60 micron focused X-ray tube and a power supply, a custom sample stage based on a stepper motor, and a customized DSLR camera for X-ray detection.

Figure 3 compares a slice of the reconstructed wax core sample scanned and reconstructed with our 25 kV system (left) to a slice from nominally the same height in the sample acquired with a commercial desktop instrument. Source energy, placement of the sample relative to the axis of rotation, and volume scanned were different, hence the differences in the background (and ring artifacts). Note, however, that the same features are visible in both images, including two Al balls (white) and the voids in the wax (darker gray left, black right).

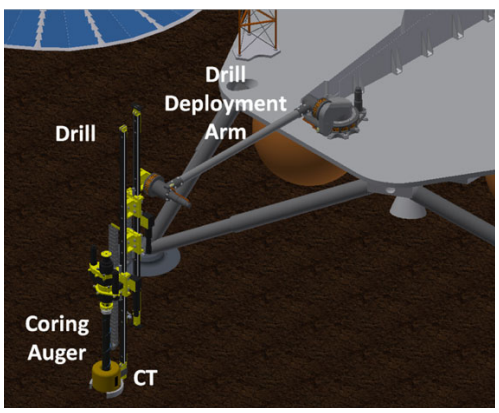

Figure 1. A CAD image of the Lander-based MISTS

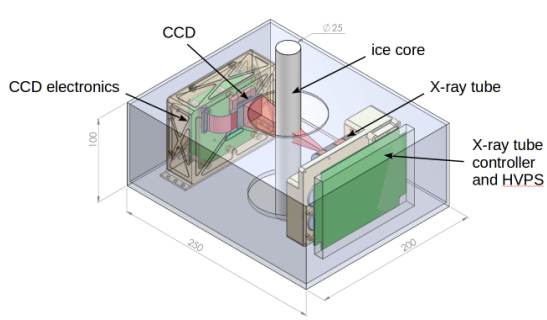

Figure 2. Rough schematic of the analytical head of MIST microCT subsystem based on flight subcomponents developed or under development at NASA ARC (derivation of MSL CheMin CCD, flight CCD electronics, micro-focused ceramic-metal tube, +25kV HVPS), dimensions in mm.

Figure 3. 3D reconstruction slice of a wax core with Al balls (0.8 mm diameter). A. MIST data at 25kV. B. same sample in commercial X-ray microCT.

References: [1] Byrne, S. (2009) Annual Review of Earth and Planetary Sciences, 37. [2] Grima C. et al. (2009) Geophys. Res. Lett., 36, L03203. [3] Phillips R. J. et al. (2008) Science, 320, 5880, 1182-1185. [4] Horgan B. H. et al. (2009) J. Geophys Res.-Planets, 114, E01005. [5] Calvin W. M. (2009) J. Geophys Res.-Planets, 114, E00D11. [6] Masse M. et al. (2010) Icarus, 209, 2, 434-451. [7] Herkenhoff K. E. et al. (2007) Science, 317, 5845, 1711-1715. [8] Putzig N. E. et al. (2009) Icarus, 204, 2, 443-457. [9] Smith M. D. et al. (2016) Icarus, 280, 234-248. [10] Bramson A. M. et al. (2015) Geophys. Res. Lett., 42, 16, 6566-6574. [11] Arthern R. J., Winebrenner D. P. and Waddington E. D. (2000) Icarus, 144, 2, 367-381. [12] Falvard S. and Paris R. (2017) Sedimentology, 64(2), 453-477. [13] Obbard R. W., Troderman G. and Baker I. (2009). J. Glaciol., 55, 194. [14] Iverson N. et al. (2017) Nature Scientific Reports, 7, 11457.

Acknowledgements: This development is funded by NASA PICASSO 17-PICASO17_2-0094, "Mars In Situ Tomography System (MISTS) Development for Characterizing the Stratigraphy of Polar Layered Deposits" (PI R. Obbard, SETI). Funding was also obtained from a NASA SBIR 2018 to eXaminArt, LLC (PI P. Sarrazin) for the parallel development of microCT instrument concept intended for the study of microCT instrument concept intended for the 3D analysis of rock fragments or rock cores, enabling the study of microstructures of potential biogenic origin.

Martian North Polar Cap: Compositional Constraints and Geodynamical Response. L. Ojha[1], S. Karimi[2], S. Nerozzi[3], K. Lewis[2], S. E. Smrekar[4], M. Siegler[5]. [1]Rutgers University, The State University of New Jersey, Piscataway, NJ, USA. [2]Department of Earth and Planetary Sciences. Johns Hopkins University. Baltimore, MD, USA. [3]Lunar and Planetary Laboratory. University of Arizona, Tucson, AZ. [4]Jet Propulsion Laboratory, California Institute of Technology. Pasadena, California, USA. [5]Planetary Science Institute. Tucson, Arizona, USA.

Introduction: While radar data has been able to provide a compositional constraint on the north polar layered deposits (NPLD) [e.g., 1], the bulk composition of the underlying basal unit (BU) has been difficult to ascertain. The BU is a low-albedo, sand-rich ice deposit lying stratigraphically between the NPLD and the underlying Late Hesperian aged Vastitas Borealis Interior Unit [2]. The BU represents a time before formation of the modern ice cap, therefore, understanding its composition may provide insights into more ancient epochs of Martian climate history.

Here, we utilize the available Martian gravity and topography data to constrain the bulk density of the north polar ice cap. We then combine the gravity-derived bulk density estimates with previously published radar data [3] to isolate the bulk density and composition of the BU. The density estimate of the north polar cap also allows us to estimate the stress imposed by the weight of the polar cap on the underlying lithosphere. We model the response of the lithosphere to the stress imposed by the north polar cap and estimate of the present-day mantle heat flow in the north polar regions of Mars. Mantle convection influences crustal tectonics and volcanism, thus, constraining the thermal state of a planet's mantle is important for understanding planetary thermal evolution.

Methods: ***(Density of the polar cap)*** The gravity field of a planet can be used to invert for geophysical properties such as the density of a surface load and elastic thickness of the lithosphere. This is typically done by examining the transfer function between gravity and topography (called admittance) in the spectral or spatial domain. In this work, we first localized the gravity and topography signature of the north polar ice cap by multiplying the global gravity and topography fields [4] of Mars by a localization window in the spatial domain. Localized admittance functions from our region of interest are compared with forward models to constrain the density of the north polar cap. The forward models were constructed by assuming that the lithosphere is a thin shell that deforms elastically in response to surface loads. By combining the results from gravity inversion with radar derived thickness maps, it is possible to estimate the density/composition of the BU. Previously, similar techniques have been used to constrain the density of the south polar cap of Mars [5].

(Mantle heat flow) The lack of appreciable lithospheric deflection in the north polar region of Mars by the weight of the polar ice cap is suggestive of low heat flow [6]. Here, we place an upper limit on the local mantle heat flow in the north polar region of Mars by modeling the flexural response of the Martian lithosphere to the stress imposed by the weight of the north polar cap using state-of-the-art finite element techniques. We use the commercially available Marc-Mentat finite element package (http://www.mscsoftware.com) to model the flexure of the lithosphere under various thermal and mechanical conditions. We treat Planum Boreum (PB) and Gemina Lingula (GL) as axisymmetric distributed loads emplaced on top of the Martian crust. We input the 2D stress profiles from PB and GL into finite element models to constrain the heat flow required to produce the roughly 100 – 200 meters of deflection observed in radar data [6]. The finite element modeling consists of three parts: i) building a finite element mesh, ii) running a thermal simulation, and, iii) running a mechanical simulation. All three aspects of the model are run in Marc-Mentat finite element package/ .

Results: ***(Density of the polar cap)*** We found two windows within the north polar ice cap with sufficient gravity-topography correlation to allow density estimation. For each location, we ensured that over 99% of the gravity and topography signals was from within our region of interest. Figure-1 shows an example of one such location where we used angular radius of 7° and a harmonic bandwidth of 37. Here, the comparison between observed and the synthetic admittance was conducted over the spherical harmonic degree of 46 and 59, where correlation is above 0.7 (Fig. 1 (b)). The best fit load-density within 1-σ of the observed admittance corresponds to 1205 ± 145 kg m^{-3} for any T_e greater than 75 km. To ensure that our estimates are devoid of biases from gravity models and regional gravity setting, we use multiple localization windows, techniques, and gravity models. The results from different datasets, locations, and gravity models do not vary significantly and yield an average bulk density of $1{,}126 \pm 38$ kg m^{-3} [7]. Combining the bulk density estimates with radar-derived thickness maps of the polar units, we find the density of the BU to be $2{,}050 \pm 450$ kg m^{-3} [7].

(Mantle heat flow) We first consider a scenario in which we set the crustal heat flow (q_c) and lithospheric mantle heat flow (q_m) to zero and only vary the heat flow provided by the lower mantle to the base of the lithosphere (q_b). This is a non-physical scenario as both

the crust and lithospheric mantle can be large sources of planetary heat. However, this scenario enables us to place an upper limit on q_b. Using hydrous rheology, crustal thickness of 35 km, and thermal conductivity of 3 and 4 W m^{-1} K^{-1} for the crust and mantle respectively, our models show that q_b higher than 7 mW m^{-2} leads to lithospheric deflection larger than 100 m at Gemina Lingula and 200 m at Planum Boreum (Fig. 2). For a thick (>350 km) stagnant lid such as expected in present-day Mars, the heat produced in a thin crust (~35 km), as expected in the north polar region from gravity data [8], has a minor influence on the magnitude of the lithospheric deflection (Fig. 2). To verify this, we set q_c to 13 mW m^{-2} and found the crustal heat flow to have a negligible influence on the magnitude of the lithospheric deflection (Fig. 2). There are several different parameters involved in our models such as conductivity, density, rheology, and thickness of the crust and mantle, however, reasonable variations in these parameters do not significantly affect our upper limit of the mantle heat flow. A comprehensive discussion of the various parameters and their effect on our mantle heat flow will be presented at the meeting.

Fig. 1. (a) A single taper of L of 37, localized within the geographical boundary of the north polar

admittance estimates.

Fig. 2. Lithospheric deflection expected from the weight of Gemina Lingula for various values of q_b and q_c.

Discussion: The relatively higher density of the BU compared to the overlying NPLD confirms the findings of previous studies in that the two units have remarkably different compositions [2]. The relatively lower density of the BU compared to basaltic dust (~3200 kg m^{-3}) suggests the BU to either contain a large amount of air or ice within its pore space. Assuming the density of H_2O ice and lithics to be 930 kg m^{-3} and 3200 kg m^{-3} respectively, our best-fit density estimate (2050 $\pm$ 450 kg m^{-3}) requires the BU to be composed of 31 – 71 % H_2O ice. The bulk dielectric constant of the basal unit in Olympia Planum is equivalent to a mixture of 38% basalt and 62% water ice, whereas, in the main lobe of Planum Boreum, water ice is the dominant fraction (80% - 90%) of the basal unit [3]. Our average density of the BU is thus in general agreement with the radar results.

We find that the mantle heat flow likely does not exceed 7 mW m^{-2} in the northern polar region of Mars. The mantle heat flow constraints from our models are lower than values predicted by numerical thermal evolution models that assume the abundances of the heat producing elements in the Martian interior to be relatively proportional to the chondritic values. This implies that either the bulk abundance of the heat producing elements on Mars is lower than expected from the chondritic model, that a larger proportion of the bulk HPE has been fractionated into the crust, that there are large-scale spatial heterogeneity in mantle heat flow, or any combination thereof. If the tentative upper limit on the mantle heat flow from our work is globally representative of Mars, then the strong fractionation between the crust and mantle on Mars may have precluded the mantle from undergoing late-stage widespread melting, significantly affecting the geological history of Mars. Future gravity investigation of the polar caps, thus, has the potential to significantly advance our understanding of the ancient Martian climate and geophysical evolution.

References: [1] Grima et al. Geophys. Res. Lett. 36, (2009). [2] Byrne & Murray. Geophys. Res. 107, 1–13 (2002).[3] Nerozzi & Holt, Geophys. Res. Lett. 46, 7278-7286 (2019). [4] Konopliv et al. Icarus 274, 253–260 (2016). [5] Wieczorek. Icarus 196, 506-517 (2008). [6] Phillips et al. Science 320, 5580 (2008). [7] Ojha et al. Geophys. Res. Lett. 46, 8671-8679 (2019). [8] Neumann et al. JGR-Planets, 109.E8 (2004).

SNOWBALL MARS: WHAT THE CURRENT STATE OF THE MARTIAN CO_2 CYCLE TELLS US ABOUT MARS' PAST CLIMATE HISTORY. D. A. Paige[1], [1]Dept. of Earth, Planetary, and Space Sciences, UCLA, Los Angeles, CA 90095 dap@mars.ucla.edu

Introduction: Mars today is a frozen planet. With the exception of the warmest near-surface regions during the warmest times of day/year, Mars is in a completely frozen state at all latitudes to kilometer depths. The cold state of the current Martian climate is fundamentally due to Mars' average distance from the sun, and the absence of sufficient atmospheric greenhouse gasses to warm the surface. Here I examine the current partitioning of carbon dioxide between the Martian polar caps and atmosphere and suggest that this current state is not coincidental, but the predictable consequence of a nearly perpetually frozen planet.

Snowball Earth: The current state of the Martian climate resembles the hypothesized state of the Earth's climate system 500-800 million years ago, when the surface of the Earth repeatedly became entirely or nearly entirely frozen [1]. "Snowball Earth" episodes are believed to have been initiated when cooling events resulted in runaway ice-albedo-temperature feedback processes that cooled the Earth from the poles to the equator. It has been proposed that Earth was able to escape from snowball states because of the accumulation of carbon-dioxide gas in the atmosphere. Earth maintains an approximate balance of greenhouse gasses over million-year timescales via feedbacks involving the aqueous weathering reaction silicate rocks, which remove CO_2 from the atmosphere, and volcanic activity, which add CO_2 to the atmosphere [2]. The cold dry climate that existed during Snowball Earth episodes drastically reduced the rates of aqueous weathering, while the emission of reconstituted carbon-dioxide from volcanos driven by plate tectonics continued unabated. The resulting spikes in CO_2 concentrations were apparently sufficient to warm the atmosphere to melt of the global surface ice layer, and to also deposit widespread "cap carbonates" which are observed to overly Snowball Earth glacial deposits [3]. Earth's geologic record includes evidence multiple earlier extreme glacial periods extending back >2.4 billion years [4]. The fact that the young sun's luminosity was only 80% of its current value during this period probably contributed to Earth's protozoic snowball tendencies.

Kahn's Hypothesis: Mars today is not covered with high albedo ice, but it's generally cold temperatures and 6 mbar CO_2-dominated atmosphere is very close to the triple point of water, and thus permits the ephemeral stability of pure liquid water only in low altitude regions during the warmest daytime periods [5]. This potential coincidence between Mars' atmospheric pressure and the triple point was noted by Kahn in 1985, and this led him to propose (which at the time was) an extremely bold hypothesis, which is that the Martian atmosphere had evolved to this state by draw-down of atmospheric CO_2 by aqueous weathering of igneous rocks [6]. In Kahn's model, if CO_2 concentrations in the Martian atmosphere were to increase and become more favorable for the widespread stability of near-surface liquid water, then aqueous weathering reactions such as the formation of carbonates would draw down the CO_2 concentration in the atmosphere to the point where surface liquid water would no longer be stable. In the intervening 35 years, a variety of new observational data has emerged that appears to support the general scenario outlined in Kahn's original paper.

Carbonates and Organics: Martian carbonates have now been definitively detected in a range of contexts, including: orbital remote sensing observations of sedimentary rock outcrops and Martian dust, landed compositional measurements in Martian soil and rocks, as well as alteration products in Martian meteorites [7]. It has also been proposed that a CO_2 can be drawn out of the Martian atmosphere to form organic carbon phases and perchlorates through the corrosion of igneous minerals in the presence of brines [8] .The products of these reactions are observed in Martian meteorites, and similar chemistry may be mirrored in the sedimentary rocks analyzed by the MSL SAM instrument at Gale Crater [8]. The quantities of carbonates and organics that have been acquired to date do not support the weathering of a dense CO_2-dominated Noachian atmosphere [7], but instead suggest low levels of carbonate formation in transient aqueous environments with limited water availability. The presence of abundant un-weathered olivine on Mars today also supports this conclusion [7].

Mars' Small South Residual Polar Cap is No Coincidence: Through orbital and infrared and radar observations, we now know that Mars' south residual polar cap contains remnant surface CO_2 deposits that are in approximate solid-vapor equilibrium with the Martian atmosphere [9], as well as a thick buried CO_2 ice deposit that contains the equivalent of 6 mbar of gaseous CO_2 [10].

The small masses of Mars' present surface and subsurface remnant CO_2 reservoirs could also be interpreted as coincidental. In Leighton and Murray's original model, if there is enough CO_2 in Mars' cap-

atmosphere reservoir to support a permanent frozen CO_2 deposit at one of the Martian poles, then the partial pressure of CO_2 in the Martian atmosphere would be determined by the vapor pressure of the permanent CO_2 deposit, which is in turn determined by its annual heat balance [11]. In their 1973 paper, Murry and Malin [12] postulated that a large permanent reservoir of excess solid CO_2 must exist today on Mars, and proposed (erroneously) that it is located within larger north residual polar cap. The perennial CO_2 deposit at Mars' south residual polar cap would appear to satisfy the need for a permanent excess CO_2 reservoir, but such a small reservoir would appear be sufficient to survive warming episodes due to decreases in its surface albedo or increases in insolation during periods of higher obliquity.

It is easy to envision how long-term draw-down of atmospheric CO_2 by weathering will inevitably diminish the mass of a residual polar CO_2 deposit. In a scenario in which the heat balance of the residual CO_2 polar cap is forced by periodic obliquity variations, or any other climate forcing parameter, CO_2 added to the atmosphere will inevitably be lost to the cap-atmosphere system due to draw-down by weathering. The end result of the process is an atmospheric pressure "ceiling" that just barely permits the formation of aqueous weathering products (i.e. Kahn's original hypotheses), but also the near complete loss of residual polar CO_2. The existence of only a small CO_2 deposit at the south residual cap today suggests that present-day global aqueous weathering rates are sufficiently small as to have negligible long-term effects. Near-surface aqueous weathering environments will only become widespread on Mars when atmospheric pressures are roughly double their present-day values. One data point that confirms that the present state of the Martian climate may be "typical" comes from analyses of gas trapped in impact glass from the 180-million-year-old Mars meteorite EETA79001. The chemical and isotopic composition of the gas in EETA79001 is a perfect match for the Mars atmosphere as measured by Viking, and show CO_2 concentrations that are between one and two times the present Martian value [13].

Implications for Long-Term Climate: It has long been recognized that the draw-down of atmospheric CO_2 by weathering has important potential climatic implications [14]. While the rates at which weathering processes take place are highly uncertain, we can expect that they would accelerate with increasing temperature, CO_2 concentration, and liquid water availability. Given that weathering processes appear to be active in Mars' current climatic state, it seems reasonable to conclude that they would become even more active earlier in Mars' history when a considerable body of geologic evidence has been interpreted to suggest that Mars had a warmer and wetter climate [15]. Previous authors have suggested that past weathering sinks for atmospheric CO_2 on Mars could have been balanced by the release CO_2 via the thermal decomposition of weathering products by volcanism [14] or impacts [16]. However, even if Mars' past inventory of CO_2 was sufficient to somehow maintain long-term or ephemeral warm wet greenhouse conditions, the inability of Mars to reconstitute weathered CO_2 products appears to have sealed its ultimate snowball fate.

References: [1] Kirschvink et al., PNAS 97, (2000). [2] Walker et al, JGR Oceans, 86, (1981) [3] Hoffman, Science 281, (1998). [4] Young, Geosci. Front. 4, (2013). [5] Haberle, JGR 106 (2001). [6] Kahn, Icarus 62, (1985). [7] Niles et al., Space Sci. Rev. 174 (2003). [8] Steele et al., Science Advances 4, (2018). [9] Paige and Ingersoll, Science 228, (1985). [10] Phillips et al., Science 332, (2011). [11] Leighton and Murray, Science 153, (1966). [12] Murry and Malin, Science 182, (1973). [13] Pepin, Nature 317 (1985). [14] Pollack and Toon, Icarus 50 (1982). [15] Ramirez and Craddock, Nature Geoscience 11 (2018). [16] Carr, Icarus 79, (1989).

EVOLUTION OF THE MARTIAN SOUTHERN SEASONAL POLAR CAP EMISSIVITY DURING SPRING OF MY24-26. A. Pankine[1], [1]Space Science Institute, 4765 Walnut St, Suite B, Boulder, CO 80301 (apankine@spacescience.org).

Introduction: Seasonal Polar Caps (SPC) form on Mars from condensing atmospheric CO_2 each winter and recede during spring. A small patch of CO_2 ice dubbed Southern Polar Residual Cap (SPRC) is present year-round near the south pole. The temperature of the surface CO_2 ice in equilibrium with atmosphere is maintained near 140 K. Early observations from orbiting spacecraft revealed brightness temperatures significantly below the equilibrium temperature over portions of the SPC [1]. Later analysis [2, 3] suggested that this 'cold spots' are due to low surface emissivity associated with the presence of fine-grained CO_2 ice on the ground. This work presents the first systematic retrievals of SPC surface emissivity during southern spring (Ls=180–270°) using data collected by Mars Global Surveyor (MGS) Thermal Emission Spectrometer (TES) [4] in Mars Years (MY) 24, 25 and 26. Evolution of the SPC in the Southern Polar region (SPR) was analyzed in [5] using TES data from the pre-mapping aero-braking phase of the mission (MY23 Ls=180–360° MY24 Ls=0–24°). This work expands this analysis to data collected during the mapping phase of the mission and uses a different retrieval approach. MY24 and MY26 were 'typical' Mars year with relatively low dust opacities over southern SPC during spring, while in MY25 a Global Dust Storm (GDS) developed in the early spring (at Ls~185°) significantly increasing dust opacities over SPC until late spring.

Retrieval methodology: Retrievals of surface emissivity and atmospheric dust opacity over Martian SPCs is a difficult problem. Low surface and atmospheric temperatures result in a low thermal contrast between atmosphere and surface, and a weak spectral signal for surface emissivity and atmospheric dust (see Figure 1 for examples of TES spectra over southern SPC). In addition, TES spectra of cold targets are significantly affected by a radiometric error at wavenumbers larger than ~800 cm^{-1}, which produces an upward slope or very low radiances at this spectral range [6]. To alleviate these problems, the dust opacity τ and surface emissivity ε are retrieved using TES radiances observed at wavenumbers 264 cm^{-1} and 508 cm^{-1} (corresponding to wavelengths of ~40 μm and ~20 μm, respectively). At these wavenumbers the dust extinction differs by a factor of ~2, while the CO_2 frost emissivity is similar for a wide range of ice grain sizes [5]. This allows distinguishing the effects of atmospheric dust from surface effects in the TES spectra. The surface temperature was fixed to the condensation temperature of the CO_2 ice over the SPC. To improve the quality of the data, 10 consecutive spectra were averaged. To improve retrieval accuracy, only the data collected between local times of 8 am and 8 pm, and only when the sun is above the horizon, were used in the retrieval. Figure 1 shows examples of TES spectra and retrievals over southern SPC in MY24.

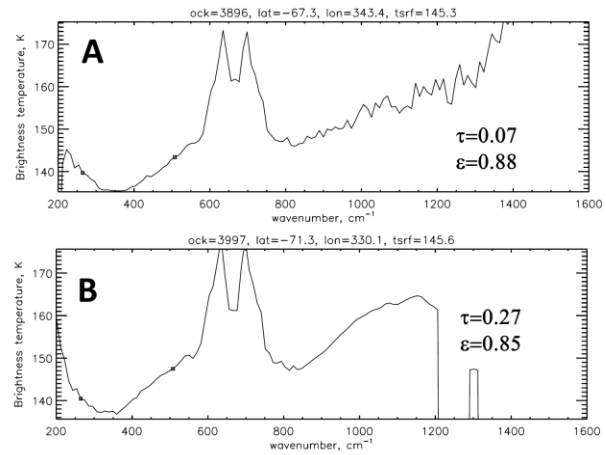

Figure 1. Examples of TES MY24 spectra and retrievals, with retrieved dust opacity values τ and CO_2 frost emissivity ε shown on the plots. A) Spectrum over SPC, low dust opacity, low CO_2 frost emissivity. B) Spectrum over SPC, high dust opacity, low CO_2 frost emissivity.

Results: Figure 2 shows polar maps of retrieved thermal reflectance (1-ε) at 20 μm at selected time periods during southern hemisphere spring (results for atmospheric dust retrieval will be presented elsewhere). CO_2 emissivity varies across the SPC and with time. At the beginning of spring high reflectance (low emissivity) areas are found near the outer edge of the SPC between longitudes 225°–360°–45° E. After Ls~245° high reflectance area occupies most of the area of the receding SPC. The spatial and temporal evolution of CO_2 emissivity is remarkably similar in the observed years (MY24–MY26) and also consistent with the evolution observed in MY23 [5]. The areas of high reflectance (low emissivity) were previously interpreted [2,3,5] as areas with small CO_2 ice grains. From comparison with emissivity estimates based on Mie modeling [7] the CO_2 particles in these areas have sizes between 1 mm and 1 cm with possible admixture of H_2O

ice and/or dust. The areas of high emissivity are interpreted as CO^2 grains larger than 1 cm and slab ice.

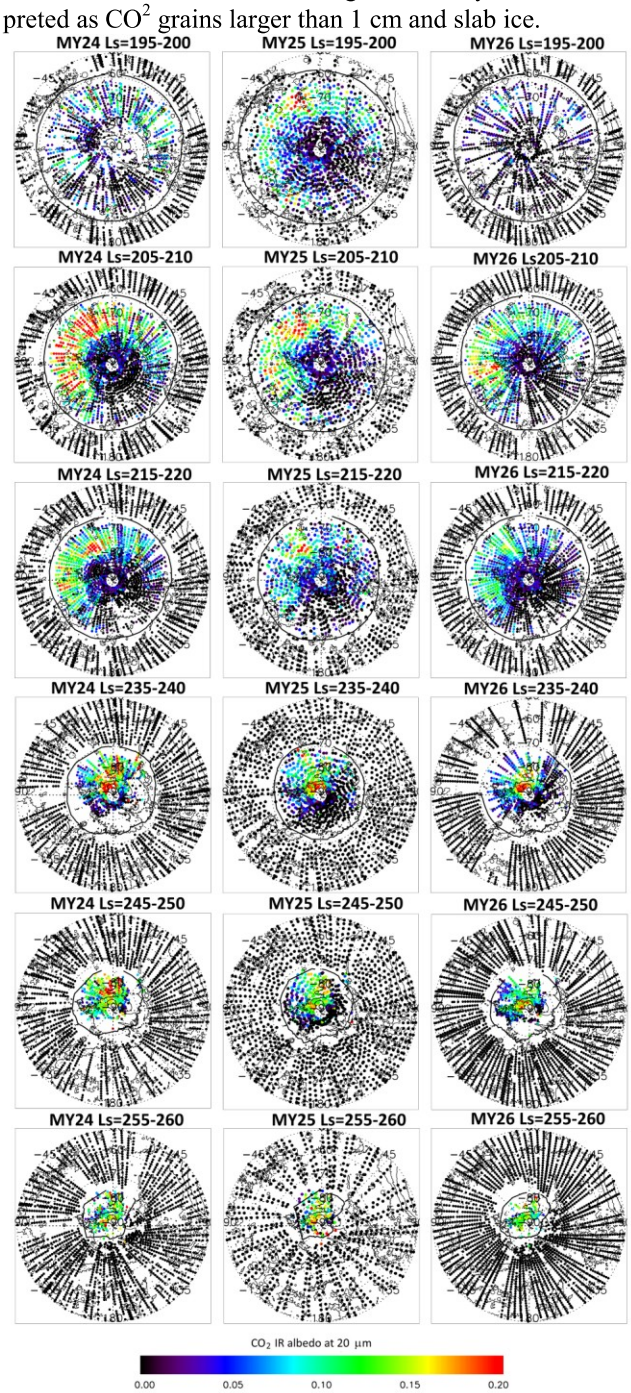

Figure 2. Polar maps of retrieved surface thermal reflectance (1-ε) at 20 µm in the SPR for Ls=195-260° in MY24–26. Outer edge of the map is at latitude -50°. East longitudes increase clockwise from top. Light contours are MOLA topography, heavy contour is approximate edge of the SPC.

The peculiar asymmetry in distribution of CO_2 grain sizes across SPC was previously interpreted as being due to two different deposition regimes arising from atmospheric circulation modified at the SPR by the large-scale topography of the Hellas impact basin (centered on 25° S and 65° E, upper right on maps in Figure 2) [8]. Over areas west of the Hellas, where low CO_2 emissivity areas are found, atmospheric precipitation dominates over surface deposition, forming smaller grains. East of the Hellas frost is accumulated by direct deposition, forming larger grains and dark CO_2 slab ice.

References:

[1] Kieffer, H. H. et al. (1976) *Science*, 194, 1341–1344. [2] Forget, F. et al. (1995) *J. Geophys. Res*., 100, 21219–21234. [3] Titus, T. et al. (2001) *J. Geophys. Res*., 106, 23181–23196. [4] Christensen, P. R. et al. (2001) *J. Geophys. Res*., 106, 23823-23871. [5] Kieffer, H. H. et al. (2000) *J. Geophys. Res*., 105, 9653-9699. [6] Pankine, A. A. (2015) *Planet. Space Sci*., 109, 64-75. [7] Titus, T. N. et al. (2008) *The Martian Surface: Composition, Mineralogy, and Physical Properties*, 578–598. [8] Colaprete, A. et al. (2005) *Nature*, 435, 184–188.

Present-day and (very) recent past influences on trough migration: Measuring the spatial variation in ice sublimation of equatorial-facing spiral trough walls. A. C. Pascuzzo[1], L. Melendez[2], and J. F. Mustard[1], [1] Dept. of Earth, Environmental, and Planetary Science, Brown University, RI, USA (alyssa_pascuzzo@brown.edu), [2]School of Geosciences, University of Southern Florida, FL, USA

Introduction: The topography and albedo of the martian north polar cap (Planum Boreum) strongly influence present-day and past exchange of water vapor between the planet's surface and atmosphere. In this study, we begin to investigate the role that the spiral troughs, which dissect the north polar layered deposits (NPLD), play in the total amount of water vapor sublimated from the Planum Boreum region.

We are interested in whether there is a measurable lateral difference in the amount of water ice sublimating along the trough walls. Our goal is to answer the following question: do local heterogeneities along a trough wall (i.e., trough wall slope, azimuth, and dust veneers) affect the amount of ice being sublimated over 100's to 1,000-year timescales that is measurable today? Answering this question is needed in order to construct a better understanding of the local scale aeolian removal and depositional processes of ice and dust that have shaped the polar cap in the very recent past. This abstract establishes the problem and tasks that lie ahead.

Motivation: *Spiral troughs.* To interpret the environmental records preserved within the troughs, including the NPLD, the processes behind the formation and modification need to be better characterized. Here, we would like to focus attention to the modification processes at the present-day surface. The evidence of spiral trough migration through time from radar data [1] and modeling [2] plus the detections of low altitude spring-summer clouds within troughs suggest that the sublimation and ablation of ice from the troughs via slope winds plays a vital role in the evolution and shape of the polar ice cap [1,3–6]. Understanding how and why recent past and present-day sublimation varies spatially at the pole can be used to help unravel the record of past climate variability in the Amazonian.

Not every trough behaves the same. Regional and local conditions can cause in situ trough ablation and sublimation rate to vary spatially [4]. Spatial variability in the intermediate to long-term sublimation rate could result from the combined variation in topography of the trough wall, albedo (e.g., dust cover or grain size), and thermal inertia (surface material, grain size, porosity). The effects of these surface characteristics on the local trough evolution are not well understood.

Geologic Context: The equatorial-facing (high side) of the trough walls expose the upper and lower sections of the quasi-alternating bright- and dark-toned layers of the NPLD. [7,8] characterized the stratigraphy of an exceptional NPLD trough exposure, designated as site N0 [9], which showed in HiRISE detail the morphologic differences in the NPLD layering both vertically and laterally. Vertically, the layering alternated between rougher dark-toned marker beds [10,8] to smoother brighter toned layers. [9,11] used the rough versus smooth layer characteristics as a proxy for erosional resistance. Using HiRISE digital terrain models (DTM), [9,11] made protrusion profiles of the layers and matched the marker beds to the most protruding later as identified by [8].

At N0, there is lateral variability in the surface characteristics of the equatorial-facing trough wall. These characteristics are the slope and direction of the wall, as well as the amount of dark mantling debris blanketing the exposed NPLD. This observation is common among other troughs as well [12–14]. Tracking westward along high-side of the trough we see the wall changes its orientation from south to south-east before return to south again (Fig. 1). The wall curves outward away from the pole at this section in the trough (Fig. 1 region B). The slope of region B is 5° shallower than the slope of region A (8° average). Following the curvature of the trough we see an increase in the amount of dark debris mantling and slightly obscuring the NPLD textures. The albedo change due to the veneer continues westward along the trough outside of the HiRISE observation (visible in CTX images). We looked at various overlapping CTX

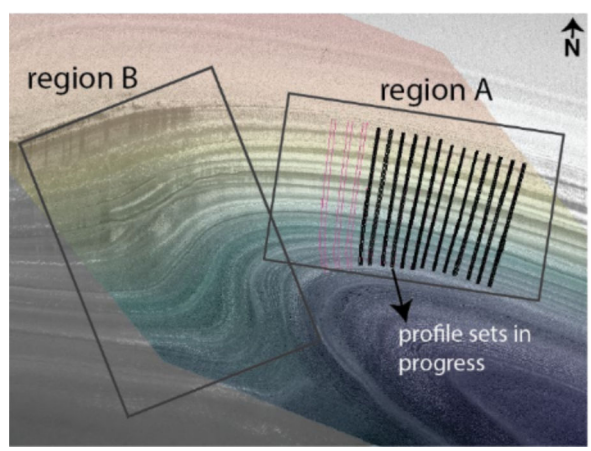

Fig 1. HiRISE DTM (colored) and HiRISE greyscale overlying CTX greyscale image of trough site N0 (87°N 92.8°E). Region A is free mantling dust and debris compared to Region B. Region B is marked by the change in trough direction, shallower slope, and thicker more extensive debris mantle that continues west off of the fig..

observations and HiRISE images from other mars years and found the mantling debris immobile from year-to-year. However, the distribution and extent were likely different 10's and 100's of years in the past.

Why does the trough wall suddenly curve (as do many others)? The answer to this question is likely coupled in understanding the processes the drive the onset of trough formation, which is yet to be fully understood. Has there been a long-term difference in ice sublimation rate between region A and region B (Fig. 1)? Has region A been migrating northward at a faster rate than region B, and why? Can we measure this difference and narrow down the processes responsible?

Methodology: The goal in this work will be to calculate the amount of relative layer protrusion and recession between the erosionally resistant-rough-marker beds and the recessive-smoother-icier layers, which sandwich the marker beds. For this, we focus on trough site N0. We want to see if there is a significant change in the amount that the layers are recessed (via sublimation/ablation) relative to their corresponding protruding marker beds as you move laterally across the trough from region A to B. To do this, we will use the orthorectified HiRISE DTMs [15,16] and take elevation profiles in sets separated by ~100 m. Each profile set will consist of 5 elevation profiles spaced ~10 m apart. This method ensures an average measurement of the protrusion for a given 50 m segment as we move along the trough wall (Fig. 1). Elevation profiles will be drawn near perpendicular to the orientation of the layering.

The elevation profiles will be used to calculate the average protrusion of each 50m segment using methods described by [9,11] as illustrated in Fig. 2a. This method detrends the elevation profile in order to produce a protrusion profile (protrusion in meters vs. elevation) (Fig. 2). Once the protrusion profiles are calculated, the protrusion peaks are identified and matched to their marker-bed as identified by [8,9]. Protrusion measurements are calculated for each marker bed by subtracting the peak protrusion value from the minimum adjacent recessive values connected by a continuum (Fig. 2b). The protrusion calculations for each sandwiched marker bed will be plotted against the trough wall slope, azimuth, and photometrically corrected albedo. We will determine if there is a measurable difference in the lateral in-situ trough ice sublimation and whether any of the following scenarios are possible explanations.

Sublimation Scenarios: If there is a measurable difference between regions A and B, we propose the following scenarios to explain spatial water ice sublimation variability along the high-side of the trough. It is likely a combination of the slope and debris cover cases proposed below. Case 1) thin dust layer would enhance sublimation of ice underneath, which would result in the dust-covered trough to result in more ice being sublimated normal to region B relative to a veneer free region A. Case 2) thick dust cover (>cm) would inhibit sublimation of underlying ice, which would result in region B having lesser difference in the amount of ice sublimated relative to a region A. Case 3) the slope of the trough is shallow, which means seasonal katabatic winds are weaker leading to less ice sublimation relative to adjacent steeper region A. Case 4) the slope of the trough is steep, which means seasonal katabatic winds are stronger, leading to more ice sublimation relative to adjacent shallower sloped wall of region B.

References: [1] Smith, I. B. and Holt, J. W. (2010) Nature, 465, 450–453; [2] Bramson, A. M. et al. (2019) JGRP, 124, 1020 1043; [3] Smith, I. B. et al. (2013) JGRP, 118, 1835–1857; [4] Smith, I. B. and Holt, J. W. (2015) JGRP, 120, 362–387; [5] Smith, I. B. and Spiga, A. (2018) Icarus, 308, 188–196; [6] Spiga, A. and Smith, I. (2018) Icarus, 308, 197–208; [7] Fishbaugh, K. E. et al. (2010) Icarus, 205, 269–282; [8] Fishbaugh, K. E. et al. (2010) GRL, 37; [9] Becerra, P. et al. (2016) JGRP, 121, 1445–1471; [10] Malin, M. C. and Edgett, K. S. (2001) JGRP, 106, 23429–23570; [11] Becerra, P. et al. (2017) GRL, 44, 2016GL071197; [12] Squyres, S. W. (1979) Icarus, 40, 244–261; [13] Rodriguez, J. a. P. et al. (2007) Mars Journal, 3; [14] Milkovich, S. M. et al. (2008) PSS, 56, 266–288; [15] Kirk, R. L. et al. (2008) JGRP, 113; [16] McEwen, A. S. et al. (2010) Icarus, 205.

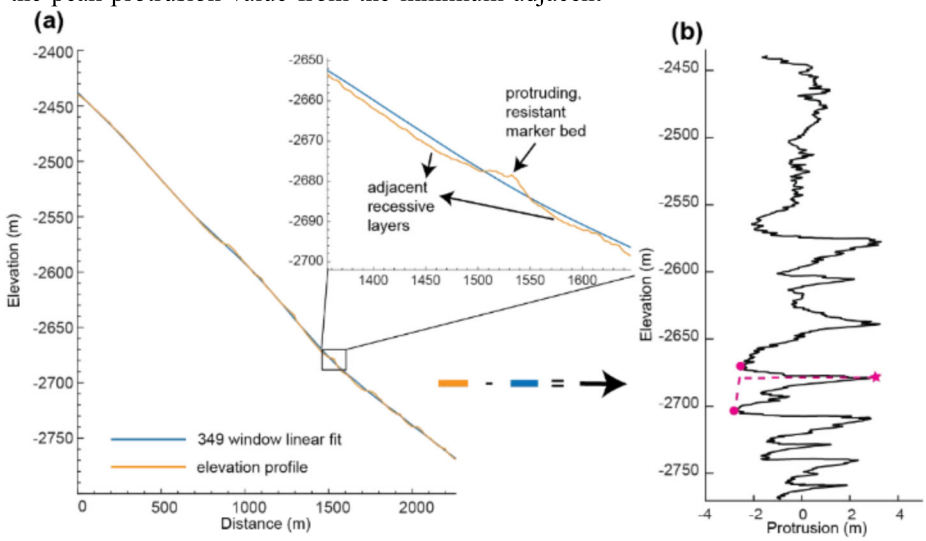

Fig 2. (a) Elevation profile from region A. (b) Protrusion profile made from subtracting the linear fit of the elevation file to the elevation profile. Pink star is the protrusion peak for the marker bed in (a). Pink circles are the minima from the adjacent recessive layers. The pink lines show how protrusion measurements will be calculated for each marker bed using the local minima to create a continuum.

Stability of Subsurface Carbon Dioxide Ice over the Obliquity Cycle. N. Patel[1], S. R. Lewis[1], A. Hagermann[2] and M. Balme[1], [1]The Open University, UK (narissa.patel@open.ac.uk), [2]University of Stirling, UK

Carbon dioxide (CO_2) ice does not remain stable at the surface of Mars for long periods of time over the obliquity cycle. We use the UK version of the LMD Mars Global Circulation Model (MGCM) [1] with a newly integrated subsurface scheme to investigate how the timescales for the stability of CO_2 ice are affected by overlying regolith at different obliquities within the range expected for Mars over the last 4 Myrs [2].

Introduction: Martian subsurface ice studies have focused on the distribution of water ice, because the amount of subsurface CO_2 ice present has been considered insignificant. This is because present day surface and subsurface temperatures are only temporarily low enough for the presence of CO_2 ice.

The large variability of martian obliquity significantly impacts surface and subsurface temperatures [3], affecting the timescale and distribution of CO_2 ice stability at the surface. At low obliquities, mean surface temperatures drop and the perennial CO_2 polar caps extend equatorward [e.g. 4, 5]. Conversely, at high obliquities, higher surface temperatures mean the CO_2 polar cap sublimates, revealing the water ice below which migrates equatorwards [e.g. 5, 6]. In all obliquity cases, it has been assumed CO_2 only occurs as either surface ice at the poles, vapour within the atmosphere or adsorbed in the regolith, ignoring the potential for subsurface CO_2 ice.

Investigations into the South Polar Layered Deposits (SPLD) using data from the Shallow Radar (SHARAD) on the Mars Reconnaissance Orbiter revealed the presence of buried CO_2 ice deposits interspersed with layers of water ice [7]. The amount of CO_2 ice stored within these deposits has been estimated to be enough to nearly double the present day atmospheric pressure if released [7, 8].

One suggested mechanism for the formation of the SPLD is that surface CO_2 ice slabs form during obliquity minima and are then buried under a water ice layer that accumulates in the south when perihelion occurs during northern summer and while the obliquity is still low enough for the CO_2 ice to remain stable [9]. Another possibility is the CO_2 ice deposits could form within the subsurface, and when the obliquity changes, these deposits would persist for longer due to the effect of the overlying regolith reducing the sublimation rate, as has been demonstrated for water ice [e.g. 10]. We investigate how the stability of CO_2 ice is affected by a thin layer of regolith compared to at the surface boundary layer that exchanges with the atmosphere over a range of obliquities.

Method: The subsurface scheme integrated into the MGCM comprises of three sets of interdependent calculations (temperature, water and CO_2). The equations used throughout the subsurface scheme are from experimental work at Mars relevant temperatures and pressures.

The thermal scheme uses a finite volume discretization of the heat conduction equation, with a thermal conductivity that varies with depth and both water and CO_2 ice content. The thermal conductivity of the empty regolith uses the method of [11], the water ice thermal conductivity is from [12] and CO_2 ice thermal conductivity is from [13].

The water scheme was developed using mostly the same water properties as in the previous subsurface scheme of the MGCM [14]. The main differences between the two schemes are a finite volume method is used to discretise the vapour diffusion equation and different equations of state have been used [from 15]. Adsorption effects have also been ignored in the new scheme because the inclusion of an adsorption isotherm has been shown to have a negligible effect on long term ice accumulation [16].

The CO_2 scheme uses the same methods as the water scheme, but with equations appropriate for CO_2. The diffusion coefficient used is from [17], the equations of state are from [18] and a variable density of CO_2 ice is used [19].

Preliminary Results and Discussion: We present results from a series of simulations with different initial amounts of both water and CO_2 at three different obliquities (15º, 25º and 35º). Figures 1 and 2 show examples of the results from these simulations, using an initial condition of 50% of the pore space filled with water ice and 50% with CO_2 ice. The initial global coverage of both ices gives an idea of where CO_2 ice could survive in the subsurface at each obliquity if already present. This is useful because the exact amount and distribution of subsurface CO_2 ice in the present day is unknown and has never been investigated, so the results from this study will be used to inform where CO_2 could be present for the initial conditions for future investigations.

Figures 1 and 2 show the number of sols CO_2 ice is stable for in the surface layer and at a depth of 0.012 m, respectively. The CO_2 ice in the surface layer equilibrates with the atmosphere near instantaneously from the changes in temperature associated with a change in obliquity, whereas CO_2 ice in the subsurface would take longer to respond to this change. The longer response time is because subsurface ice is not in direct contact with the atmosphere and vapour needs to diffuse through the overlying regolith before equilibrating with the atmosphere. The diffusion coefficient

[16] controls the rate of this diffusion and has a range of 0.00018 m/s to 0.11 m/s when the porosity ranges from 0.01 (when ice nearly fills the pore space) to 0.5 (with no ice) at 150 K.

The observed effect of the overlying regolith on the rate of sublimation in these simulations demonstrates that subsurface CO_2 ice could remain stable for longer periods than surface ice after a change in obliquity. This allows enough time for a water ice layer to deposit over the CO_2 ice, trapping it within the subsurface. Future investigations will involve running simulations with more realistic initial CO_2 ice distributions, such as using the resulting distribution at one obliquity as an initial condition for a different obliquity

References: [1] Forget, F. et al. (1999) JGR: Planets, 104, 24155-24175 [2] Laskar, J. et al. (2004) Icarus, 170, 2, 343-364 [3] Schorghofer, N. (2008) Geophys. Res. Lett., 35, 18 [4] Head J.W. et al. (2003) Nature, 426, 6968, 797-802 [5] Pollack J.B., Toon O.B. (1982), Icarus, 50, 2, 259-287 [6] Mellon M.T., Jakosky B.M. (1995) JGR:Planets, 100, 6, 2156-2202 [7] Phillips R.J. et al. (2011) Science, 332 (6031), 838-841 [8] Bierson, C.J. et al. (2016) Geophys. Res. Lett., 43, 4172-4179 [9] Manning C.V. et al. (2019) Icarus, 317, 509-517 [10] Chevrier, V. et al. (2007) Geophys. Res. Lett.,34, 2 [11] Grott, M. et al. (2007) JGR: Planets, 112, 2156-2202 [12] Klinger, J. (1981) Icarus, 47, 3, 320-324 [13] Ross, R. G. and Kargel, J. S. (1998) in Solar System Ices, Springer, 33-62 [14] Steele L.J. et al. (2017) Icarus, 284, 233-248 [15] Hardy, B. (1998) in Proc. 3rd Int. Symp. Humidity and Moisture, London, UK [16] Schorghofer, N. and Aharonson, O. (2005) JGR: Planets, 110, 2156-2202 [17] Fanale, F. P. (1982) JGR: Solid Earth, 87, 10215 – 10225 [18] Kasting, J. (1991) Icarus, 91, 1 [18] Mangan, T. P. et al. (2017) Icarus, 294, 201-208

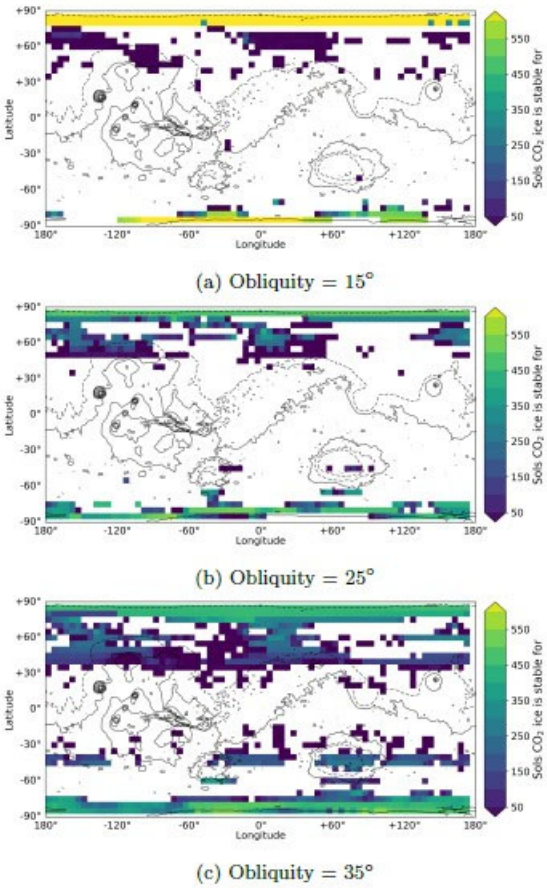

(a) Obliquity = 15°

(b) Obliquity = 25°

(c) Obliquity = 35°

Figure 1: Number of sols CO_2 ice remains stable at the surface for the entire day at an obliquity of (a) 15° (b) 25° (c) 35°. The plots show the results for the second year of a simulation with an initial condition of 50% of the pore space filled with water ice and 50% with CO_2 ice.

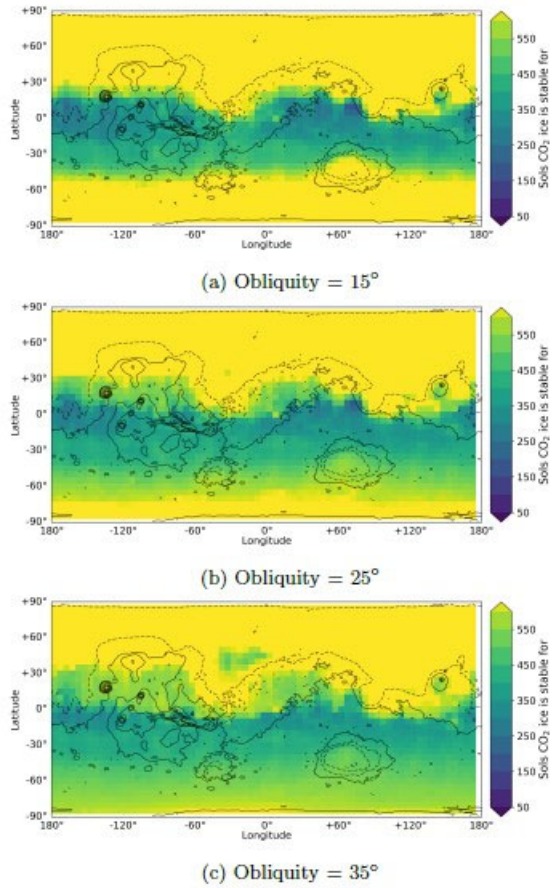

(a) Obliquity = 15°

(b) Obliquity = 25°

(c) Obliquity = 35°

Figure 2: Number of sols CO_2 ice remains stable at a depth of 1.2 cm for the entire day at an obliquity of (a) 15° (b) 25° (c) 35°. The plots show the results for the second year of a simulation with an initial condition of 50% of the pore space filled with water ice and 50% with CO_2 ice.

SULPHUR CREEK AND GALENA CREEK, WYOMING: LABORATORIES FOR UNDERSTANDING THE PRESERVATION OF DEBRIS-COVERED GLACIERS ON MARS E. I. Petersen[1], T. Meng[1], J. W. Holt[1], J. S. Levy[2], B. Tober[1], and M. Christoffersen[1]. [1]Lunar and Planetary Laboratory, University of Arizona (petersen@lpl.arizona.edu), [2]Colgate University

Introduction: Large, extensive debris-covered glaciers are found in the mid-latitudes of Mars at the bases of escarpments, in valley systems, and filling craters [1-6]. They likely preserve ice deposited during previous high spin-axis obliquity "ice ages," and are thus a record of ice transport between the polar and mid-latitude regions of Mars [7-8]. Understanding the processes by which debris-covered glaciers accumulate and are preserved will help us decode Martian climate history.

A terrestrial analog for Martian debris-covered glaciers are ice-cored rock glaciers, which contain buried ice covered entirely by talus debris. Many, such as Galena Creek Rock Glacier in the Absaroka Mountains, Wyoming, are known to preserve cores of pure ice from past alpine glaciation [9,10]. However, few studies examine the process of transition from alpine glacier to rock glacier [11]. We examine this transition by presenting a case study comparing Galena Creek Rock Glacier with the complex glacial system at Sulphur Creek ~3 km distance away.

Methods: This work integrates field observations with geomorphic mapping of a 24 cm/px orthophoto and DEMs produced from airborne photography acquired in September, 2016 and October, 2019.

Ground-penetrating radar (GPR) at 100 MHz and 50 MHz was also acquired at select locations across the features, in order to measure the thickness and purity of buried ice as well as image internal structure.

Results: *Site Geomorphology:* Galena Creek Rock Glacier has been previously mapped into a number of rock glacier lobes by [12] (Figure 1a). The upper 2/3 of the system is known to be cored by up to 20 m of pure glacier ice under 0.8-1.0 m of continuous debris cover, while the lower 1/3 of the system is composed of ice-cemented rock beneath 2-3 m of surface debris [9].

At the Sulphur Creek system we mapped the following three geomorphic regimes (shown in Figure 2a) based on traits seen in the photogrammetric products, as well as ground-based observations:

(1) A partly debris-covered alpine glacieret extending ~300-600 m from the headwall, ~3120-3500 m.a.s.l., exhibiting crevasses, debris-covered hillocks, and ending in a raised moraine. A snow pit dug in August, 2019 measured 138 cm of seasonal snow. Debris thickness increases towards the terminal moraine, from discontinuous ~10 cm debris in the lower accumulation zone to 20 cm continuous debris 110 m from the moraine to > 50 cm within 20 m of the moraine.

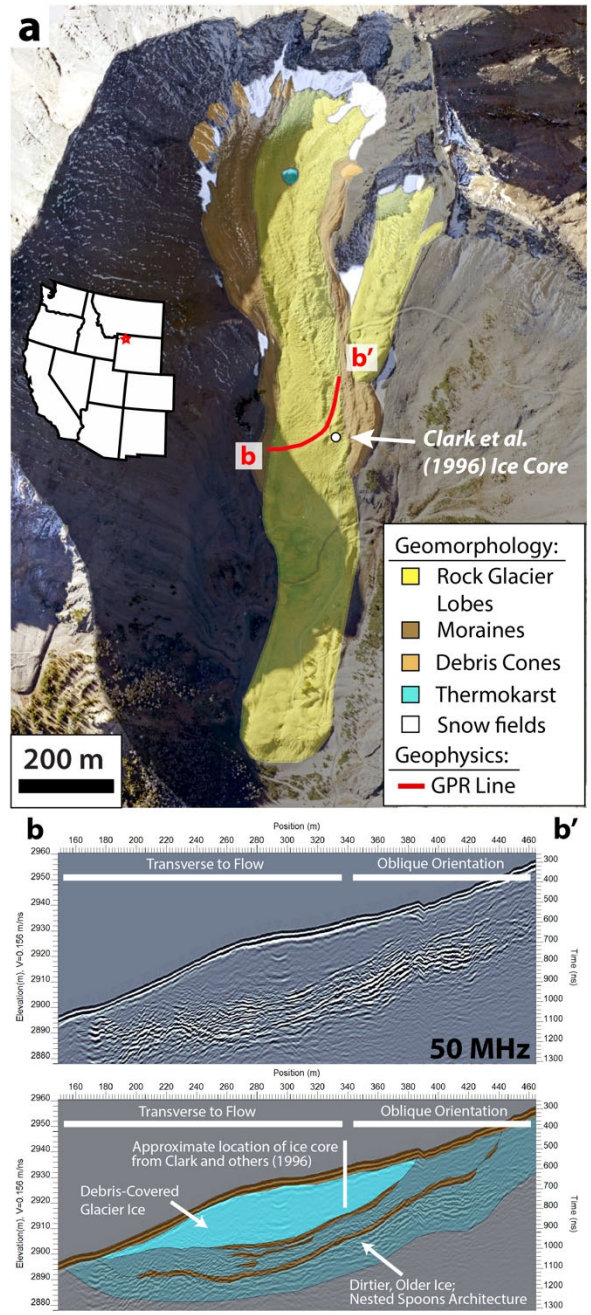

Figure 1: *(a) Map displaying orthophoto of Galena Creek Rock Glacier with gross geomorphic regimes and GPR surveys displayed. Inset indicates location in western USA. (b) GPR data across the rock glacier mid-section; 20-25 m thick core of glacier ice along with underlying nested spoons architecture is revealed. Note the convex-up surface topography.*

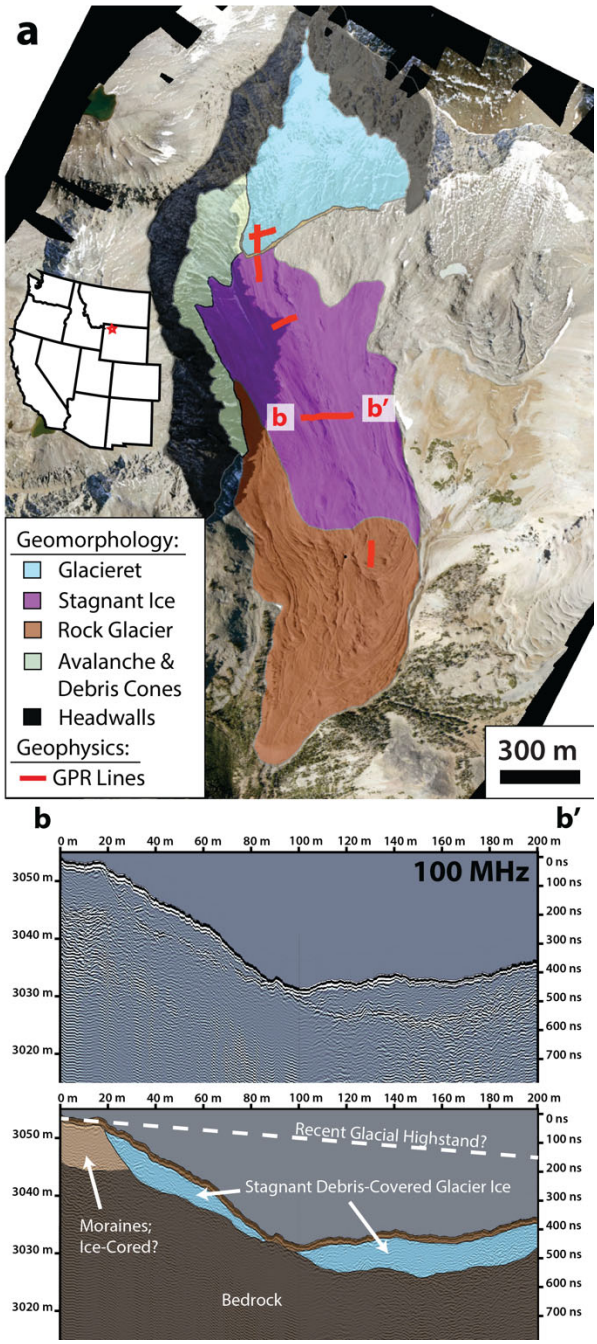

Figure 2: *(a) Map displaying an orthophoto of the Sulphur Creek system with gross geomorphic regimes and GPR surveys displayed. (b) GPR data across the mid-section of the valley; thin (< 10 m thick) ice deposits are revealed. Note the v-shaped surface topography.*

(2) A debris-covered stagnant ice zone ~1.1 km long at ~2880-3120 m.a.s.l. with highly deflated topography and abundant active thermokarst features. This region is cut off dynamically from the glacieret above. Ice exposures are abundant. Debris thickness is highly variable, ranging between 20 cm and ~1 m.

(3) A rock glacier tongue ~900 m long at ~2660-2880 m.a.s.l. with abundant compressional fold morphology, some thermokarst scars and ponds, ending in an oversteepened toe ~50-60 m high. Surface debris is up to 1.8 m thick.

Ground-Penetrating Radar: The results of a 50 MHz radar transect across the mid-section of Galena Creek Rock Glacier are shown in Figure 1b. A debris-covered ice core 20-25 m thick was imaged over a set of reflectors forming a nested spoons architecture.

The results of a 100 MHz radar transect across the stagnant ice mid-section of Sulphur Creek are shown in Figure 2b, displaying localized ice deposits < 10 m thick. The upper glacieret was measured locally at up to 18 m, thickening upslope, while the lower rock glacier was measured at ~30 m thickness.

60 diffraction hyperbolae were measured in radar data on Sulphur Creek, providing statistics on the dielectric constant and composition of measured deposits. The glacieret and stagnant ice zones yielded results that were statistically the same, with mean $\varepsilon' = 3.7 \pm 0.2$ for an ice content of >77%. The rock glacier yielded mean $\varepsilon' = 5.8 \pm 0.6$ for an ice content of ~26-50%.

Discussion: At both Galena and Sulphur Creek we find high ice purity in the deposits in the upper 2/3 of the valley in contrast to a more ice-poor lower rock glacier body. At Sulphur Creek the ice deposits are significantly thinner, more localized, and buried by surface debris up to 4-5 times thinner than the surface debris at Galena Creek.

We hypothesize that both valleys previously consisted of active alpine glaciers overrunning more ancient rock glaciers. At Galena Creek, sufficient debris cover allowed the glacier to be preserved in the form of the 20-25 m thick ice core observed in Figure 1b. However, at Sulphur Creek the debris cover was insufficient to preserve a significant amount of ice; the glacier retreated to its current glacieret state, leaving behind the stagnant ice deposits.

This study highlights the influence of debris availability on the preservation of glacier ice in otherwise very similar geologic settings. We will use these sites to quantify the debris-availability threshold for preserving glaciers and extrapolate our findings to Martian debris-covered glaciers.

References: [1] Squyres, S. (1979), JGR: Solid Earth, 84, 8087-8096 [2] Head, J., et al. (2009), EPSL, 294, 306-320. [3] Holt, J., et al. (2008), Science, 322, 1235-1238. [4] Plaut, J., et al. (2009), GRL 36. [5] Levy, J., et al. (2014) JGR: Planets, 119(10), 2188-2196. [6] Petersen et al. (2018), GRL 45(21). [7] Forget et al. (2006), Science [8] Madeleine et al. (2009), Icarus 203(2). [9] Potter (1972), GSA Bulletin 83(10). [10] Clark et al. (1998), Geogr. Ann. A: Phys. Geogr. 80(3-4). [11] Jones et al. (2019), Global and Planetary Change 181. [12] Ackert Jr. (1998), Geogr. Ann. A: Phys. Geogr. 80(3-4).

Atmospheric CO_2 Depletion at the Surface in the Polar Regions of Mars. E CSZ O a 4 UCSWLeRU C B ; KbWO 7 @ K A ; CK_OW) 7 = @M6 UCOO O @ DSMRK[N XW = F EMRXPSCUN = ERS[UCb =C] C[XY USXW KLX[K]X[b 6 KLSPX[VSK W]S]]OXP F OMRWXLX b GE4 (GVS_C[S]b XP 6 XLX[KNX 5 X UNC[GE4 1); K Y]XWGVS_C[S]b GE4 1 4 CXLS DO CK[MR GE4 1 =C DC]S[CN

Introduction: F RO bCK[Ub KVSW KWN KaSW XP]RO CK XWKU YXUK[MKY [OY[O OWY XWO XP]RO X] N[K K]SMOaY[O SXW XP]RO 6 B(MbMCO XW@K[S]R K S_O K X W] XP MK[LXW NSXaSNO MbMSMKUb OaY# MRKW ON LC] OOW]RO K] X YRC[O KWN]RO [PKMO I J 4 6 B(MKWNOWO XW]RO [PKMO SW]RO UXMKU 9 KLUKWN H SW]C[WXW#MKWNOWKLUO YOMSO [O KSWKWN KMM # UK]O SW]RO K] X YRC[SMMKU W [O U]SW SWK NOM[CK O XP]RO 6 B(YK[]SKUY[O [O KWN]R K UX C[SW XP]RO 6 B(F[X] YXSW]O YC[K] [O(% I(J H ONC]C[SWO]RO UX C[SW XP F 6 B(KWN NS M S] S YKM] XW]RO YXUK[OWC[b L N C] KWN [O SXWKLMS[M UK]SXW

Methods: F X NC]C[SWO(% O LSW@K[6 US# K]O EX WNC[@6 E XW@K[DOMKWWKS KWWO B [LS]C[I) J [C[SO_CN [PKMO]O YC[K] [O KMZ S[CN WCK[((F((KWN (j F (X_C[ ]RO CXUK[DO SXW f SW UK]S] NO KWN f WX[NC[ ]X XL]KSWTSWC]SM [PKMO]O YC[K] [O O YC[PX[K WOMO K[b O S S_S]b MK[# [OM]SXWI J LOMK O6 B(SMOO S S_S]b NOYOWN][XW# Ub XWM[b]KU S:O F RO O S S_S]b MK[[OM]SXW[CUSO XW]RO VSZ O YOM[KUY[XYC[]SO XP 6 B(SMO K] (KWN((j 9S [O U]SW SWK Z K S USWCK[[CUK]SXWRSY LC] OOWF (KWN F (k F((OO I J KWN 9S (H ROW F (3 F((SW]C[MOY] XP]RO [O [O SXWUSWO]RO [PKMO O S S_S]b] KYY[XKMR KWN]RO L[S R]WO]O # YC[K] [OCZ KU]RO TSWC]SM]O YC[K] [O(%

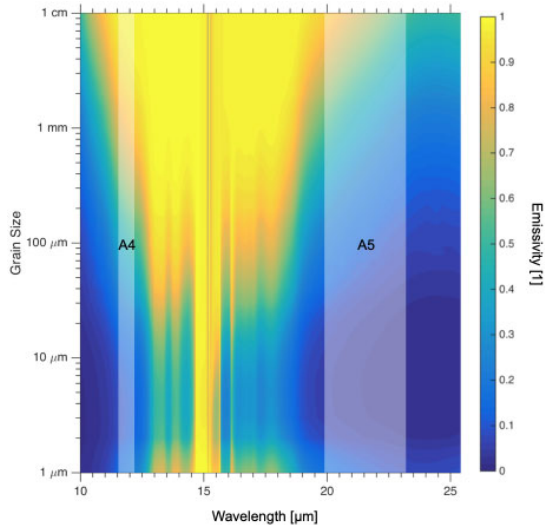

Fig. 1 0 @XNCUCN 6 B(SMO O S S_S]b K K P WW]SXW XP M[b]KU S:O KWN K_CUCW]R O S SXW KW UO XP - f]b YSMKUXP @6 E @6 E 6 RKWWCU 4 F (KWN 4 F((K[O SWWSMK]ON SW RS]O

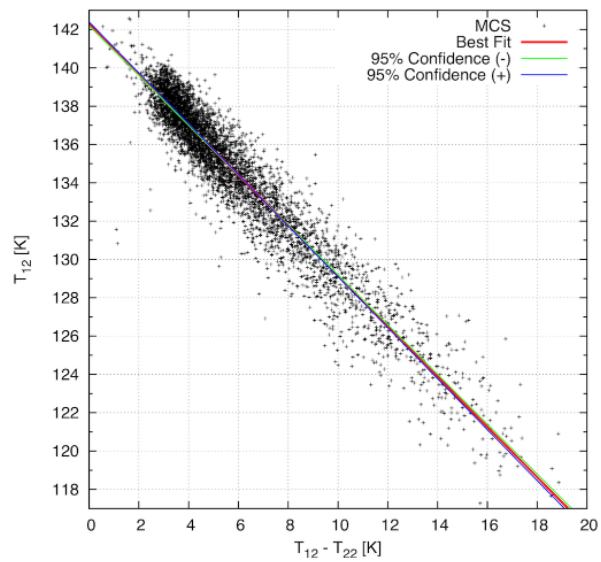

Fig. 2 0 8 aK YUO XP NC[S_K]SXW PX[F 6 B(PX[NK]K K] f2 2 (f #/ f2 K]S] NO2#. f H RC[O F (3 F(( ]RO [PKMO O S S_S]b S KWN F (3 F 6 B(W]RS OaY# K YUO]RO/ MKWWSNOWWO S _C[b KUU 2

E [PKMO 6 B(SMO MKW]K SWK]SXWLb N] KWN; (B SMO NX WX] CK [KLUb SW]C[PC[O S]R K MMO P UNC[S_K#]SXW XP F 6 B(LOMK O]RO b SCUN O S S_S]SO K[X WN K] ((KWN (j G WWC[]KSW]SO K[O NC]C[SWCN Lb PS]SW / MKWWSNOWWO [O [O SXW USWO 9S (H O]ROW MK YK[O F 6 B(S]R]RO]ROX[C]SMKU [PKMO P[X] YXSW] O YC[K] [O MKUM UK]ON SW]RO X]Y] XP K: OWC[KU 6 S[M UK]SXW@XNCUKWN 6 UKYOb [XW UK I J KWN MKW# _C[]]RO]O YC[K] [O NOY[O SXW]X KWCZ S_KUCW 6 B(YK[]SKUY[O [O 9[X RC[O O MKUM UK]O]RO OW]SMR# OW] SWWXW#MKWNOWKLUO K O OaY[O ON RC[O K]RO 4 [OWRKWWO OW] PKM]X[8 9 4[9S) KWN

Results: W]RO EX]R 9S) WCK[# [PKMO WXW# MKWNOWKLUO K O OWRKWWO OW] YCKT K] d d/ f K _KU O SWWSMK]S_O XP]K]SM SW]KLSUS]b KWN USTCUb _C[]SMKU SaSW XP]RO OW]S[O K] X YRC[SMMKU W I, J WNOON MKU WSW]O [K]ON 4 [MKWWOW[K]SXW NS# YUKb S SUK[_KU O O 2 8 9 4[2, LK ON XWNK]K KWKU# b S F[X]RO@K[B Nb Ob: K K D Kb E YOM[X C[C[: DE I-J MKWPS[SW]RO OaYOM]ON _C[]SMKUNSPP SXW E [PKMO NOYUC]SXW YXUO K[N XP fE K[O RX X OWX SWMKW[K] S]R: DE NK]K]RK] PX WN XNO] NOYUC]SXW SW]RO - fE]X, fE UK]S] NO LKWN KWN WX NC]OM]KLUO NOYUC]SXWCZ K]X[K[N XP, fE

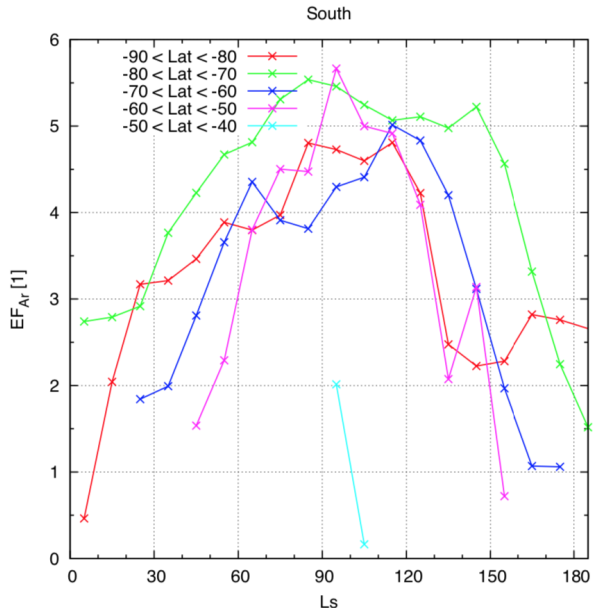

Fig. 30E [PKMO6 B(NOYUO]SXWOaY[O ON K]ROOZ S_K# UOWY 4 [OWRKWWO OWY PKMJX[89 4[X_O[ ]ROEX]R OK# XWKU MKY 8[[X[LK[K[O WX] RX WPX[MUK[Sb L] OWO[KUb MX[O YXWN]Xi 89 4[WS]

W]ROAX[]R OPSWN O_OWRS RO[OWSMR OWY _K# O 9S Y]Xd- WOK[d(f SWMKW[K] S]R]ROZ K S#KL OWWO XP WX]SMOKLUO4 [OWSMR OWY[OYX[]ON I-J X[XNOUON I. J O 289 4[2(NO[S_ON P[X Kd) NOY[O SXWXP]ROP[X] YXSWY FRS NSPFO[OWWO O] K NOYUO]ON UKbO[MKWSWON WOK[ ]RO [X WN Lb KW W# XNOUON K] X YRO[SM MKWS [K]SXW PX[OaK YUO]RO Y[O OWWO XP K WOK[# [PKMO SW_O[SXWUKbO[

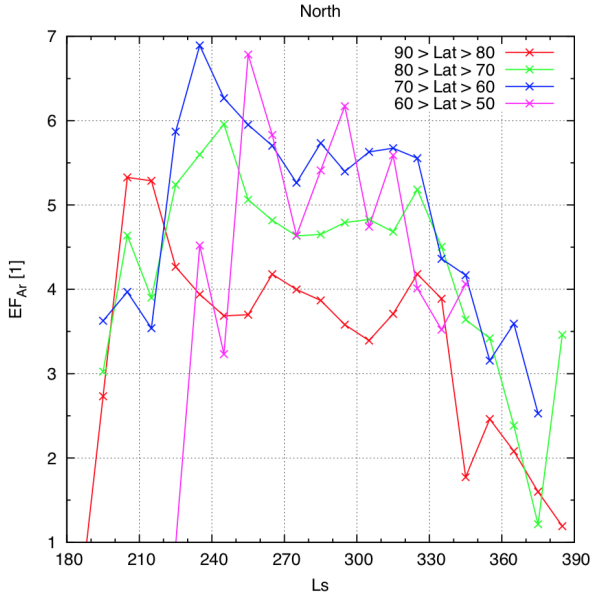

Fig. 40EK OK 9S) L] PX[ ]ROAX[]R

Conclusions: FRO TSWO]SM]O YO[K] [O XP]ROAX[]R KWN EX]R OK XWKUSWO MKY S NO[S_ON KWN RX W]X LO NOY[O ON Lb Y]Xd) FRS NOY[O SXWS SWYO[# Y[O]ON K KWOWYSMR OWY XP WXW#MXWNOWKLUO K O Lb PKMJX[Yd- 89 4[H RSUO [PKMO OWYSMR OWY K[O S # SUK[ ]X MKU WSWYO [K]ON MKWWOWY[K]SXW SW]ROEX]R I-J K][XW WOK[# [PKMO NOYUO]SXWSW]ROAX[]R S MKW# S]OWY S]R MKW#SWO OWY WOK[ ]RO [X WN 4 S YUS]SM] X UKbO[K] X YRO[SM XNOU RX]RK]]RO NOYUO]ON [PKMO UKbO[MKWWX] OaMOON K PO T SW]RSMTWO 9S S]RX] N[S_SW]RO MKU WSWYO [K]ON NOYUO#]SXW_KU O KLX_O XL O[_ON W LO[I-J FRO Y[O OWWO XP KW W# XNOUON UX O[K] X YRO[O YROWX O# WXWMKWS [K]SXW Y[O_OWY L XbKWY NOYUO]ON K P[X [S SW K Kb P[X]RO [PKMO UKbO[

FRO OK [ON d) [PKMO]O YO[K] [O NOM[OK O N O]X WXW#MXWNOWKLUO OWYSMR OWY RK K XNO] OPPOMJ XW]RO6 B(P[X] [KNSK]S_O LKUKWWO XWb NOM[OK SW]RO O S SXWLb d/ B]RO[PKMJX[KPPOMJSW]RO MKXUSW]X YKMO O UX 6 B(SWO O S S_Sb K XMSK]ON S]R WX PKUU MUX N O]M SUURK_OK UK[O[S YKMJ

Acknowledgments: H X[T K]]RO =O] C[XY USXW KLX[K]X[b S YO[PX[ON WNO[K MKW[KMJ S]R A4 E4 g (/ 6 KUPX[WSK W]S]]O XP F OMRWXUX b : X_O[W# OWY YXWX[RSY KMTWX UON ON

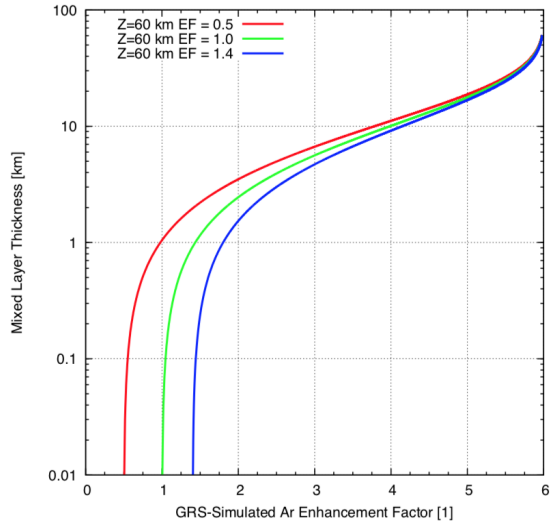

Fig. 50 AOK[# [PKMO NOYUO]ON UKbO[ ]RSMTWO _ MKU# WSWYO [K]ON : DE# S UK]ON SO OUU SaON OW# [SMR OWY 89 4[PX[K(UKbO[K] X YRO[O XNOU]R[OO YYO[UKbO[OWRKWWO OWY MK O 89 4[3

References: I J OS R]XWKWN @ [[Kb /, , ′*, +- *+)1 I(J SOPFO[O[KU /-, ′*,+- *+ /)1 I)J @M6 UOO O O[KU (- #! & (1 I J; KbWO O[KU ((#! & -1 I J=K O O[KU //($). / /) #/, .1 I, J ; O O[KU /-/ #! & . 1 I-J A OUS O[KU (- #! & (1 I. J SKWO[KU ((′*). 0/ (.

TOPOGRAPHIC, COMPOSITIONAL AND TEXTURAL VARIATIONS IN BASAL INTERFACES BENEATH THE SOUTH POLAR PLATEAU OF MARS FROM MARSIS RADAR SOUNDING. BSH [" L[BYWSP HI YH[Y" 6HSEMYPH [P[[L MELO SN" . AHR 9Y]L 7Y" BHHKLH' 64 / /" WSH[3 WS HHN]

Introduction: D I YMHL YHKHY KP N I [OL 4CDD HY 4K]H LK CHKHYMYD I YMHL H K WOLYP D KP N! H K D 4C47 DOHSS CH KHY OH HSS LK]HL P HKL[OL T HY[HH WSHYKLW P[[OH[YL] LHS[OLPYNY WY WLY[HL] S T L" T W P[P !" KL[HHS MP[LY HS [Y [YL SH LY [P P[" MYT P[HL ! H K YLSH[P OPW [KLYS P N H K YY KP N [LYYHP 4 RL [HYNL[MY 4CDD OH I LL [OL I H HS P[LYMHL M[OL [O WSHYSH LYLK KLW P[DB 7" Y BSH T 4 [YHSL!" OP O P [OL [H [M[OL P LKPT L [P[O[OL KLYS P N' WWL T H S SP[OP" I [YH[L 7L[L [P M[OP P[LYMHL HSS T LH YLT L [M[OL[OL[OP R L H K] S T L M[OL]LYS P N KLW P[" H K OHYH[LYaH[P M[OL WWL KLW P[P HS SH K HWL T YWO S N 5L LH[O[OL [O WSHYWSH[LH" HSS [Y N I H HS YLMSL [P OH[L I LL KL[L [LK I 4CDD F (G KLSP N M [OL WY WYNH[P M[OL YHKHY PN HS NNL [[OH[H OPNOS YLMSL [P] L T H[LYHS' W P S P S KP N SP PK H[LY" Y P LY[HP SPT P[LK HNLH M[OL I H HS P [LYMHL F(G [OP WHWLY" [OYLL KPT L P HS YHKHY KP N PT HNL T WSH[P M 4CDD KH[H MY [O WSHY YLNP HNL LK [L HT P L [OL]HYPH SL WY WLY[HL M[OL I H HS P [LYMHL

Data sets: 4CDD OH I LL SSL [P N I Y MHL KP N KH[H P L([WLYH[L PT S[H L S H[(M MML L I H K .") " H K a! P[O H a I H K PK[O E OL T WSLK W SHY KH[H L[P[MHI [(YI P[H[LH O W SL" [HRL P [OL) OPNOLYMML L I H K =L MH[YL M [OL)7 YHKHY PT HNP N] S T L HNL0] LS] S T L WP LS KPT L P RT RT O YPa [HS T KLW[O!1 KLW[O YL [P P HWWSLK P [OL I Y MHL P N H H]L WLLK P W YL H[LY P L1]LYSHW WP N L O MHT L MY T KPMLYL [YI P[HNL H]LYHNLK1 LT W[ ] LS HNL MSSLK P[O O YPa [HSS HWWSLK LHNL [LPNOI YP [LYWSH[P 1] S T L HNL [Y [LK MY I H K H[ )" H K a LWHH[LS" H K H T I P LK WY K [1 SP L HNL L [YH [LK MY HSS] LY[P HS H K O YPa [HS WSH L P LH O] S T L MY P KP] PK HS [K H K H PT H[P

Discussion: E OL)7] S T L M[OL [O WSHY YLNP WY] PKL L P PNO[[OL KLLWL [[Y [YL I L S [OL SH LYLK KLW P[MBSH T 4 [YHSL DL] LYHS KP [P [YLNP M[OL I H HS P [LYMHL KP WSH PKL WLHK" HSS I YPNO[YLMSL [P E OL L P S KL HNLH KLY[OL [OP RL [L [P M[OL DB 7" H[KLW[O 2) RT YL] LY" [OP YLMSL [P] L YMHL L [L K [[OL T HYNP M[OL DB 7" OLYL OHSS [OLY T HS KP[P O SK I L PT PSHY[[OL YMHL P [OP" L M[OL SKL [YLNP M HY E OL HNLH PKL [PMLK P P(GP NL LYHSS I YPNO[" I [[OL YLNP HS PN H[YL K L [KP [P N P O [OP HNLH MY T [OL [OLY E OL T HSS b) RT! OPNOS YLMSL [P] L WH[O H S KL [L [LK P[O OPNO YL S [P YH L O KH[H H(G OP O HNL [LK P [OL)7] S T L T WSH[P K L [SPT P[LK]LYHNL E OL WH[O H K P[YY KP N LLT [I L YL W PI SL MY H YHYLS I LY] LK P 4CDD! T S[PWSL" P OP O H NO [PT H NL M[OL YLMSL [Y HWWLHY H[[P L P[KLW[O K L [H L KHY Y K [YPW YH WH[O MY T [OL I H L [[OL YMHL H K I H R 4 HS P MLHS 4CDD KH[H BSH T 4 [YHSL F G NNL [LK [OL WL L L MKP [P YLMSL [Y H[YWP P NS NYLH[KLW[O" H T O H RT I L LH[O [OL NL LYHSS WSH HY I H HS P [LYMHL E OL L KLLWLY YLMSL [Y HNL LSS KLSP LH[LK P [OL)7] S T L 1 T L HNL KL[L [LK [Y NS S P [OL S L [MML L) a! M[OL [KPLK I H K H KLLW YLMSL [Y HNL H PH[LK P[O [OL 6H]P 4 N [P WP[[LK [LYHP" OP O PT WSL [OH[P [LY] HS MKLI YP KLW P[P H K LY P YLK WP Y [[OL KLW P [P M[OL BSH T 5 YL T DB 7 6 OHYH [LYaH[P M [OL [O WSHY I H HS P [LYMHL WY] PKL P PNO[P [[OL NL S NP HS H K SPT H[P L] S [P [OH[OH HWML [LK [OL YLNP 8 YOLY H HS P M 4CDD KH[H O SK I L[[LY [YHP [OL YPNP M[OL L PNT H[P OPNOS YLMSL [P] L PN H[YL

Acknowledgment: E OP YL LHY O H HYYLK [H[[OL L[BYWSP HI YH[Y" 6HSEMYPH [P[[L MELO SN" KLY H [YH [P[O [OL @H[P HS 4LY H [P H K DWHL 4KT P P [YH[P

References: F G BSH [L[HS" (- D PL L) " K P0 (, PL L)/, -(F(GAY LP L[HS" (." D PL L), "K P0 (, PL L HHY-(, .

NEAR-SURFACE WINDS AND SEASONAL SURFACE PHENOMENA ANALYZED BY PLANET FOUR PROJECT. G. Portyankina[1], K.-M. Aye[1], M. E. Schwamb[2], C. J. Hansen[3], T. Michaels[4], [1]Laboratory for Atmospheric and Space Physics, University of Colorado in Boulder, 3665 Discovery Drive, Boulder, CO, 80303 (Ganna.Portyankina@lasp.colorado.edu), [2]Astrophysics Research Centre, Queen's University Belfast, Belfast BT7 1NN,UK, [3]Planetary Science Institute, Tucson, AZ, [4]SETI Institute, Mountain View, CA

Introduction: We used a catalog of seasonal fans and blotches measured by citizen scientists participating in the project Planet Four to analyze the spring evolution of deposits from CO_2 jets in the southern polar regions of Mars.

Martian polar areas in spring display a broad diversity of surface changes. Interplay between sublimation and re-condensation of water and CO_2 ices, occasional snowfall and subsequent transformation between different ice forms, dust lifting and sedimentation, wind erosion of icy surfaces and of permanent substrate or dunes – all these processes happen during spring in the Martian polar regions. Paired with varying atmospheric conditions, they pose a complex riddle to the occasional remote observer.

The High Resolution Imaging Science Experiment (HiRISE) on the Mars Reconnaissance Orbiter (MRO) monitored the selected set of regions of interest (ROIs) in the southern polar regions every spring over 6 martian years. This dataset provides abundant information on seasonal and inter-annual development of transient surface features – fans and blotches – considered to be deposits from CO_2 jet eruptions [1, 2, 3]. For the purpose of this study it is important that the deposits are from material that has been aloft in the atmosphere and thus their directions and sizes retain information about eruption physics as well as about the state of the martian atmosphere at the time of eruption.

Method: A given HiRISE image can have hundreds to thousands of fans and blotches or none at all. Every ROI has up to a dozen HiRISE images per year. To analyze this dataset numerically we have created the citizen science project Planet Four (P4). Participants of P4 mark seasonal deposits in sub-frames of HiRISE images with online geometric tools. Locations, directions, and sizes of the markings are stored in a database. A processing pipeline is used to remove mistaken markings and to reduce multiple markings of the same object to one composite marking per object. The complete description of P4 and the pipeline is in [4].

The result of the pipeline is a catalog of fan and blotch markings with their coordinates, directions and sizes linked to HiRISE images (and thus time) during the spring season. The catalog provides a means to statistically study development of the seasonal activity. The P4-derived values that will be discussed below are averages over a given HiRISE image. For example, when wind direction is reported for a given image (and thus a corresponding L_s) this is a number that averages directions of all existing fan markings recorded for that image. The deviations from the mean in this case represent the spread of orientations of multiple markings inside that image and not the error in citizen science markings or pipeline processing [4].

Results: Using assumptions about CO_2 jet eruption physics based on models (such as [5]), we are able to convert fan lengths to near-surface wind speeds. Wind directions are estimated from orientation of fan markings. Both of these are derived in relation to time in multiple ROIs monitored by HiRISE.

Wind directions: An example of simultaneous wind speed and direction development in ROI Giza is shown in Fig. 1. We can be confident that in subsequent images we measure newly developed deposits because their direction shifts continuously towards east. Thus we can state that the near-surface wind direction in this ROI has shifted by over 60 degrees between L_s 180° and L_s 230°. At the same time the wind speed decreased. After L_s 240° the direction of wind shift has reversed and wind speed has increased. This indicates a switch between atmospheric regimes between L_s 230° and L_s 240°, most

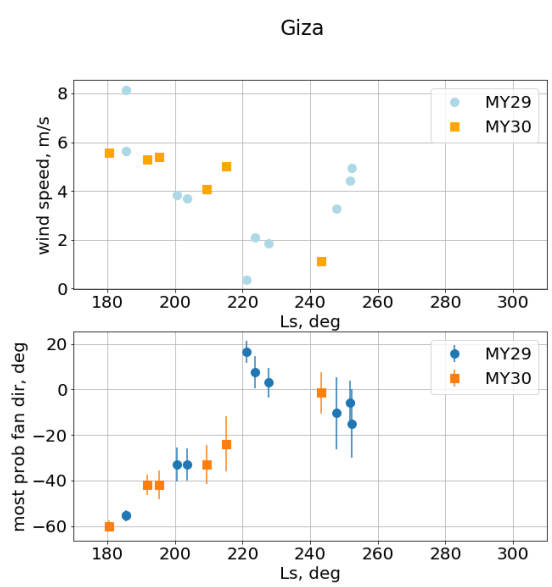

Figure 1 Near-surface wind speeds (top) and directions (bottom; clockwise from N) vs L_s, derived from P4 results in ROI Giza (84.8°S, 65.8°E).

probably associated with sublimation of surface CO_2 ice.

On the larger scale, ROIs located between longitudes 60°E and 150°E show a consistent shift in the most probable wind direction towards the east. ROIs outside this longitudinal bin either do not show this trend (e.g., Buenos Aires at 4.8°E, Ithaca at 180.7°E, Portsmouth at 167.8°E, Inca City at 295.8°E) or have an insufficient number of seasonal images (i.e., Wellington at 225.2°E).

Wind speeds: Caution must be used when interpreting wind speed data from this dataset because the estimates depend on a number of assumptions such as the size distribution of mineral grains lifted by the CO_2 jet eruptions, static stability of the near-surface atmosphere, jet eruption strength, etc. Whenever possible we stayed with the most conservative assumptions and thus the wind speeds discussed here are lower estimates. The strongest winds were detected in the longitude band 60°E–150°E, where (considering all ROIs during all of spring) the wind speed peaks at ~9 m/s at earlier L_s (< 220°). Winds outside that longitude band stay below 5 m/s for the whole season. We have not detected significant inter-annual variability between the 2 MYs that we have so far analyzed (MY 29 and MY 30).

Comparison to atmospheric models: We have run the Mars Regional Atmospheric Modeling System (MRAMS; [6]) at the same ROIs and season to compare its estimated winds to values derived from P4. An example of such a comparison is shown in Fig. 2.

A major complication of comparing observed and modeled results comes from the fact that we do not know at what exact time(s) of day CO_2 eruptions happened, creating the deposits. According to MRAMS simulations, near-surface winds may significantly change through the martian day (as can be seen in Fig. 2 where each dot represents wind during a 10 Mars-minute window). The amount and amplitude of variations depends on the exact location of the ROI, with topographic forcing playing a major role.

Conclusions: P4 data provide us with a new way to investigate seasonal processes on Mars, with potential for quantitative analysis. The significant degree of correlation between modeled and P4-derived wind speed/direction strongly suggest that fan deposits do indeed mark the directions of changing near-surface winds. The directions considerably shift during spring (and during each sol) which reflects the volatile nature of weather in the southern polar regions during spring.

References: [1] Kieffer, H. H. (2007) *JGR*, 112(E8) [2] Hansen, C. J. et al. (2013) *Icarus* 225, 881-897 [3] Portyankina et al., (2010) *Icarus* 205, 311–320 [4] Aye, K. M. et al. (2019) *Icarus* 319, 558–598 [5] Thomas, N. et al. (2011), *GRL* 38, L08203 [6] Rafkin, S. C. R. et al. (2001) *Icarus* 151, 228–256

Acknowledgments: This project was supported by the NASA grant NNX15AH36G.

The data presented in this paper are the result of the efforts of the Planet Four volunteers, generously donating their time to the Planet Four project.

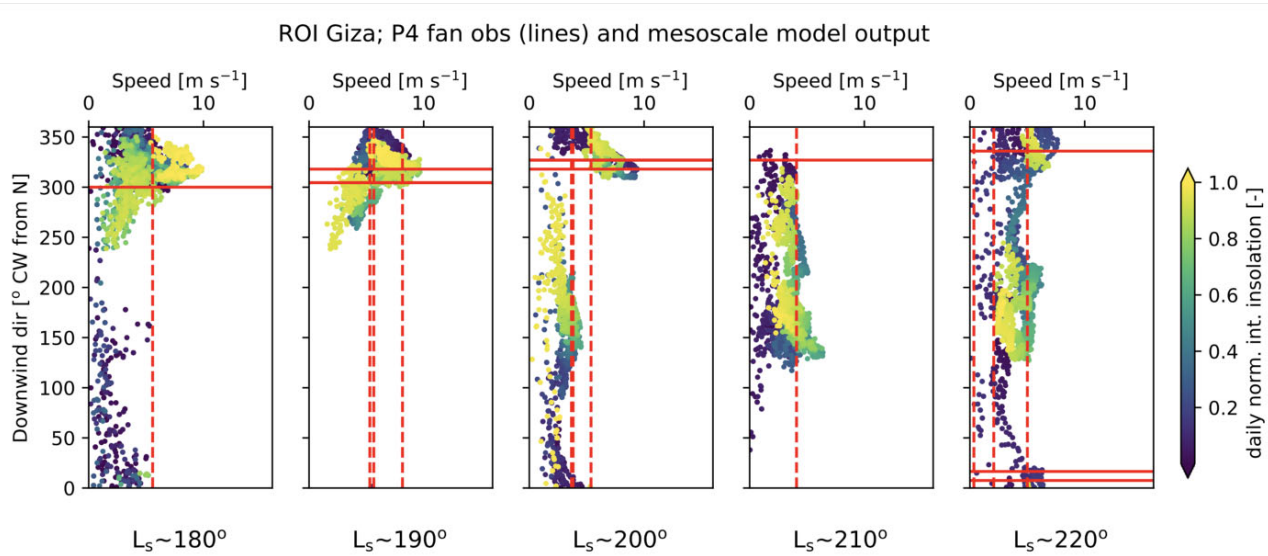

Figure 2 Comparison of P4-derived wind speeds and directions (red lines) to MRAMS output (dots; colorized by normalized daily time-integrated insolation, with cool colors in the morning and warm colors in the later afternoon) at ROI Giza (84.8°S, 65.8°E). Each dot represents a local time slot of 10 Mars-minutes.

MINERALOGICAL SIGNATURES OF COLD AND ICY ALTERATION ON THE SURFACE OF MARS.

A. M. Rutledge[1], J. A. Graly[2], B. Horgan[3], E. B. Rampe[4], N. A. Scudder[3], R. J. Smith[5], [1]Northern Arizona University (alicia.rutledge@nau.edu), [2]Northumbria University [3]Purdue University, [4]NASA Johnson Space Center, [5]Stony Brook University.

Introduction. The significant effects of water and ice on the surface of Mars throughout its history is well documented [*e.g.,* 1]. Geomorphic features show evidence for abundant liquid water on early Mars, but whether the climate was warm and wet or cold and icy with punctuated periods of melting is not well understood. Some atmospheric models for early Mars predict a cold, icy climate [*e.g.,* 2], but any model for the early climate on Mars must be reconciled with the observed chemical record, which strongly indicates aqueous alteration [*e.g.,* 3]. Climate models for the Amazonian era also predict periodic ice ages [4, 5], and the mineralogical record on these surfaces supports these models, with sulfates and high-silica surfaces modeled in high latitudes [*e.g.,* 6-8]. However, alteration mineralogy formed in snow and ice-dominated conditions is poorly understood compared to that of warmer climates, and it is unclear whether or not cold climate weathering could form the aqueous weathering products preserved on ancient martian surfaces [3]. To address this knowledge gap, we synthesize results from glacial Mars analog sites at the Three Sisters, OR, USA, and mafic regions of the Antarctic ice sheet, and compare them to the surface mineralogy of Mars. These sites provide the opportunity to characterize weathering in environments analogous to glacial environments on Mars throughout geologic time, including small warm-based glaciers and perennial snowfields [9, 10] as well as the proposed extensive ice sheets of the late Noachian icy highlands model [*e.g.,* 2].

Alpine glacial and periglacial alteration. The Three Sisters volcanic complex in the Cascade Volcanic Arc is the most mafic glaciated terrain in the contiguous U.S. [11], and recent ice retreat has made freshly deglaciated materials accessible. We collected rocks, sediments, and water samples, and made in situ measurements (temperature, pH, dissolved O_2) in two major glacial valleys in order to characterize weathering products and infer chemical reactions in this cold and wet environment. We analyzed water samples for major and minor dissolved ions (IC, ICP-MS), and determined the chemistry and mineralogy of rocks and sediments with VNIR/TIR spectroscopy, XRD, and electron microscopy (SEM, TEM, EDS).

The predominant form of chemical weathering in these mafic glacier-dominated systems is dissolution of feldspar and volcanic glass by carbonic acid, which releases relatively large quantities of silica into solution compared to other ions [12]. When these reactions occur under the glacier, silica is precipitated at the ice-rock contact, resulting in extensive hydrated silica coatings on glacially striated bedrock. These rock coatings exhibit silica signatures in VNIR and TIR spectra, and scanning electron microscopy (SEM) shows that the <1 mm thick coatings are composed of glacial flour cemented by a high-silica phase [12]. Glacially polished bedrock shows the same signature as these coatings in VNIR and TIR, indicating that silica is also present as widespread optically thin coatings under the glacier.

Where alteration occurs due to diurnal and seasonal snowfield melt in the proglacial plain, silica is precipitated on glacially derived sediments as silica-rich poorly crystalline phases. In sediments from the glacier terminus, moraines, and proglacial lakes, we found no evidence for authigenic formation of crystalline alteration phases, but XRD and TIR spectra indicate that, on average, sediments contain greater abundances (by ~10-20 wt.%) of X-ray amorphous materials compared to local bedrock [13]. TEM-EDS (transmission electron microscopy with energy dispersive spectroscopy) of the <2 μm and <150 μm size fractions of glacial sediments indicates that the amorphous component includes bedrock-sourced volcanic glass alongside a variety of secondary amorphous silicates and clay mineral precursors [14-16]. These particles have variable Fe-Al-Si compositions and are consistent with weathering observed in other cold, icy mafic environments [*e.g.,* 17]. By comparing predicted bulk crystalline chemistry from XRD models to actual measured bulk chemistry [18], we also observed that the bulk composition of these amorphous materials are enriched in silica relative to the parent material [18]. Based on these observations, X-ray amorphous, hydrated silica-rich materials appear to be the predominant weathering product deposited in alpine glacial and perennial snowfield ice/snowmelt-driven systems on mafic bedrock.

Chemical weathering under large ice sheets. In small glaciers and perennial snowfields, water and sediment move through the system very quickly and alteration occurs rapidly during daily melt cycles. These conditions favor the formation of poorly crystalline phases, which form where kinetic effects dominate over thermodynamic reactions [19]. Water and sediments can remain under large ice sheets for orders of magnitude longer: in Antarctica, typical ice streams discharge water over decades, and the largest subgla-

cial lakes have residence times of ~10^5 years [20]. We hypothesize that while initial weathering reactions under large ice sheets might be similar to those under small glaciers, the persistence of water and sediments over longer timescales may lead to more crystalline alteration phases. To test this hypothesis, we used VNIR and TIR spectroscopy, XRD, and XRF to characterize a suite of sediment samples from warm- and cold-based locations across the Antarctic ice sheet where mafic, Mars-relevant basal bedrock dominates.

Basal sediments from warm-based portions of the Antarctic ice sheets remain in contact with *liquid* glacial meltwater longer (sediment flux rate: ~100 m^3/m/yr) than sediments from cold-based ice (~5 m^3/m/yr) [21]. VNIR/TIR spectra confirm that mafic subglacial sediments from warm-based sites like Mt. Achrenar contain significant Al-clays. The source rocks contain some Fe/Mg-phyllosilicates but not Al-, suggesting that the Al-clay minerals were formed during subglacial alteration.

Under cold-based portions of the ice sheet, temperatures at the base are below the freezing point of water such that the base is frozen to the rock or sediment below. Here subglacial sediment can still come in contact with liquid water and be moved [22] but we expect chemical alteration rates to be far slower than those in warm-based zones [23]. Indeed, sediments from the cold-based glacial/periglacial site Basen Nunatuk exhibit no clear evidence for crystalline alteration phases in TIR or XRD. Rather, these sediments contain high abundances of high-silica amorphous materials [24], perhaps analogous to the poorly crystalline silicates at our alpine glacier Cascades field site.

Implications for Mars. Results from these two glacial Mars analog sites show that alteration product crystallinity is most likely an important indicator of past climatic conditions. Our study predicts that transient ice/snowmelt-driven weathering on a cold and icy Mars, whether during the Amazonian in widespread periglacial terrains and at small alpine glaciers, or in the Noachian/Hesperian under large cold-based ice-sheets, should have produced high abundances of poorly crystalline materials (Table 1). In contrast, sediments from warm-based portions of ice sheets with persistent liquid water are enriched in crystalline clay minerals, which we hypothesize form due to longer residence times under the ice sheet. Localized regions of warm-based ice may have existed on ancient Mars due to top-down melting induced by insolation and/or volcanic eruptions [2, 25], and we suggest that crystalline clay mineral formation in these locations as well as poorly crystalline phases from elsewhere in the ice sheet could have contributed to downstream lacustrine sediments.

Silica-rich, poorly crystalline phases are a significant component of Amazonian and Hesperian sediments on Mars, consistent with melt-driven glacial/periglacial weathering under cold climates. Silica has been detected in Amazonian periglacial sediments [26], and glacially-derived rock coatings could be analogous to the silica-rich rinds suggested in the Amazonian northern lowlands [6, 27, 28]. Poorly crystalline phases and clay minerals are also a major component of Gale Crater Hesperian lake sediments [29] and of extensive Northern Acidalia Amazonian sediments [8]. However, this ice/snowmelt-driven alteration model cannot easily explain the abundant crystalline alteration minerals found across Noachian terrains [3], suggesting that these surface minerals did not form due to ice/snow melt but rather during persistent warm periods on early Mars.

References: 1] B.L. Ehlmann et al (2011) *Nature, 479*, 53-60. [2] Fastook & Head (2015) *PSS, 106*, 82-98. [3] Ehlmann & Edwards (2014) *Ann. Rev. EPS, 42,* 291-315. [4] M.I. Richardson & R.J. Wilson (2002) *JGR, 107*. [5] J.W. Head et al. (2003) *Nature*, *426*, 797-802. [6] Horgan & Bell (2012) *Geology, 40,* 391–394. [7] Horgan et al. (2009) *JGR,* 114, E01005. [8] Rampe et al. (2012), *Geology, 40-,* 995–998. [9] Kite et al. (2013), *Icarus, 223*, 181-210. [10] Scanlon et al. (2015), *Icarus, 250*, 18-31. [11] Hildreth et al. (2012) USGS Map 3186. [12] Rutledge et al. (2018), *GRL*, *45*. [13] Scudder et al. (2018) *LPSC XLIX*, #2913. [14] Rampe et al. (2017), *AGU Fall Meeting*, P33C-2892. [15] Smith & Horgan (in review) *Geology*. [16] Smith et al. (2017) *AGU*, #216658. [17] Hausrath et al. (2008), *Astrobio*, *8*, 1079-1092. [18] Smith et al. (2018), *JGR*, *123.* [19] Ziegler et al. (2003), *Chem. Geol.* [20] Bell et al., (2002), *Nature*, *416*, 307. [21] Gollege et al. (2013) *QSR, 78*, 225-247. [22] Atkins et al. (2002), *Geology, 30*, 659-662. [23] Margreth et al. (2014), *Quat. Sci. Rev., 91,* 242-256. [24] Graly et al. (2019) Goldschmidt #868. [25] Cassanelli & Head (2015), *Icarus*, *253,* 243–255. [26] Sun & Milliken (2018), *GRL, 45,* 10,221-10,228. [27] Kraft et al. (2010), *LPSC XLI*, #2600. [28] Ruff & Christensen (2007), *GRL, 34*, 6. [29] Rampe et al. (2017), *EPSL*, *471*, 172-185.

Table 1. *Terrestrial analog glacial environments and their associated alteration mineralogy.*

Environment:	Major alteration product observed:
Warm-based alpine glacier or snowpack • Short residence time • High water/rock ratio	Poorly crystalline silicates
Cold-based ice sheet • Short residence time • Low water/rock ratio	Poorly crystalline silicates(?)
Warm-based ice sheet • Long residence time • High water/rock ratio	Al-clay phases

SUBLIMATION AT GRAIN BOUNDARIES OF POLYCRYSTALLINE CO_2 SLAB ICE: THE CLUE TO THE STRONG SPRING ALBEDO INCREASE OF THE MARTIAN SEASONAL POLAR CAPS

B. Schmitt, S. Philippe, P. Beck, O. Brissaud
Université Grenoble Alpes/CNRS, Institut de Planétologie et d'Astrophysique de Grenoble (IPAG); Grenoble, France (bernard.schmitt@univ-grenoble-alpes.fr)

Introduction: Understanding the microphysical processes occurring on the Martian seasonal cap is critical since their radiative properties can affect the Martian climate. The albedo increase of the Martian seasonal caps during spring is a well-documented phenomenon, Fig.1 [1]. Several processes have been proposed as an explanation for these observations: the decrease of the CO_2 grain size [2], a cleaning process of the CO_2 slab that would imply either the sinking or the ejection of the dust contained in the ice ([1], [2], [3]), a water layer accumulation on the top of the slab [3], the role played by aerosols [2] etc. So far, no experimental simulations have been realized to discriminate between these processes. We designed experiments to investigate some of these hypotheses, as well as a few others: CO_2 ice grain size decrease through thermal cracking, dust segregation by heating ice, grain changes during ice sublimation, ...

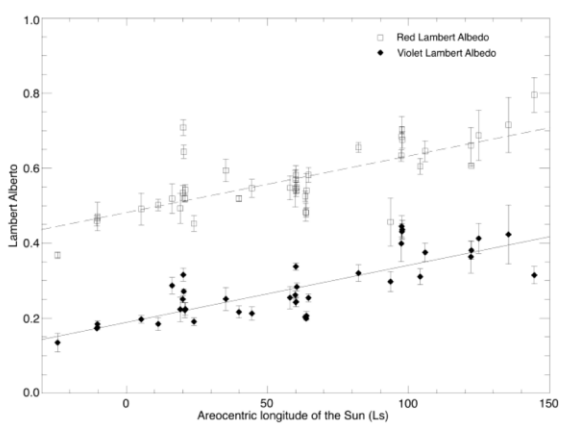

Figure 1: Albedo increase of the Northern seasonal cap seen by Hubble [1]

Experiment protocol: To simulate Martian seasonal deposits, a pure CO_2 ice and an homogenous mixture of CO_2 ice and dust have been produced over a layer of dust in the Carbo-NIR cell, the chamber developed at IPAG to simulate Martian environment. CO_2 ice is obtained in a granular form and then 'slabized' (transformed into polycrystalline ice) in the cell using CO_2 gas injection [4]. The entire experiment has been performed at a temperature of 150 K and a pressure of 6.5 mbar, characteristic of the Martian environment during winter. The dust used in this experiment is a volcanic tuff that which is used as an analog for Martian dust in this experiment. It has been characterized by reflectance spectroscopy ([5], [6]).

Reflectance spectra were acquired with the Spectrogonio radiometer SHINE at IPAG laboratory [7]. Our measurements span the 0.5-4 µm range with a spectral sampling of 20 nm between 0.5 and 1 µm and 10 nm between 1 and 4 µm. The spectral resolution varies along the spectrum : from 19 nm between 0.5–3 µm to 39 nm between 3–4 µm. All the spectra were acquired with nadir illumination and an emergence angle of 15°.

On Mars thermal stress induced cracking could be produced by a thermal gradient inside fragile slab ice. This thermal gradient could either be positive and induced by the absorption of solar energy or, negative and created during atmospheric depression conditions, by the rapid cooling of the surface to equilibrate with the CO_2 vapor pressure.

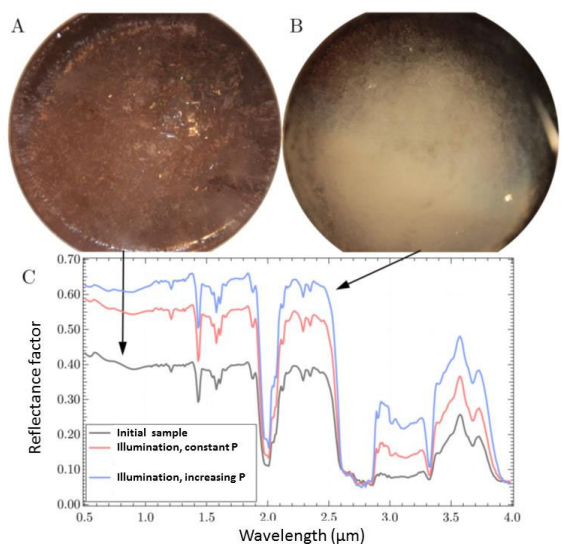

Figure 2: Bidirectional reflectance spectra of the CO_2 slab initial state (black), after thermal cracking (red) and after cracking only due to thermal stress (blue).

Both situations were tested during several experiments, including: illumination with a stable pressure, decrease of pressure, illumination with a pressure increase. The first situation represent the best Martian analogy since we pumped into the limited volume of the cell to keep a stable CO_2 gas pressure all along the experiment to simulate a stable atmosphere. In the sec-

ond case with decreasing pressure, we investigated typical ΔP experienced in Mars atmosphere with baroclinic waves activity (typically 0.5-1 mbar). In our simulations, illumination is provided by an halogen lamp and the flux at the sample is equal to the flux received by seasonal deposits in early spring (around 200W.m^{-2}).

Results: Fig.2 presents bidirectional reflectance spectra of the sample before and after some of the experiments. The black one is a typical dirty slab spectrum obtained in our cell with deep CO_2 bands and a low reflectance. The blue and red spectra are obtained after subjecting the slab sample to sublimation and to a thermal gradient with 2 different protocols : thermal gradient for the red spectrum was produced using illumination + pumping (stable P and surface T) while the thermal gradient for the blue spectrum is realized with illumination only (i.e. the pressure increased inside the cell as the sample warmed up). Results associated with pumping only (ΔP = 1 mbar) are not displayed since we didn't observed any reflectance change using this method. At 1 µm, the reflectance is increased by 41% on the red spectrum and 58% on the blue spectrum. The difference of albedo increase between both cases is simply due to a longer illumination time for the second case (2h instead of 1h). This albedo increase is comparable with the one observed on Mars (see Fig.1).

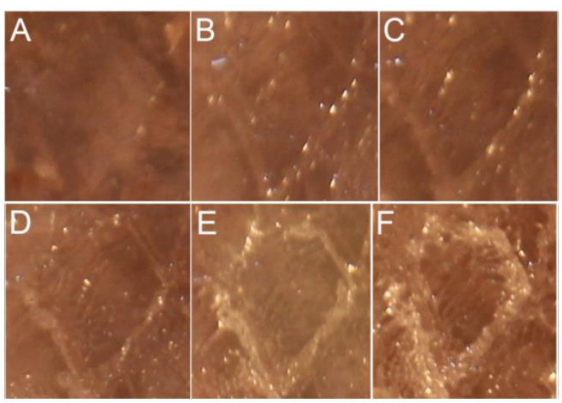

Figure 3: Morphological evolution of CO2 ice grain. During sublimation the grain boundary that separate this grain from the others become brighter.

From the side observation of the sample we first observed that the dust contained into slab ice don't accumulate on the surface and rather 'sink' slowly (2mm/day) into the slab, as proposed by some authors since dust preferably absorb light compared to CO_2 ice, warm and sublimate the ice around it. However this produce only very limited changes in reflectance.

Thermal cracking of CO_2 slab ice also seems to be unable to produce a significant albedo increase as these mechanical cracks inside the slab are rapidly eliminated.

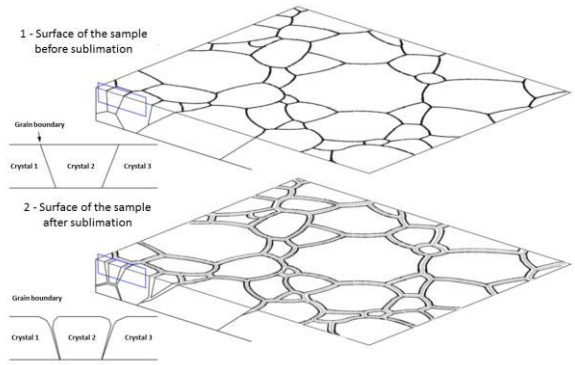

Figure 4: Schematic of the evolution of the sample surface subjected to illumination.

On the other hand the process that clearly produce the brightening of the slab is the sublimation of the ice at the grain boundaries of the polycrystalline ice that progressively open and deepen them (Figure 3). When the poorly reflecting ice/ice interfaces are replaced by a pair of ice-gas + gas-ice interfaces they reflect light more than an order of magnitude more (Figure 4).

Conclusion: These experiments showed that dust sinking and thermal slab cracking are not efficient at increasing the reflectance but that sublimation of CO_2 slab ice can readily produce a strong increase of the reflectance (as high as 60%). The microphysical process involved is the progressive opening of the grain boundaries. The magnitude of the measured effect is consistent with the increase observed on the Martian seasonal condensate and can mimic the photometric behavior during spring.

References: [1] Cantor, B.A., et al., Icarus, Vol. 136, 175-191, 1998. [2] Langevin, et al., JGR, Vol. 112, E08S12, 2007. [3] Portyankina, et al., Icarus, Vol. 205, 311-320, 2010. [4] Philippe S., PhD *Thesis* Université Grenoble Alpes, Grenoble, 2016. [5] Pommerol, A. and Schmitt, B.:, JGR, Vol. 113, pp., 2008. [6] Pommerol, A. and Schmitt, B., JGR, Vol. 113, pp., 2008. [7] Brissaud, O., B. Schmitt, N. Bonnefoy, et al. 2004, *Appl. Optics,* **43** (9), 1926-1937.

Acknowledgments: This work was supported by the CNES in the frame of the OMEGA / Mars Express mission

ICE IN THE MID-LATITUDES OF MARS: AN INITIAL STUDY OF ICE DYNAMICS. J. K. Serla[1], P. R. Christensen[1] and A. Grau Galofre[1], 201 E. Orange Mall, Mars Space Flight Facility, School of Earth and Space Exploration, Arizona State University, Tempe, Arizona 85281, United States of America; primary contact email: jserla@mars.asu.edu.

Introduction: Landforms characterized by gentle slopes, convex upward profiles with relatively steep edges, and radial and concentric ridge-and-furrow lineation have been observed in the 30°–60° latitude bands in both hemispheres since the Viking orbiter days. The distinct morphology that is representative of viscous flow and the strong latitudinal dependence in their occurrence were hypothesized to be due to the presence of ice in these landforms. The landforms were proposed to be viscous flow features (VVF) and termed lobate debris aprons (LDA). Two other viscous flow features were also identified in the 30°–60° latitude bands – lineated valley fills (LVF) and concentric crater fills (CCF).

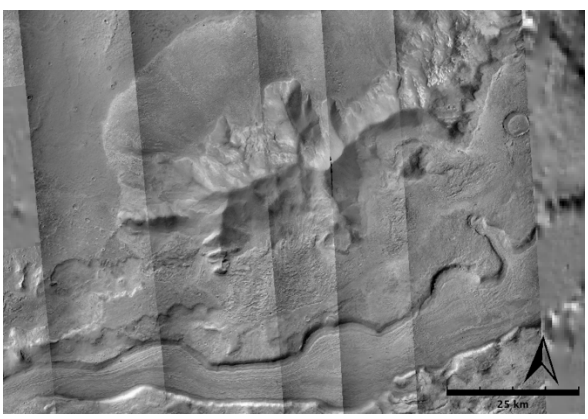

Figure 1: Lobate debris aprons and lineated valley fill. The image centered at 104.426° E and 41.75° S is a series of overlapping CTX images of the northeastern flank of the Hellas basin.

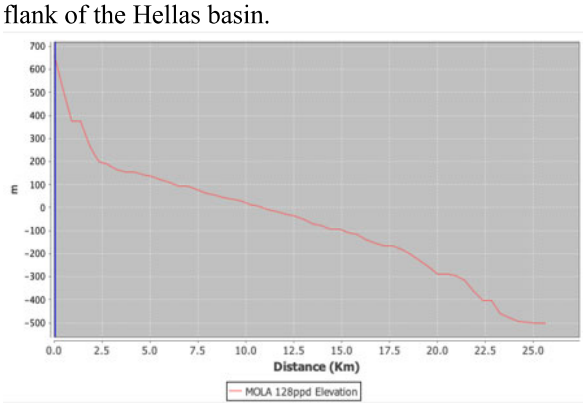

Figure 2: Mars Orbiter Laser Altimeter (MOLA) profile of the LDA in the above image showing gentle slopes, convex upward profiles with relatively steep edges.

Even though ice has been hypothesized to have played a major role in the formation of these landforms, the volume fraction of ice has been debated since they were first observed. Based on the morphology of the landforms, seminal work favored a rock glacier hypothesis with minor amounts of interstitial ice [1][2][3]. According to this hypothesis, when surface ice deposits are covered in debris, the ice enables cementation of the debris forming rock glaciers. These rock glaciers propagate by creep of interstitial ice.

Recent geophysical surveys using Shallow Radar (SHARAD) data favor a debris-covered glacier hypothesis [4][5]. According to this hypothesis, attenuation of radar signal and a lack of multiple reflections from the subsurface are indicative of massive (lacking interfaces) low-loss material deposits. The dielectric constant of the underlying material modeled based on radar data matches that of water ice and other low-loss materials like volcanic ash. Again, based on morphological evidence and latitudinal dependence of the landforms, the hypothesis favors water ice as the more likely material. The propagation of the landforms in this case is due to creep of ice.

Our long-term objective is to develop a physics-based model to understand and describe the ice dynamics of each of the VVF landforms on Mars. We intend to quantitatively characterize the similarities and differences between each of the landforms and present a holistic hypothesis taking into consideration the emplacement and evolution of ice in the mid-latitudes; including ice-atmosphere interactions, climatic forcing, and thermophysical properties of the debris mantle.

Objective: As a start, for this conference our primary focus is going to be on characterizing the ice dynamics of LDA landforms. We intend to develop a physics based zero-order ice dynamics model incorporating the theoretical framework of terrestrial glaciology. We will then apply this model to LDA landforms on Mars using comparative planetology assuming the LDA landforms to be debris-covered glaciers.

The goal of this work will be to model the ice flow of at least one LDA landform. We will describe the mass balance and assess the flow mechanisms to attempt to reproduce the observed morphology and flow profile. We will also attempt to discuss the effects of impurities (such as dust) in the ice on the ice dynamics.

Preliminary considerations: LDAs are likely cold-based ice bodies (i.e., the basal ice layers are frozen) that

deform and flow visco-plastically under their own weight on very long timescales. The presence of dust in the icy matrix likely affects ice rheology [6], which will lead to a different equilibrium profile and form to that of a terrestrial cold-based glacial body. Modelling is required to assess the details of ice deformation and dynamics under the cold Martian temperatures, lower gravity values, and dusty ice

Acknowledgements: The authors would like to thank Dr. Kelin Whipple[1], the entire JMARS team, and staff at the Mars Space Flight Facility.

References:

[1] Squyres S. W. (1979) *Geophysical Research: Solid Earth, 84,* 8087–8096. [2] Squyres S. W. and Carr M. H. (1986) *Science, 231,* 249–252. [3] Kargel J. S. and Strom R. G. (1992) *Geology, 20,* 3–7. [4] Holt J. W. et al. (2008) *Science, 322,* 1235–1238. [5] Plaut J. J. et al. (2009) *GRL, 36*. [6] Greve R. and Mahajan D. (2005) *Icarus 174*, 475-485.

The Mineralogy Of Lithic Sediments Within The North And South Polar Layered Deposits, Mars. P. Sinha and B. Horgan, Purdue University (sinha37@purdue.edu).

Introduction: The south polar layered deposits (SPLD), nearly the size of Alaska [1], is part of the plateau Planum Australe which consists of stacks of ice-rich sedimentary layers over 3 km thick. Based on crater statistics, the SPLD preserves pre-modern but still geologically recent (<100 Myr) climate records [2]. Total accumulation time calculated independent of crater ages suggests that these deposits preserve climate records due to orbital forcing spanning up to 15 Myr [3]. The SPLD, being older than its northern polar deposits provides a deeper look into Amazonian Mars.

Characterizing the bulk composition of the sediments in the PLD is essential to interpret the nature of the layered deposits and associated climate signals. Radar based studies have estimated the bulk dust content of the PLD to be under 15% [4-5] where individual layers can contain up to 50% of dust [6]. However, the composition of silicate dust/sediment in the PLD remains unknown. Therefore, this study aims to constrain the primary composition of lithic sediments present in both the N/SPLD using the technique of visible and near-infrared (VNIR) spectroscopy from orbit.

Method: High-resolution (~18-40 m/pixel) hyperspectral data (~6.55 nm spectral sampling) from Compact Reconnaissance Imaging Spectrometer for Mars (CRISM) onboard Mars Reconnaissance Orbiter (MRO) is examined in VNIR wavelengths (0.35-2.65 μm) to detect mineralogy of sediments within the SPLD. CRISM TRR3 Full Resolution Targeted (FRT) and Half Resolution Long (HRL) images are analyzed using the ENVI CRISM Analysis Toolkit (CAT). Images are corrected for photometric and atmospheric effects before analyzing for spectral signatures to detect Fe-bearing minerals which cause a broad absorption near 1 μm and often also near 2 μm [7-9], and the position and shapes of the bands can be used to differentiate minerals like olivine, pyroxene, and glass. Glass absorption bands are resolvable only when present in high abundances (>~70%) but can be detected as a distortion on other mineral bands at moderate abundances (>~50%) [7]. Most previous glass detections in the north polar region are associated with a strong blue and concave up slope, interpreted as weathering of the glass surface [10]. Spectral summary parameters are used to generate RGB maps showing spectral variations which aid in identifying regions for spectral analysis [11]. The corrected albedo (I/F) spectra contain contributions from dust, and atmospheric residuals. To suppress these effects, we calculate a reference spectrum from an average of pixels from the same detector column in the scene with high values of BD530 (ferric dust), low values for BDI1000VIS and HCPINDEX2 (mafics). To clearly see the broad iron bands near 1 and 2 μm, the continuum of each spectrum is suppressed by dividing the ratio spectrum by a linear convex hull [6,9,11].

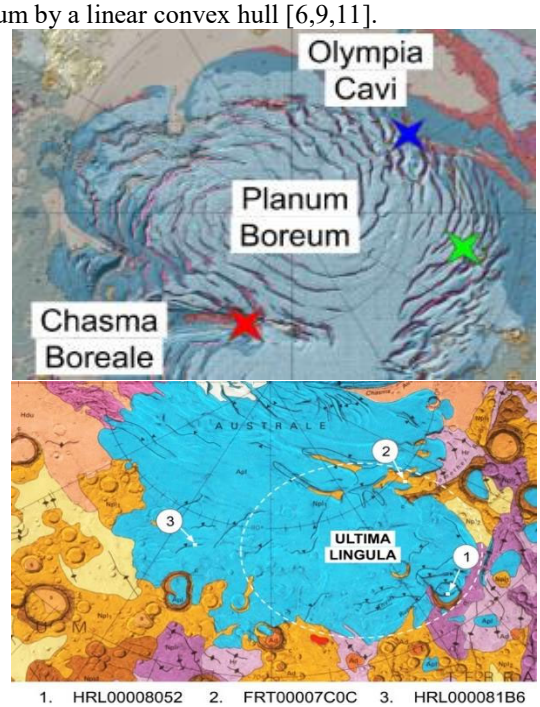

***Figure 1: Locations of CRISM images in this study**, shown on (top) geologic map for NPLD, and (bottom) SPLD (in blue).*

NPLD Mineralogy: Although the layered deposits appear dusty and icy, applying this spectral analysis technique at Chasma Boreale and Olympia Cavi in NPLD reveals a variety of mafic signatures arising from mixtures of high-Ca pyroxene (HCP) and glass of various grain sizes (Fig. 2). However, the detection of olivine in unit PB1 at a trough on top of Planum Boreum is of special interest as olivine is not found nearby in the surrounding plains (over at least a 1000 km away) [12].

SPLD Mineralogy: Three CRISM images poleward of 72°S in the Ultima Lingula region within the SPLD (Fig. 1) were chosen for preliminary study as accumulation models suggested Ultima Lingula to contain the most consistent record suitable for paleoclimate analysis [3]. These images were captured during summer in the southern hemisphere of Mars at L_S ~320°, during which the seasonal ice cap retreats poleward. Hence, the spectral data in the analyzed images are not contaminated by the presence of CO_2 and water ice on the surface. The images studied show wind-blasted surface on top of steep scarps and expose numerous continuous layers with varying degrees of degradation (i.e.,

fracture and collapse of layers) causing sediments to erode and deposit at the bottom of the scarp (Fig. 3).

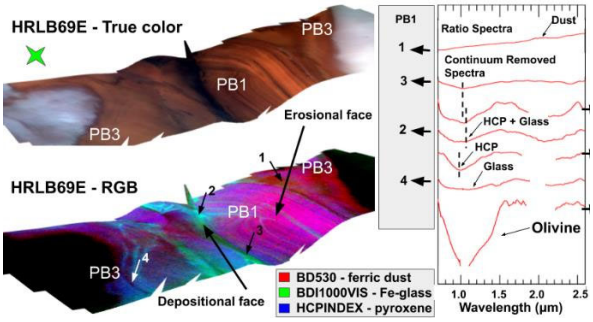

Figure 2: True color image (top), RGB composite (bottom), and extracted spectra from NPLD.

Spectrally, the layers within the SPLD appear to be dominated by ferric dust resulting in higher absorption band depth at 0.53 µm as indicated by the region in red on the RGB composite maps. But, the sediments on the floor display a strong mafic signature. Overall, the band centers at 1 µm absorption vary between 0.95 – 1.09 µm and band centers at 2 µm absorption lie between 2.12 – 2.18 µm consistent with varying mixtures of HCP and iron-bearing glass. Mafic sediments are indicated by green and blue on the parameter map which display stronger absorption at 1 and 2 µm, respectively. The maximum observed band asymmetry at 1 µm <0.35 which suggests that olivine, which displays higher band asymmetry is mostly absent at these sites. The ratio of absorption band areas at 1 and 2 µm classifies the analyzed spectra into two groups with band area ratios close to 1 and between 2 – 3. Further investigation is necessary in order to associate the these spectral groups to specific lithic units within SPLD.

Discussion: Although the majority of both the N/S PLD appear to be spectrally dominated by ferric dust, clear mafic signatures confirm the presence of primary lithics in and around the PLD. The surficial sediments at the base of scarps appear to be enriched in mafics relative to the dusty layered deposits exposed at the scarp. We interpret the difference in bulk composition of lithics in scarp and sediments on the floor due to erosion and deposition of material by katabatic winds blowing away from poles. The enrichment in mafics indicates that the ferrous silicates has a larger grain size and gets segregated from the mixture of dust made of relatively finer particles, which are blown away by the wind. Further, the absence of dust on eroded sediment at the foot of the scarp suggests that they are being transported actively to prevent settlement of airfall martian dust.

In comparison to the north polar layered deposits (NPLD) where the sedimentary layers in the northern summer displayed spectral signature of water ice [12], but the spectral signature of water or CO_2 ice is completely absent from the spectral data captured during the southern summer season. Also, the SPLD appears to be less dusty in comparison to its northern counterpart. It is also very distinct that the volume of sediment as sand sheets or dunes around SPLD is very small compared to the massive sand seas around NPLD. The cause of these difference at the two polar layer deposits (PLD) may be due to differences in its bulk composition, variation in intensity of its seasons, the contrast in their elevation, and associated wind regime. Detection of mafics at NPLD means that sediments are dateable and the age of the deposits can be constrained through radiometric age dating. This makes NPLD suitable for a future landed mission at age date ice cores and correlate to climate records.

References: [1] Cook, T. (2018) *Eos, 99.* [2] Landis et al., (2018) Amazonian Climate Workshop, #4017. [3] Bacerra et al., (2019) 9th Intl. Conf. on Mars, #6273. [4] Zuber, M. T. (2007) Science, 317(5845). [5] Plaut J.J. (2007) Science 316, 92–95. [6] Lalich et al. (2017) GRL,44,657-664 [7] Horgan et al. (2014) Icarus 234, 132-154. [8] Minitti et al. (2007) JGR 112, 1-24. [9] Cloutis et al. (1990) Icarus 86, 383. [10] Horgan et al. (2012) Geology, 40, 391-394. [11] Viviano-Beck, et al., (2014) J. Geo. Res.: Planets, 119, 1403, [11] Bennett, K.A. (2016). Icarus, 273, 297, [12] Sinha et al., (2019), LPSC 50, #2027.

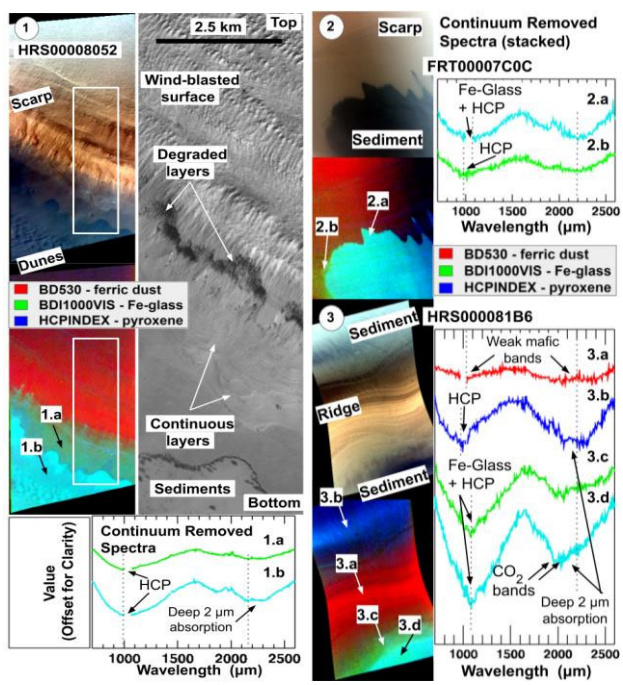

Figure 3: Results from the SPLD. *At each location (SPLD sites 1, 2, and 3), a true color image (top left), CRISM RGB composite of spectral parameters BD530/ BDI1000VIS/ HCPINDEX (middle left), and CTX image of the region within the white box, along with spectra extracted.*

SAND-E: A ROVER-BASED MARS ANALOG STUDY OF A MAFIC SEDIMENTARY ENVIRONMENT, ICELAND. P. Sinha[1], B. H. N. Horgan[1], R. C. Ewing[2], E. A. Rampe[3], M. G. A. Lapotre[4], M. Nachon[2], M. Thorpe[3], C. Bedford[5], K. Mason[6], E. Champion[2], P. C. Gray[7], E. Reid[8], , M. Faragalli[8], [1]Purdue University (sinha37@purdue.edu), [2]Texas A&M University College Station, [3]NASA Johnson Space Center, [4]Stanford University, [5]Lunar and Planetary Institute, [6]University of Arkansas, [7]Duke University, [8]Mission Control Space Services.

Introduction: Most studied rock exposures on Mars are sedimentary [1] and mafic [2], however, it is not well understood how physical fractionation and aqueous alteration affect mafic sediments during glacial, eolian, and fluvial processes [3-4], inhibiting the use of sediment composition to decipher martian paleoenvironments. Therefore, analog studies of sediment-grain properties and mineralogy in complex mafic mixtures are needed to bridge this gap [6-7]. Semi-Autonomous Navigation for Detrital Environments (SAND-E), a NASA-supported Planetary Science and Technology through Analog Research (PSTAR) project, aims to both advance the current state of rover operations and science framework within a mafic detrital environment by conducting Mars analog research in the glacio-fluvial-eolian landscapes of Iceland. This study investigates the material and grain-size dependent effects of chemical and physical weathering on sediments subjected to glacial, fluvial, and eolian processes in a cold and wet basaltic environment. Simultaneously, a rover-based semi-autonomous terrain analysis and an unmanned aerial system (UAS), simulating NASA's 2020 Mars Helicopter, is integrated within science workflows to test for efficiency in navigating and characterizing terrains as well as selecting science targets. Currently, automated geologic terrain maps are not used extensively for science in rover operations [7-8]. Incorporating terrain data captured by the rover into science operations has the potential to improve operation protocols towards greater tactical efficiency[9-11].

Fieldwork: Skjaldbreidauhraun and Dyngjusandur are glacio-fluvial-eolian sand plains (Fig. 1A) surrounding volcanic systems in the cold and wet mafic environment of Iceland [12-13]. Katabatic and regional winds drive eolian transport across sand sheets, which are characterized by ripples, dunes, wind-sculpted bedrock, wind-deflated rocky plains, and sand drifts similar to martian landscapes [13-14]. Skjaldbreidauhraun sands are dominated by crystalline phases, whereas Dyngjusandur contains abundant glass, making it directly relevant to Mars [15-16]. For initial reconnaissance of the site, we created false color images from Google Earth imagery using a Digital Correlation Stretch (DCS) [17], which reveal color differences that are largely due to variability in the composition of sediments (Fig. 1C,D). The fluvial system flows across a glacial outwash plain from a known basaltic source, and was divided into three locations for field work (Fig. 1B) - proximal, medial, and distal.

At each location, various science operations scenarios were implemented using the Mission Control Space Services, Inc., (MCSS) rover Argo J-5 (Fig. 2A). The rover, suited for soft soil and rough terrain, is mounted with a stereo camera, hazard cameras, a high-resolution mast camera, and a computer for navigation. Besides providing real-time estimates of trafficability metrics such as wheel sinkage, skid, tilt, etc., the rover classifies terrain type and predicts traversability using machine learning algorithms employed by the Autonomous Soil Assessment System (ASAS) [7-8,10-11]. Our various science-operation scenarios integrate combinations of automated terrain analysis, UAS images (3.2 cm/pixel), simulated HiRISE images (25 cm/pixel), field-of-view rover images, science data, and on-site geologists (Fig. 2).

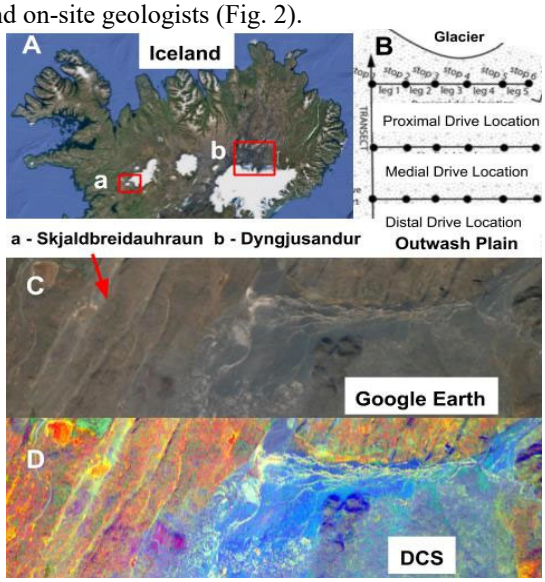

Figure 1: (A) Location of study sites in Iceland, (B) each operation scenario was tested at proximal, medial, and distal sites on the sedimentary transect in the direction away from basaltic source, (C&D) true color image is compared with DCS image to highlight compositional variability at Skjaldbreidauhraun.

Field work was conducted at Skjaldbreidauhraun in July of 2019 and is scheduled for the summer of 2020 at Dyngjusandur. Operation scenarios were designed to quantify operational efficiency with and without ASAS and UAS in combination with other inputs. Parameters such as time of operation, distance travelled, bandwidth, usefulness and accuracy of target, traversability

and terrain assessment are all considered to measure effectiveness of autonomy for driving and target selection in comparison to human validation. Concurrent science data include X-ray fluorescence (XRF), visible/near infrared (VNIR) reflectance spectra, context imagery, and high resolution targeted imagery, all taken using portable instruments and camera by field scientists to simulate the rover payload. Ground scientists in simulation were confined to the Ground Control Center (Fig. 2B) and were tasked to plan traverse maps and select science targets based on returned rover inputs. Additionally, samples were collected for laboratory X-ray diffraction (XRD), thermal-IR emission spectroscopy, scanning and transmission electron microscopy (SEM and TEM), and Camsizer particle analysis at the end of the field season.

Potential Impacts: Science results from the SAND-E project will shed new light into the variability of weathering along a glacio-fluvial-eolian transect in a cold and wet environment, and constrain its dependence on type/source of mafic materials, grain size, and sediment sorting. The cold and wet basalt-rich sedimentary environments of Iceland may serve as analogs to sedimentary and geochemical processes occurring during ancient icy climate episodes or in more recent times at/around the polar layered deposits (PLD) on Mars (although likely at different rates and intensity). The PLD garners significant interest from the scientific community as it preserved Mars' recent climatic records [18]. Detrital ice-rich sediments within the PLD are a complex mixture of mafic minerals and weathering products from multiple sources and is continuously reworked [18-21]. Insights from this study may provide new constraints for modelling polar chemical and physical processes, mechanisms and rates of weathering for both crystalline and amorphous silicates in and around the PLD, and as such, provide new avenues to interpret Mars' polar deposits in terms of climatic signals. Establishing a reliable relationship between mineralogy, grain size, transport pathways, water activity, and weathering will directly feed into our understanding of the processes that prevail at the PLD and other glacial terrains on Mars. Additionally, integrating terramechanics in the science workflow of rover missions can make traversing longer terrains feasible (e.g., 10s of km across a polar trough), driving in more complex terrains (e.g., ice-rich sedimentary surfaces), speed up identification of high-quality science targets, etc., ensuring more science returns within the lifetime of a putative PLD rover mission.

References: [1] Malin M. C., & Edgett K. (2000) *Science*, 290(5498), 1927-1937. [2] Hurowitz J. et al. (2006) JGR: Planets, 111(E2). [3] Siebach K. et al. (2017) *JGR: Planets*, 122(2), 295-328. [4] Lapotre M. et al. (2017) *JGR: Planets*, 122, 2489-2509. [5] Rampe. E. B. GRL, 45, 9488-9497. [6] Fedo C. et al. (2015) *Earth Planet Sci Lett*, 423, 67-77. [7] Stack K. et al. (2016) *Icarus*, 280, 3-21. [8] Yingst R. et al. (2017) *Acta Astronautica*, 132, 268-281. [9] Arvidson R. et al. (2017) *J. of Terramechanics*, 73, 73-93. [10] Wong C. et al. (2017) IEEE conference, pp 237-244. [11] Gonzales R. et al. (2017) *J of Field Robotics*, 35, 231-247. [12] Mangold et al. (2011) *Earth & Planet Sci Lett*, 310(3), 233-243. [13] Baratoux et al. (2011) *Earth Surface Processes and Landforms*, 36(13), 1789-1808. [14] Ewing R. C. et al. (2017) *JGR: Planets*, 122, 2544-2573. [15] Horgan et al. (2014) Icarus 234,132-154. [16] Horgan et al. (2017) *JGR: Planets*, 122, 172-202. [17] Gliiespie A. R. et al. (1987) Rem. Sen. of Envi., 20, 209-235. [18] Smith I. B. et at. (2018*) Keck Institute of Space Studies Report*. [19] Tanaka K. (2005) *Nature*, 437, 991-994. [20] Massé et al. (2010) *Icarus*, 209(2), pp.434-451 [21] Sinha et al. (2019) *LPSC Abstract*, vol 50.

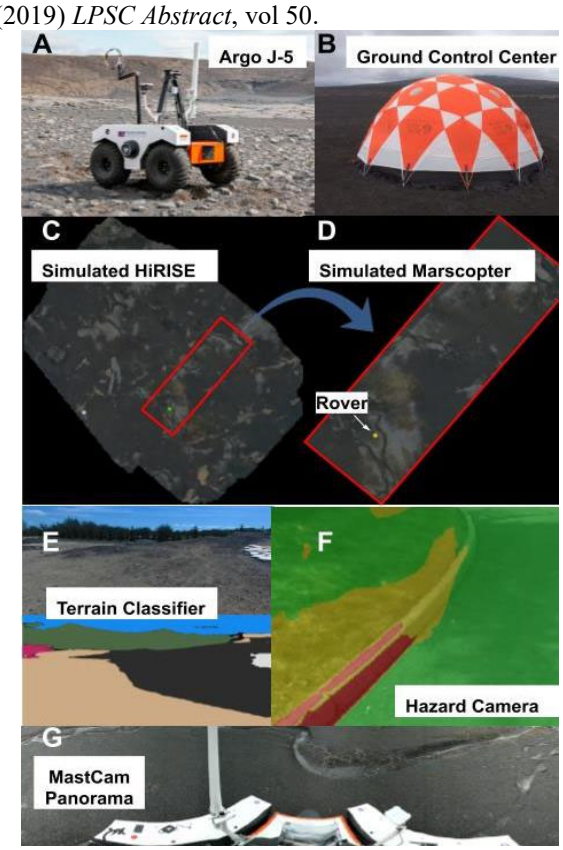

Figure 2: (A) MCSS rover Argo J-5, (B) Ground Control Center for science operation, (C) Simulated HiRISE image of a test site captured by UAS at 25 cm/pixel, (D) Simulated Mars Helicopter image at a higher resolution of 3.2 cm/pixel, (E) ASAS-generated terrain classification map, (F) pixel-wise hazard map from rover, (G) rover field of view for path planning and target selection within the workspace.

A Hypothesis for the "No-Flow" Mars' North Polar Layered Deposits Observations

I. B. Smith[1,2] , [1]York University, Toronto, Canada; [2]Planetary Science Institute, Denver, CO. (ibsmith@yorku.ca)

Introduction:

Flow scenarios:

Evidence against bulk flow:

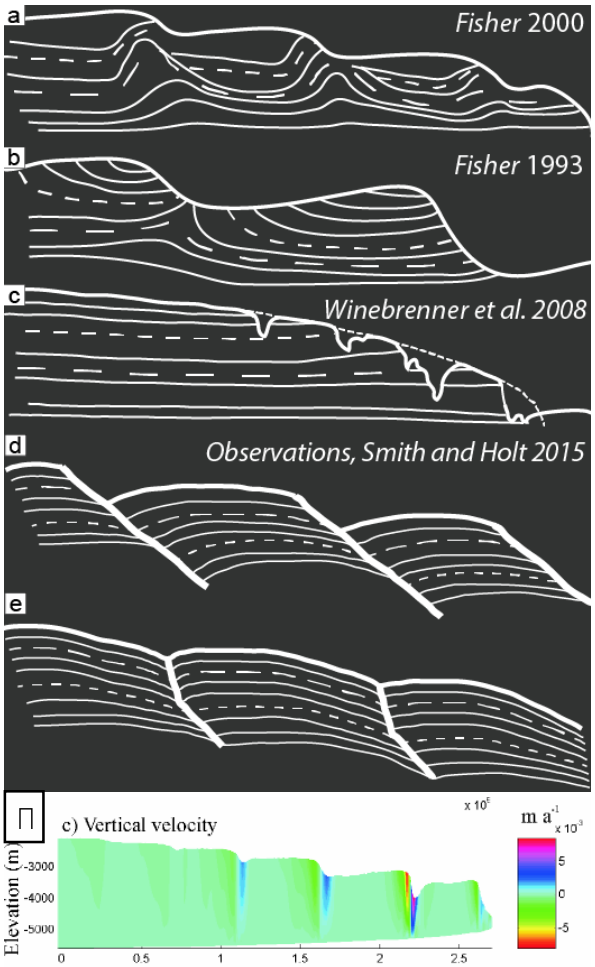

Figure 1: *Flow predictions and observed stratigraphy. a) and b) Stratigraphy used to explain the persistence of spiral troughs while the north PLD undergoes flow [7,8]. c) Predicted stratigraphy of a flowing ice sheet with spiral troughs later cut into the surface [11]. d) and e) Interpreted stratigraphy near the spiral troughs. The troughs have persisted for extended durations, and their stratigraphy is incompatible with any flow hypothesis [5]). f) Modeled velocities that result from flowing ice near the spiral troughs [9]*

Controversy:

small particle fractions and small particle sizes have a negligible effect on ice flow behavior.

Cause of Unobserved Flow:

***Figure 3**: Image and quote from [21] "the bulk flow strength of layered composites increases with decreasing thickness of the layer" and "thin-layered rocks compressed normal to the layering are rheologically stronger than homogeneous, isotropic mixtures under the stone deformation condition"*

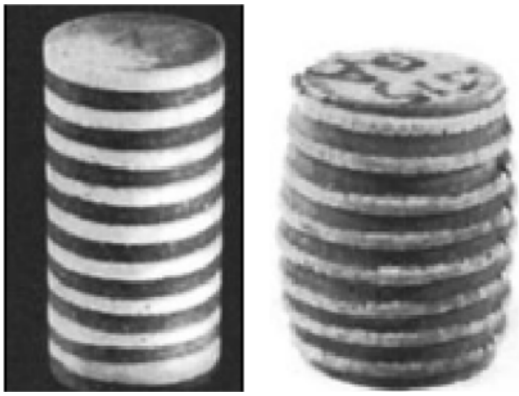

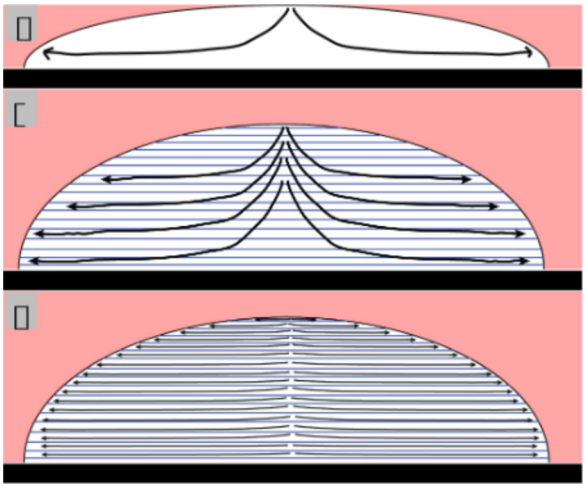

***Figure 2:** Flow scenarios. a) Generic ice sheet. Flow spreads from center outwards. b) Long-time interpretation of the NPLD. The volume of ice flows as in (a), and the layers do not play a major role. Stratigraphy like in Fig 1a should occur when spiral troughs are present. c) Flow interpretation that includes a multi-layer, stacked composite ice sheet. Each layer flows, as would a thicker ice sheet, but very little vertical deformation can occur.*

References: *J. Geophys. Res., 78* *Icarus* *J. Geophys. Res.* *The Cryosphere* *Icarus* *EPSL* *Icarus* *Icarus* *A. of Glaciology* *Icarus* *et al.,* *Icarus* *et al.* *Icarus* *JGR Planets* *GRL* *JGR Planets* *et al.* *GRL* *Icarus* *GRL* *JGR: Solid Earth*

GRAVITATIONAL CONSTRAINTS ON MID-LATITUDE ICE… AND THE NEED FOR MORE GRAVITY DATA AT MARS M.M. Sori[1,2], A.M. Bramson[1,2], S. Byrne[2], P.B. James[3], and J.T. Keane[4]. [1]Purdue University, West Lafayette, IN (msori@purdue.edu), [2]University of Arizona, Tucson, AZ, [3]Baylor University, Waco, TX, [4]California Institute of Technology, Pasadena, CA.

Introduction: Recent analysis of radar data from the Mars Reconnaissance Orbiter (MRO) has suggested that the mid-latitudes of Mars contain thick (tens to over 100 meters) sheets of buried excess ice [1, 2]. This inference is supported by geomorphologic analysis [3], high-resolution images [4], and neutron data [5], although alternative interpretations of the radar data may also be possible [6]. The presence of these ice sheets is important for a variety of scientific reasons, such as understanding the exchange of water between mid-latitude reservoirs and the larger polar deposits [7]. Additionally, any near-surface mid- or low-latitude ice represents a relatively accessible inventory of water that may be a critical resource for future human exploration or habitation of Mars.

Here, we use gravity to constrain putative buried mid-latitude ice sheets on Mars. Gravity is a powerful tool to study subsurface crustal structure, and while it has been previously used to quantify polar ice on Mars [8–10], it has not yet been considered in the analysis of mid-latitude ice sheets. We focus our study on the proposed ice sheets at Arcadia Planitia [1] and Utopia Planitia [2]. Water ice has substantially lower bulk density than the average Martian crust, and the presence of ice sheets should thus create a negative Bouguer gravity signature. If this signature can be confidently detected in the regions of Arcadia and Utopia Planitia, it can be used to estimate the volume of subsurface ice. Alternatively, the lack of an identifiable signature would imply an upper limit on the volume of ice, which depends on the precision of the known Martian gravity field.

Analysis: We consider the most recently published static gravity field of Mars, GMM-3, that has been inferred by radio tracking of Mars-orbiting spacecraft [11]. In our regions of interest, the local degree strength (the maximum spherical harmonic degree in the gravity field which has power greater than uncertainty) is ~80. This degree strength corresponds to a half-wavelength resolution of 133 km, and the proposed buried ice sheets in Arcadia and Utopia Planitia have lengths between 500–1100 km. We therefore argue that the ice sheets would likely be laterally extensive enough to analyze in GMM-3, and any gravitational signature or lack thereof constrains their thicknesses.

Gravity solutions are inherently non-unique. In the absence of constraints from other datasets or reasonable geophysical assumptions, observed gravity anomalies have infinite possible mathematical interpretations. Mars commonly has Bouguer anomalies of order 100s of mGals. Therefore, it is important to not simply interpret any negative Bouguer anomalies as evidence of buried ice; rather, plausible evidence comes in the form of locally low Bouguer anomalies that are spatially correlated with geological, radar, or thermal evidence of subsurface ice sheets.

We model the gravitational anomaly that would be expected from a buried ice sheet. We model the ice as a rectangular prism with an upper surface at the Martian surface and a lower surface defined by the ice thickness T. The Bouguer gravity anomaly from such an ice sheet is dependent upon the ice density ρ_i and the crustal density ρ_c, and given by equations 1–3 in [12] (although for this simple model, the anomaly is effectively the same as that given by a mass sheet approximation). Assuming ρ_i = 917 kg/m^3 and ρ_c = 2582 ± 209 kg/m^3 [13], the amplitude of the Bouguer gravity anomaly above the ice sheet is shown in Fig. 1 for various values of ice thickness and the density of the underlying crust.

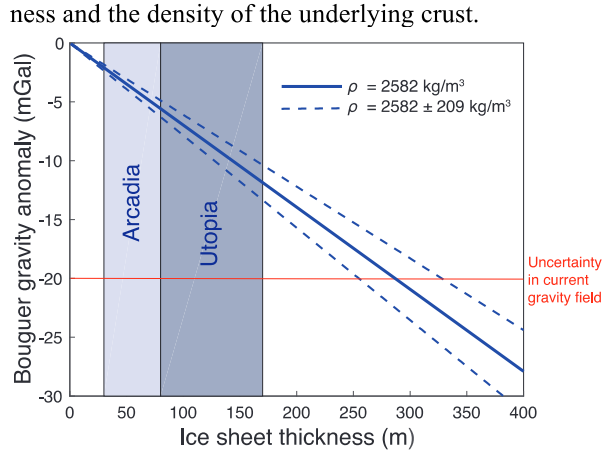

Figure 1. Modeled gravity anomalies from buried ice sheets as a function of their thickness and the Martian crustal density. Overlain are the proposed thicknesses of ice sheets in Arcadia (30–80 m) [1, 7] and Utopia (80–170 m) [2] Planitia, and the uncertainty in the inferred Martian gravity field [11] in those regions.

We do not observe any locally low Bouguer anomalies in Arcadia or Utopia Planitia that are spatially correlated with areas of proposed subsurface ice. However, the plausible gravity anomalies associated with buried ice sheets on Mars are relatively small. For example, a pure ice sheet that is 500 m thick (which is thicker than expected) would create a Bouguer anomaly of -35

mGal, and the most likely solutions based on current thickness estimates yield <10 mGal signatures. Additionally, the GMM-3 field [11] has uncertainty of nearly 20 mGal in these regions, so this result is interpreted as evidence that any subsurface ice is < 330 m thick (Fig. 1). Thicker ice sheets would have produced an observable gravity anomaly.

This result scales inversely with the difference in density between the putative ice and the surrounding crust; for example, if the ice is not pure but instead contains 10% dust (that has density 2500 kg/m^3) mixed in, the density difference between the ice and surrounding crust decreases, and the upper limit on the ice thickness is instead 370 m.

Our methodology described above represents analysis performed on gravity data in the spatial domain. Our ongoing work that will be presented at this meeting involves analysis performed on gravity data in the spectral domain [e.g., 9]. A spectral analysis of gravity reveals variations in the gravity anomaly at various wavelengths, an important property because different wavelengths are sensitive to different ranges of depths in the Martian subsurface.

A need for more gravity data! Currently, gravity science at other planets in our solar system is fundamentally lagging behind gravity science in the Earth-Moon system. At the Moon, measurement of the static gravity field to extremely high resolution with spacecraft-to-spacecraft tracking [14] has provided an unprecedented look at how planetary crusts form and evolve [15]. On Earth, similar mission architecture, plus gradiometry [16], have measured the time-varying gravity field to enable the study of dynamic processes like hydrological cycles and climate change. Similar advances can be made at Mars with new missions that adapt these mission architectures outside the Earth-Moon system, fly at lower altitudes, and/or develop other technologies.

Specific to this work, new gravity data could be used to support or refute the proposed water ice deposits at Arcadia or Utopia Planitia (or at other locations), thereby elucidating Martian climate change and mapping resources to enable human exploration. At the moment, uncertainty in the Martian gravity field is inconveniently maximized in the region of the possible Arcadia and Utopia ice sheets (Fig. 2). This locally high uncertainty is the result of a combination of MRO's polar orbit (more passes over high latitudes) and elliptical orbit (closer passes over the southern hemisphere), leaving the northern mid-latitudes as the area with the least precise gravity field. This deficiency can be realistically rectified with future missions or instruments. Furthermore, increasing the degree strength of the Martian gravity field will allow planetary scientists to isolate anomalies in the upper crust and thereby estimate ice volume more robustly.

We have compiled a list of which goals and objectives could be addressed by new gravity data at Mars. Investigations into the proposed buried ice sheets at Arcadia and Utopia Planitia would address at least 3 goals and 5 objectives of Mars science as defined by the Mars Exploration Program Analysis Group (MEPAG), at least 5 questions as defined by the Ice and Climate Evolution Science Analysis Group (ICESAG), and at least 2 objectives as defined by the Next Orbiter Science Analysis Group (NEXAG). Other benefits of a new gravity field hold similar promise for supporting Mars polar science. For example, more precise gravity fields would allow for scientific investigations into the distribution of buried carbon dioxide ice deposits, addressing several MEPAG and ICESAG objectives, while also supporting future entry/descent/landing of future robotic or crewed missions. New missions can elevate gravity science from only being a geophysical tool, enabling a multitude of other polar-science-related disciplines, including geomorphology, atmospheric science, hydrology, and human exploration.

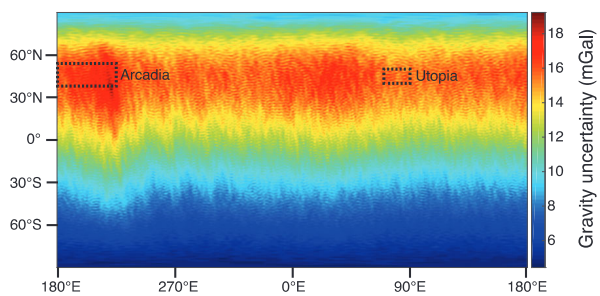

Figure 2. Uncertainty in the currently known Martian gravity field [11], with locations of proposed ice sheets in Arcadia [1] and Utopia [2] Planitia.

References: [1] Bramson A.M. et al. (2015), *GRL* 42, 6566–6574. [2] Stuurman C.M. et al. (2016), *GRL* 43, 9484–9491. [3] Viola D. et al. (2015), *Icarus* 248, 190–204. [4] Dundas C.M. et al. (2018), *Science* 359, 199–201. [5] Wilson J.T. et al. (2018), *Icarus* 299, 148–160. [6] Campbell B.A. and G.A. Morgan (2018), *GRL* 45, 1759–1766. [7] Bramson A.M. et al. (2017), *JGR: Planets* 122, 2250–2266. [8] Zuber M.T. et al. (2007), *Science* 317, 1718–1719. [9] Wieczorek M.A. (2008), *Icarus* 196, 506–517. [10] Ojha L. et al. (2019), *GRL* 46, 8671–8679. [11] Genova A. et al. (2016), *Icarus* 272, 228–245. [12] Sori M.M. et al. (2016), *Icarus* 273, 284–295. [13] Goossens, S. et al. (2017), *GRL* 44, 7686–7694. [14] Zuber M.T. et al. (2013), *Science* 339, 668–671. [15] Wieczorek M.A. (2013), *Science* 339, 671–675. [16] Cesare S. et al. (2010), *Acta Astronautica* 67, 702–712.

Ice related landforms in crater Hale and its relation with sun energy. M. G. Spagnuolo[1], D. A. Winocur[1], M.. Mantegazza[2] and A. Rodriguez, [1]IDEAN (UBA-CONICET) (mgspag@gmail.com), [2]FCEyN, UBA.

Introduction: Hale crater is a large complex crater formed at the source region of Uzboi Vallis, along the northern rim of the Argyre basin within the Nereidum Montes region and is one of the largest martian impact craters presently known to have generated channels that radiated outward from the impact site [1]. Hale crater reveal lots of evidences of ice related landforms such as rock glaciers, moraine deposits [2,3] and gullies related to ice melting processes [4]. Nevertheless, there is still some controversy since the lack of identification of water ice, plus some discussions in relation to the gullies formation and presence of water. Here we attempt to make a details map of landforms in Hale crater, describing them in the view of terrestrial analogs that have a clear water ice origin. We also use make an insolation analysis to determine if there is a correlation between those features and the energy received [5].

Landforms mapping: Using CTX base images and HIRISE we identified ice related landforms. We then compared each landform with a terrestrial analog, mainly from Iceland (Fig.1). After the identification of each landform, we plot in a GIS the location of each one. Between the landforms we recognized rock glaciers in, thermokarst, solifluction lobes, polygonal patterns and moraines [6].

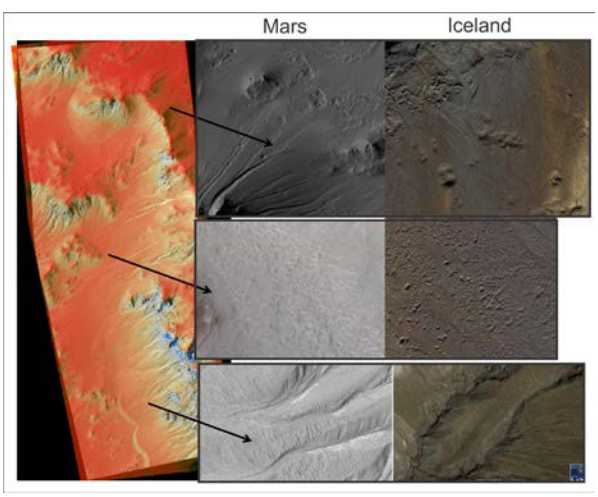

Fig. 1: Comparison between ice related landforms in Mars and Iceland.

Illumination Analysis: For the solar flux we used the MarsLux code [5] for a hole Martian year making a calculation every half hour. With the results we generated maps of mean energy, maximum, minimum and number of intervals between light and darkness. Using this results together with derived slope maps and topography we implemented machine learning technics in R to generate a final map with 5 classes. This five classes correspond to specific illumination parameters and topographic characteristics.

Discussions: Preliminary results from the illumination analysis with the map of the ice related landforms we recognized a clear correlation between areas with actual poor illumination conditions and ice related features. Moreover in areas with maximum illumination no distinguish ice related morphologies are observed.

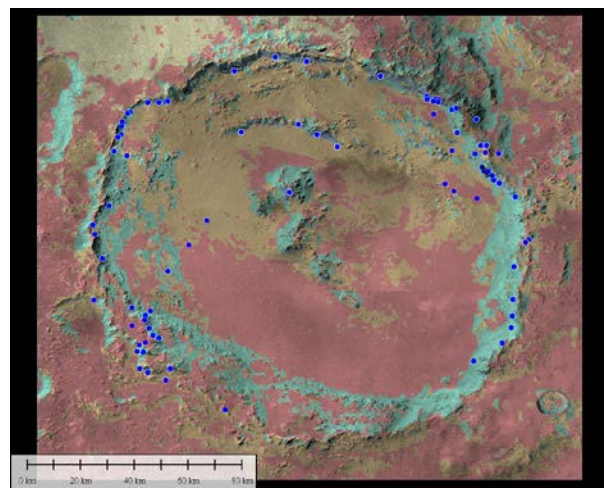

References:

[1] El-Maarty M. R. et al. (2013) Icarus, 226, 905-922. [2] Hauber E. et al. LPSC 41, 1922. [3] Hauber E. et al. Analog Sit. Mars Miss. (2011) 6011.[4] Reiss et al. (2009) Planet & Space Sci., 57, 958-974. [5] Spagnuolo et al. (2019) E&SS, 6, 146-155 [6] Ulrich M. et al. (2011) Geomorphology, 134, 197-216.

WE SHOULD SEARCH FOR LIFE IN MARS N. POLAR GROUND ICE. [illegible]

Introduction: [illegible]

Rationale for a Habitable Environment: [illegible]

Surface Age Analysis: [illegible]

Discussion: [illegible]

[illegible]

Icebreaker Mission Concept: [illegible]

References: [illegible] *J. Geophys. Res.* [illegible] *J. Geophys. Res.* [illegible] *Science,* [illegible] *Science* [illegible] *Nat. Rev. Microbol.* [illegible] *J. Geophys. Res.* [illegible] *Nature* [illegible] *Icarus* [illegible] *Appl. Env. Microbiology* [illegible] *PNAS* [illegible] *Icarus* [illegible] *Icarus* [illegible] *Astrobiology* [illegible] *AbSciCon* [illegible]

MARTIAN POLAR VORTEX DYNAMICS AND THE 2018 GLOBAL DUST STORM. P. M. Streeter[1], S. R. Lewis[1], M. R. Patel[1,2], J. A. Holmes[1], [1]School of Physical Sciences, The Open University, Walton Hall, Milton Keynes MK7 6AA, U.K. (paul.streeter@open.ac.uk), [2]Space Science and Technology Department, Science and Technology Facilities Council, Rutherford Appleton Laboratory, Harwell Campus, Didcot, Oxfordshire OX11 0QX, U.K.

Introduction: Mars' winter atmosphere is characterized by a polar vortex of low temperatures around the winter pole, circumscribed by a strong westerly jet [e.g. 1]. These vortices are a key part of the atmospheric circulation and impact heavily on dust and volatile transport. In particular, they have a complex and asymmetrical (north/south) relationship with atmospheric dust loading [1]. Regional and global dust events have been shown to cause rapid vortex displacement [2,3] in the northern vortex, while the southern vortex appears more robust. This has implications for tracer transport through the zonal jets associated with the vortices, including the intra-vortex transport of dust itself [4]; a more coherent and low-latitude zonal jet should provide a more effective barrier against tracers entering the polar regions.

Suspended atmospheric dust aerosol is a crucial active component of Mars' atmosphere, with significant radiative-dynamical effects through its scattering and absorption of radiation [5]. The exact nature of these effects depends on a variety of factors: aerosol optical depth is important, as are the specific radiative properties of the aerosol particles [6,7], and the vertical distribution of the dust itself [8].

Mars Global Dust Storms (GDS) are spectacular, planet-spanning events which dramatically increase atmospheric dust loading. The 2018 GDS was observed through its lifecycle by the Mars Climate Sounder (MCS) instrument aboard the Mars Reconnaissance Orbiter [9]; using data assimilation [10] to integrate MCS retrievals [11] with the LMD-UK Mars Global Circulation Model (MGCM) [12] therefore offers an opportunity to examine the effects of the GDS on the polar vortices, and the interplay between the factors described above. The reanalysis contains the MGCM's best possible representation of the GDS geographical, temporal, and in particular vertical structure.

Model and assimilation scheme: We use the LMD-UK Mars Global Circulation Model (MGCM), which solves the meteorological primitive equations of fluid dynamics, radiative and other parameterised physics to calculate the state of the martian atmosphere [3,8]. The UK version of the MGCM possesses a spectral dynamical core and semi-Lagrangian advection scheme [13], and is a collaboration between the Laboratoire de Météorologie Dynamique, The Open University, the University of Oxford, and the Instituto de Astrofisica de Andalucia. The model was run at spectral spatial resolution T42 and a vertical resolution of 50 levels, the latter spaced non-linearly. The assimilation scheme used was a modified version of the Analysis Correction scheme developed at the Met Office, adapted for use on Mars [6]. This method has the advantage of being computationally inexpensive, and its use of repeated insertion, weighted over a time window of about six hours, helps counter the issue of relaxation of the atmospheric state – an especially significant problem given the low thermal inertia of Mars' atmosphere.

Retrievals used: The retrievals used in this study are from the Mars Climate Sounder (MCS) instrument aboard the Mars Reconnaissance Orbiter (MRO) [4], which now has amassed over five full martian years' worth of data. For this study, the assimilated MCS variables were temperatures, derived column dust optical depth (CDOD), and dust profiles. Temperature profiles extend from the surface to approximately 100 km, and dust profiles from as low as 10 km above the surface up to a maximum height of approximately 50 km. Retrieval of dust profiles allows MCS to observe the complex vertical dust structure in the atmosphere. The retrieval version used is 5.2, a re-processing using updated 2D geometry [7]. This results in improved retrievals, especially in the polar regions.

Results: The 2018 GDS had a large impact on dynamics at both poles. Figure 1 shows the impact of the storm in its growth stage (L_S=180-210°) on the southern zonal jet, "impact" here being relative to the relatively quiet year MY 30. The most notable effect of the GDS here was to significantly reduce the strength of the high-altitude westerly zonal jet, effectively accelerating the progression of the circulation from an equinoctial to a solsticial mode through diabatic dust-related heating of the southern hemisphere. This diminished the high-low latitude temperature contrast which drives the polar westerly zonal jet. We present further results on the effects of the GDS on both southern and northern polar dynamics, and how this relates to transport of tracers (specifically dust).

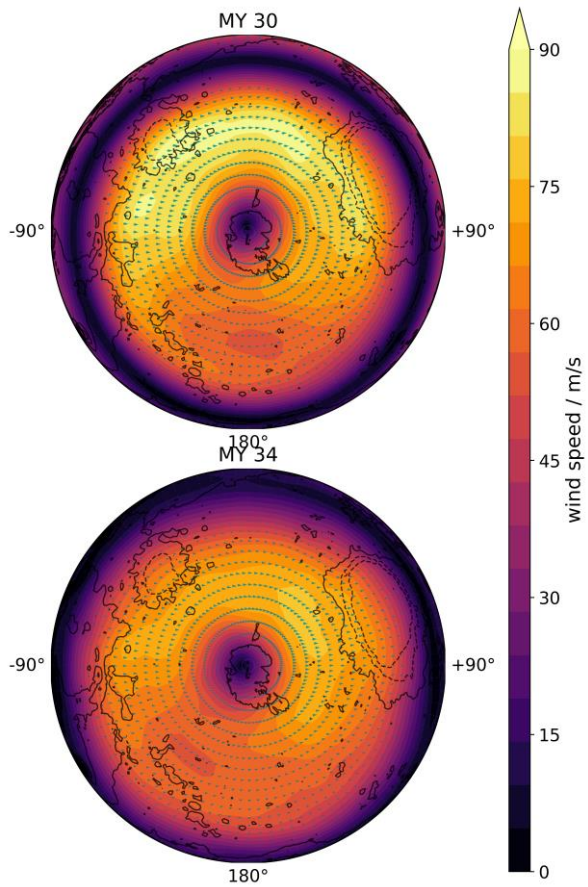

Figure 1: Wind speeds over the southern hemisphere at 50 km above the surface averaged over the period L_S=180-210° for MYs 30 and 34. Arrows show the direction of the westerly jet.

Discussion: Previous reanalysis studies of the polar vortices have used TES data [9,11]; MCS contains temperature profiles for higher in the atmosphere as well as dust vertical profiles, allowing for investigation of higher-altitude phenomena plus the impact of the dust vertical distribution on polar dynamics (and vice versa). Additionally, MCS dust profile retrievals are not restricted to areas with relatively warm surface temperatures (>220 K) as TES CDOD retrievals are [14], which excludes CDOD over the seasonal caps for the latter.

In particular for this work, the 2018 GDS dataset allows the opportunity for investigation of the polar dynamical effects of that specific event, the first fully observed by MCS. We present results from our reanalysis, and compare to free-running MGCMs, reanalyses of previous GDS events, and reanalyses of the older MCS retrieval set. We focus on the dynamics of the vortices themselves, zonal jet structure, and cross-vortex dust transport. The polar vortices and associated zonal jets act as a barrier for cross-vortex tracer transport; their weakening can therefore allow dust to be transported onto the seasonal CO_2 ice caps. Understanding how these barriers work is therefore important for, among other things, understanding the evolution of Mars' past climate: the Mars' ice caps contain a record of past dust deposition [e.g. 15].

Upcoming retrievals from the ExoMars 2016 Trace Gas Orbiter and its NOMAD spectrometer suite [16] will allow for further investigation of tracer transport and an opportunity to both cross-validate and jointly assimilate NOMAD and MCS data. NOMAD will also provide the crucial feature of observing over a range of martian local times, which will enable investigation of the diurnal cycles of tracer transport and atmospheric dynamics at the poles.

References: [1] Waugh, D. W. et al (2016) *J. Geophys. Res. Planets, 121,* 1770-1785. [2] Guzewich, S. D. et al (2016) *Icarus, 278,* 100-118. [3] Mitchell, D. M. et al (2015) *Q.J.R. Meteorol. Soc., 141,* 550-562. [4] McCleese D. J. et al (2010) *J. Geophys. Res.*, *115*(E12016). [5] Gierasch P. J. and Goody R. M. (1972) *J. Atmos. Sci., 29*(2), 400-402. [6] Turco R. P. et al (1984) *Scientific American, 251*(2), 33-43. [7] Madeleine J.-B. et al (2011) *JGR (Planets), 116* (E11010). [8] Guzewich, S. D. et al (2013) *J. Geophys. Res. Planets, 118*, 980-993. [9] Shirley J. H. et al (2018) *AGU Fall Meeting Abstracts 43*. [10] Lewis S. R. et al (2007) *Icarus, 192*(2), 327-347. [11] Kleinböhl A. et al (2017) *J. Quant. Spectrosc. Radiat. Transfer*, *187*, 511-522. [12] Forget F. et al (1999) *JGR, 104*, 24155-24175. [13] Newman, C. E. et al (2002) *JGR, 107*, 5123. [14] Smith, M. D. (2004) *Icarus*, *167*, 148-165. [15] Tanaka, K. L. (2000), *Icarus*, *144*(2), 254-266. [16] Patel, M. R. et al (2017), *Appl. Opt., 56*(10), 2771-2782.

DUST DEVIL ORIENTATION AND MARTIAN SURFACE WINDS. L. K. Tamppari[1], V. Ochoa[2], V. Sun[1]. [1]Jet Propulsion Laboratory/California Institute of Technology, Pasadena, CA, USA. [2]Arizona State University, Phoenix, AZ, USA.

Introduction: Dust devils tracks (DDTs) are seen over much of the Martian surface [1]. They are thought to be caused by surface-atmosphere temperature contrast causing convective vortices that lift (typically, higher albedo) dust, leaving behind a relatively dark track. A few years prior to the Phoenix north polar lander mission (2008; landing location 68.22°N, 234.25°E, [2]), the supposition was that dust devils would not occur at such high latitudes given the presumed smaller surface-atmosphere temperature contrast. However, many dust devil tracks were seen using MGS MOC data in the 65-72N latitude band of Mars [3], which included the four potential landing sites for the Phoenix lander. Once Phoenix landed, dust devils were observed nearby with the Solid State Imager [4] and pressure vortices consistent with passing dust devils ("dustless" devils) were observed via their characteristic pressure signature using Phoenix meteorology pressure sensor [5,6]. This study extends in time the catalog of dust devil tracks using more than 500 images from the Mars Reconnaissance Orbiter's Context Camera (CTX,[7]), and uses the dust devil track orientation as a proxy for the wind direction for comparison of the winds detected by the Phoenix Telltale wind indicator [8].

Data and Methods: *DDT location and orientation.* MRO CTX images in the 65-72 N latitude band were examined to find and catalog DDTs. ArcMap, a geographic information system, was used to view the georeferenced and map-projected images, to trace DDTs, and determine their longitudes and directions (North corresponds to 0º and East corresponds to 90º). Most of the images that were analyzed were taken during Mars Year 29 (2008-2009), overlapping with the Phoenix mission (May-November, 2008). Over 9,500 visible dust devil tracks were individually traced.

Wind speed and direction. It is desirable to know the wind direction associated with the DDTs. However, DDTs are an ambiguous record of wind direction, since DDT oriented at 0º or 180º could indicate winds from either North or South. Thus, wind speed and direction data from the Telltale wind indicator throughout the 151-sol Phoenix mission were examined. Hundreds of wind measurements were made every sol beginning on Sol 3 until Sol 151, resulting in more than a total of 7,000 wind measurements at various times of the day during the mission.

Results: *DDT location and orientation.* DDTs were found at all longitudes in the 65-72N band (Fig. 1), although some octants had a higher concentration of DDTs than others. The octant with the largest number of DDTs was L-7 (270-315E), which had 3,403 DDTs. The octant with the fewest DDTs was L-3 (90-135E) with only 26. Each octant's DDTs also in orientation. For example, in L-6 (225-270E), DDTs are primarily north-south and east-west oriented. But in L-7 (270-315E), one 45-degree bin to the East, DDTs are primarily northwest-southeast oriented.

Fig. 1: Polar projection of dust devil tracks found in the 65-72N band (red circles) of Mars. Longitudes sectors are separated into eight 45-degree bins. L-1 is 0-45º E, L-2 is 45-90º E, etc. CTX images are represented by dark grey rectangular boxes with white strips inside. Pink shading within these boxes indicates DDTs. Overlain are N-S-aligned rose diagrams showing the number of DDTs and their orientations for that octant.

Dust devil track changes. A time series of CTX images that overlapped the Phoenix landing site octant and mission duration were studied to search for occurrence and disappearance of DDTs. Two CTX images that include the Phoenix landing site stood out: P22_009725_2484 and B01_009857_2484, which will hereafter be referred to as Image 1 and Image 2, respectively (Fig. 2, left and right, respectively). Image 1 was taken on 2008-08-23 (Sol 89) and had no visible DDTs and Image 2, taken only 9 sols later on 2008-09-02 (Sol 98), had 109 DDTs. Dust devils formed and left tracks sometime between the acquisition dates of these two CTX images. The DDTs occur with two distinct orientations: north-northeast to south-southwest, and northwest to southeast (Fig. 3).

Comparison of DDTs to Phoenix wind data. Using contemporaneous Phoenix Telltale wind measurements, the directions of the dust devils that left tracks between Phoenix Sols 89-98 were determined. Phoenix took 726 wind measurements between Sols 89-98. On Sol 93, Phoenix saw an increase in dust devil activity [8] and measured winds coming from the southeast (~135º), closely matching one DDT orientation mode. On Sol 94, most of the wind data shows the direction having a value of about 20º which corresponds to winds coming from the north-northeast towards the south-southwest, closely matching the other DDT orientation mode (Fig. 3).

Fig. 2: (Left) CTX image ID P22_009725_2484 acquired on 2008-08-23 (Sol 89). (Right) CTX image B01_009857_2484 acquired on 2008-09-02 (Sol 98) with DDTs in purple. Phoenix landing site marked with a red 'x'.

Fig. 3 (Top) Rose diagram of dust devil track orientation from image B01_009857_2484. (Bottom-left) Wind direction for Sol 93 of Phoenix mission. (Bottom-right) Wind direction for Sol 94 of Phoenix mission.

Discussion: *DDT location and orientation.* A larger number of DDTs appear to occur between 225-360º E (Fig. 1; L-6 through L-8). This may be due to the fact that there are more CTX images in those octants and therefore a higher chance that a DDTs will be found. Alternatively, different surface materials could be present in this area allowing dust devil tracks to appear more easily; only 14% of dust devils may leave behind tracks [9]. The area within that longitude may also be more conducive to DDT formation as it is a known storm track region [10].

Comparison of DDTs to Phoenix wind data. The observed DDTs that occurred between sols 89-98 are most likely associated with a passing low pressure system. On sol 93-95, the Phoenix pressure sensor measured a pressure drop associated with such a passing system [11]. Examination of the Telltale wind measurements for these days show that winds speeds were primarily > 8 m/s (Fig. 4), whereas, typically, wind speeds were < 8 m/s. In fact, only 84 of the 726 measurements taken over sols 89-98 exceeded 8 m/s, and 82 of these 84 measurements occurred during sols 93-94. This indicates that, for the Phoenix vicinity, higher velocities may be necessary to drive dust devils that leave behind tracks.

Conclusions: DDTs occurring in the 65-72N latitude band during MY29 were cataloged using CTX data. DDTs were found in all longitudes, but were more commonly found between 225 -360º E. Although this region is a known storm track region which may be responsible for more DDTs, this may also be an observation bias due to the greater CTX coverage. Images which included the Phoenix lander and were taken during the Phoenix mission were examined to search for changes. A significant number of DDTs were observed to occur between sols 89-98. A low-p system passed over Phoenix on sols 93-95 and increased winds (>8 m/s) were observed on sols 93-94. The orientations of the DDTs compare well to the higher-speed wind directions measured on sols 93-94.

These results demonstrate for the first time that the correlation of dust devil tracks, detected from orbital imagery, with in-situ surface weather measurements can help constrain formation conditions for Martian dust devil tracks.

Fig. 4: (Left) The number of wind measurements > 8 m/s per directional bin for Sol 93; total n=27. (Right) Same for Sol 94. Total n=55.

References: [1] Hausmann *et al.* (2019) *LPSC 50 #2132.* [2] Smith *et al.* (2009) *Science* **325**(5936). [3] Drake *et al.* (2006) *GRL* **33**. [4] Lemmon *et al.* (2008) *LPSC 39 #2156.* [5] Ellehoj *et al.* (2010) *JGR* **115**(E00E16). [6] Taylor *et al.* (2008) *JGR* **113**(E00A10). [7] Malin *et al.* (2007) *JGR* **112**(E05S04). [8] Holstein-Rathlou *et al.* (2010) *JGR* **115**(E00E18). [9] Cantor *et al.* (2006) *JGR* **111**(E12002). [10] Tamppari *et al.* (2000) *JGR* **105**(E001133). [11] Taylor *et al.* (2010) *JGR* **115**(E00E15).

CURRENT AND FUTURE EUROPEAN HARDWARE CONTRIBUTIONS TO MARS POLAR SCIENCE.

N. Thomas[1], P. Becerra[1], I. Smith[2], G. Cremonese[3] and the CaSSIS team Physikalisches Inst., University of Bern, Sidlerstrasse 5, CH-3012 Bern, Switzerland (nicolas.thomas@space.unibe.ch),[2]York University, Toronto, Canada [3]Osservatorio Astronomico di Padova, INAF, Padova, Italy,

Introduction: The ExoMars Trace Gas Orbiter (TGO) was launched on 14 March 2016 and entered Mars orbit on 19 October 2016. The spacecraft reached its primary science orbit (360 km x 420 km; inclination = 74°) on 9 April 2018. TGO carries a high-resolution colour and stereo camera system: the Colour and Stereo Surface Imaging System (CaSSIS) [1]. The objectives of CaSSIS are to (1) characterise sites on the Martian surface which have been identified as potential sources of trace gases, (2) investigate dynamic surface processes (e.g. sublimation, erosional processes, volcanism) that may help to constrain the atmospheric gas inventory, and (3) certify potential future landing sites by characterising local slopes (down to ~10 m).

The instrument capabilities include acquisition of images (1) at scales of ~4.5 m/px, (2) in 4 broad-band colours optimised for Mars photometry, (3) with swathes up to 9.5 km in width, and (4) with quasi-simultaneous stereo pairs over the full swath width for high res. digital terrain models. A full instrument description is provided in [2], and details about the ground calibration in [3]. Spectral-image simulations to assess the colour and spatial capabilities of CaSSIS are in [4], with recommended colour display combinations given in [5]. Photometric correction of instrument data is presented in [6].

Although the spacecraft orbit inclination is only 74 deg, this still allows observations of seasonal processes as well as layered terrains in, for example, the Ultima Lingula formation. CaSSIS observations at high latitudes will be discussed.

The European Space Agency has recently issued a call for "White Papers" for future mission concepts and ideas across the science community. Martian climate studies featured significantly in the responses to this call. The options for ESA (including the possibilities for collaboration with NASA) will be discussed.

We include additional details on these two aspects.

Current Polar Imaging with CaSSIS: CaSSIS has acquired over 8123 images of Mars through to 12 October 2019 (roughly 70% of the prime mission). Over 750 of these have been acquired southward of 66° S and just over 400 have been acquired northward of 66° N. 372 of these are images of South Polar Layered Deposits (SPLD), or other buried layered deposits that have been identified as ice [7] (Figure 1). Hence, these images form a significant additional resource for studying Mars polar terrains.

A recent example from the northern hemisphere is shown in Figure 2, which shows polar dunes exhibiting evidence of small scale geyser activity. What is particularly interesting is that the substrate shows a set of linear, quasi-parallel ridges that may be related to aeolian features such as longitudinal dunes with large particles sizes.

An example from the southern hemisphere (Sisyphi Cavi) is shown in Figures 3 and 4 where we see residual ices evident at the base of a south-facing cliff, and an outcrop of the SPLD exposed in the margin of Ultima Lingula. The image in Figure 3 (taken at Ls =287.9°) was acquired at 18:00 LST and illustrates that additional information may come from CaSSIS as a consequence of the non-Sun synchronous orbit.

Future European Contributions to Mars Polar Science: The situation in Europe is one in which the Human and Robotic Exploration directorate is now leading an optional Mars programme, and should ExoMars be successful, ESA (through HRE) will seek to participate in Mars Sample Return as a joint international mission with NASA (and possibly other agencies). This mission could be a precursor to the manned exploration of Mars, which would be consistent with the perceived aims of the HRE directorate.

The case has been made to the Science Programme of ESA, that missions and instruments such as TGO/CaSSIS and Mars Express/MARSIS could be followed up by exploration of the poles and specifically the polar layered deposits within a joint programme with NASA. (see www.cosmos.esa.int/web/voyage-2050/white-papers). ESA could contribute by evaluating possibilities for:

- deep drilling systems,
- rovers,
- near-surface flight (drones),
- surface networks, and/or
- orbital reconnaissance

Although financial limitations will restrict what could actually be implemented so that it is unlikely that ESA could lead such an endeavour.

There are various ways in which NASA-ESA collaborations can occur and we shall present how this could be achieved with specific application to the Mars Polar Layered terrains.

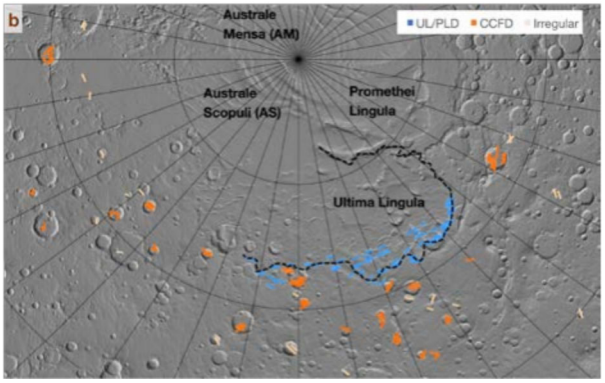

Figure 1. CaSSIS stamps of icy layered deposits in the SPLD, and within Circumpolar Crater Filling Deposits and Irregular deposits as defined by [7].

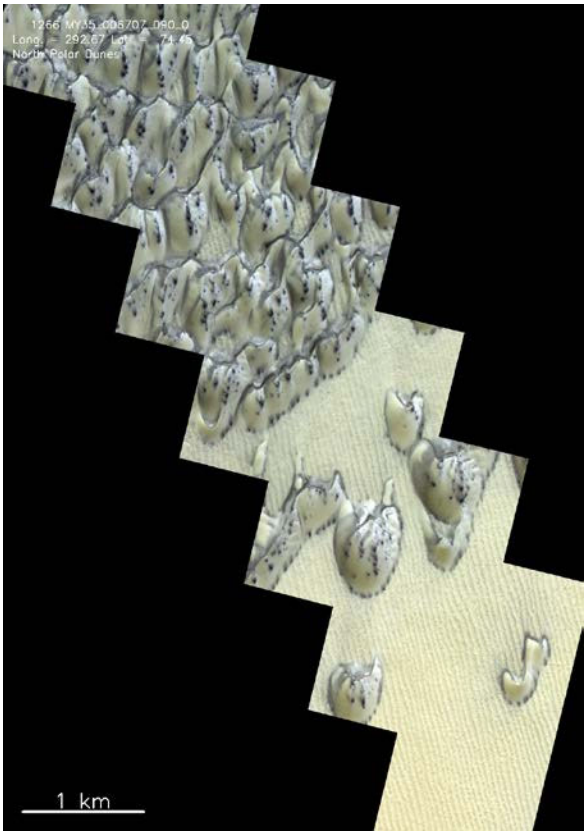

Figure 1 North polar dunes acquired at close to the maximum latitude observable with CaSSIS TGO. Note the linear, quasi-parallel ridges in the substrate that may be related to longitudinal dunes.

Figure 3 CaSSIS observation from Sisyphi Cavi showing residual ices at the base of south facing cliffs.

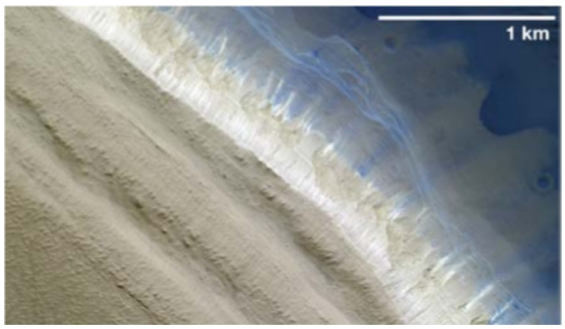

Figure 4. CaSSIS Image of SPLD marginal deposits in Ultima Lingula. The icier units of the SPLD can be distinguished from more silicate-rich basal deposits.

References:

[1] Vago, J., et al. (2015), Solar System Research, 49, 518-528. [2] Thomas, N. et al. (2017) Space Sci. Rev., 212, 1897. [3] Roloff, V. et al. (2017) Space Sci. Rev., 212, 1871. [4] Tornabene, L.L. et al. (2018) Space Sci. Rev., 214, 18. [5] Tornabene, L.L., et al. (2019) Mars 9 abstract. [6] Pommerol, A. et al. (2019) Mars 9 abstract. [7] Sori et al., (2019), *JGR*

Acknowledgement: The authors thank the spacecraft and instrument engineering teams for the successful completion and operation of CaSSIS. CaSSIS is a project of the University of Bern funded through the Swiss Space Office via ESA's PRODEX programme. The instrument hardware development was also supported by the Italian Space Agency (ASI) (ASI-INAF agreement no.I/018/12/0), INAF/Astronomical Observatory of Padova, and the Space Research Center (CBK) in Warsaw. Support from SGF (Budapest), the University of Arizona (Lunar and Planetary Lab.) and NASA are also gratefully acknowledged.

NORTH POLAR SPRINGTIME REMOVAL OF COLD-TRAPPED H_2O ICE THROUGH INSOLATION-INDUCED BASAL SUBLIMATION OF CO_2. T. N. Titus[1], K. E. Williams[1] and G. E. Cushing[1], [1]US Geological Survey, Astrogeology Science Center, 2255 N. Gemini Dr., Flagstaff, AZ 86001

Introduction: The H_2O and CO_2 cycles on Mars are coupled processes, and conditions in the north polar springtime seasonal ice cap demonstrate how these volatiles modify each other's condensation and sublimation rates.

Background: Both modeling [1-3] and observations [4-9] support the theory that a sublimation lag of H_2O ice is left behind when the edge of the seasonal CO_2 ice cap retreats. As the surface continues to warm, the H_2O ice lag also sublimes and some of that H_2O vapor is transported over the CO_2 ice cap edge where it is cold-trapped within the cap interior. This process acts like a conveyor belt transporting the water poleward until all of the CO_2 ice has sublimed.

Observations: The retreating north polar seasonal cap has been observed by numerous spacecraft instruments over a wide spectral range. Mars Global Surveyor Thermal Emission Spectrometer (TES) [10], Mars Express Mars Observatoire pour la Minéralogie, l'Eau, les Glaces et l'Activité (OMEGA) [11], Mars Reconnaissance Orbiter (MRO) Compact Reconnaissance Infrared Spectrometer for Mars (CRISM) [12] and the Mars Odyssey THermal EMission Imaging System (THEMIS) [13] are the focus for this study although several other instruments provide corroborating observations.

TES. Observations of both solar (albedo) and thermal spectral regimes enabled the tracking of seasonal ice cap edges. Temperature observations can be used to determine whether bright materials are CO_2 ice or are being thermally buffered by CO_2 ice [5,7].

OMEGA/CRISM. Both OMEGA and CRISM had short-wave infrared (SWIR) subsystems with the ability to spectrally distinguish between volatile types. Unlike TES, SWIR observations only sense the top few micrometers of the surface, such that an optically thick layer of one type of volatile (even if physically thin), can obscure the spectral signature of underlying materials. It is these observations that show H_2O ice is removed while CO_2 ice is still present.

THEMIS VIS. Observations of clouds over the early morning seasonal cap (Fig. 1) suggest a southward airflow in the bottom few kilometers of the atmosphere [14-15]. The presence of lee clouds and cloud streets shows the presence of H_2O vapor at a temperature near the dew point with little to no vertical mixing. The afternoon observations show a lack of lee clouds and cloud streets, suggesting either a warmer or more turbulent lower atmosphere. In both times of day, what appears to be ice-fog is prevalent.

The Model:

Getting the water in: There are two theories as to how the water ice that is observed in the cap interior is transported: (1) prior to the seasonal cap formation [12] and (2) after the seasonal cap formation [1-3,10-11].

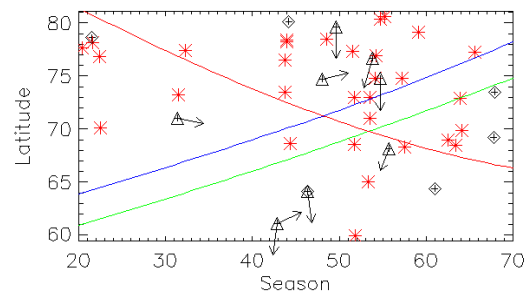

Figure 1: MY 33 northern spring morning clouds observed by THEMIS VIS. Red asterisks indicate ice-fog. Triangles indicate lee clouds. The arrow indicates the direction the cloud is moving based on a 360-degree azimuth. Diamonds indicate cloud streets. The red line indicates the edge of polar day. The blue line indicates the average CO2 cap edge latitude while the green line indicates the average H2O cap edge [16].

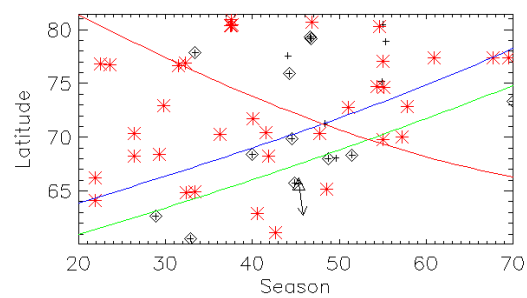

Figure 1: MY 33 northern spring afternoon clouds observed by THEMIS VIS. Legend is the same as in Fig. 1. The "+" signs indicate stratocumulus clouds.

Theory 1 requires H_2O ice to condense onto the polar surfaces in early autumn, and be sufficiently rough that it protrudes above the seasonal CO_2 ice as early as L_s=11°. At this season, the CO_2 ice in the interior of the seasonal cap may exceed a meter in depth [5,17]. Additional modeling is needed to determine if intimately mixed H_2O ice that condensed with the CO_2 ice during the fall can account for this early detection of H_2O absorption features.

Theory 2 (Fig. 3) requires the existence of either a Mars polar cell or that the baroclinic waves penetrate deep into the cap interior. Observations of early morning lee clouds and cloud streets favor the Theory #2 scenario [14-15], as their formation indicates high concentrations of water vapor in the bottom few kilometers of the atmosphere.

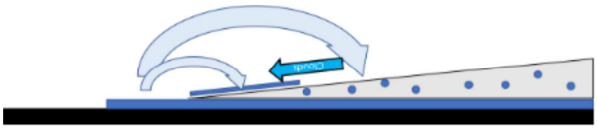

Figure 2: General movement of water vapor near the cap edge. The water vapor that forms the low-altitude water-ice clouds (dark blue arrow) are from the same vapor source that results in the cold-trapped water ice on the surface.

Getting the water out: As pointed out by Brown et al. [9], removing a thin cold-trapped layer of H_2O ice that is in direct contact with CO_2 ice through sublimation of the top layer is not plausible. We propose that the same process that has been used to explain spots and fans on the southern seasonal cap[18-21] and spots on defrosting northern dunes [22] can be scaled to the north polar seasonal cap. In this scenario, insolation induces basal sublimation of a semi-transparent slab of CO_2 ice, just as in the south. However, instead of the CO_2 gas being concentrated and then released at vents, the escape of gas is widely distributed – more akin to seepage than jets. The seeping CO_2 gas may initially levitate the optically thick, but physically thin, layer of cold-trapped H_2O ice. The H_2O ice layer quickly fractures where the smaller fragments are lofted into suspension and the larger fragments are pushed aside to form ring-shaped micro-piles. The tops of these micro-piles are no longer in direct contact with the underlying CO_2 ice, possibly enhancing sublimation during the warmer parts of the day. (Fig. 4) These micro-piles could also be eroded into blowing H_2O snow as suggested by Brown et al. [9], by katabatic winds. The ice fogs observed by THEMIS-VIS could be blowing H_2O snow.

Summary: The conceptual model presented here explains many of the observations of the northern springtime seasonal cap. Water vapor is transported into the interior of the seasonal cap either through deep penetrating baroclinic waves or by a Mars polar cell. The vapor transported is the source for both clouds and observed cold-trapped water ice. Seepage of CO_2 gas from insolation-induced basal sublimation fractures cold-trapped water ice on the CO_2 ice surface, thus removing the H_2O ice from direct thermal contact with the underlying CO_2 ice. Smaller fragments can be lofted – either subliming, being carried away in suspension, or falling back on the surface as snow-like material. Larger fragments are pushed aside into concentric piles, which can either be eroded or sublimate.

The solid greenhouse effect may be a widespread process on the springtime seasonal caps – the morphology of the process may be determined by the pressure and volume of the escaping gas, e.g. seepage vs. jets.

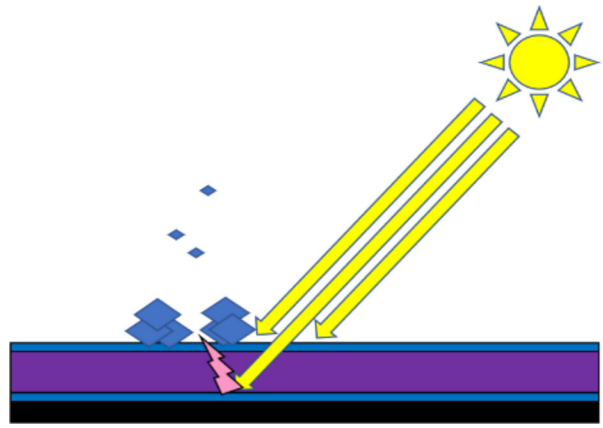

Figure 3: Insolation induced basal sublimation causes CO_2 gas to seep through the CO_2 ice slab. When the gas reaches the surface, the pressure fractures the H_2O cold trapped layer, where large fragments are pushed aside into micro-piles and small pieces are carried away in suspension.

References: [1] Houben H. et al. (1997) *JGR, 102*, 9069-9084. [2] Richardson M. I. & Wilson R. J. (2002) *JGR, 107*, 5031. [3] Montmessin F. et al. (2004) Icarus, 183, 403-410. [4] Bass D. & Paige D. (2000) Icarus, 144, 397-409. [5] Kieffer H.H. & Titus T.N. (2001) Icarus, 154, 162-180. [6] Schmitt B.S. et al. (2006) 4th Mars Polar Sci. Conf. [7] Wagstaff et al. (2008) PSS, 56, 256-265. [8] Appere T. et al. (2011) JGR, 116, CiteID E05001. [9] Brown A. et al. (2012) JGR, 117, CiteID E00J20. [10] Christensen et al. (1992) JGR, 97, 7719-7734. [11] Bibring et al. (2005) Sci., 307, 1576-1581. [12] Murchie S. et al. (2007) JGR, 112, E05S03. [13] Christensen et al. (2004) SSR, 110, 85-130. [14] Titus T.N. et al. (2019a) 9th Intern. Conf. on Mars, Abstract #6232. [15] Titus T.N. et al. 2019b in preparation. [16] Titus, T. N. (2005) LPS XXXVI, Abstract #1993. [17] Titus T.N. & Cushing G.E. (2017) LPS XLVIII, Abstract #1198. [18] Kieffer, H.H. (2000) 3rd Conf. On Mars Polar Sci. & Explor., Abstract#8083 [19] Piqueux, S. et al. (2003) JGR, 108, CiteID 5084. [20] Kieffer H.H. et al. (2006) Nature, 442, 793-796. [21] Kieffer H.H. (2007) JGR, 112, E08005. [22] Hansen et al. (2013) Icarus, 225(2), 881-897.

AGE-DATING OF MID-LATITUDE MARTIAN THERMOKARST AND MANTLE DEPOSITS: A PRELIMINARY ASSESSMENT. D. Viola, NASA Ames Research Center, Moffett Field, CA.

Introduction: Outside of the Mars polar caps, water ice is abundant in the shallow subsurface of the planet's mid-latitude plains [e.g., 1-6], and the deposition and removal of this ice mantle over time are thought to be closely linked to climate [7], particularly to the planet's obliquity cycles [8-9].

The degradation of mid-latitude ice has been inferred from the presence of dissected mantle [10] and thermokarst-like depressions [e.g., 11-12]. On Earth, "thermokarst" refers to landforms that form as a result of the melting of ground ice in excess of the available pore space [13]. On Mars, mechanisms invoking thaw processes [14-15] or sublimation alone [16] have been proposed. Under current climatic conditions, however, it is very difficult to theoretically produce significant amounts of liquid water to produce thermokarst akin to that of Earth. It is unclear whether thermokarstic degradation is an ongoing process under the present climate (due to the slow rate of sublimation-modification and the short time over which high-resolution imagery is available), but crater age-dating of the thermokarstic depressions and the intact mantle that surrounds them can help to provide some temporal constraints on mantle deposition and thermokarstic modification.

Scalloped depressions are a common thermokarstic morphology found on Mars. These features are topographic depressions with steep pole-facing scarps and a shallow equator-facing slopes, with arcuate edges that sometimes contain one or more parallel ridges downslope of the outermost pole-facing scarp face. They typically range in diameter from a few hundred meters to ~3 km and sometimes coalesce into larger assemblages [12, 17-18]. Another feature interpreted as thermokarst in origin are "expanded" craters, with central crater bowls, a shallow apron to the surrounding surface, and a lack of crater rims such that the diameter of the craters appear to have widened over time, attributed to the removal of shallow excess ice and collapse of crater rims/dry dust overlying ice into the crater depression [16, 19].

Methods: Crater age-dating is a common method used to approximate how long a planetary surface has been exposed and accumulating impact craters. Absolute age-dating requires some assumptions about the crater production rate; lunar crater distributions can be linked directly to radiometric dating of returned samples [e,g., 20], and those production functions have been extrapolated to planets like Mars [21-22]. While there are some challenges to using this method for very small and/or very young surfaces [23], it can nevertheless provide valuable constraints on the timing of geologic processes. Key considerations include ensuring that craters are only counted within a single geologic unit and not spanning different surface types that could have formed at different times.

To help accomplish separation among geologic sub-units, terrain mapping will be performed to delineate the intact mantle from the regions that have been thermokarstically-altered. Superposed craters will be subdivided between these types of units to provide estimates of the surface age dates; while the subunits of intact mantle are geographically separate in some cases, they bear similar characteristics and are interpreted as remnants of the same topography-blanketing unit. Thus, the total number of superposed craters per total mantled area will be considered in obtaining age estimates. All mapping is performed using images from the Context Camera on the Mars Reconnaissance Orbiter, as this data set has near-global geographic coverage at fairly-high resolution (6 m/pixel) [24].

Study Areas: This study will focus on the northern mid-latitudes of Mars, primarily within Utopia Planitia, as well as a small study area in Arcadia Planitia (Figure 1). Utopia Planitia contains abundant scalloped depressions [e.g., 17], and it is thought that these scallops are young based on a qualitative observation that there are few impact craters observed in the regions where they are found. However, little quantitative work has been done in this regard. A region of Utopia Planitia (~60,000 sq. km) has been identified for preliminary mapping work (Figure 1); the preliminary results from a test swath within this region are presented here.

In addition, a small section of Arcadia Planitia will be similarly analyzed. Arcadia Planitia contains thermokarstically-expanded secondary craters [19], and a dense region of thermokarstic alteration has been identified for more focused surface crater counts. The age of the secondary craters was previously approximated using crater counts superposed on the source primary craters and their ejecta, where they were found to be on the order of tens of millions of years old. This estimate is anomalously-high for the anticipated age of mantle deposits throughout the northern plains of Mars of 0.5-2.1 Myr [7]; additional age-dating of the mantle surface immediately sur-

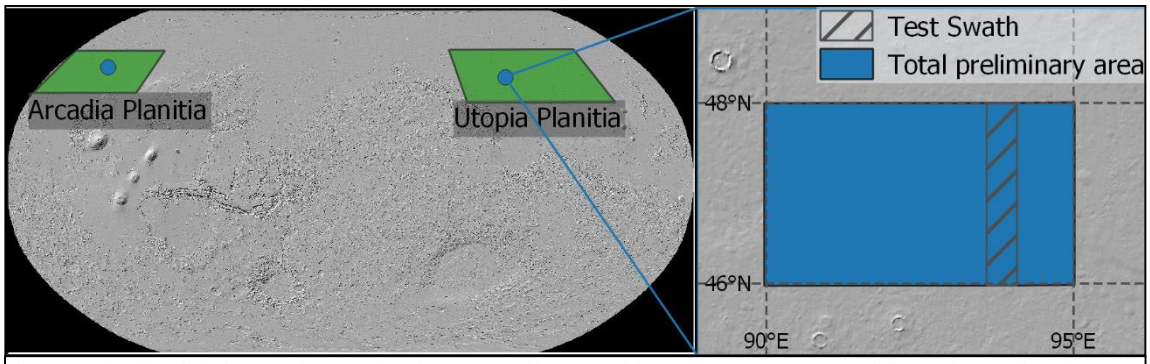

Figure 1: (Left) Global map of Mars showing areas of interest; blue points represent specific study area locations. (Right) Utopia Planitia study area; striped region represents a preliminary test-swath (results shown in Figure 2).

rounding the thermokarstically-expanded secondary crater clusters may help to resolve this difference.

Discussion: Age estimates of an early analysis of a test swath in the Utopia Planitia region were performed. The swath is ~40 km wide; geographic location is delineated in Figure 1, and the mapped terrains and age-dating results are shown in Figure 2. This analysis revealed age estimates for the mantle of ~1.1 ± 0.3 Myr, whereas the thermokarstically-degraded regions had an age estimate of 280 ± 100 kyr (Figure 2). These results are roughly consistent with the expectation that both the mantle and thermokarstic depressions are fairly young, and likely associated with geologically-recent climate changes. However, work is ongoing to obtain age estimates over a larger area, and these approximations are subject to change with the mapping of larger areas. In addition, continued work in Arcadia Planitia may help account for the age of the mantle deposit and the timing of thermokarstic alteration. The overall aim of this analysis is to better understand the history and of these non-polar shallow ice deposits, particularly as it pertains to the timing of both ice deposition and thermokarstic degradation, which are closely related the planet's climate history.

References: [1] Boynton et al. (2002). *Science, 297*:81-85. [2] Feldman et al. (2004). *JGR, 109*:E09006. [3] Bandfield & Feldman (2008). *JGR, 113*:E08001 [4] Mouginot et al. (2010). *Icarus, 210*:612-625. [5] Smith et al. (2009). *Science, 325*:58-61. [6] Byrne et al. (2009). *Science, 325*:1674-1676. [7] Head et al. (2003). *Nature, 426*:797-802. [8] Laskar et al. (2004). *Icarus, 170*:343-364. [9] Chamberlain & Boynton (2007). *JGR: Planets, 112*:E06009. [10] Mustard et al. (2001). *Nature, 412*:411-414. [11] Costard & Kargel (1995). *Icarus, 114*:93-112. [12] Sejourne et al. (2012). *Planet. Space Sci., 60*:248-254. [13] Davis (2001). *Univ. of AK Press.* [14] Soare et al. (2008). *Earth & Planet. Sci. Letters, 272*:382-393. [15] Costard et al. (2016). *Geomorphology, 275*:80-89 [16] Dundas et al. (2015). *Icarus, 262*:154-169. [17] Lefort et al. (2009). *JGR, 114*:E04005. [18] Morganstern et al. (2007). *JGR, 112*:E05S02 [19] Viola et al. (2015). *Icarus, 248*:190-204. [20] Turner (1977). *Phys. Chem. Earth, 10*:145-195. [21] Ivanov (2001). *Space Sci. Rev., 96*:87-104. [22] Hartmann (2005). *Icarus, 174*:294-320. [23] Williams et al. (2017). *Met. & Planet. Sci., 53*:554-582. [24] Malin et al. (2007). *JGR: Planets, 112*:E05S04.

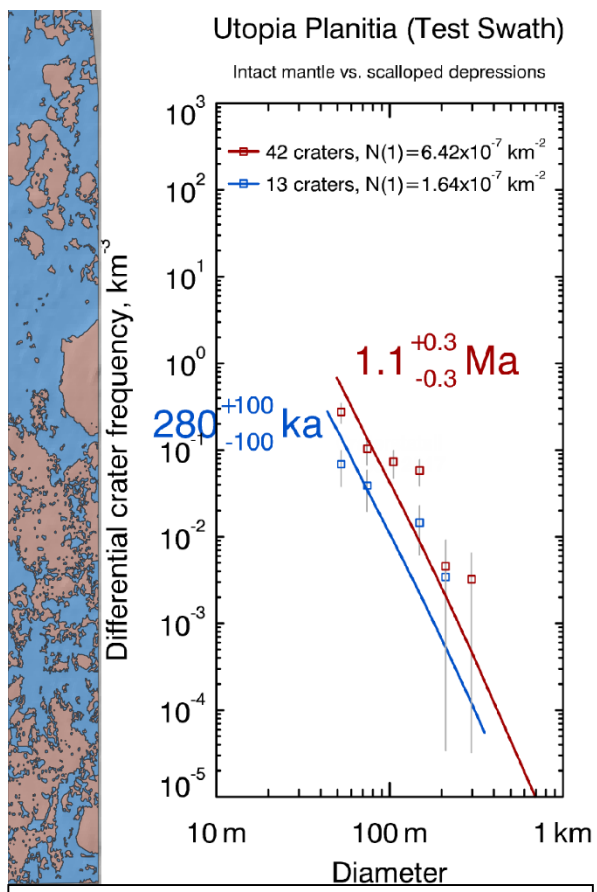

Figure 2: (Left) Mapped terrains in the Utopia Planitia test swath (area shown in Figure 1), where red is intact mantle and blue is scalloped terrain. (Right) Age-dating results for the two terrain types. Red corresponds to the crater distribution superposed on the intact mantle, and blue represent those found within scalloped depressions.

The Role of Mid-Latitude Ground Ice in North Polar Layered Deposits Formation. [illegible]

Introduction:

[illegible]

Methods:

[illegible]

1. Global Climate Model (GCM): [illegible]

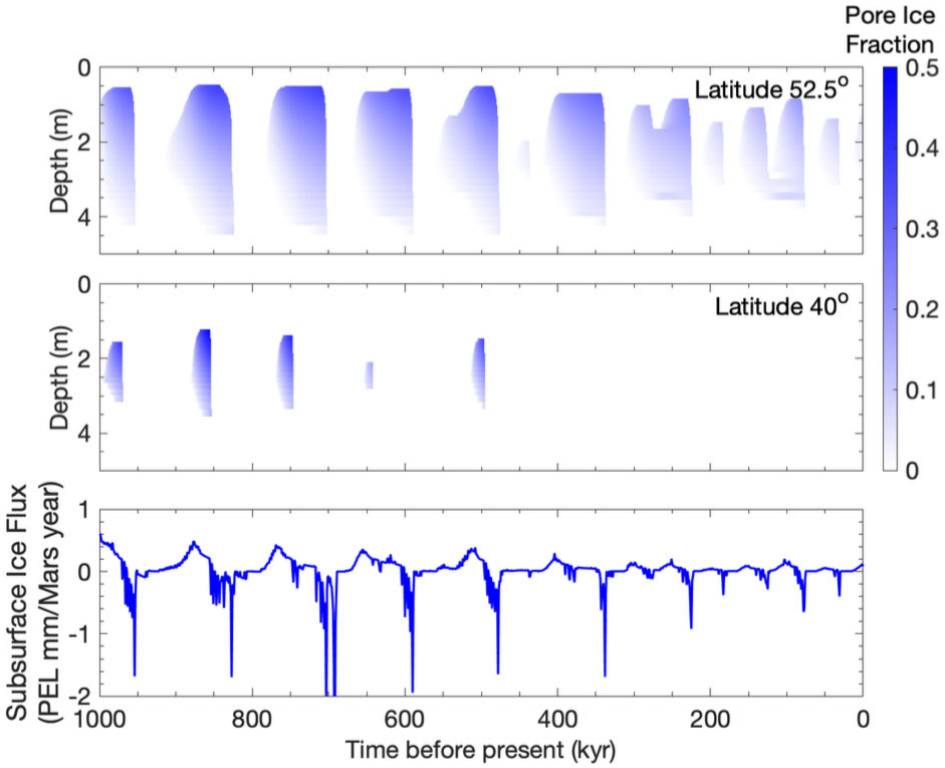

Figure 1: [illegible]

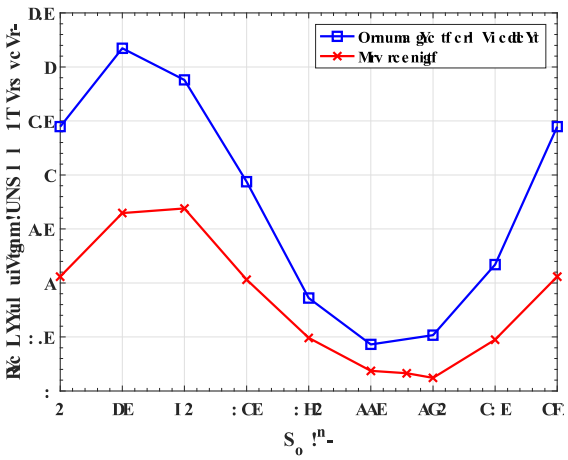

Figure 2: [illegible] L_p 5 [illegible]

2. Mars Subsurface Ice Model (MSIM): [illegible]

Results:
[illegible]

Discussion: [illegible]

References:
[illegible]

SURFACE TEXTURES OF LINEAR ROUND-TOPPED RIDGES IN THE SOUTHERN HIGHLANDS: EVIDENCE FOR A COLD-BASED GLACIATED LANDSCAPE. Kobe Y. Wang (ycwang430@ucla.edu) and An Yin (yin@epss.ucla.edu), Dept. of Earth, Planet., and Space Sci., UCLA, California 90095-156702, USA

Introduction: Linear round-topped ridges are common features in the southern highlands of Mars (**Fig. 1**). They are up >500 km long and about 10s of km wide. The surface of the ridges are generally smoother than the irregularly shaped ridges and high-elevation regions in the southern highlands (**Fig. 1**). These ridges commonly bound linear troughs radiating from the south polar ice cap. To our knowledge, the origin of the ridge morphology has not been discussed in the literature.

Motivations: It has long been speculated that the southern highlands of Mars were once occupied by a single ice sheet [1]. Debate has been centered on whether the ice-transport process during the inferred glaciation event was wet-based [2] or cold-based ([3], [4]). The two competing models make specific predictions that are testable by photogeologic mapping. Specifically, the wet-based models predict the occurrence of kames, drumlins, sub-glacial channels, lateral and frontal moraine ridges, and water-assisted soft-sediment deformation features such as isoclinal folds [5]. In contrast, the cold-based ice-transport model predicts a pavement of angular boulders along glacial-flow paths, poorly development or complete absence of lateral and frontal moraine ridges, and a lack of water-assisted soft-sediment deformation features [6]. The goal of this study is to (1) establish whether glaciation had occurred across the southern highlands and (2) to determine, if it did occur, whether glacier transport was dominated by wet- or cold-based mechanism.

Data and Methods: MOLA topographic data are used for locating major round-topped ridges (**Fig. 1**). HiRISE images are then used to examine the landforms and textures of the ridge surfaces. The results are compared against the landforms and textures of the surfaces and sedimentary/volcanic deposits in the nearby basins.

Preliminary Results: *Observations* A matrix-support boulder-bearing unit is widely distributed over the ridge tops near the south polar region (**Figs. 2A and 2B**). The boulders have an average size of 2-5 m and the grain size of the matrix material is below the resolution of HiRISE images. The boulders formed semi-circular patterns and the matrix material displays polygonal patterns, which are commonly associated with periglacial landforms on Earth. At the mid-latitude, the surface of the ridges show much lower densities of boulders than those to the south closer to the south pole. Subsurface materials excavated by impact craters are dominated by layered boulder-bearing material (**Fig. 2C**). Closer to the northern rim of the southern highlands but before reaching the north-sloping Arabia terra ramp, the surface of the round-topped ridges contain only scattered and lineated boulder trains (**Fig. 2D**). Directly next to the Arabia terra, however, the surface of the ridges exposes bedrocks only without the presence of overlain boulder-bearing material. Striated surfaces are common and often associated with step-like features perpendicular to the lineation direction (**Fig. 2E**).

Interpretation The boulder-bearing unit could either be generated by deposition of impact ejecta, glaciation, or a combination of both. The close association of the boulder unit with periglacial landforms near the polar region and with striated surfaces near the Arabia terra led us to favor a glaciation origin for the deposition of the boulder unit. However, it is possible that some of the boulders were first generated by impact processes and were later entrained into glacier flows. The lack of subglacial channels (i.e., eskers) and water-assisted soft-sediment deformation features suggests that glaciation is cold-based. This interpretation is further strengthened by the observations that the basins and troughs next to the striated ridges contain boulder-bearing materials interpreted as glacial deposits, but they do not have well-developed moraine ridges. Our work tentatively supports the notion that the southern highlands were occupied by a continuous ice sheet moving across a pre-existing landscape ([4], [7]). The presence of abundant valley networks may have resulted from *in-situ* melting of this ice sheet, as suggested by many earlier researchers ([8], [9]).

References: [1] J.S. Kargel & R.G. Strom (1992) *Geol. 20*, 3-7. [2] J.S. Kargel et al. (1995) *JGR 100*, 5351-5368. [3] B.K. Lucchitta (1980) *LPSC 11,* 634-636. [4] J.L. Fastook & J.W. Head (2014), Planet. Space Sci. 91, 60-76. [5] D. Benn, D., & D.J. Evans (2014). Glaciers and glaciation. Routledge. [6] C.B. Atkins (2013) *Geol. Soc. London Spe. Publ. 381*, 299-318. [7] R. Wordsworth et al. (2013) Ica*rus 222*, 1-19. [8] V.R. Baker (2001) *Nature 412*, 228-236. [9] R.M. Ramirez and R.A. Craddock (2018) *NG. 11*, 230-237.

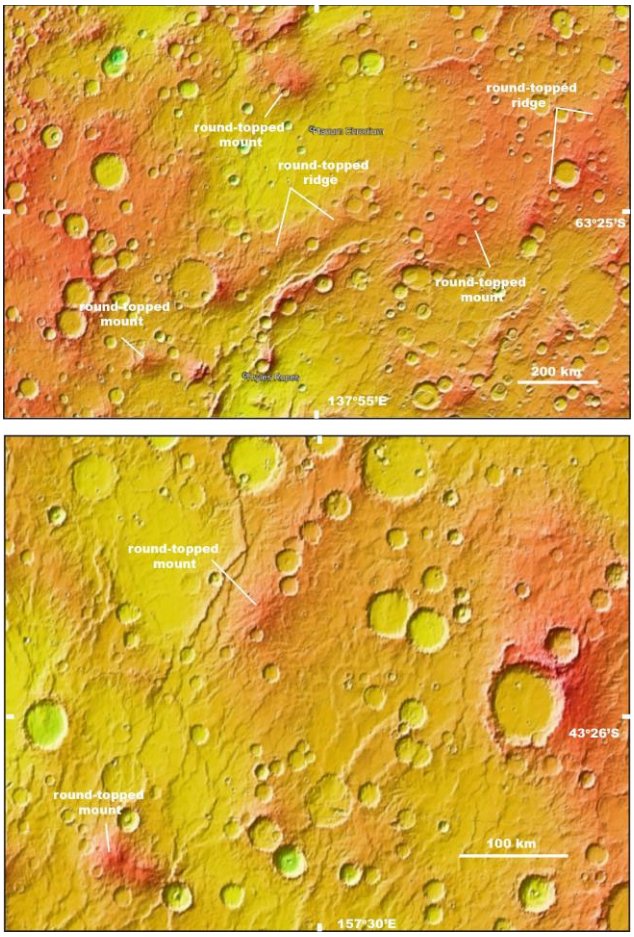

Figure 1 (above). Round-topped ridges and mounts in southern highlands of Mars. Note that the linear ridges bound linear troughs or elongated basins where the density of craters is significantly less than that of the nearby ridges.

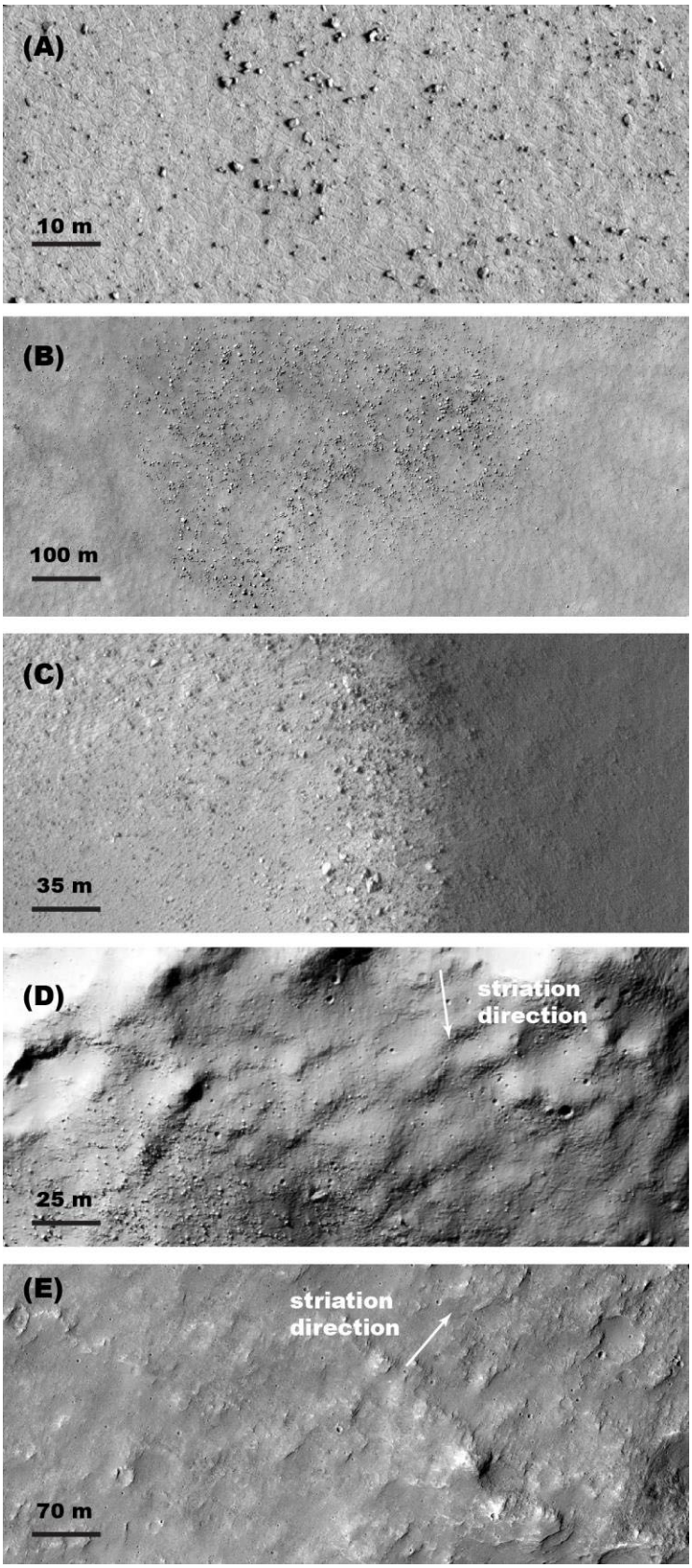

Figure 2 (right). A south-to-north display of surface textures of linear round-topped ridges across southern highlands. (A) smooth polygonal surface dotted by scattered boulders (PSP_005761_1145). (B) Patterned boulder arrangements on a ridge surface (ESP_013989_1185). (C) Boulder material exposed at the wall of an impact crater (ESP_011628_1260). (D) Striated surface with scattered boulders on the ridge surface (ESP_017482_1440). (E) Striated ridge surface without the presence of boulders (ESP_037591_1535).

PLACING CONSTRAINTS ON THE COMPOSITION AND EMPLACEMENT OF THE DORSA ARGENTEA FORMATION. J. L. Whitten[1], B. A. Campbell[2], J. J. Plaut[3] [1]Department of Earth and Environmental Sciences, Tulane University, New Orleans, LA 70118 (jwhitten1@tulane.edu), [2]Center for Earth and Planetary Studies, Smithsonian Institution, Washington DC, 20013, [3]NASA Jet Propulsion Laboratory, California Institute of Technology, Pasadena, CA.

Introduction: The Dorsa Argentea Formation (DAF) represents a large potentially ice-rich deposit, dated to the Early Hesperian period [1–3], that encircles the Amazonian-aged south polar layered deposits (SPLD). The DAF has been interpreted as the remnants of an Hesperian-aged ice cap that has largely melted away, but other formation mechanisms are still under consideration (e.g., volcanic activity, debris flows, aeolian deposition) [2, 4–7]. This interpretation means that the DAF represent the oldest record of climate in the south polar region of Mars and, if it occurred, may preserve evidence for the presence of multiple ice sheets in the south polar region throughout the geologic history of Mars.

The DAF is an areally extensive deposit, ~1.5×10^6 km^2 (Fig. 1). Most of the DAF is contiguous, except for a deposit of material on the floor of the Prometheus Basin around 90°E. The DAF extends from the northernmost extent of the SPLD up to 55°S. There is a diverse suite of geologic landforms contained within the DAF, including pedestal craters, sinuous ridges, and pitted terrain. Previous researchers have subdivided the deposit into up to six morphologic subunits [2, 5].

If volatile-rich materials are detected in the DAF, that would provide support for a glacial origin. Here, we use a combination of radar sounder data, topography and imagery to characterize the composition of DAF materials. Because DAF represents one of the oldest and largest potential water ice reservoirs, determining its composition would provide critical information for understanding the early climate fluctuations and the hydrological cycle on Mars.

Methods: Radar sounder data from both the SHARAD instrument on NASA's Mars Reconnaissance Orbiter spacecraft [8] and the MARSIS instrument on ESA's Mars Express [9] are used to map subsurface radar reflectors in the south polar region of Mars. SHARAD has a chirp frequency center at 20 MHz and a bandwidth of 10 MHz. The along-track resolution of the data is 0.3–1.0 km and the vertical resolution is ~15 m in free space, or ~8 m in geologic materials. MARSIS operates at four frequencies (1.8, 3.0, 4.0, and 5.0 MHz) and has a bandwidth of 1 MHz. The along-track resolution of the MARSIS dataset is 5–10 km and the cross-track resolution is on the order of 10–30 km.

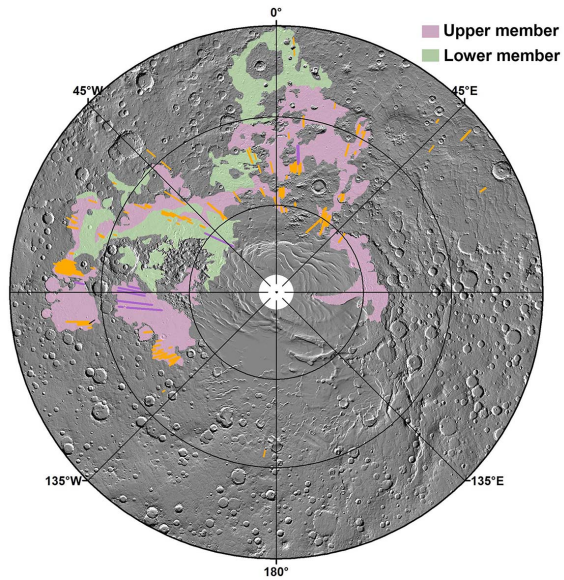

Figure 1. Location of SHARAD subsurface reflectors identified in the DAF (orange lines). Purple lines are SHARAD surface reflectors associated with confined near-subsurface scattering. Geologic map of the upper and lower members of the DAF [5, 11].

For this study, MARSIS data collected at 4.0 and 5.0 MHz and processed using the technique of [10] are used to identify and map the distribution of subsurface reflectors that correspond to the mapped extent of the DAF [5, 11]. Loss tangent values were calculated [e.g., 12, 13], assuming a homogeneous layer of material between the surface and subsurface radar reflectors, to estimate the composition of the materials.

In addition to the radar datasets, Context Camera (CTX) images and Mars Orbiter Laser Altimeter (MOLA) Precision Experiment Data Record (PEDR) data are employed to estimate the thickness of materials in the pitted regions of the DAF (Fig. 2) and assessing the morphology of the surface immediately above detected SHARAD and MARSIS reflectors. Thickness measurements will be used to assess plausible dielectric constant values for materials adjacent to DAF cavi deposits. CTX data will also be used to assess variations in morphology, based on the extent of the six DAF subunits identified [2], and differences in radar properties observed in the SHARAD and MARSIS datasets.

Preliminary Results: Several dozen MARSIS tracks were used to calculate loss tangent values for the

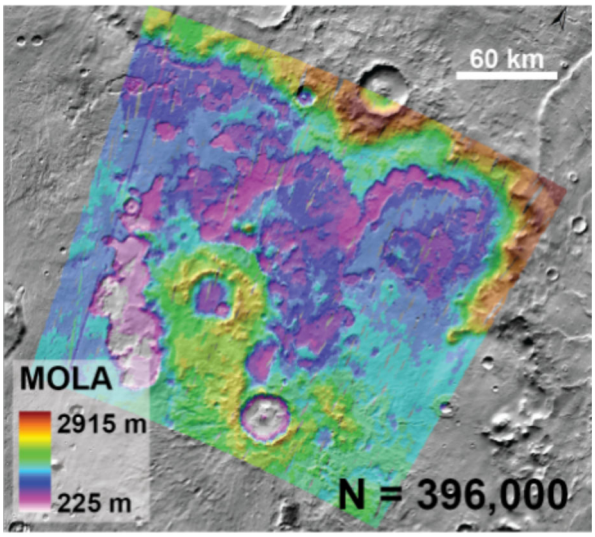

Figure 2. Variations in the thickness of the pitted terrain of Sisyphi Cavi that can be used to estimate the dielectric constant of proximal SHARAD tracks. MOLA PEDR data, 396,000 points.

DAF. The majority of the MARSIS data gave relatively high loss tangent values, >0.005, consistent with values derived for dry sediment [12] and basalt [13] using SHARAD data. Less than five tracks produced values consistent with some fraction of water ice (<0.005 [14]) (Fig. 3). Based on an assessment of confidence levels, the higher loss tangent calculations are more reliable than the lower values. This has to do with the increased variability in power and time-delay for the MARSIS dataset, compared with the SHARAD dataset.

Identified SHARAD reflectors in the DAF are much closer to the surface and represent a change in material properties in the near subsurface. Several identified subsurface SHARAD reflectors are near Cavi Angusti and Sisyphi Cavi. These SHARAD reflectors will be used to approximate the dielectric constant of the DAF in these regions, assuming a thickness derived from the MOLA PEDR measurements. Preliminary measurements of Sisyphi Cavi produce thickness estimates on the order of 100 m to 500 m. Most of the Sisyphi Cavi materials have a depth of ~200 m.

There is a loose correlation between the different behaviors observed in SHARAD data and at least two geologic subunits identified in the DAF (Fig. 1). Focused reflectors are identified in SHARAD data, as well as discrete regions of near-subsurface scattering. Generally, the regions of near-subsurface scattering are associated with the upper member of the DAF, while the more focused subsurface reflectors are associated with the lower member of the DAF. These results will also be compared with the six subunits that have been defined [2].

The current loss tangent results suggest that the DAF is composed predominantly of dry sediments or more consolidated materials, such as basalt. Based on the derived loss tangent results and other geologic landforms observed within the DAF (e.g, pedestal craters, cavi, dorsa, channels originating from the DAF boundary), the deposit was likely emplaced as a large ice sheet was receding or melting. Any volatiles associated with the original incarnation of the DAF have been removed from the current DAF materials; there is little evidence for preserved ancient massive ice in the DAF.

References: [1] Plaut J. J. et al. (1988) *Icarus, 75,* 357–377. [2] Tanaka K. L. & Kolb E. J. (2001) *Icarus, 154,* 3–21. [3] Kress A. M. & Head J. W. (2015) *PSS,* 109–110, 1–20. [4] Head J. W. & Pratt S. (2001) *JGR,* 106, 12275–12299. [5] Tanaka K. L. & Scott D. H. (1987) USGS I-Map 1802-C. [6] Kargel J. S. & Strom R. G. (1992) *Geology*, 20, 3–7. [7] Jöns H.-P.(1992) *LPSC* 23, Abstract 1314. [8] Seu R. et al. (2004) *PSS*, 52, 157–166. [9] Picardi G. et al. (2005) *Science, 310*, 1925–1928. [10] Campbell B. A. and Watters T. R. (2016) *JGR*, 121, 180–193. [11] Skinner J. A. et al. (2006) *LPSC* 37, abstract #2331. [12] Campbell B. A. et al. (2008) *JGR*, 113, E12010. [13] Carter L. M. et al. (2009) *GRL*, 36, L23204. [14] Plaut J.J. et al. (2007) *Science*, *316*, 92–95.

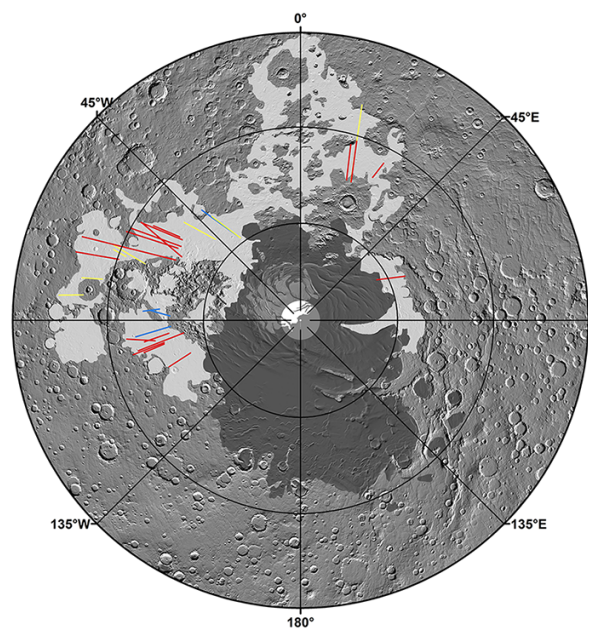

Figure 3. Loss tangent results derived from the MARSIS dataset. Red lines correspond to materials with loss tangent values from 0.010 to 0.037 that are consistent with more consolidated materials. Yellow lines represent loss tangent values between 0.005 and 0.009 (dry sediment) and blue lines represent values <0.005, consistent with water ice.

- / ', .) . / 1 3 0/ , 1 1' 2 4 , 0 24 1(' 3' 5 3 4 1' . 1' '. 3 1' 24 1(.)
A. X. Wilcoski and P. O. Hayne, Laboratory for Atmospheric and Space Physics, University of Colorado, Boulder CO 80309 (andrew.wilcoski@lasp.colorado.edu).

CA@8D7C@ The Martian North Polar Residual Cap (NPRC) is a water ice deposit that overlies most of the North Polar Layered Deposits (NPLD). The NPRC is thought to be the topmost layer of the NPLD and the portion of the NPLD that is currently interacting with the atmosphere [1]. The present-day mass balance of the NPRC is not known, nor is it clear if it is in a current state of net accumulation or ablation. Observations of the NPRC surface have shown evidence for both accumulation and ablation, which may vary depending on region and time of year [2,3]. Landis et al. (2016) estimated the surface age of the NPRC to be ~1.5 ka, and suggested that this age likely corresponds to a recent resurfacing event [4].

The surface texture of the NPRC may hold clues as to its current mass balance and age. The NPRC surface is characterized by depressions and mounds that have dominant spatial wavelengths on the order of ~10 m and heights of ~1 m [5]. This texture has been compared to sublimation hollows observed on terrestrial snow/ice sheets, suggesting it may indicate net ablation [6]. We model the evolution of this surface texture in time and explore its utility as evidence of net accumulation or ablation. We investigate the timescales over which these features form and suggest that the characteristic wavelengths of surface features on the NPRC may be indicative of the exposure ages of those surfaces.

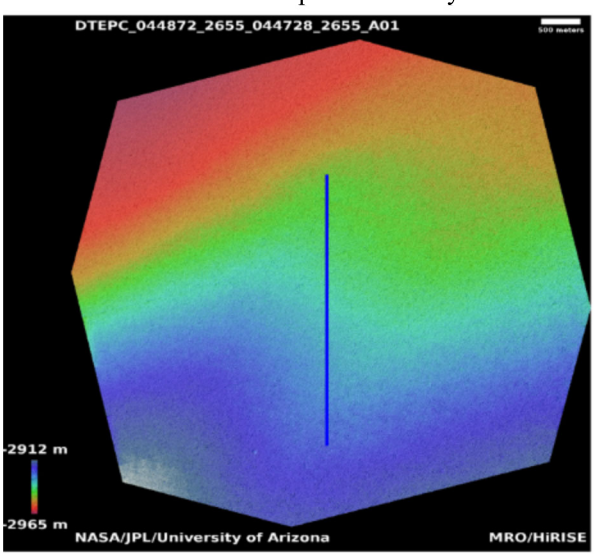

(= DA9 HiRISE DTM of the NPRC surface. Color represents elevation. The blue vertical line denotes the transect along which a cross-section was taken. The power spectra of this cross-section is shown in Figure 3, along with that of a modeled cross-section. (DTEPC_044872_2655_044728_2655_A01) (NASA/JPL/University of Arizona)

- 9C<@8B We use a 1D coupled thermal and atmospheric model to calculate ice fluxes on a perennial NPRC ice surface. The thermal model balances incident energy due to solar radiation adjusted for atmospheric effects, reradiated and reflected energy from nearby surfaces, vertical heat conduction, and latent heat exchange, with infrared emission from the surface in order to calculate surface temperatures. The model also takes into account shadowing from topography and the seasonal accumulation/sublimation of CO_2 frost due to the advance and retreat of the Martian seasonal CO_2 caps. The thermal model is validated using data from the Mars Climate Sounder (MCS) instrument onboard the Mars Reconnaissance Orbiter (MRO) [7]. The atmospheric model mixes water vapor in a 1D vertical column above the surface and calculates water vapor densities directly above the surface, similar to [8]. The upper boundary of the atmospheric model is constrained using water mixing ratio estimates obtained from the Mars Climate Database [9]. Surface temperatures and water vapor densities are used to calculate ice accumulation or ablation that occurs at the surface.

The 1D thermal and atmospheric model is applied to each point on a 2D (height and length) surface. The surface is initialized with small scale (~1 mm) vertical roughness and a uniform power distribution across all wavelengths. The model is run for one Mars-year, after which each point on the surface is adjusted in position based on the ice flux calculated at each point. The model is then multi-stepped over ~10s of Mars-years to decrease computation time, before it is run again. In this manner, the surface is allowed to evolve in time.

We compare the evolved model surface to a Digital Terrain Model (DTM) of the NPRC surface (Fig. 1) derived from a stereo pair of images acquired by the High Resolution Imaging Science Experiment (HiRISE) instrument onboard MRO [10]. We take a cross-section of the DTM (blue line in Fig. 1), subtract out the strong north-south slope of the DTM, and then compare the power spectra of the DTM cross-section with that of the model cross-section.

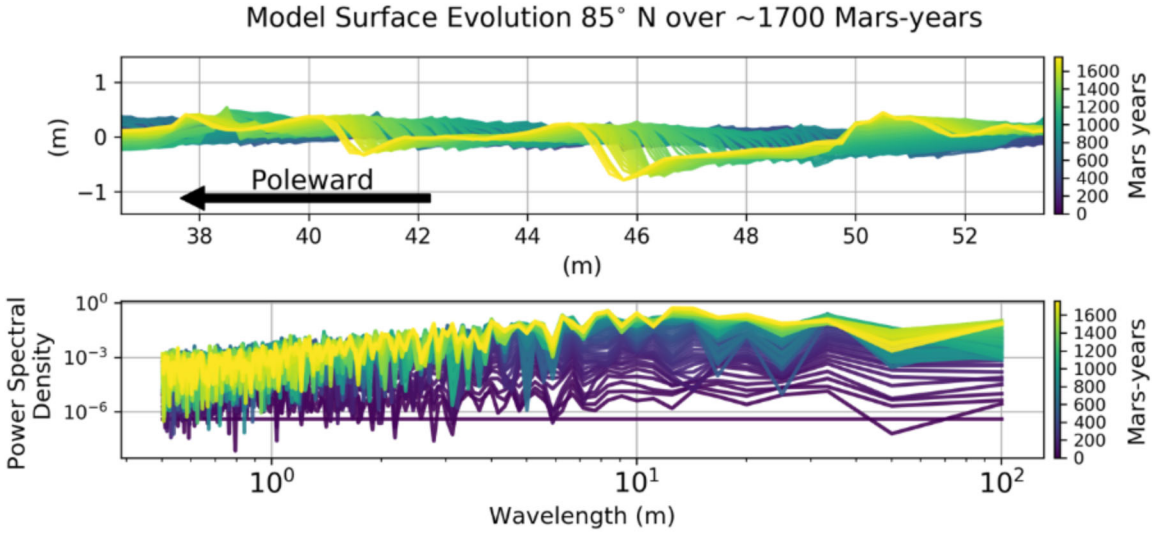

(= DA9 ! An example of a surface evolution model run for a period of ~1700 Mars-years. The top plot shows a ~15 m long section of a 100 m long surface at each stage of its evolution. The color corresponds to time after the beginning of the model run, with initial surface in purple and the final surface in yellow. The bottom plot shows the PSD of the entire surface versus wavelength at each stage of its evolution.

1 9ED CB 6 8 =B7DBB=@ Figure 2 demonstrates the ability of our insolation-driven accumulation/ablation model to grow surface topography over time. Small perturbations to the virtually flat initial surface give rise to depressions and mounds that tend to have steep south-facing slopes and lower angle north-facing slopes, both of which migrate pole-ward with time. The growth of surface topography occurs for both cases of net accumulation and net ablation of ice. This suggests that the NPRC surface texture is not necessarily indicative of net accumulation or ablation.

We use the power spectral density (PSD) of the surface to analyze the wavelengths of the dominant features of the surface over time (Fig. 2). The PSD comes to an equilibrium at shorter wavelengths that manifests as a roughly linear trend in log-log space.

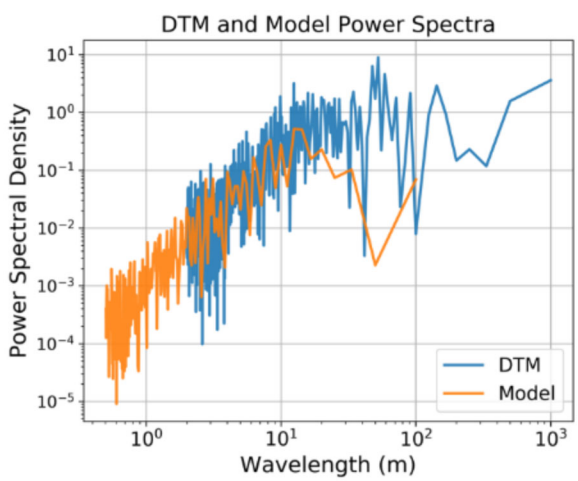

(= DA9 " PSD of the DTM cross-section shown in Fig. 1 compared with the PSD of the final modeled surface shown in Fig. 2.

We define the characteristic wavelength of the surface to be the wavelength of topographic features for which peak power occurs in the PSD. This characteristic wavelength increases over time as surface features grow, suggesting that the characteristic wavelengths of surface features on the NPRC may reflect how long those surfaces have been exposed. Figure 3 shows a comparison of the PSD of a cross-section taken of the DTM in Figure 1 and that of the final surface in the model run shown in Figure 2. The exponential trend in power versus wavelength is shared by both spectra at shorter wavelengths. Both spectra diverge from this trend close to their peak power (i.e. characteristic wavelength). Both cross-sections have characteristic wavelengths on the order of 10 m, as is typical of NPRC surface topography. Our model forms surface topography with characteristic wavelengths on the order of 10 m over ~1000s of Mars-years. This is a comparable timescale to the most recent NPRC surface age estimates made by [4] of ~1.5 ka, and supports the idea of relatively recent resurfacing of the NPRC.

1 9:9A9 79B [1] Tanaka K. L. (2005) *Nature*, 437(7061), 991-994. [2] Langevin Y. et al. (2005) *Science,* 307, 1581-1584. [3] Brown A. J. et al. (2016) *Icarus*, 277, 401-415. [4] Landis M. E. (2016) *GRL,* 43, 3060-3068. [5] Milkovich S. M. et al. (2012) LPSC 43, #2226. [6] Milkovich S. M. and Head J. W. (2006) *Mars,* 2, 21-45. [7] McCleese D. J. et al. (2007), *JGR*, *112*(E5). [8] Bapst J. et al. (2018) Icarus, 308, 15-26. [9] Navarro T. et al. (2014) JGR, 119(7), 1479-1495. [10] McEwen A. S. et al. (2007) *JGR*, 112(E5).

BOULDER-LAYER PAVEMENT ACROSS THE SOUTHERN HIGHLANDS AND COLD-BASED CONTINENTAL-SCALE GLACIATION. An Yin (yin@epss.ucla.edu) and Kobe Y. Wang, Department of Earth, Planetary, and Space Sciences, University of California, Los Angeles, California 90095-156702, USA

Introduction: A first-order question in the studies of Mars is whether most or the entire southern hemisphere highlands were once occupied by a single ice sheet ([1], [2], [3]). A related question is whether the inferred glaciation occurred only in the Noachian ([1], [4]]) or extended into the Hesperian-early Amazonian ([5], [6]) and even the late Amazonian ([7]). Additionally, debate has also been centered on whether the proposed ice sheet was moving through wet-based ([8]) or cold-based ([9], [10], [11]) processes. The two end-member ice-transport models make specific predictions that are testable by photogeologic mapping. The wet-based transport model predicts (1) *water-assisted soft-sediment deformation*, and (2) *presence of eskers, kames, subglacial lacustrine deposits, and drumlins* ([16]). The cold-based transport model predicts (1) *the absence of the aforementioned features* [16], (2) *basal debris entrainment and pavement-like deposition* ([12], [13], [14], (3) *a lack of frontal and lateral moraine ridges* ([14], [15]), (4) *a bimodal sand-boulder size distribution* ([14], [16]), and (5) *partial preservation of pre-glaciation landforms* (e.g., [17]). The goal of this study is to test the two end-member ice-transport models. By doing so we address the fundamental question of whether the southern highlands were once occupied by a single ice sheet.

Data and Methods: MOLA topographic data are used for locating possible glacial flow paths (**Fig. 1**). HiRISE images are then used to examine the landforms and textures of layered deposits exposed on the steep walls of younger craters and cliffs of irregularly shaped cookie-cutter-like depressions. Similar analysis was also conducted along ridges bounding the hypothesized glacier flow paths.

Preliminary Results: *Observations* Our reconnaissance work reveals the widespread occurrence of a boulder-pavement unit across the southern highlands. This unit occurs preferentially in linear troughs and irregularly shaped basins outlined in **Fig. 1**. The boulder-bearing unit filled up older craters and is exposed on the steep walls of younger craters and irregularly shaped depressions (**Fig. 2A**). The surface of the boulder-bearing unit is mostly flat except near the headwater regions of the major outflow channels; the boulder-unit surface is traceable for 10s-100s km and displays much lower densities of craters than those on the surfaces of the bounding high-elevation regions. The boulder-unit surface is commonly associated with irregularly shaped "cookie-cutter-like" depressions (**Fig. 2A**) covered in most sites by a layer of fine-textured and light-toned mantling material; the mantling layer displays polygonal patterns in the south (**Figs. 2B and 2C**) but occurs as a dust layer obscuring bedrocks below in the north near the dichotomy boundary. The boulder-bearing unit is crudely layered and exhibits matrix-support texture (**Fig. 2D**). The clast size of the boulders is ca. 2-5 m, with the percentage and size decreasing northward. The grain size of the supporting matrix is smaller than the pixel size (25-35 cm) of the HiRISE images. The boulder unit locally occurs as piles with outward radiating ridges close to the heads of the major outflow channels; the piles have undulating surfaces and exhibit lobate debris flow/apron features (**Fig. 3**). The higher-elevation regions bounding the boulder-bearing troughs are generally absent of the boulder-bearing units; their surfaces exhibit ostensibly higher densities of craters. Our preliminary survey of the Thaumasia plateau does not reveal a regionally extensive boulder unit associated with irregular depression, filled craters, and lobate flow features.

Interpretations. The parallel layering at scales of > a few km to a few tens of km suggests that the boulder material was laid down through a blanketing process, either by deposition of impact ejecta or a high-energy-transported sediments. However, the generally absence of the boulder pavement unit along the trough-bounding ridges in the southern highlands suggests that the boulders were laid down preferentially in topographically low regions, which is not consistent with the impact-ejecta interpretation. In addition, the close association of boulder deposits with lobate-flow features and irregularly shaped cookie-cutter-like depressions also does not support the impact-deposition interpretation. Here, we suggest that the boulder-pavement unit has a glacial origin: lobate features are ice-bearing debris and irregularly shaped depressions were sites of ice blocks removed by sublimation. The absence of (1) lateral and frontal moraine ridges, (2) drumlins, and (3) water-assisted soft-sediment-deformation features rule out wet-based ice-transport processes. The lack of boulder pavement in the Thaumasia plateau suggests that the interpreted glaciation predates the latest Noachian and early Hesperian. Thus, our preliminary results favor the cold-based – ice-transport mechanism and the Noachian icy-highlands hypothesis [4]. The lack of boulder deposits along the ridges bounding the linear troughs and irregularly shaped basins in **Fig. 1** is also consistent with a cold-based ice-transport mechanism [14]. Rather than a single ice sheet as suggested in the earlier studies (e.g.,

[1], [4]), we envision that the southern highlands were occupied mostly by numerous valley glaciers (**Fig. 1**). Outbursts of supra-glacial lakes and breakthrough of large englacial reservoirs may have created episodic flooding along the outflow channels. The cold valley ice was mostly sublimated away *in situ* without creating large liquid-water lakes.

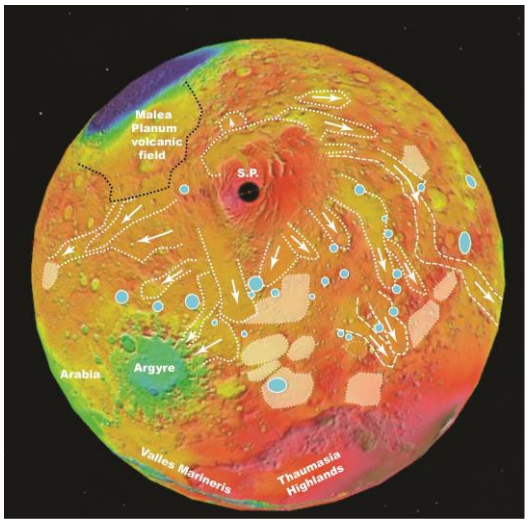

Figure 1. Hypothesized pathways of valley glaciers across southern highlands (white dashed lobes) and glaciated topographic depressions (gray regions).

References: [1] J.S. Kargel & R.G. Strom (1992) *Geol. 20*, 3-7 [2] R. Wordsworth et al. (2013) Ica*rus 222*, 1-19. [3] R.M. Ramirez and R.A. Craddock (2018) *NG. 11*, 230-237. [4] R. Wordsworth, *AREPS 44*, pp.381-408. [5] V.R. Baker et al. (1991) *Nature 352*, 589-594 [6] V.R. Baker (2001) *Nature 412*, 228-236. [7] Dickson et al. (2008) *Geol. 36*, 41-44. [8] J.S. Kargel et al. (1995) *JGR 100*, 5351-5368. [9] B.K. Lucchitta (1980) *LPSC 11,* 634-636. [10] J.L. Fastook & J.W. Head (2014), Planet. Space Sci. 91, 60-76. [11] J.P. Cassanelli and J.W. Head (2015) Icarus 253, 243-255. [12] G.S., Boulton (1970) *J. glacio. 9*, 213-229. [13] C.M. Clapperton (1975), *J. glaocio. 14*, 395-406. [14] C.B. Atkins (2013) *Geol. Soc. London Spe. Publ. 381*, 299-318. [15] M.A. Paul & N. Eyles (1990) *Quat. Sci. Rev 9*, 51-69. [16] M.J. Hambrey & N.F. Glasser (2012) *Sed. Geol. 251*, 1-33. [17] P.R. Bierman et al. (2015) Geol. 43, p. 1059-1062.

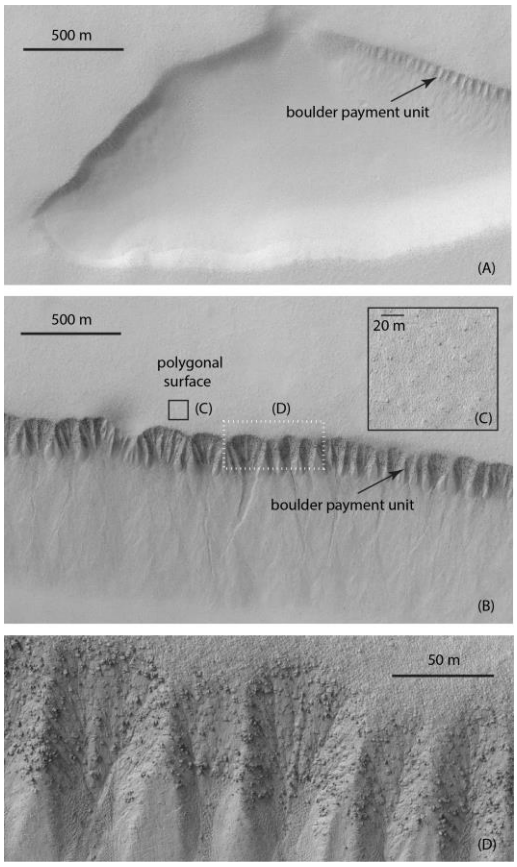

Figure 2. (A) "Cookie-cutter-like" depression. (B) and (C) Polygonal mantling surface. (D) Matrix-supported boulder unit. All from HiRISE image ESP_013651_1075.

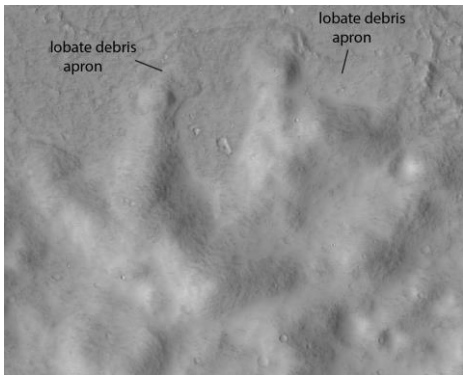

Figure 3. A boulder-bearing pile with lobate debris aprons and undulating surface (HiRISE image PSP_003279_1585).

ASSESSING TERRESTRIAL DUST WITHIN ICE CORES AS A PROXY FOR DUST TRAPPED IN THE POLAR LAYERED DEPOSITS OF MARS. Z. Yoldi[1], C. Hvidberg[1], P. Vallelonga[1] and H. Kjær[1], [1]Physics, Ice and Climate of Earth. Niels Bohr Institute, University of Copenhagen. (zurine.yoldi@nbi.ku.dk)

The Polar Layered Deposits (PLDs) of Mars: Layered deposits of ice and dust cover the Martian poles. PLDs have been mapped with unprecedented accuracy by optical, topographic and radar techniques from orbiter missions, revealing a stratigraphy thought to be linked with changes in the orbital parameters of Mars [1, and references therein]. Thus, PLDs constitute a record of the past climate of the planet. During the last decades, many efforts have been made to correlate these layers with the orbital evolution of the planet [e.g. 2, 3, 4].

Fig 1: North polar layered deposits (NPLD) as seen by HiRISE [5].

Dust in Terrestrial Ice Cores: At the same time, ice sheets on Earth reflect glacial-interglacial climate changes and temperature variations in sequences of high and low dust concentrations [6]. The accessibility of terrestrial ice allows for in-situ measurements of the dust trapped within the ice. For instance, the study of ice cores from Greenland and Antarctica has shown that production, transport and deposition of dust on Earth is influenced by climatic changes on glacial-interglacial scales: temperature variations during glacial periods account for up to 90% of the dust variability, whereas dust and temperature are not correlated during interglacial periods [7]. Such studies are essential inputs to the study of dust and climate coupling on Earth; we know now that dust is a key element in the climatic system of Earth that both affects and responds to climate change [8,9]

Fig 2: Scan image from a Greenlandic glacial ice core. Bright layers reveal the presence of dust, while black layers are pure ice. Image extracted from [10].

Focus on the Size and Shape of the Dust: On Earth, the study of dust particles informs of the atmospheric transport, the storminess, the conditions in the local source regions, etc. The isotopic composition of the particles reveals the origin of the dust, the size distribution is used to distinguish local or remote dust sources, or tephra layers [11]. The size of particles trapped in the ice informs as well about the atmospheric transport; for instance, the altitude at which dust is transported or the patterns in the wind needed to deliver it [8]. The shape of the particles influences their radiative interaction and settling behaviour. [12]

Furthermore, the size and shape of dust have shown to be crucial in modelling the reflectance from ice and dust mixtures [13]. By understanding the patterns in size and shape of the particles that get trapped in terrestrial ice, we can make assumptions on the size and shape of the particles trapped on Mars, which will eventually allow us to link deposition models [2] to brightness measurements of the PLD [3].

Introducing a Collaboration Between Mars and Earth Scientists: The Martian community can vastly profit from the studies that our terrestrial counterpart conducts on the ice core archives of dust. Indeed, the similarity between the questions addressed by the terrestrial and planetary communities is striking, yet no many links have been established between these communities.

We present an on-going collaboration at the University of Copenhagen between Martian and terrestrial ice and dust scientists. We will first give an overview of the dust and climate coupling on Earth as an exercise of comparative planetology. Then, we will show results of particle size measurements retrieved from a melting campaign conducted in Copenhagen with continuous flow analysis (CFA) and discuss the repercussion and viability of extrapolation to the dust trapped at the Martian PLDs.

References: [1] Smith I. B. et al. (2016) *Icarus, 308*, 2-14. [2] Hvidberg C. S. et al. (2012) *Icarus, 221,* 405-419. [3] Becerra P. et al. (2017) *GRL, 44*, 66-70. [4] Becerra P. et al. (2019) *GRL, 46,* 7268-7277 [5] McEwen A. S. et al. (2007) *JGR, 112* [6] Steffensen J. P (1997) *JGR:Oceans, 102* [7] Lambert F. et al. (2008) *Nature, 452* [8] Vallelonga P. T. and Svensson A. (2014) *Springer Science*, 463-485 [9] Shaffer G. and Lambert F. (2018) *PNAS, 115*, 2026-2031 [10] Svensson A. et al. (2005) *JGR, 110* [11] Aarons S. M. et al. (2017) *QSR, 162,* 60-71 [12] Scheuvens D. and Kandler K. (2014) *Springer Science*, 15-50 [13] Yoldi Z. et al. (2015) *GRL, 42*, 6205-6212

Building An archive Library On Mars

Svetozar Zirnov, Austin Mardon,

The Antarctic Institute of Canada

Contact:aamardon@yahoo.com

Abstract:

This paper outlines the importance and necessity of building an archive library on mars moon, and the effect it may have on future generations and our distant descendants. Building an archive library will help in many ways and one of them is by preserving the history of humanity, civilization, and the history of the various cultures, nations, languages, genres, and time periods for generations to come and by preserving humanity's collective knowledge for our distant descendants to use. A non-profit organization called the "Arch Foundation" which was created in 2015 with a goal of setting up archives of humanity's culture in various places throughout the cosmos in order to inspire people about space. Thus, building a lunar library will help to create a backup of humanity's history and knowledge from natural disasters, equipment impairments, wars, and other worldly problems. So, this way all that humanity has produced may be preserved for millions or billions of years in space, so that future humans may find it, read it, and use it for their own achievements and survival. All the collected data will be put on a DVD- sized metal disk which will have 200GB of data. All the data will be stored on 25 nickel disks and each of them would be about 40 microns which is approximately 1 of 600th of an inch thick. Building an archive library will help us be assured that all the knowledge that we as humans have generated over time is not going to be lost forever, but will be preserved for future generations and our distant descendants, and hopefully may be used by them for their own benefits and achievements.

References:

[1] How to Build a Billion-Year Library on the Moon. (2019, April 02). Retrieved from https://thenewstack.io/how-to-build-a-billion-year-library-on-the-moon/

[2] Messier, D. (n.d.). The Arch Mission Foundation Announces Launch of Lunar Library Aboard Beresheet Lander. Retrieved from http://www.parabolicarc.com/2019/02/25/arch-mission-foundation-announces-launch-lunar-library-aboard-beresheet-lander/

The Use of Mars Lava Tubes As Emergency Shelters and Storage

Svetozar Zirnov, Daniel Polo, Austin Mardon

The Antarctic Institute of Canada

Contact: aamardon@yahoo.ca

Abstract:

This paper outlines the importance of Mars lava tubes and how they may be used as emergency storages for supplies and emergency dwellings, once humans will step on Mars' surface again. Lava tubes are formed from fast moving lava which later on cools and thus constitutes caves that may serve for various functions on future space explorations to Mars. There are many issues that astronauts may face while on a space exploration mission to Mars, which include but are not limited to fatal levels of radiation, exposure to rapidly changing extreme temperatures, as well as falling micrometeorites. While on Mars' surface, radiation levels are much higher than those on earth, and exposure to such fatal levels of radiation is both harmful to the human body, and even deadly. Radiation comes in many ways on Mars' surface such as solar flares which are constituted similarly to the solar wind, but the individual particles hold higher energies, and galactic cosmic rays which are composed of very high energy particles, mostly protons and electrons. Lava tubes may help to protect astronauts from such levels of radiation, while on a space mission. Also, it is important to take into account that while on earth we have an atmosphere and magnetic field which are able to provide sufficiently great protection from the high levels of radiation, while Mars lacks it. Exposure to extreme temperatures likewise must be taken into account, for Mars is located further from the sun, than the earth, thus the temperatures on Mars are much colder than on earth. The average daytime temperature on Mars in the winter season is about -80 degrees Fahrenheit, or -60 degrees Celsius in the daytime, while about -195 degrees Fahrenheit, or -125 degrees Celsius at night. In the summer time, the average daytime temperature is heating up to about 70 degrees Fahrenheit and 20 degrees Celsius.

References:

[1]Dunbar, B. (2009, July 14). Micrometeoroids and Space Debris. Retrieved from https://www.nasa.gov/audience/foreducators/topnav/materials/listbytype/Micrometeoroids_Space_Debris.html.

[2] Williams, M. (2016, November 21). How bad is the radiation on Mars? Retrieved from https://phys.org/news/2016-11-bad-mars.html

[3] Sharp, T., & Sharp, T. (2017, November 30). What is the Temperature of Mars? Retrieved from https://www.space.com/16907-what-is-the-temperature-of-mars.html

Keywords:

Mars, Lava tubes, Emergency Shelters, Storage, Surface, Space exploration, Radiation, Extreme temperatures, Micrometeorites.